UNIVERSITY OF LJUBLJANA
FACULTY OF MATHEMATICS AND PHYSICS

Janez Gale

# Fluid-Structure Interaction for simulations of fast transients

Doctoral thesis

ADVISOR: Prof. Dr. Iztok Tiselj
CO-ADVISOR: Prof. Dr. Leon Cizelj

Ljubljana, 2008

UNIVERZA V LJUBLJANI
FAKULTETA ZA MATEMATIKO IN FIZIKO

Janez Gale

# Sklopitev linijske konstrukcije in dvofaznega toka tekočine med hitrimi prehodnimi pojavi

Doktorska disertacija

MENTOR: prof. dr. Iztok Tiselj
SOMENTOR: prof. dr. Leon Cizelj

Ljubljana, 2008

*To manage a system effectively,*

*you might focus on the interactions of the parts*

*rather than their behavior taken separately.*

Russell L. Ackoff

**Acknowledgements/Zahvale**

This work was financially supported by the Ministry of Higher Education, Science and Technology, Republic of Slovenia (contract number 3311-02-831052), and the Reactor Engineering Division of Jožef Stefan Institute.

It is meaningless to put so much effort on study of interactions between matters and at the same time to forget the most important interactions between people! I am grateful to my supervisors, all coworkers, colleagues and friends for all personal interactions i.e. professional and technical assistance, discussions, even chats, understanding and every nice word or smile. Iztok, Robi, Andrej P., Luka Š., Zoran, Matjaž, Boštjan K., Tanja, Leon, Borut, Miro, Andrija, Andrej S., Mitja, Ivo, Mare K., Marko, Igor, Boštjan Z., Ljubo, Iztok P., Romana, Zlata, Petra, Luka S., Melita, Mare G., Tone (dr. Anton Bergant, for discussion and experimental data), Arris (dr. Arris Tijsseling, for experimental data and correspondence), and other unnamed friends: Thank you!

Interaction refers to exchange of energy, and no energy was more valuable to me than energy gained from the family. Branka, Teja and Anja: your missing and tired daddy is thankful to you!

# Fluid-Structure Interaction for simulations of fast transients

**Keywords:**
- Arbitrarily shaped fluid-filled piping systems
- Fast transient (water hammer)
- Two-phase flow (cavitation)
- Structural dynamics
- Fluid-Structure Interaction
- Characteristic upwind numerical method

**Abstract:** The Fluid-Structure Interaction (FSI) in one-dimensional arbitrarily shaped and deformable piping systems of circular cross-section conveying a single or two-phase transient flow is being studied. The pipe wall, which represents the control volume for the fluid, exhibits significant deformations as the FSI evolves in considerable extent. The physical model for the thermo-fluid dynamics i.e. the balance equations, which originate from the Navier-Stokes system of equations, is derived for two-phase flows in arbitrarily shaped and deformable piping systems (Lagrangian coordinate system). New terms appear in the balance equations for the description of the junction coupling FSI mechanism at curvatures of the pipe, for the description of the pipe deformations and for the description of the Poisson coupling FSI mechanism. The developed physical model enables simulations of two-phase flow transients in arbitrarily shaped piping systems. It is strongly coupled with axial structural dynamics and relatively weakly with lateral, rotational and torsional structural dynamics. The axial, lateral, rotational and torsional structural dynamics models are derived for a general arc length parameter and are applicable for arbitrarily shaped piping systems. Several new terms appear for the junction coupling between basic variables at curvatures.

The thermo-fluid dynamics and the structural dynamics equations are grouped into several physical models of various complexities, applicable for various FSI problems. The applied physical models are nonlinear i.e. the eigenvalues and the eigenvectors of the system are changing with time and position. The eigensystem is then linearized for each control volume within each computational time step. The high-resolution characteristic upwind finite difference numerical method, which is based on Godunov methods for conservation laws, is applied for integration of the physical model. The method behaves as a second order accurate. An essentially explicit scheme applies implicit iterations when needed to solve the problem with stiff source terms. For stiff relaxation source terms, the two-step operator splitting technique is applied, where the convection with the non-stiff terms is solved by means of the characteristic upwind method in a first step, and the relaxation is integrated with first order explicit Euler method in a second, separate step.

The isothermal quasi-two-phase flow model is applied for the description of inertially controled cavitation which accurately describes cavitation in systems where mass and heat exchange between phases is negligible. The accurate description of the elbows and any other curvatures and their stiffness and anchorage is crucial for accurate consideration of the FSI. The flexibility factors were incorporated into the physical model for description of the loss of the stiffness at the curvatures. The physical model further enables reinforcement of the pipe wall at the elbow, enables other kinds of geometric changes, and enables consideration of elastic or stiff supports, external loads, forces etc. The local stress situation in the pipe wall defined by the stress tensor is represented as a scalar value using the von Mises approach.

The proposed advanced physical model and the characteristic upwind numerical scheme are verified by means of experimental data, available verified computer codes and several benchmark problems. The FSI and all accompanying phenomena are successfully simulated by the proposed approach and are discussed in detail. The procedures to control FSI are indicated.

**PACS:** 47.10.-g, 43.40.+s, 45.20.-d, 05.70.-a, 47.55.-t, 02.60.-x, 02.70.Bf

# Sklopitev linijske konstrukcije in dvofaznega toka tekočine med hitrimi prehodnimi pojavi

**Ključne besede:**
- poljubno ukrivljeni cevovodi napolnjeni s tekočino
- hitri prehodni pojav (vodni udar)
- dvofazni tok (kavitacija)
- dinamika konstrukcij
- interakcija med tekočino in konstrukcijo
- karakteristična privetrna numerična metoda

**Povzetek:** V disertaciji smo preučevali interakcijo med tekočino in konstrukcijo (ITK) v poljubno ukrivljenih linijskih cevovodih okroglega preseka napolnjenih z enofazno ali dvofazno tekočino v kateri poteka hitri prehodni pojav. Iz Navier-Stokesovega sistema enačb so bile izpeljane ravnovesne enačbe za dvofazni ali dvotekočinski tok v poljubno ukrivljenem in deformabilnem cevovodu (Lagrangejev koordinatni sistem). Stena cevi namreč predstavlja kontrolni volumen za tekočino; kontrolni volumen pa se lahko v določenih primerih ITK znatno premika in deformira. V enačbah nastopijo novi členi za opis lokalne vozliščne sklopitve v krivinah cevovoda, za opis deformacij cevovoda in za opis mehanizma Poissonove sklopitve med tlakom v tekočini in osne ter obodne deformacije v cevovodu. Izpeljane ravnovesne enačbe tekočine omogočajo simulacije dvofaznega toka v poljubno ukrivljenih cevovodih in so močno sklopljene z osno dinamiko cevovoda, medtem ko je sklopitev s prečno, rotacijsko in torzijsko dinamiko cevovoda razmeroma šibka. Osni, prečni, rotacijski in torzijski modeli dinamike konstrukcije so bili izpeljani za opis poljubno ukrivljenega cevovoda s pomočjo splošnega parametra krožnega loka. V enačbah nastopajo novi členi, ki opisujejo mehanizem vozliščne sklopitve osnovnih spremenljivk v krivinah.

Izpeljane enačbe za termodinamiko tekočine in dinamiko konstrukcije so združene v različno kompleksne fizikalne modele, ki omogočajo simulacije različnih primerov ITK. Tako sestavljeni fizikalni modeli so nelinearni, kar pomeni, da se lastne vrednosti in lastni vektorji sistema enačb spreminjajo tako s časom kot s pozicijo. Pri numeričnem reševanju so enačbe znotraj enega časovnega koraka in znotraj posameznega kontrolnega volumna linearizirane. Za reševanje parcialnih diferencialnih enačb je uporabljena karakteristična privetrna shema visoke resolucije, ki izvira iz numeričnih metod Godunova za ohranitvene zakone. Metoda se obnaša kot metode drugega reda natančnosti. Karakteristična privetrna shema je eksplicitna, vendar se po potrebi uporabi implicitne iteracije za integracijo togih izvirov. Problem togih izvirov zaradi relaksacije med fazama je rešen z integracijo v dveh korakih, pri čemer je v prvem koraku uporabljena osnovna karakteristična privetrna shema, v drugem koraku za relaksacijo (če potrebno) pa eksplicitna Eulerjeva shema prvega reda natančnosti.

V vsakem časovnem koraku se v vsakem računskem volumnu iz parnih tabel izračunajo prave lastnosti stanja tekočine. Za opis inercijsko gnane kavitacije je uporabljen poenostavljen kvazi-dvofazni model dvofaznega toka, ki zelo dobro opiše pojav kavitacije v sistemih kjer je izmenjava toplote in snovi med fazama zanemarljivo majhna. Za natančen opis ITK je potrebno točno opisati kolena in druge krivine cevovoda, njihovo togost in podprtost. Izguba togosti v krivinah cevovoda je opisana s pomočjo faktorja fleksibilnosti. Sistem enačb skupaj z numerično metodo omogoča vključitev raznih izboljšav kot so ojačitve stene cevi v kolenih, druge spremembe geometrije, upoštevanje elastičnih ali togih podpor, zunanje obremenitve ipd. Lokalni tenzor napetosti je predstavljen kot skalarna vrednost s pomočjo teorije von Misesa.

Sistem enačb in uporabljena numerična shema sta bila preverjena z različnim primerjalnimi problemi ITK, z različni preverjenimi programi in eksperimentalnimi podatki. ITK z vsemi spremljajočimi pojavi je bila uspešno simulirana in podrobneje razložena. Nakazane so možnosti preprečitve ITK oziroma možnosti kontrole izmenjave (kinetične) energije med tekočino in konstrukcijo.

**PACS:** 47.10.-g, 43.40.+s, 45.20.-d, 05.70.-a, 47.55.-t, 02.60.-x, 02.70.Bf

# Table of contents


**1. INTRODUCTION ..... 1**

1.1. BASIC CONCEPTS OF FSI ..... 1
1.2. LITERATURE REVIEW ..... 6
*1.2.1. Physical models for FSI ..... 7*
*1.2.2. Numerical methods for FSI ..... 8*
*1.2.3. Two-phase flow and cavitation models for FSI ..... 9*
*1.2.4. Code coupling approach for FSI ..... 9*
1.3. OBJECTIVES AND ACHIEVEMENTS OF THE THESIS ..... 10
1.4. OVERVIEW OF THE THESIS ..... 11

**2. BALANCE EQUATIONS FOR A FLUID IN LAGRANGIAN COORDINATES ..... 12**

2.1. INTRODUCTION ..... 12
2.2. DEVELOPMENT OF GENERAL BALANCE EQUATION ..... 13
2.3. MASS, MOMENTUM AND ENERGY BALANCE EQUATIONS ..... 18

**3. DYNAMICS OF ARBITRARILY SHAPED PIPING SYSTEM ..... 22**

3.1. INTRODUCTION ..... 22
3.2. AXIAL DYNAMICS ..... 23
3.3. LATERAL AND ROTATIONAL DYNAMICS ..... 24
*3.3.1. In-plane dynamics ..... 25*
*3.3.2. Out-of-plane dynamics ..... 27*
3.4. RADIAL DYNAMICS ..... 29
3.5. TORSIONAL DYNAMICS ..... 29
3.6. NATURAL FREQUENCY OF AN ARBITRARILY SHAPED PIPING SYSTEM ..... 30

**4. PHYSICAL MODELS ..... 32**

4.1. FLUID BALANCE EQUATIONS WITH FSI ..... 33
*4.1.1. Two-phase flow with FSI ..... 33*
*4.1.2. Homogeneous equilibrium two-phase flow with FSI ..... 35*
*4.1.3. Isothermal single-phase liquid flow with FSI ..... 35*
*4.1.4. Isothermal quasi two-phase flow with FSI. ..... 36*
4.2. PHYSICAL MODELS IN MATRIX FORM ..... 37
*4.2.1. Thermo-fluid dynamics physical models ..... 37*
*4.2.2. Structural dynamics physical models ..... 40*
*4.2.3. FSI physical models ..... 42*
*4.2.4. Schematic FSI physical models ..... 47*
4.3. INITIAL CONDITIONS ..... 49

**5. NUMERICAL SCHEME ..... 51**

5.1. CHARACTERISTIC FORM OF THE PHYSICAL MODEL ..... 51
5.2. BASIC FINITE DIFFERENCE METHODS ..... 52
5.3. HIGH RESOLUTION FINITE DIFFERENCE SCHEMES ..... 54
5.4. SOURCE TERMS ..... 58
5.5. NUMERICAL ERRORS AND DIFFICULTIES ..... 60
5.6. OUTLOOK OF THE CODE ..... 62
5.7. BOUNDARY CONDITIONS ..... 62

**6. NUMERICAL EXAMPLES ..... 65**

6.1. AXIAL AND LATERAL OSCILLATIONS OF A PIPE ..... 65
6.2. DELFT HYDRAULIC BENCHMARK PROBLEMS ..... 72
*6.2.1. Delft hydraulic benchmark problems A and B ..... 72*
*6.2.2. Delft hydraulic benchmark problems C, D and E ..... 78*
6.3. VALVE CLOSURE EXPERIMENT IN SINGLE ELBOW PIPE ..... 80
6.4. ROD IMPACT EXPERIMENTS IN HANGING PIPING SYSTEMS ..... 87
*6.4.1. Rod impact experiment in a straight pipe ..... 87*
*6.4.2. Rod impact experiment in a single elbow pipe ..... 94*

**7. CONCLUSIONS ..... 105**

**APPENDIX A. GAUSS THEOREM AND LEIBNIZ RULE ..... 115**

**APPENDIX B. DERIVATION RULES FOR VECTORS IN FRESNET FRAME..... 117**

**APPENDIX C. THERMO-FLUID DYNAMICS EQUATIONS IN EULERIAN COORDINATES ..... 119**

C.1. SINGLE-PHASE FLOW EQUATIONS ..... 119
C.2. TWO-PHASE FLOW EQUATIONS ..... 120
C.3. CLOSURE RELATIONS ..... 122

**APPENDIX D. EQUATION OF STATE ..... 126**

D.1. COMPRESSIBILITY AND SPEED OF SOUND ..... 126
D.2. EFFECTIVE SPEED OF SOUND ..... 128

**APPENDIX E. HOOKE'S LAW OF ELASTICITY ..... 129**

**APPENDIX F. TIMOSHENKO'S BEAM THEORY ..... 132**

**APPENDIX G. SKLOPITEV LINIJSKE KONSTRUKCIJE IN DVOFAZNEGA TOKA TEKOČINE MED HITRIMI PREHODNIMI POJAVI - POVZETEK V SLOVENSKEM JEZIKU ..... 134**

G.1. UVOD ..... 134
G.2. RAVNOVESNE ENAČBE V LAGRANGEJEVEM KOORDINATNEM SISTEMU ..... 135
G.3. DINAMIKA POLJUBNO UKRIVLJENEGA CEVOVODA ..... 138
G.4. FIZIKALNI MODELI ZA OPIS ITK ..... 138
G.5. NUMERIČNA SHEMA ..... 141
G.6. RAČUNSKI PRIMER ..... 143
G.7. ZAKLJUČEK ..... 148

# Nomenclature

**Uppercase letters**

| | |
|---|---|
| $A$ | Cross-section ($m^2$) |
| $C_D$ | Drag coefficient |
| $C_i$ | Interfacial friction coefficient |
| $C_{vm}$ | Virtual mass coefficient ($kg/m^3$) |
| $E$ | Young elasticity modulus ($Pa$) |
| $G$ | Shear modulus ($Pa$) |
| $H$ | Vol. heat transfer coeff. ($W/m^3/K$) |
| $I$ | Moment of inertia ($m^4$) |
| $K$ | Fluid bulk modulus ($Pa$), Abbreviations |
| $L$ | Pipe length ($m$) |
| $M$ | Bending momentum ($Nm$) Matrix dimension |
| $N$ | Axial force ($N$) Eigensystem dimension |
| $P$ | Wall surface area ($m^2$) |
| $Q$ | Lateral force ($N$) Interface heat transfer ($W/m^3$) |
| $R$ | Pipe inner radius ($m$) |
| $Re$ | Reynolds number |
| $R_p$ | Radius of curvature ($m$) |
| $S$ | Fluid cross-section area ($m^2$) |
| $S_t$ | Pipe cross-section area ($m^2$) |
| $T$ | Temperature ($K$, $°C$) Abbreviations |
| $T_p$ | Radius of torsion ($m$) |
| $V$ | Volume ($m^3$) |
| $We$ | Weber number |
| $X$ | Saturation quality |

**Lowercase letters**

| | |
|---|---|
| $a_{gf}$ | Interfacial area concentration |
| $b$ | Outer radius of the pipe |
| $c$ | Speed of sound Elements of Jacobian matrix |
| $d_0$ | Average slug diameter ($m$) |
| $e$ | Pipe wall thickness ($m$) Specific internal energy ($J/kg$) |
| $e_{tot}$ | Specific total energy ($J/kg$) |
| $f$ | Frequency ($Hz$) Arbitrary function External force per unit length ($N/m$) |
| $f_{CFL}$ | Time step correction factor |
| $h$ | Specific enthalpy ($J/kg$) Elevation of the rod ($m$) |
| $i$ | Phase factor |
| $k$ | Flexibility factor |
| $m$ | Mass, mass of the load ($kg$) |
| $\dot{m}$ | Mass flux ($kg/s$) |
| $p$ | Fluid pressure ($Pa$) |
| $s$ | General axial coordinate parameter |
| $t$ | Time ($s$) |
| $u$ | Velocity of the pipe ($m/s$) |
| $v$ | Fluid velocity ($m/s$) |
| $x$ | Axial coordinate parameter |
| $x_{Sg}$ | Distance of gravity center to the center of the section ($m$) |
| $w$ | Specific internal energy (J/kg) Displacement ($m$) |

**Uppercase Greek letters**

| | |
|---|---|
| $\Sigma$ | Lateral surface (pipe wall) |
| $\Gamma$ | Vapor generation rate ($kg/m^3/s$) |
| $\Psi$ | Arbitrary variable |
| $\Omega$ | Section perimeter |

**Lowercase Greek letters**

| | |
|---|---|
| $\alpha$ | Angle change at elbow Vapor volume fraction |
| $\beta$ | Shear transformation in lateral shear Damping constant Compressibility ($1/Pa$) |
| $\gamma$ | Pipe inclination Geometrical factor at curvatures |
| $\varepsilon$ | Unit strain Dissipation coefficient (numerical) |
| $\lambda$ | Eigenvalues |
| $\kappa$ | Timoshenko shear coefficient |
| $\nu$ | Poisson ratio |
| $\varphi$ | Rotational velocity ($rad/s$) |
| $\phi$ | Flux limiter Angle of bending rotation |
| $\theta$ | Relaxation time Phase of oscillation |
| $\mu$ | Derivative (scale factor) of $s$ over $s_0$ |
| $\mu_k$ | Derivative (scale factor) of $s$ over $t$ |
| $\mu_f$ | Liquid dynamic viscosity ($kg / m\ s$) |
| $\rho$ | Density ($kg/m^3$) |
| $\sigma$ | Stress ($Pa$) Surface tension ($kg/s^2$) |
| $\omega$ | Angular frequency |

**Subscripts**

| | |
|---|---|
| $0$ | Initial value |
| $1,2,3,4$ | Consecutive number |
| $1F$ | Single-phase flow |
| $2F$ | Two-phase flow |
| $AQ2F$ | Axial quasi-two-phase model |
| $AXI$ | Axial dynamics model |
| $R$ | Relaxation source term |
| $S$ | Enthalpy |
| $T$ | Thermal variables, Temperature |
| $TIM,in$ | In-plane Timoshenko beam model |

| | |
|---|---|
| *TIM,out* | Out-of-plane Timoshenko beam model |
| *TOR* | Torsional dynamics model |
| *b* | Mass of the beam |
| *bub* | Bubbly |
| *c* | Circumferential strain |
| | Valve closing time |
| *cm* | Centric mass |
| *con* | Contraction |
| *d* | Damped |
| *ecm* | Eccentric mass |
| *ext* | Extension |
| *f* | Fluid phase |
| *g* | Gas phase |
| | Gravity |
| *i* | Interphase, interface |
| *k* | *f* for fluid and *g* for gas |
| *m* | Mixture |
| *max* | Maximal value |
| *out* | External value |
| *p* | Index (*p = 1, ..., 8*) |
| *rod* | Rod index |
| *sat* | Saturation |
| *sim* | Simulation |
| *b* | Mass of the beam per unit length |
| *v* | Yield stress |
| *t* | Pipe |
| | Wall friction |
| *x,y,z* | local coordinates |

**Superscripts**

| | |
|---|---|
| *+, -* | positive and negative direction |
| **, **, m* | integration steps |
| *n* | Time level |
| *T* | Transpose |

**Matrices and vectors**

| | |
|---|---|
| **A**, **B** | Matrices of the system in vectorial form |
| **C** | Jacobian matrix |
| **F** | Correction factors (diagonal matrix) |
| **I** | Identity tensor |
| **L** | Eigenvectors |
| $\mathbf{V}_k$ | Viscous part of the stress tensor |
| $\mathbf{\Lambda}$ | Eigenvalues (diagonal matrix) |
| $\vec{\mathbf{F}}$ | Vector of body forces |
| $\vec{S}$ , $\vec{R}$ | Source terms |
| $\vec{\mathbf{U}}$ | Displacement velocity |
| $\vec{\mathbf{n}}$ | Vector normal to the surface |
| $\vec{\mathbf{t}}$ , $\vec{\mathbf{n}}$ , $\vec{\mathbf{b}}$ | Vectors of the Fresnet frame |
| $\vec{v}$ | Vector of fluid velocity |
| $\vec{\psi}$ | Vector of basic variables |
| $\vec{\xi}$ | Vector of characteristic variables |
| $\vec{\varepsilon}$ | Vector of acceptance criterions |
| $\vec{\Omega}$ | Vector of Fresnet frame rotation veloc. |
| $\vec{\varphi}$ | Vector of pipe rotation velocity |
| $\vec{\mathbf{w}}$ | Vector of pipe translations |
| $\vec{\mathbf{\Phi}}$ | Vector of pipe rotations |
| $\vec{\mathbf{M}}$ | Vector of pipe internal moments |

**Abbreviations**

| | |
|---|---|
| *1D* | One-dimensional |
| *2D* | Two-dimensional |
| *3D* | Three-dimensional |
| *CFL* | Courant-Friedrichs-Levy condition |
| *CIWH* | Condensation-induced water hammer |
| *DHB* | Delft Hydraulics Benchmark |
| *FEM* | Finite element method |
| *MOC* | Method of characteristics |
| *NPP* | Nuclear power plant |
| *PDE* | Partial differential equation |
| *SGWH* | Steam generator water hammer |
| *TBT* | Timoshenko beam theory |
| *USAR* | Updated Safety Analysis Report |

**Operators**

| | |
|---|---|
| $\langle\ \rangle$ | Area average on section *S* |

# 1. Introduction

Fluid-Structure Interaction (FSI) is a general term that stands for a phenomenon of **exchange of (kinetic) energy between a moving fluid and a flexible structure**. The extent of the energy exchange strongly depends on the flexibility and/or deformability of the structure and its resistance that is governed by geometric properties, elasticity and anchorage. In equal extent, the energy exchange depends also on the fluid, with its gradient and amplitude of the induced pressure waves, compressibility and other fluid state properties. The FSI appears in the systems where the fluid is conducted by the structure, in the systems where the structure is immersed into the fluid, or both. The FSI field is very comprehensive, spanning from aeronautics, civil engineering, energy production, chemical and oil industry, and many more sciences to finally music instruments and human body. FSI surrounds us (breathing, weather, bottle of soda water, tap water systems, car engine, wind, air resistance, boats, pipelines, etc).

The present thesis is focused on a small fraction of the wide FSI field: on a slender hollow arbitrarily shaped structures conveying and interacting with an internal fluid flow during a water hammer transient. Engineering examples of slender (one dimensional) hollow structures interacting with internal fluid flows are all fluid-filled **piping systems** and other flexible pipes and conduits containing a flowing fluid, central-heating systems, air-vent systems, oil and gas pipelines, heat exchanger tubes, thin-shell structures used as heat shields in aircraft engines, jet pumps, etc. Physiological examples may be found in the pulmonary and urinary systems and in hemodynamics. Pipelines and piping systems provide transport for a wide range of substances (water, chemicals, petrochemicals, etc.) and they fulfill safety functions (cooling systems in nuclear power plants). Pressure pulsations and mechanical vibrations during fast transient occurrence affect performance and safety of the piping system. Failure of the piping system can have disastrous effects, leading to injuries and fatalities as well as to substantial cost to industry and environment. Symptoms include vibrations, noise and fatigue damage to piping systems, supports and machinery. FSI is not a widely recognized phenomenon and it is quite possible that it is responsible for a significant number of unexplained piping failures and other unacceptable behaviors. Tijsseling [113] gave some examples: (i) failure due to the fatigue could in fact be FSI induced; (ii) failure due to the corrosion could again be partially attributed to the FSI.

The FSI in piping systems is a relatively new line of research, especially multi-phase coupling although the roots of the water hammer research dates back in the 18th century. Svingen 1996 [108] classifies the work that has to be done and is being done with respect to the FSI in piping systems into four points:

- Experimental **research** to give a broader basis for development of good computer programs and to increase the general understanding and knowledge.
- Development of **physical models** and numerical schemes compiled into computer programs, both as a research tool and for use in engineering work.
- Make **guidelines** based on experiments, on site measurements and **computer programs** as to show when the FSI is of importance through calculations of a piping system.
- Find **design criteria** for piping systems that can be used for everyday engineering purposes to prevent unwanted FSI to occur.

The research work presented in this dissertation directly addresses the second point, development of advanced physical models and numerical schemes. The first point (experimental research) is used to validate the developed computer program, while the third and the fourth naturally result from the analysis of the obtained results.

## 1.1. Basic concepts of FSI

**Fluid dynamics.** The fluid dynamics is the sub-discipline of the fluid mechanics dealing with fluids (liquids and gases) in motion. The solution of the fluid dynamics problems typically involves the calculation of various properties of the flow, such as velocity, pressure, and temperature, as functions of space and time. Hydrodynamics, also known as hydraulics is fluid dynamics applied to liquids, such as

water, alcohol, oil, and blood. Fluid dynamics concerns water hammer in single-, two-, and multi-phase flows.

The **single-phase water hammer**, more generally fluid hammer (it can be induced in any fluid), also named hydraulic transient, is a pressure surge or wave caused by kinetic energy of a fluid in motion when it is forced to stop or to suddenly change flow velocity or direction. Pressure waves are spreading inside the fluid at the acoustic velocity. For example, a rapidly closed valve at an end of a piping system initially conveying steady state flow, generates an upstream propagating water hammer wave (example in Appendix C, Figure C-2). The magnitude and the traveling velocity of the pressure wave strongly depend on the state properties of the fluid (density, speed of sound, temperature, etc.).

The research on single-phase water hammers has a long tradition starting with Blaise Pascal in 15$^{th}$ century. Joukowsky [66] already in 1898 developed the fundamental equation of the single-phase water hammer that relates pressure changes $\Delta p$ to velocity changes $\Delta v_f$ in the fluid:

$$\Delta p = \rho_f c_f \Delta v_f \tag{1}$$

where $c_f$ is the speed of sound and $\rho_f$ is the density. The equation is known as Joukowsky equation. However there are several other researchers like Frizell 1898 [42], Kries 1883 [73], Rankine 1870 [5], and Allievi 1903 [3,4] who separately derived Eq. (1) unaware of the achievements of their contemporaries. According to Wylie and Streeter [150], the classical water hammer equations (continuity and momentum balance) for a fluid in Eulerian coordinates read:

$$\frac{1}{\rho_f c_f^2}\frac{\partial p}{\partial t} + \frac{\partial v_f}{\partial s} = 0 \qquad \text{and} \qquad \rho_f \frac{\partial v_f}{\partial t} + \frac{\partial p}{\partial s} = 0 \tag{2}$$

where $p$ is the pressure, $t$ is the time, and $s$ is the axial coordinate parameter. The classical water hammer theory describes the propagation of pressure waves in single-phase liquid-filled piping systems. Wylie and Streeter [150] showed that the classical theory correctly predicts extreme pressures and wave periods, but it usually fails in accurately calculating damping and dispersion of wave fronts, since field measurements usually show more damping and dispersion.

The **two-phase** (liquid-vapor) and two-fluid (liquid-liquid) **water hammer** flows are common in practice. During the water hammer in a liquid, the pressure can cycle between large positive and negative values. The magnitude of the negative values is constrained by the saturation pressure. Vapor cavities can form when the pressure drops to the saturation pressure. There are two relaxation phenomena alternating in two-phase single-fluid flow during the fast transient: vaporization and condensation. Vaporization and condensation of the bubbles considerably affect the transportation of the water hammer waves and consequently FSI and have to be described accurately. The speed of sound in two-phase flow is drastically reduced (from *~1450 m/s* to *~10 m/s*), and a section with two-phase flow can actually split the transient in the fluid into two independent transients/sections at the left and right side of the vapor. These liquid sections are re-connected after condensation of the cavities and the two colliding fluid columns generate an additional pressure wave that is superimposed to the existing transient. Two-phase flow with local cavitation concentrated in a single position is usually denoted as column separation water hammer (one large bubble). Cavitation can be also distributed along larger sections of the piping system (bubbly flow region). Vapor bubbles i.e. cavities in a particular section of the pipe appear as a consequence of the thermodynamical state in the fluid or as a consequence of the flow convection.

Ishii and Hibiki [62] stated that the two-phase flow thermo-fluid dynamics is “an order of magnitude” more complicated subject than that of the single-phase flow due to the existence of moving and deformable interfaces and the interactions with the phases. Each particular phase of the two-phase flow is described with a system of conservation laws derived from the Navier-Stokes equations (continuity, momentum and energy law of conservation), and can be found in several classical textbooks regarding fluid mechanics like Ishii and Hibiki [62], Moody [89], Toro [128], Warsi [135], etc. The accuracy of the two-phase flow models is usually diminished by inclusion of numerous closure relationships that are based on engineering approximations and are introduced as a simplification for (i) informations lost during development of the physical model, (ii) thermal and mechanical relations between phases, and (iii) relations between each phase and surroundings. The closure relationships are developed and

validated only for a certain range within one flow regime. A flow regime is a typical distribution of the phases across the pipe cross-section with particular characteristic properties of the flow. There are several commercial and research codes that enable simulations of two-phase flows, especially in the field of nuclear thermal hydraulics, like RELAP5 [20], CATHARE [13], ATHLET [17], TRACE and TRAC [129], WAHA [126] etc. FSI models are not integrated into these codes. Various standard approaches in single and two-phase flow modeling are collected in Chapter 2 and Appendix C.

**Thermodynamics.** Each fluid is composed of particles, whose average motions define its properties, which in turn are related to one another through the equations of state. The thermodynamics studies the effects of changes in temperature, pressure, and volume on physical systems at the macroscopic scale by analyzing the collective motion of their particles using statistics. In essence thermodynamics studies the movement of the energy and how the energy instills movement. The starting point for most thermodynamic considerations is the first law of thermodynamics, which postulates that energy is exchanged between the physical systems as heat or work.

The pressure drastically changes during the water hammer transient in the fluid and the phasic temperature changes as a result of heat and mass exchange. Thermodynamics is applied in thermo-fluid dynamics whenever equations of state are utilized to account for variable density or internal energy as a response to the change of pressure or temperature. The most frequently used FSI theory excludes thermodynamics and assumes constant density, temperature, compressibility and speed of sound in the fluid, regardless the real pressure or temperature. This theory is often called elastic water hammer theory due to the analogy with Young elasticity modulus and the approximation of constant speed of sound in solids. Thermodynamics becomes important also for cases with considerable amount of heat and mass interfacial exchange in two phase flow. Exact values of the thermodynamic state can be extracted from the equation of state functions (complex or simplified) or water properties tables. Although consideration of exact water properties is an important improvement for the accuracy of the simulation, comparisons with experimental data show that for practical cases conducted in cold water, simplified approaches based on constant water properties yield results with sufficient accuracy.

**Structural dynamics.** A dynamic load is any load whose magnitude, direction, and position vary with time. The structural response to the dynamic load is also time varying, or dynamic. Clough and Penzien [25] applied the terms deterministic and nondeterministic (random dynamic) loading for the evaluation of the structural response to dynamic loads. Prescribed dynamic loading is any loading where temporal variation of loading is fully known, even though it may be highly oscillatory, and the analysis of the response of any specified structural system to a prescribed dynamic loading is defined as a deterministic analysis. The dynamic load of the fluid during the FSI is not fully known in advance, it depends also on the mutual dynamics between the fluid and the structure. However, the load of the fluid is attributed as a prescribed dynamic loading. The structural response to any prescribed dynamic loading is expressed basically in terms of the displacements of the structure. A deterministic analysis leads directly to displacement time-histories corresponding to the prescribed loading history; other related response quantities such as stresses, strains, internal forces, etc., are usually obtained as a secondary phase of the analysis. The fundamental equation of structural dynamics also known as the equation of damped simple harmonic motion, is defined as:

$$\frac{\partial^2 w}{\partial t^2} + \beta \frac{\partial w}{\partial t} + \omega^2 w = 0 \tag{3}$$

where $w$ is an arbitrary displacement, $\beta$ is the damping constant, and $\omega$ is the angular frequency. Svingen [108] stressed that it is possible to extend Eq. (3) also to the pipe structures. The pipe can bend in two directions, stretch in one direction and obtain torsional momentum. All equations describing pipe dynamics are wave equations that are not coupled with differential terms but only through source terms at curvatures. The pipe is considered as a thin-shelled structure but for the majority of piping structures this simplification has literally no measurable effect, because the length-to-diameter ratio is large, so that all frequencies of interest are either axial or lateral. Clough and Penzien [25] stated that the beam equations are almost exclusively solved with the finite element method, both in frequency and time

domain, and many commercial programs for structural and piping calculations exist starting with products of the ABAQUS [1] and ANSYS [6] corporations.

**Multiphysics coupling.** FSI analyses belong to the rapidly growing field known as multiphysics modeling. Multiphysics treat simulations that involve multiple physical models and typically involve solving a coupled systems of partial differential equations (PDEs). Standard FSI analyses couple fluid dynamics and structural dynamics and standard two-phase flow analyses couple thermodynamics and fluid dynamics. The FSI simulations considered in this study involve appropriate physical models and numerical methods for coupling between the fluid dynamics, structural dynamics, and thermodynamics.

A calculation is coupled when two or more different variables affect each other mutually through one or more coupling mechanisms. A coupling is a mechanism that links two types of variables to each other. Tijsseling [115], Casadei et al. [22], and Erath et al. [38] stated that if one variable is linked to another, the coupling is one-way (the simulation is assigned as uncoupled), while if the other variable is linked back, we talk about a two-way coupling. The term FSI, as used in this thesis, is a synonym for a two-way coupled simulation.

Tijsseling [113] stressed that it is not unusual to perform an uncoupled FSI calculation. In standard uncoupled water hammer analyses pipe elasticity is incorporated into the propagation speed of the pressure waves, while pipe inertia and pipe motion are not taken into account. Pressure histories, resulting from the water hammer analysis, are used as dynamic loading in the structural dynamics analysis and the calculation is called uncoupled since the predicted structural response does not influence the liquid pressures. An example of uncoupled calculation can be found in Tiselj and Cizelj 1993 [121]. They performed an analysis of stresses in steam generator U tubes during a large loss of coolant accident in the Krško nuclear power plant.

During the transient in the fluid–filled piping system the pressure waves are induced in the fluid and the axial, flexural, rotational, radial and torsional stress waves are induced in the piping system. According to interactions (couplings) between these waves it is possible to distinguish the following types of the coupling mechanisms [115,75,155]:

- **Poisson coupling**: The pressure waves in the fluid are coupled with axial and radial stress waves in the structure through changes of the pipe cross-section (hoop stress). Poisson coupling is figuratively known as pipe breathing. Interesting and important side effects of the Poisson coupling are precursor waves. The origin of the precursor waves are axial and hoop stress waves in the pipe wall, while changes of pipe cross-section or length, through Poisson coupling, yield to changes in pressure in the fluid. Precursor waves travel faster than pressure waves in the fluid and are thus forerunners of the water hammer.
- **Junction coupling**: Different waves are appropriately coupled at geometric changes like elbows, cross-section changes, valves, junctions, pipe ends, etc. Junction coupling is considered through the boundary conditions or more accurately through the closure relations derived for arbitrary shaped piping systems.
- **Friction coupling**: Axial stress waves in the structure are initiated due to different fluid and structure velocities. It is often negligible compared to the intensity of the junction and Poisson coupling.

The coupling forces in Poisson and friction coupling mechanisms are distributed along the pipe while the junction coupling forces act locally at geometric irregularities.

The coupling between the fluid dynamics and thermodynamics is actually very frequent in (nuclear) thermo-fluid dynamics practice, but the corresponding community usually does not consider it as a coupling. As the multiphysics field is growing, for the sake of clarity, we will classify the field of thermo-fluid dynamics as a field of coupling between the fluid dynamics and thermodynamics. The main characteristic of a coupled system is that the real state properties of the fluid are applied, which follow pressure and temperature changes of the fluid during the transient and the coupling mechanisms are given by the state functions of the fluid.

For example, the steady state flow in a fluid-filled straight piping system has a downstream valve that is rapidly closed and a water hammer wave is induced. Then the characteristic velocity of the spreading of

the induced pressure wave $c$ and the height of the pressure wave $\Delta p$ (Joukowsky equation) depend on the state properties of the fluid (for example pressure and temperature):

$c = f\,(p,T,$ *pipe geometry and material)* See Korteweg relationship in Appendix D.

$\Delta p = f\,(\rho(p,T), c(p,T), \Delta v_f)$ See Joukowsky relationship in Appendix C.

It is obvious that the pressure (pressure rise) near the valve after the valve closure strongly depends on the state properties of the fluid (beside initial velocity), on the other hand, the state properties of the fluid depend on the value of that pressure. The pressure - fluid properties - pressure cycle is thus closed and in terminology of multiphysics one can say, that consideration of real state properties of the fluid causes two-way coupling of the thermodynamics and fluid dynamics. Standard simulations based on the elastic water hammer theory, where constant water properties and constant velocity of the spreading pressure waves are applied, exclude thermo-fluid dynamic coupling and are denoted as uncoupled simulations.

**FSI in pipelines and piping systems.** Statistical data of the USA Office of Pipeline Safety [83] for the years 1986-2000 under column "Failed Pipe (Internal Force)" show that there have been a total of 5979 accidents, with 357 deaths and 3494 injuries, costing over $1 billion. These accidents can be directly attributed to FSI. Although Wylie in 1996 [115] estimated that 98% of the piping systems are not subjected to significant FSI during the transient he recommended the conduction of FSI analyses for every piping system. Wylie was actually concerned with the fact that there was (and still is) no reliable criterion, which would signify whether the FSI is relevant for the particular piping system or not. There are some qualitative criteria based upon engineering judgement like Casadei's [22] who recommended FSI analysis in flexible piping systems (lower number of supports, thin walls) with sharp pressure waves in less compressible single-phase liquid. Lavooij and Tijsseling [75] proposed and validated the first and the only reliable criterion for the inspection of the FSI in a single elbow piping system, which is based on natural frequency of the piping system, dynamic loading of the transient and the valve closing time. If the FSI effects are estimated to become important, the dynamic behavior of the liquid and piping system should be treated simultaneously. Calculations with FSI are always necessary in situations with high safety requirements, mostly encountered in nuclear and chemical industry. Appropriate FSI analysis followed by an appropriate design and definition of the optimal operating procedures is the best prevention against detrimental effects of the FSI. The FSI analyses may also be useful in post-accident analyses [94]. Methods and models for analysis of FSI including simulations, discussion and comparisons to experimental data are given in the present thesis.

A number of ways of classifying FSI in piping systems have been proposed. Païdoussis [95,96] gave a very simple and logical classification in terms where the initiating force acts: (i) structure-induced (transient originates in the structure) and (ii) fluid-induced (transient originates in a fluid). The most common causes of structure-induced FSI are vibrating machinery mounted on the structure, vibrations transferred through supports and structure of the building (traffic, other machinery, etc.), earthquakes, impact of a falling objects, etc. The most common causes of the fluid-induced FSI are pressure waves that are generated through accelerating/decelerating flow. The initiators of the accelerating flow are valves (closing/opening), pumps (start up/shut down) or pipe breaks. Another possible source of the pressure wave generation is the condensation of vapor cavities or vapor slugs in a fluid and explosions in chemically active fluids. The fluid-induced transients appear more frequently and are more severe (Westinghouse, [138]). Generally, forces and displacements in structure-induced transients are reduced due to the FSI coupling mechanisms because the energy is transferred from the structure to the fluid, while the extreme pressures might be even increased in the fluid-induced transients.

**FSI in piping systems of Nuclear power plants.** The most important information that characterizes the fluid flow in a pressurized water reactor nuclear power plant (NPP) is that pressurized ($p \sim 155$ *bar*) hot ($T \sim 600$ *K*) water is used as a medium for energy transfer from the reactor vessel through the steam generators to the turbine. Westinghouse technology advanced manual [138] recognizes the fluid-induced water hammer as a default initiating mechanism of the FSI events in NPPs. The US Nuclear Regulatory Commission [138] during the early 1970s detected the increasing frequency of water hammer events in piping systems of the NPPs. For pressurized water reactors, the major contributor to

the potential challenges to the system integrity and operability was the steam generator water hammer (SGWH). The Updated Safety Analysis Report (USAR) for Krško NPP states that water hammer in the reactor coolant system primary loop piping is precluded because of the system design, testing, and operational considerations. Nevertheless, the water hammer with FSI can appear in all remaining non-safety related piping systems of NPPs. Westinghouse technology advanced manual [138] classifies the following major types of water hammer:

- **Classical water hammer (column separation)** is usually the result of a sudden, nearly instantaneous flow change of a moving fluid (unexpected valve closures, backflow against a check valve, pump startup into voided lines where valves are closed downstream, etc.).
- **Condensation-induced water hammer** (CIWH) appears when cold water (such as auxiliary feedwater) comes in contact with hot steam. Conditions conductive to this type of water hammer are an abundant steam source and a long empty horizontal pipeline being refilled slowly with cold water. As the steam condenses, the countercurrent flow of steam and cold water is established. As the pipe fills up, the steam velocity increases, setting up waves on the surface of the water, and eventually causing a fluid slug. Slugs entrap steam pockets, that rapidly condense. Condensation is extremely fast and when the water slug suddenly strikes the water in a previously filled pipe, it produces a traveling pressure wave which imposes loads of the magnitude that would be similar to the load induced by classical water hammer in the piping network. This CIWH phenomenon occurred at San Onofre Nuclear Generating Station Unit 1 (SONGS-1) in 1985. **The CIWH occurred also in NPP Krško** in 1979, where the water-hammer extended back into the feedwater piping.
- **Steam generator water hammer** (SGWH) can occur following a reactor trip when the steam generator top feedring drains and refills with cold auxiliary feedwater. The mechanism of SGWH is similar to CIWH but it had occurred principally in pressurized water reactors with the steam generators having top feedrings for feedwater injection. The significance of this event varied from plant to plant, but it is concernable that the SGWH could cause a complete loss of feedwater and affects the ability of a plant to remove decay heat after a reactor trip. Damage from the SGWH has been generally confined to the feedring and its supports and to the steam generator feedwater nozzle region. In 1978, the generic subject of water hammer was classified as an unresolved safety issue (USI A-1). The SGWH resulted in a fractured weld in a feedwater line at Indian Point Nuclear Power Plant Unit 2 in 1972. The SGWH was later precluded by redesign of the feedwater inlet.

Stadke and Bestion [105] stressed that nuclear technology strongly depends on numerical simulations of processes. There are two major reasons: (i) the impracticality of executing full-scale experiments and (ii) the absence of simplified scaling laws for the governing processes (transfer of results from small scale test facilities to the full size plant). The most challenging task for nuclear thermo-fluid dynamics codes is related to the modeling of transient two-phase flow processes including boiling and condensation heat transfer. The development of reliable two-fluid models is largely attributable to the work of Ishii [61], Boure [15], Delhaye and Achard [31] and Drew and Lahey [36]. The models are coded in various programs as RELAP5 [20], ATHLET [17], CATHARE [13], TRAC and TRACE [129], WAHA [126], etc.

## 1.2. Literature review

Since 1970's a substantial amount of research in the FSI field has been focused on understanding and quantifying interactions between the transient flow in the fluid and the resulting vibrations of the piping system. A short overview of the FSI field in this section excludes very comprehensive fields of the pure thermo-fluid dynamics and pure structural dynamics. Textbooks like Ishii and Hibiki 2006 [62], Moody 1990 [89], Toro 1999 [128], Warsi 1998 [135], Mills 1999 [88], and many others for thermo-fluid dynamics, and Clough and Penzien 2003 [25], and others [1,6] for structural dynamics are recommended. Models for thermo-fluid dynamics and models for structural dynamics have been coded and verified in countless computer codes developed for scientific or commercial purposes.

The main stream of the FSI research in fluid-filled piping systems is currently based upon the principle of coupling between the fluid and the structure at the level of a physical model represented with a set of

one-dimensional partial differential equations. The equations are then solved with a numerical method and coded in a single computer code. There are two main branches of investigation: (i) steady state induced vibrations and (ii) transient induced FSI. Representative for the first are publications of Païdoussis 1998 [95,96] who performed an exhaustive summary over the FSI field with a special emphasis on a steady state flow induced flutter, vibration and resonance. Representatives of the second are publications of Wiggert and Tijsseling [113, 115, 144] who performed several systematic reviews of the experimental and theoretical research in the field of the fluid-filled piping systems. Their work is very valuable and exhaustive and represents a fundamental reading for everyone working in the field of transient pipe flow. Although the majority of the work of Tijsseling and Wiggert is dedicated to a single phase transient pipe flow, they applied and discussed also the quasi-two-phase flow model known as the concentrated cavity model. The theory and the numerical procedure described and discussed in this dissertation contribute to the latter branch i.e. to the field of transient induced FSI.

### 1.2.1. Physical models for FSI

In 1960 Regetz [99] investigated the pressure and velocity fluctuations in a straight pipe filled with rocket fuel. He incorporated velocity measurements recorded at the free end in classical water-hammer theory in the frequency domain. He proved that the axial dynamics of the pipe influences the behavior of the fluid. In 1967 Holomboe and Rouleau [58] reported about the problems with FSI encountered in their spiral experimental apparatus. The problems were not eliminated until their spiral pipe was embedded in concrete. Wood 1968 [147,148] presented conclusions of his work where the liquid was subjected to periodic disturbances and where disturbances were excited with a rapid valve closure. He proved that the pressure defined by Youkovsky equation is significantly exceeded if axial pipe deformations are allowed. Wood and Chao 1971 [149] performed parametric investigations on 30°, 60°, 90°, 120° and 150° bends and a perpendicular T junction. They did not model the structure; they just used measured junction velocities as input to the structural analysis. They proved that FSI is negligible if the pipe elbows are rigidly supported; meanwhile unrestrained elbows are considerably affected by FSI. Jones and Wood 1972 [65] gave an analytically derived expression for the oscillations of the pressure around Joukowsky value in the case of a rapid valve closure.

In 1956 Skalak [104] defined a set of four linear first order partial differential equations (PDEs) for the simulations of interactions between the transient in the fluid and the axial movement of the straight section of the pipe. Skalak derived the FSI four equation model as an extension of Joukowsky's method and as the low-frequency limit of two-dimensional fluid and shell representations. He showed that this model permits solutions that are waves of arbitrary shape traveling without dispersion at the phase velocity of either liquid or pipe, but he made no attempt to solve the four equations in general [117]. Vardy and Fan 1986 [132], Tijsseling 1996 [115], Tijsseling and Lavooij 1996 [116], Tijsseling 2003 [117], Gale and Tiselj 2005 [44], and many other researchers proved the validity and effectiveness of this model by both theoretical and experimental studies in the time and frequency domains. The linear constant coefficient model, mostly solved with the Method of Characteristics (MOC), was so widely used, discussed and verified in practice, that it became the fundamental model in the FSI field [19, 116, 143]. The models that came out from the Skalak's model are based upon essentially the same assumptions; they differ in the number of equations i.e. in the number of the tracked waves that travel along the pipe and interact with each other. These waves are axial, flexural, rotational, radial and torsional stress waves in the piping system and pressure waves in the fluid. The models based on Skalak's model are summarized by Wiggert and Tijsseling [113, 115, 144]. All models have continuity and momentum balance equations for the description of the water hammer in the fluid. Elansary and Contractor 1993 [37] used Skalak's model and added gravity and friction to the water hammer part of the equations to solve the problem of the rapid valve closure in a tank-pipe-valve system. They prescribed a procedure for the optimum closure of a valve in a given time interval to minimize the reaction forces and verified it with experiments. Walker and Phillips 1977 [134] used Skalak's model and added two equations for radial forces and inertia in a theoretical study of the propagation of a short-duration pressure pulses in a straight elastic pipe. Schwarz 1978 [101] performed a similar approach in a numerical study of coupled axial liquid and pipe motion in a single straight pipe, but afterwards he neglected relatively unimportant radial inertia terms and solved the four-equation model.

Valentin, Phillips and Walker in 1979 [131] studied the reflection and transmission of the fluid transients at an elbow of a liquid-filled pipe with constant radius of curvature in a single plane. Valentin, Phillips

and Walker solved the eight-equation model with four generalized constitutive equations and four equations of motion for fluid, axial, lateral and rotational forces. With other words, Valentin, Phillips and Walker used Skalak's four-equation model and added four equations of the Timoshenko beam (see Appendix F, and Taylor and Yau 2003 [110], Menez et al. 2005 [87]). Hu and Phillips 1981 [59] used similar model and validated results with experimental data, Tijsseling, Vardy and Fan 1996 [114] added a concentrated cavity model and analyzed FSI in water hammer transient with two-phase flow. All these physical models were derived in 'stiff' Eulerian coordinate system. Gale in 2007 [45] derived a nonlinear eight-equation model for simulation of deformable arbitrarily shaped piping systems and simulated rod impact experiment. He developed the physical model in 'deformable' Lagrangian coordinate system. Gale compared results and validated his model with experimental results.

Joung and Shin 1985 [67] presented a nine-equation model. Fourteen-equation model (axial, flexural, rotational and torsional motion in 3D space) was presented and solved in the frequency domain by Wilkinson 1978 [145]. Wiggert, Hatfield and Stuckenbruck 1987 [143], Tijsseling and Lavooij 1996 [116] and also Obradovič 1990 [94] who performed the simulation of an accident in a nuclear power plant by using the method of characteristics to solve a fourteen-equation model in the time domain.

Forces of friction coupling are usually negligible compared to the forces of junction and Poisson coupling. Tentarelli 1990 [111] is one of the few that performed an analysis with friction coupling in the time domain. Zhang et al. 1999 [155] considered the friction coupling in analyses performed in the frequency domain.

Two mathematical properties of the above mentioned physical models are very important, and these properties are actually properties of all physical models derived and discussed in the present thesis. Every physical model can be written in the following vectorial form (see Chapter 4 for details):

$$\frac{\partial \vec{\psi}}{\partial t} + \mathbf{C}\frac{\partial \vec{\psi}}{\partial s} + \vec{R} = 0 \tag{4}$$

and the physical model is addressed as **hyperbolic** (and thus diagonalizable) if the Jacobian matrix **C** with dimension *M* has *M* unique real eigenvalues and has a corresponding set of *M* independent eigenvectors. Hyperbolicity is not inherited in every physical model (six-equation two-phase flow model) however, it can be introduced by appropriate additional differential terms (virtual mass). A hyperbolic physical model together with initial and boundary conditions represents a **well-posed mathematical problem** (Trapp and Ransom [130]), which means that the solution exists, is unique, and depends on initial and boundary conditions.

### 1.2.2. Numerical methods for FSI

Mathematical models from Skalak's four-equation (Skalak 1956 [104]) to Wilkinson's fourteen-equation model (Wilkinson 1978 [145]) were mainly solved with the Method of Characteristics (MOC). Wylie and Streeter 1978 [150] described the MOC method as convenient for hyperbolic systems of equations with constant eigensystem where the characteristic speeds of the traveling waves are constant with time and position irrespective to the current fluid state and pipe properties. The method enables an (almost) exact treatment of the steep gradients. It is exact within the rough assumption of the physical model. This approach has been applied in the FLUSTRIN FSI code [40]. Tijsseling and Fan 1991 [112], Heinsbroek and Tijsseling 1993 [54], Tijsseling and Lavooij 1996 [116], and Heinsbroek 1997 [55] compared two techniques to solve the basic equations in the time domain: the mixed MOC-FEM (method of characteristics - finite element method) procedure and the MOC method. The main concern of the researchers was the comparison of two completely different procedures. Their linear eight-equation model was made up of two uncoupled sets of equations. The first set was the four-equation linear axial model and it was in both cases solved with method of characteristics (MOC). The second set of equations was the four-equation model for lateral and rotational dynamics (Timoshenko beam equations) which was solved with the MOC method in the first case and with the finite element method (FEM) in the second case. Heinsbroek 1993 [53] concluded that for axial waves the MOC procedure is preferred, since it leads to almost exact solutions. For lateral waves, the MOC requires very fine computational grids compared to the MOC-FEM (because of the stiff source terms – discussion in Section 5.4). Heinsbroek and Tijsseling reported that solutions obtained with MOC-FEM procedure are adequate for the computation of FSI occurrences in practical piping systems. The MOC-FEM, that

includes Poisson coupling, corresponds to the component-synthesis method of Wiggert, Otwell and Hatfield 1985 [141] where the standard water hammer procedure was coupled to a modal representation of the structural motion. They conducted laboratory tests on a large test rig consisted of a *77.5 m* long and *0.11 m* diameter steel pipeline with six miter bends (*45°*) allowing significant FSI in order to validate their numerical approaches. Heinsbroek 1997 [55] performed FSI analyses of a pipeline in a nuclear power plant with the MOC-FEM. Lee and Kim 1999 [79] performed several FSI analyses with the MOC. Casadei et al. 2001 [22] combined the Finite Element Method for the structure and the Finite Volume Method for the fluid and confirmed that the presented method is very applicable for simulations of large industrial components thanks to its robustness and generality. The weaker side of his method is the fluid-structure interface where it is necessary to define boundary conditions for accurate coupling of the nodal forces of the finite element and volumetric forces of the finite volume. The fluid is described with the Euler equations. This method was applied in the EUROPLEXUS code [22]. Tijsseling 2003 [117] presented exact solution of the Skalak's four-equation model obtained with improved MOC. Gale 2007 [45] developed a nonlinear eight-equation model for FSI in arbitrarily shaped piping systems and solved the model with a high resolution characteristic upwind finite difference numerical method, which is based on Godunov methods for conservation laws. The method is second order accurate for smooth solutions and becomes first order accurate at discontinuities. The characteristic upwind method is essentially an explicit scheme but in some rare cases applies implicit iterations to solve problems with the stiff source terms.

### 1.2.3. Two-phase flow and cavitation models for FSI

Most of the researchers in the field of FSI neglect two-phase flow. As in Skalak's model, they conservatively assume constant fluid density and single-phase flow. Youngdahl et al. 1980 [154] and Wiedermann 1982 [140] applied the concentrated cavity model where the FSI mechanisms were taken into account only when the pipe was plastically deformed. Fan and Tijsseling 1992 [39] described and applied the concentrated cavity model, also referred to as discrete vapor cavity model, for simulations of the cavitating transient pipe flow. The concentrated cavity model treats the flow as single phase, cavities can appear at limited number of certain positions along the pipe. The appearance of the cavity triggers splitting of the piping system into two independent calculational sections with single-phase flows. The cavitation is considered only as an inertially controlled process, where heat and mass transfers are assumed as infinitely fast whereas the amount of heat and mass transfer is assumed to be negligible. Muller 1987 [91] simulated HDR experiments [115] with the aid of a CFD computer code including thermo hydrodynamic effects. He coupled the code to a structural dynamics FEM code to include FSI, but he did not describe the coupling mechanism. He concluded that FSI is unimportant as long as the two-phase conditions prevail, since the compressibility of the fluid is then essentially greater than the elasticity of the pipes. Tijsseling 1996 [115] agrees with Muller's conclusions but only with respect to the Poisson coupling while disregards with respect to the junction coupling. Tijsseling furthermore warns that in some cases of two-phase flows, shock waves may develop, which are stronger than in a single-phase flows and can impose severe loads on the pipelines. Tijsseling, Vardy and Fan 1996 [114] presented experimental and numerical results on a one-elbow pipe system, where the concentrated cavity model was incorporated in the FSI eight-equation model. They stressed that the use of the concentrated cavity model is legitimate only if no distributed cavitation is present. Tijsseling and Lavooij 1996 [116] presented the results of the calculations of a column separation water hammer with FSI in a tank-pipe-valve system. Cavitation in their model could appear at only one position corresponding to the specified grid point, justifying the denomination one column separation model. Tijsseling and Fan 1991 [112] presented similar results obtained with column separation model, where cavitation can appear at two (and more) positions along the pipe simultaneously. They obtained excellent agreement with experimental data of Vardy and Fan 1986 [132]. Bettinali et al. 1991 [14] used the concentrated cavity model in their FSI computer code.

### 1.2.4. Code coupling approach for FSI

The FSI simulations based on the code coupling principle became quite attractive recently. For end-users as well as commercial code developers it is desirable to avoid a redevelopment of new simulation codes for coupled problems and to maintain the knowledge and experience of well accepted and verified highly standardized mono disciplinary codes. The main idea behind is to create a universal platform that

manipulates with inputs and outputs of two different commercial codes within each time step (for thermo-fluid dynamics and structural dynamics). The platform implies a standardized and portable library for solving coupled problems even with codes that are provided by independent software vendors with no access to the source codes. The most comprehensive code interface is MpCCI (Mesh based Code Coupling Interface) [90] that currently enables coupling of about 10 codes (number depends on version and platform). The MpCCI 3.0.6. for Microsoft Windows XP platform on Intel x86 supports the structural dynamics codes (FEM applications) ABAQUS 6.7 [1] and ANSYS 11.0 [6], and thermo-fluid dynamics codes (CFD applications) like FLUENT 6.3.26, RadTherm 8.1.1, and Flux 9.3.2 (see MpCCI manual [90] for more details on supported codes). Interactions between the independent thermo-fluid dynamics code and the independent structural dynamics code are based on Newton's third law of action and reaction and second law where force acting on a body gives acceleration in the direction of the force with a magnitude inversely proportional to the mass of the body. The same approach was used also in coupling of the EASYPIPE and KEDRU [38]. The EUROPLEXUS [22] code used similar code-coupling approach, the difference is that the fluid and the structural part of the code were developed with the purpose to be coupled, and therefore some coupling steps and interpolations are simplified and realized with a higher order of accuracy. These essentially three dimensional approaches are currently too processor demanding for analyses of piping systems and are used only for analyses of local FSI effects in small parts like elbows, valves, T-connections, branches etc.

## 1.3. Objectives and achievements of the thesis

The present thesis is directed towards the modeling of the fluid-structure interaction (FSI) during single or two-phase transient flows in piping systems. The extensive research and scientific opus of prof. Tijsseling [112 - 118] represents a state-of-the-art of the simulations of the FSI during transient flow in piping systems with numerically solved hyperbolic physical models i.e. systems of coupled partial differential equations. Tijsseling and other members of the FSI community almost exclusively use the method of characteristics (MOC) for the numerical solution of the physical models. The MOC enforces the application of linear hyperbolic physical models with constant coefficients and systematically excludes the application of more accurate nonlinear and nonlinear physical models. The linear constant coefficient models exclude coupling between thermodynamics and fluid dynamics, they exclude consideration of basic elements of the piping system that affect local junction and distributed Poisson coupling like elbows and curvatures, variable thickness, radius and other variable geometric and material properties. The identification of the limiting part of the current MOC-based approach yields the main objective of the present thesis which is to overcome the limitations of the MOC by utilization of the high resolution characteristic upwind finite difference numerical method. The objective was founded in our experiences gained during development of the computer code WAHA [126], which is used for simulations of the two-phase transient flow, and in the fact that variations of the characteristic upwind numerical methods for conservation laws have been successfully applied in various engineering problems worldwide during the last decade [44,45,125,127]. The application of the characteristic upwind numerical method enables the establishment of other important objectives of the present thesis which are (i) to derive nonlinear balance equations for two-phase flow in deformable and arbitrarily shaped Lagrangian coordinates, (ii) to derive equations for description of structural dynamics of arbitrarily shaped piping systems, (iii) to assemble appropriate FSI physical models and (iv) to compile these physical models into an effective computer code for simulations of the FSI transient pipe flow.

The present thesis represents an original contribution in the field of the fluid-structure interaction in piping systems conveying single-phase or two-phase transient flows. Our research yields the following original achievements:

1. Development of appropriate nonlinear physical models for advanced simulations of the FSI during two-phase transient flow in arbitrarily shaped piping systems:
    - The general balance equation is derived in deformable and arbitrarily shaped Lagrangian coordinates and utilized for establishment of mass, momentum and energy balance equations. The two-fluid model of the two-phase flow, the quasi-two-phase flow and the homogeneous equilibrium two-phase flow physical models for thermo-fluid dynamics are established.

- The physical models for axial, lateral, rotational, and torsional structural dynamics of arbitrarily shaped fluid-filled piping systems are derived.
- Physical models of thermo-fluid dynamics are coupled with models for structural dynamics into various FSI (multi) physical models of various complexity.

2. Application of the high resolution characteristic upwind numerical method for the numerical solution of nonlinear physical models and derivation of procedure for integration of stiff source terms in Timoshenko beam equation through implicit iterations.
3. Development and validation of the computer code for simulations of the cavitating transient pipe flow with significant FSI. Additional sub-models and improvements are coded and are available for utilization (consideration of real water properties, flexibility factor, thick-walled model, external load and forces, elastic and stiff supports, von Mises stress, valve, tank and closed end pipe elements, etc.)

Some results of our research were published in the Journal of Pressure Vessel Technology (Gale and Tiselj [45]), namely the nonlinear eight-equation physical model for the description of single-phase flow transients coupled with axial, lateral and rotational dynamics of the piping system lying in 2D plane was solved with the characteristic upwind numerical method and successfully applied for the simulation of single phase transients in the single-elbow rod impact experiments.

## 1.4. Overview of the thesis

The introductory chapter is followed by Chapter 2 where the derivation of the balance equations for the fluid dynamics in arbitrarily shaped and deformable piping systems is given. Chapter 3 gives the derivation of the structural dynamics equations expressed with a general parameter for arbitrary shaped piping systems. All fundamentals for the understanding of the derivations in Chapters 2 and 3 and comparison with standard approaches are collected in the appendices. The balance equations for the fluid with the FSI and then, the two-phase flow, the homogeneous equilibrium two-phase flow, and the quasi-two-phase flow models for thermo-fluid dynamics are described in Chapter 4. All available combinations of physical models that that can be used for simulations of the FSI are collected further. The models are grouped according to the physics of the phenomenon into the following groups: thermo-fluid dynamics, structural dynamics and FSI physical models. Each set of partial differential equations is made up of the equations developed in Chapters 2 and 3; each physical model is described and when possible, the eigensystem is evaluated analytically. The most comprehensive physical models are described schematically. The high resolution characteristic upwind numerical method is described and discussed in Chapter 5. Chapter 6 contains a review of results with validation and discussion of the FSI phenomenon itself and discussion on applied physical models and numerical method. The results are compared to the analytical solutions, to the results of the computer codes based on the MOC method and to experimental results. Concluding remarks are given in Chapter 7.

# 2. Balance equations for a fluid in Lagrangian coordinates

Eulerian coordinates are fixed in space while Lagrangian coordinates are fixed to a given parcel of the deformable pipe and move in space. Lemonnier [82] states that derivation of the system of equations from Eulerian coordinates into Lagrangian coordinates is necessary for an accurate description of the thermo-fluid dynamics in moving and deforming piping systems. This chapter gives the derivation of the general balance equation of thermo-fluid dynamics in deformable and arbitrarily shaped Lagrangian coordinates and then the application of the general balance equation for derivation of mass, momentum and energy balances. The derived balance equations, closure relations and solution procedures are strongly correlated with the standard balance equations derived in Eulerian coordinates (fundamentals of the standard thermo-fluid dynamics are given in Appendix C). The derivation of the equations in deformable and arbitrarily shaped Lagrangian coordinates introduces several new terms that enable FSI coupling with the piping system. Therefore, there are new terms that belong to the pipe structure (axial pipe velocity, lateral pipe velocity, axial force). These terms cannot be evaluated without coupled consideration of the pipe dynamics.

Although the theory derived and discussed in this Chapter refers to any fluid, note that the fundamental fluid applied in this thesis is water.

## 2.1. Introduction

Coutris [26] and Lemonnier [82] gave an obvious generalization of the typical six-equation two-phase equations for the fixed, straight and undeformable pipe (Eulerian coordinates), which is mostly used in thermo-fluid dynamics, to a general form of the 1D averaged two-fluid model equations in a deformable pipe of arbitrary shape undergoing arbitrary motions (Lagrangian coordinates). The crucial step toward their model is the area averaging of the balance equations and then the derivation and application of the Gauss (divergence) theorem for the spatial derivatives and the Leibniz integral rule for temporal derivatives for averaged quantities on the section (Appendix A). The derivation and then the application of the general form of the 1D averaged two-fluid model equations for a deformable pipe of arbitrary shape undergoing arbitrary motions is unique in the field of thermo-fluid dynamics and especially in the considered fast transient FSI field and is thus described in detail in the next sections.

A natural way to describe a pipeline or the fluid domain inside that pipeline consists in considering a line such as the neutral fiber of the pipe and a section sliding on this line (see Figure 1). The sliding section on the line generates a domain that Coutris [26] denominates as a fluid filament. Mathematically, the neutral fiber of the pipe is described by a parameter arc length $s_0$. Lemonnier [82] states that the arc length is appropriate for purely fluid structures, but it may become useless for FSI problems. The sections of interest are physically attached to the pipe, but due to the compression or stretching of the pipe (Figure 2), measuring sections, boundaries or any kind of hydraulic singularity are never located at a constant arc length measured from one end of the pipe. The values of the arc length vary with time; therefore, quantities of interest should be referenced by a more general parameter $s$ that relates the section of interest to that of the reference state of the pipe.

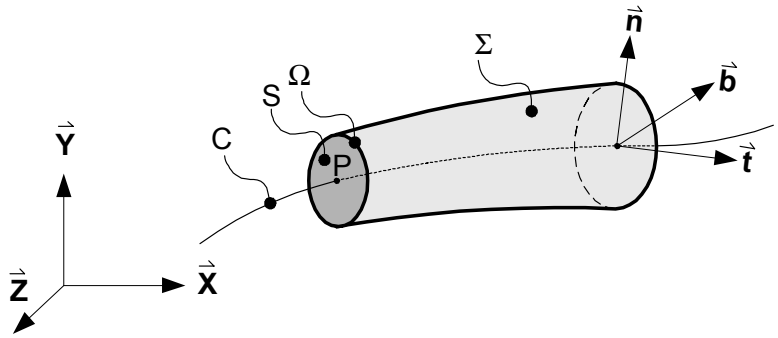


Fig. 1: A fluid filament generated by the motion of the section $S$ limited by circle $\Omega$, the center of which is $P$ and lies on the curve $C$.

## 2.2. Development of general balance equation

**General arc length parameter and coordinate system.** The fluid filament shown in Figure 1 is defined by the inner space of a moving and deforming pipe of circular cross-section. With a general arc length coordinate *s* instead of $s_0$, the pipe singularities, ends and measuring sections are at a fixed coordinate *s*, moreover, the normalized length of the calculation domain is fixed. The general parameter *s* is related to the arc length $s_0$ with relationship:

$$s(t) = s_0(t) + y(s,t) \tag{5}$$

where *y* is the displacement of the section (see Figure 2). At any time *t*, the position *s* along *C* can be calculated as a function of the arc length $s_0$. Under undistorted conditions, the parameter *s* is equal to the reference state $s_0(t=0)$. The derivative of $s_0$ is defined as:

$$\left(\frac{\partial s_0}{\partial s}\right)_t = 1 - \frac{\partial y}{\partial s} \tag{6}$$

A curve *C*, determined by a single parameter *s* and a circular plane section *S* sliding with its normal tangent to the *C*, generates the inner surface of the pipe. The center point *P* of the section *S* is located on *C* and it is defined as: *P = P(s,t)*. It is clear that the motion of the point *P* attached to *C* defined by:

$$\vec{\mathbf{U}}_C = \left(\frac{\partial \mathrm{P}}{\partial t}\right)_s \tag{7}$$

depends on the choice of parameter *s*. The cross-section is assumed to remain perpendicular to *C* at any time and the radius *R* of the cross-section is assumed to depend on the arc length.

Figure 1 shows that section *S* on the curve *C* is described by the local basis built upon the Lagrangian reference frame also known as Fresnet frame $(\vec{\mathbf{t}},\vec{\mathbf{n}},\vec{\mathbf{b}})$, the vectors of which are respectively the tangent to the curve, the normal to the curve and the binormal (Appendix B). The local basis at the cross-section *S* at position of the point *P* is therefore $(P,\vec{\mathbf{n}},\vec{\mathbf{b}})$, and the corresponding coordinates of a point located on the section *S* are *(P,y,z)*. The vector tangent to *C*, the vector normal to *C* (points towards the center of curvature), and the binormal of the Fresnet frame are defined as:

$$\vec{\mathbf{t}} = \frac{\partial P}{\partial s_0} \quad \text{and} \quad \vec{\mathbf{n}} = \frac{\partial \vec{\mathbf{t}}}{\partial s_0} \Big/ \left|\frac{\partial \vec{\mathbf{t}}}{\partial s_0}\right| \quad \text{and} \quad \vec{\mathbf{b}} = \vec{\mathbf{t}} \times \vec{\mathbf{n}} \tag{8}$$

The vectors of the Fresnet frame obey the following derivation rules:

$$\frac{d\vec{\mathbf{t}}}{ds_0} = \frac{\vec{\mathbf{n}}}{R_p}, \qquad \frac{d\vec{\mathbf{n}}}{ds_0} = -\frac{\vec{\mathbf{t}}}{R_p} - \frac{\vec{\mathbf{b}}}{T_p}, \qquad \frac{d\vec{\mathbf{b}}}{ds_0} = \frac{\vec{\mathbf{n}}}{T_p} \tag{9}$$

where $R_p$ is the radius of curvature of the pipe and $T_p$ is the radius of torsion of the pipe.

The following relationships hold for any function *f*, considering the relation between *s* and $s_0$ in Eq. (5):

$$f(s,t) = f\left(s\left(s_0,t\right),t\right) = \tilde{f}\left(s_0,t\right) \tag{10}$$

The derivatives of *f* and $\tilde{f}$ are then defined by:

$$\frac{\partial \tilde{f}}{\partial s_0} = \frac{\partial f}{\partial s}\left(\frac{\partial s}{\partial s_0}\right)_t = \frac{\partial f}{\partial s}\mu \quad \text{and} \quad \frac{\partial \tilde{f}}{\partial t} = \frac{\partial f}{\partial t} + \frac{\partial f}{\partial s}\left(\frac{\partial s}{\partial t}\right)_{s_0} = \frac{\partial f}{\partial t} + \frac{\partial f}{\partial s}\mu_t \tag{11}$$

where $\mu$ is the scale factor close to 1 if the deformation of the pipe is small and $\mu_t$ is recognized as velocity of the point $P$ on $C$ ($\vec{\mathbf{U}}_C$) projected onto tangential direction $\vec{\mathbf{t}}$. The parameters $\mu$ and $\mu_t$ are given as [82]:

$$\mu = \left(\frac{\partial s}{\partial s_0}\right)_t = \frac{1}{\sqrt{1+2\vec{\mathbf{t}}_0 \cdot y' + y'^2}} \quad \text{and} \quad \mu_t = \left(\frac{\partial s}{\partial t}\right)_{s_0} = \vec{\mathbf{U}}_C \cdot \vec{\mathbf{t}} = u_x \tag{12}$$

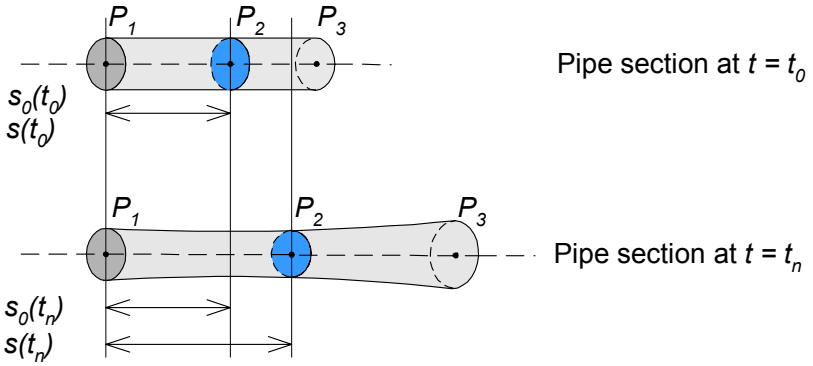


Fig. 2: Initial and deformed shape of the pipe. Differences between the arc length parameter $s_0$ and the general arc length parameter $s$ are indicated.

**General balance equation.** Each particular phase of the single or multi-phase flow can be described with the Navier-Stokes system of equations. The Navier-Stokes system, which contains the continuity, momentum and energy equation and an additional equation of state, is defined for the space exclusively filled with one phase and bounded with the wall and/or the other phase. There are numerous textbooks describing the Navier-Stokes system (see Moody [89], Ishii and Hibiki [62], Davis [28], Warsi [135], etc.). According to Ishii and Hibiki [62] the general balance equation yields:

$$\frac{\partial}{\partial t}\rho_k\psi_k + \nabla\cdot\left(\rho_k\vec{\mathbf{v}}_k\psi_k\right) + \nabla\cdot\mathbf{J}_k - \rho_k\phi_k = 0 \tag{13}$$

where $\rho_k$ is the density of the phase $k$ ($k = f$ for fluid and $k = g$ for gas phase, see also Figure 3), and $\vec{\mathbf{v}}_k$ is the fluid velocity vector. The appropriate mass, momentum and energy balance equations are obtained by application of variable definitions given in Table 1.

*Table 1: Variables for the application of the generalized balance equation for the phase k, where $e_k$ is the specific internal energy, $e_{tot,k}$ is the specific total energy, $\vec{F}_g$ are the body forces, $\vec{\mathbf{q}}_k$ is the heat flux, $\mathbf{I}$ is the identity vector, and $\mathbf{V}_k$ is the viscous part of the stress tensor.*

| **Balance** | $\psi_k$ | $\mathbf{J}_k$ | $\phi_k$ |
|---|---|---|---|
| Mass | 1 | 0 | 0 |
| Momentum | $\vec{\mathbf{v}}_k$ | $p\mathbf{I} - \mathbf{V}_k$ | $\vec{F}_g$ |
| Total energy | $e_{tot,k} = e_k + 0.5v_k^2$ | $\vec{\mathbf{q}}_k + \left(p\mathbf{I} - \mathbf{V}_k\right)\cdot\vec{\mathbf{v}}_k$ | $\vec{F}_g\cdot\vec{\mathbf{v}}_k$ |

**Area averaged general balance equation.** The cross-section area averaged general balance equation is obtained by integration of the general balance equation (13) over the considered section $S_k$ of the filament filled with the phase $k$ (see Fig. 3):

$$\int_{S_k(P,t)}\left(\frac{\partial}{\partial t}\rho_k\psi_k + \nabla\cdot\left(\rho_k\vec{v}_k\psi_k\right) + \nabla\cdot\mathbf{J}_k - \rho_k\phi_k\right)\lambda dS = 0 \tag{14}$$

where $\lambda$ is the geometrical factor, generally very close to *1*, accounting for the lesser weight of points of the section $S_k$ lying closer to the center of curvature of the neutral fiber *C* at curvatures:

$$\lambda = 1 - {}^{x}\!/_{R_p} \tag{15}$$

In the 1D approach adopted in the present thesis, evolution equations for averaged quantities on the section are needed while the averaging of the local balance equations yields integrals of time or space derivative terms. For transformation of the latter type of terms into the former, the Leibniz integral rule for the time derivatives and the Gauss (divergence) theorem for the spatial derivatives are applied. Lemonnier [82] noted that the derivation of the two-fluid balance equations is possible if these theorems are valid for an arbitrary section, while Coutris [26] proved that the Gauss theorem and the Leibniz integral rule preserve the same form when the section of the filament has an arbitrary shape. The Leibniz integral rule and the Gauss theorem are defined in Appendix A.

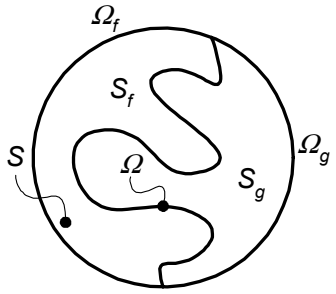


Fig. 3: A filament cross-section showing the domain $S_k$ occupied by the phase $k$ = *f or g*. Each phase is limited by the phasic interface $\Omega$, and the fraction of the perimeter of *S* pertaining to the phase *k* is $\Omega_k$.

Using the Gauss theorem and the Leibniz rule and by further assuming that the wall of the filament $\Omega_k$ is impermeable (no mass transfer through the pipe wall):

$$\left(\vec{\mathbf{v}} - \vec{\mathbf{U}}_\Sigma\right) \cdot \vec{\mathbf{n}}_\Sigma = 0 \qquad on \quad \Omega_k \tag{16}$$

the following area averaged general balance equation for phase *k* (*k* = *g* or *f*) yields:

$$\frac{\partial}{\partial t}\int_{S_k} \rho_k \psi_k \lambda dS + \frac{\partial \vec{\mathbf{U}}_C}{\partial s_0} \cdot \vec{\mathbf{t}} \int_{S_k} \rho_k \psi_k \lambda dS + \vec{\mathbf{U}}_C \cdot \vec{\mathbf{t}} \frac{\partial}{\partial s_0} \int_{S_k} \rho_k \psi_k \lambda dS + \frac{\partial}{\partial s_0} \int_{S_k} \left(\rho_k \psi_k \left(\vec{\mathbf{v}}_k - \vec{\mathbf{U}}_S\right) + \mathbf{J}_k\right) \cdot \vec{\mathbf{t}} dS$$
$$+ \int_\Omega \frac{\left(\rho_k \psi_k \left(\vec{\mathbf{v}}_k - \vec{\mathbf{U}}_i\right) + \mathbf{J}_k\right) \cdot \vec{\mathbf{n}}_k}{\vec{\mathbf{n}}_{k\Omega} \cdot \vec{\mathbf{n}}_k} \lambda d\Omega + \int_{\Omega_k} \frac{\mathbf{J}_k \cdot \vec{\mathbf{n}}_k}{\vec{\mathbf{n}}_{k\Omega} \cdot \vec{\mathbf{n}}_k} \lambda d\Omega - \int_{S_k} \rho_k \phi_k \lambda dS = 0 \tag{17}$$

where $\vec{\mathbf{n}}_k$ is the vector normal to the surface of phase *k*, $\vec{\mathbf{n}}_\Sigma$ is the vector normal to the pipe wall, $\vec{\mathbf{n}}_{k\Omega}$ is the unit vector normal to the interface between the phases, $\vec{\mathbf{U}}_i$ is the displacement velocity of the interface, $\vec{\mathbf{U}}_\Sigma$ is the displacement velocity of the lateral surface (pipe wall), $\vec{\mathbf{U}}_S$ is the displacement velocity of the section *S*, and $\vec{\mathbf{U}}_C$ is the velocity vector of a point *P* attached to the line *C*.

The average on the section is introduced and has a special form suggested by the limiting forms of the Leibniz rule and the Gauss theorem. This procedure closely follows that of Delhaye [32] for the straight pipe and that of Coutris [26]:

$$\langle f \rangle = \frac{\int_{S_k} f \lambda dS}{\int_{S_k} \lambda dS} = \frac{\int_{S_k} f \lambda dS}{\tilde{S}_k} \qquad \Rightarrow \qquad \int_{S_k} f \lambda dS = \tilde{S}_k \langle f_k \rangle \tag{18}$$

where $\tilde{S}_k$ is the volume occupied by phase *k* per unit length of the pipe. This definition for any constant value *a* satisfies condition: $\langle a \rangle \equiv a$, but the relationship can not be satisfied if the factor $\lambda$ is omitted in the denominator of Eq. (18). The integrals of variables across $S_k$ can be substituted with the area-averaged quantities in accordance with Eq. (18), and the area averaged general balance equation yields:

$$\begin{aligned}&\frac{\partial}{\partial t}\tilde{S}_k\left\langle\rho_k\psi_k\right\rangle+\frac{\partial\vec{\mathbf{U}}_C}{\partial s_0}\cdot\vec{\mathbf{t}}\tilde{S}_k\left\langle\rho_k\psi_k\right\rangle+\vec{\mathbf{U}}_C\cdot\vec{\mathbf{t}}\frac{\partial}{\partial s_0}\tilde{S}_k\left\langle\rho_k\psi_k\right\rangle+\frac{\partial}{\partial s_0}\tilde{S}_k\left\langle\left(\rho_k\psi_k\left(\vec{\mathbf{v}}_k-\vec{\mathbf{U}}_S\right)+\mathbf{J}_k\right)\cdot\frac{\vec{\mathbf{t}}}{\lambda}\right\rangle+\\&\int_{\Omega}\frac{\dot{m}_k\psi_k+\mathbf{J}_k\cdot\vec{\mathbf{n}}_k}{\vec{\mathbf{n}}_{k\Omega}\cdot\vec{\mathbf{n}}_k}\lambda d\Omega+\int_{\Omega_k}\frac{\mathbf{J}_k\cdot\vec{\mathbf{n}}_k}{\vec{\mathbf{n}}_{k\Omega}\cdot\vec{\mathbf{n}}_k}\lambda d\Omega-\tilde{S}_k\left\langle\rho_k\phi_k\right\rangle=0\end{aligned}\tag{19}$$

where $\dot{m}_k$ is the mass flux density through the phasic interface $\Omega$ (Fig. 3) and is defined as:

$$\dot{m}_k=\rho_k\left(\vec{\mathbf{v}}_k-\vec{\mathbf{U}}_i\right)\cdot\vec{\mathbf{n}}_k\tag{20}$$

The velocity of any point on surface *S*, $\vec{\mathbf{U}}_S$ is related to the velocity of the point *P* on curve *C*, $\vec{\mathbf{U}}_C$ by:

$$\vec{\mathbf{U}}_S=\vec{\mathbf{U}}_C+y\frac{\partial\vec{\mathbf{n}}}{\partial t}+z\frac{\partial\vec{\mathbf{b}}}{\partial t}=\vec{\mathbf{U}}_C+\vec{\Omega}\times\vec{\mathbf{r}}\tag{21}$$

where $\vec{\Omega}$ is the angular velocity of rotation of the Fresnet frame (see Appendix B). In practice it represents the convection induced by the rotation of the section *S* around its center *P* - this term is small and it is neglected, then $\vec{\mathbf{U}}_S = \vec{\mathbf{U}}_C$.

The fourth term in Eq. (19) is the convective term. Introduction of the relationship between the velocities of the section *S* and point *P* attached to the curve *C* yields the convective term in expanded form:

$$\begin{aligned}\frac{\partial}{\partial s_0}\tilde{S}_k\left\langle\left(\rho_k\psi_k\left(\vec{\mathbf{v}}_k-\left(\vec{\mathbf{U}}_C+\vec{\Omega}\times\vec{\mathbf{r}}\right)\right)+\mathbf{J}_k\right)\cdot\frac{\vec{\mathbf{t}}}{\lambda}\right\rangle=&\ \frac{\partial}{\partial s_0}\tilde{S}_k\left\langle\left(\rho_k\psi_k\vec{\mathbf{v}}_k+\mathbf{J}_k\right)\cdot\frac{\vec{\mathbf{t}}}{\lambda}\right\rangle&&\text{term 1}\\&-\frac{\partial\vec{\mathbf{U}}_C}{\partial s_0}\cdot\vec{\mathbf{t}}\,\tilde{S}_k\left\langle\rho_k\psi_k\frac{1}{\lambda}\right\rangle&&\text{term 2}\\&-\vec{\mathbf{U}}_C\cdot\vec{\mathbf{t}}\frac{\partial}{\partial s_0}\tilde{S}_k\left\langle\rho_k\psi_k\frac{1}{\lambda}\right\rangle&&\text{term 3}\\&-\vec{\mathbf{U}}_C\cdot\frac{\partial\vec{\mathbf{t}}}{\partial s_0}\tilde{S}_k\left\langle\rho_k\psi_k\frac{1}{\lambda}\right\rangle&&\text{term 4}\end{aligned}\tag{22}$$

where the first term is the convective term in the absence of section motion. The second term resembles the stretching term. The third term resembles the tangential displacement induced convective term with the scale factor $\lambda$ included and the fourth term represents the contribution of the displacement to the convection at curvatures of the pipe. The balance Eq. (19) rewritten with the expanded convective term given in Eq. (22) then yields:

$$\begin{aligned}&\frac{\partial}{\partial t}\tilde{S}_k\left\langle\rho_k\psi_k\right\rangle+\frac{\partial\vec{\mathbf{U}}_C}{\partial s_0}\cdot\vec{\mathbf{t}}\tilde{S}_k\left\langle\rho_k\psi_k\left(1-\frac{1}{\lambda}\right)\right\rangle+\vec{\mathbf{U}}_C\cdot\vec{\mathbf{t}}\frac{\partial}{\partial s_0}\tilde{S}_k\left\langle\rho_k\psi_k\left(1-\frac{1}{\lambda}\right)\right\rangle+\int_{\Omega}\frac{\dot{m}_k\psi_k+\mathbf{J}_k\cdot\vec{\mathbf{n}}_k}{\vec{\mathbf{n}}_{k\Omega}\cdot\vec{\mathbf{n}}_k}\lambda d\Omega+\\&\frac{\partial}{\partial s_0}\tilde{S}_k\left\langle\left(\rho_k\psi_k\vec{\mathbf{v}}_k+\mathbf{J}_k\right)\cdot\frac{\vec{\mathbf{t}}}{\lambda}\right\rangle-\vec{\mathbf{U}}_C\cdot\frac{\partial\vec{\mathbf{t}}}{\partial s_0}\tilde{S}_k\left\langle\rho_k\psi_k\frac{1}{\lambda}\right\rangle+\int_{\Omega_k}\frac{\mathbf{J}_k\cdot\vec{\mathbf{n}}_k}{\vec{\mathbf{n}}_{k\Omega}\cdot\vec{\mathbf{n}}_k}\lambda d\Omega-\tilde{S}_k\left\langle\rho_k\phi_k\right\rangle=0\end{aligned}\tag{23}$$

Equation (23) is particularly complicated for use and understanding, therefore several assumptions were made to get simplified form of the area averaged general balance equation. Table 2 collects all approximations and definitions applied for simplification of the one dimensional form of the area averaged general balance equation. The introduction of the flat profile assumption, the relationship for the void fraction and geometrical factor, the replacement for the phase surface fraction etc. then yield:

$$\frac{\partial}{\partial t} S\alpha_k \rho_k \psi_k + \frac{\partial}{\partial s_0} S\alpha_k \rho_k \psi_k v_k + \frac{\partial}{\partial s_0} S\alpha_k \mathbf{J}_k \cdot \vec{\mathbf{t}} - \frac{u_y}{R_p} S\alpha_k \rho_k \psi_k + P_i \left( \dot{m}_k \psi_k + \mathbf{J}_k \cdot \vec{\mathbf{n}}_k \right) + P_k \left( \mathbf{J}_k \cdot \vec{\mathbf{n}}_k \right) - S\alpha_k \rho_k \phi_k = 0 \quad (24)$$

*Table 2: Approximations and definitions for derivation of the simplified equation (24).*

| Description of the approximation | Equation |
|---|---|
| Flat profile approximation | $\langle f \rangle = f \quad and \quad \langle f\, g \rangle = f\, g$ |
| The void fraction and phase surface fraction approximations | $\alpha_k = \langle \alpha \rangle \approx \langle \tilde{\alpha} \rangle = \langle \alpha \rangle (1 - x_{Sg}/R_p)$ * <br> $\langle \tilde{\alpha} \rangle = \tilde{S}_k / S$ <br> $S_k \langle f \rangle = S \langle \tilde{\alpha} \rangle f = S\alpha_k f$ <br> $\tilde{S}_k \left\langle f \frac{1}{\lambda} \right\rangle = S \langle \alpha \rangle f = S\alpha_k f$ |
| The geometrical factor approximation | $\lambda \approx 1 \quad \Rightarrow \quad \left(1 - \frac{1}{\lambda}\right) \approx 0$ |
| **Description of the definition** | **Equation** |
| The fluid velocity vector (lateral velocities are equal to the pipe wall velocity) | $\vec{\mathbf{v}}_k = v_k \vec{\mathbf{t}} + u_y \vec{\mathbf{n}} + u_z \vec{\mathbf{b}}$ |
| The velocity vector of a point *P* at curve *C* | $\vec{\mathbf{U}}_C = u_x \vec{\mathbf{t}} + u_y \vec{\mathbf{n}} + u_z \vec{\mathbf{b}}$ |
| The interfacial area per unit length of the pipe | $P_i = \int_{\Omega} \frac{\lambda d\Omega}{\vec{\mathbf{n}}_{k\Omega} \cdot \vec{\mathbf{n}}_k}$ |
| The wall surface area wetted by phase *k* per unit length of the pipe | $P_k = \int_{\Omega_k} \frac{\lambda d\Omega}{\vec{\mathbf{n}}_{k\Omega} \cdot \vec{\mathbf{n}}_k}$ |
| Derivation rule for tangential vector Eq. (9) | $\frac{d\vec{\mathbf{t}}}{ds_0} = \frac{\vec{\mathbf{n}}}{R_p}$ |

** $X_{Sg}$ is the distance of the centre of gravity of $S_k$ to the centre of the section. The error may be small if the radius of the curvature of the pipe is large with respect to the pipe, or if the phases are evenly distributed in the pipe section*

**General area averaged balance equation in Lagrangian coordinates.** Using the rules for the transformation of the balance equations from the parameter arc length $s_0$ to the general parameter $s$ that are defined in Eq. (11), the area averaged balance equation (24) expressed in the Lagrangian coordinates gives:

$$\frac{\partial}{\partial t} S\alpha_k \rho_k \psi_k + u_x \frac{\partial}{\partial s} S\alpha_k \rho_k \psi_k + \mu \frac{\partial}{\partial s} S\alpha_k \rho_k v_k \psi_k + \mu \frac{\partial}{\partial s} S\alpha_k \mathbf{J}_k \cdot \vec{\mathbf{t}} - \frac{u_y}{R_p} S\alpha_k \rho_k \psi_k + P_i \left( \dot{m}_k \psi_k + \mathbf{J}_k \cdot \vec{\mathbf{n}}_k \right) + P_k \left( \mathbf{J}_k \cdot \vec{\mathbf{n}}_k \right) - S\alpha_k \rho_k \phi_k = 0 \quad (25)$$

The general area averaged balance equation in Lagrangian coordinates is applicable for any phase *k*, namely fluid *f* or gas *g*, and Table 3 collects appropriate indices for the application of the equation for the fluid and gas phase of the two-phase flow.

*Table 3: Application of the area averaged general balance equation fluid and gas phase.*

| Property | index *k* | vapor volume fraction $\alpha_k$ | phase factor *i* |
|---|---|---|---|
| Fluid | *f* | 1 - $\alpha$ | 1 |
| Gas | *g* | $\alpha$ | -1 |

## 2.3. Mass, momentum and energy balance equations

**Mass balance.** The mass balance equation is derived from the area averaged general balance equation in Lagrangian coordinates Eq. (25) by inserting definitions $\psi_k = 1;\quad \mathbf{J}_k = 0;\quad \phi_k = 0$ from Table 1, and using the relationship for vapor generation rate $\Gamma_g$:

$$P_i \dot{m}_k = iS\Gamma_g \qquad \text{where} \qquad i = \begin{cases} 1 & \text{for fluid phase} \\ -1 & \text{for gas phase} \end{cases} \tag{26}$$

Then the mass balance equation (continuity) is written as a first order partial differential equation:

$$\frac{\partial}{\partial t} S\alpha_k \rho_k + u_x \frac{\partial}{\partial s} S\alpha_k \rho_k + \mu \frac{\partial}{\partial s} S\alpha_k \rho_k v_k = \frac{u_y}{R_p} S\alpha_k \rho_k - iS\Gamma_g \tag{27}$$

where all differential terms are collected on the left hand side and nondifferential terms (source terms) are collected on the right hand side.

**Momentum balance.** The momentum balance equation is obtained by inserting definitions: $\psi_k = \vec{\mathbf{v}}_k$, $\mathbf{J}_k = p\mathbf{I} - \mathbf{V}_k$, and $\phi_k = \vec{F}_k$ from Table 1 into the general balance equation in Lagrangian coordinates, Eq. (25). Projection of the general balance equation in tangential direction $\vec{\mathbf{t}}$ gives:

$$\begin{aligned} &\frac{\partial}{\partial t} S\alpha_k \rho_k \vec{\mathbf{v}}_k \cdot \vec{\mathbf{t}} + u_x \frac{\partial}{\partial s} S\alpha_k \rho_k \vec{\mathbf{v}}_k \cdot \vec{\mathbf{t}} + \mu \frac{\partial}{\partial s} S\alpha_k \rho_k v_k \vec{\mathbf{v}}_k \cdot \vec{\mathbf{t}} + \mu \frac{\partial}{\partial s} S\alpha_k \left(p\mathbf{I} \cdot \vec{\mathbf{t}}\right) \cdot \vec{\mathbf{t}} - \\ &\mu \frac{\partial}{\partial s} S\alpha_k \left(\mathbf{V}_k \cdot \vec{\mathbf{t}}\right) \cdot \vec{\mathbf{t}} - \frac{u_y}{R_p} S\alpha_k \rho_k \vec{\mathbf{v}}_k \cdot \vec{\mathbf{t}} + P_i \dot{m}_k \vec{\mathbf{v}}_k \cdot \vec{\mathbf{t}} + P_i \left(p\mathbf{I} \cdot \vec{\mathbf{n}}_k\right) \cdot \vec{\mathbf{t}} - P_i \left(\mathbf{V}_k \cdot \vec{\mathbf{n}}_k\right) \cdot \vec{\mathbf{t}} + \\ &P_k \left(p\mathbf{I} \cdot \vec{\mathbf{n}}_k\right) \cdot \vec{\mathbf{t}} - P_k \left(\mathbf{V}_k \cdot \vec{\mathbf{n}}_k\right) \cdot \vec{\mathbf{t}} - S\alpha_k \rho_k \vec{F}_k \cdot \vec{\mathbf{t}} = 0 \end{aligned} \tag{28}$$

The following relationships are applied to simplify Eq. (28):

- Normal and binormal velocities of the fluid velocity vector defined in Table 2 are usually negligible compared to the axial fluid velocity in the pipe:

$$\vec{\mathbf{v}}_k \approx v_k \vec{\mathbf{t}} \qquad \text{therefore (see also Eq. (B-13)):} \qquad \frac{\partial \vec{\mathbf{v}}_k}{\partial t} \cdot \vec{\mathbf{t}} = \frac{\partial v_k}{\partial t} \tag{29}$$

- The following pressure identity can be derived by applying the Gauss theorem on the diagonal tensor $p\mathbf{I}$ (see Appendix A, Eq. (A-6) and Table 2):

$$\mu \frac{\partial}{\partial s} \alpha_k S \left(p\mathbf{I} \cdot \vec{\mathbf{t}}\right) \cdot \vec{\mathbf{t}} + P_i \left(p\mathbf{I} \cdot \vec{\mathbf{n}}_k\right) \cdot \vec{\mathbf{t}} + P_k \left(p\mathbf{I} \cdot \vec{\mathbf{n}}_k\right) \cdot \vec{\mathbf{t}} = \mu \alpha_k S \left(\nabla \cdot p\mathbf{I}\right) \cdot \vec{\mathbf{t}} = \mu \alpha_k S \frac{\partial p}{\partial s} \tag{30}$$

- The classical assumption of the two-fluid modeling states that the tangential viscous stress and the tangential heat flux are negligible (Delhaye, Giot and Riethmuller [32]) compared to the convective terms. It is known that this assumption is violated in some rare cases like shocks waves, but it is reasonable in most of the other situations:

$$\left(\mathbf{V}_k \cdot \vec{\mathbf{t}}\right) \cdot \vec{\mathbf{t}} \approx 0 \qquad \text{and also} \qquad \vec{\mathbf{q}}_k \cdot \vec{\mathbf{t}} \approx 0 \tag{31}$$

- The interface vapor generation term gives ($v_i$ is the velocity of the interfacial area):

$$P_i \dot{m}_k \vec{\mathbf{v}}_k \cdot \vec{\mathbf{t}} = P_i \dot{m}_k v_k = iS\Gamma_g v_i \qquad v_i = \begin{cases} v_f & \Gamma_g \geq 0 \\ v_g & \Gamma_g < 0 \end{cases} \tag{32}$$

- The interface friction force $F_i$ is defined as:

$$P_i \left(\mathbf{V}_k \cdot \vec{\mathbf{n}}_k\right) \cdot \vec{\mathbf{t}} = iSF_i \tag{33}$$

- The wall friction term for each phase with wall friction force $F_{k,t}$ is defined as:

$$P_k\left(\mathbf{V}_k\cdot\vec{\mathbf{n}}_k\right)\cdot\vec{\mathbf{t}} = -SF_{k,t} \tag{34}$$

- The body force per unit volume due to gravity in a pipe with inclination angle $\gamma$ is written as:

$$\vec{F}_g\cdot\vec{\mathbf{t}} = F_{gx} \tag{35}$$

Then the first order partial differential equation for momentum balance yields:

$$\begin{aligned}&\frac{\partial}{\partial t}\alpha_k S\rho_k v_k + u_x\frac{\partial}{\partial s}\alpha_k S\rho_k v_k + \mu\frac{\partial}{\partial s}\alpha_k S\rho_k v_k v_k + \mu\alpha_k S\frac{\partial p}{\partial s} = \\ &\frac{u_y}{R_p}\alpha_k S\rho_k v_k - iS\Gamma_g v_i + iSF_i + SF_{k,gx} - SF_{k,t}\end{aligned} \tag{36}$$

where all differential terms are collected on the left hand side and all non-differential terms (source terms) are collected on the right hand side of the equation. Appendix C shows that some of the empirical correlations used for description of the source terms may sometimes contain also differential terms.

**Energy balance.** The energy balance equation is obtained by inserting definitions: $\psi_k = e_{tot,k}$, where $e_{tot,k} = e_k + v_k^2/2$, $\mathbf{J}_k = \vec{\mathbf{q}}_k + \left(p\mathbf{I} - \mathbf{V}_k\right)\cdot\vec{\mathbf{v}}_k$, and $\phi_k = \vec{F}_k\cdot\vec{\mathbf{v}}_k$ from Table 1 into the general balance equation in Lagrangian coordinates, Eq. (25):

$$\begin{aligned}&\frac{\partial}{\partial t}S\alpha_k\rho_k e_{tot,k} + u_x\frac{\partial}{\partial s}S\alpha_k\rho_k e_{tot,k} + \mu\frac{\partial}{\partial s}S\alpha_k\rho_k v_k e_{tot,k} + \mu\frac{\partial}{\partial s}S\alpha_k\vec{\mathbf{q}}_k\cdot\vec{\mathbf{t}} + \mu\frac{\partial}{\partial s}S\alpha_k\left(p\mathbf{I}\cdot\vec{\mathbf{v}}_k\right)\cdot\vec{\mathbf{t}} - \\ &\mu\frac{\partial}{\partial s}S\alpha_k\left(\mathbf{V}_k\cdot\vec{\mathbf{v}}_k\right)\cdot\vec{\mathbf{t}} - \frac{u_y}{R_p}S\alpha_k\rho_k e_{tot,k} + P_i\dot{m}_k e_{tot,k} + P_i\vec{\mathbf{q}}_k\cdot\vec{\mathbf{n}}_k + P_i\left(p\mathbf{I}\cdot\vec{\mathbf{v}}_k\right)\cdot\vec{\mathbf{n}}_k - P_i\left(\mathbf{V}_k\cdot\vec{\mathbf{v}}_k\right)\cdot\vec{\mathbf{n}}_k + \\ &P_k\vec{\mathbf{q}}_k\cdot\vec{\mathbf{n}}_k + P_k\left(p\mathbf{I}\cdot\vec{\mathbf{v}}_k\right)\cdot\vec{\mathbf{n}}_k - P_k\left(\mathbf{V}_k\cdot\vec{\mathbf{v}}_k\right)\cdot\vec{\mathbf{n}}_k - S\alpha_k\rho_k\vec{F}_k\cdot\vec{\mathbf{v}}_k = 0\end{aligned} \tag{37}$$

The following approximations and relationships are considered in derivation of the Eq. (37):

- Tangential viscous stress and tangential heat flux are negligible (see Eq. (31)) and because $\vec{\mathbf{v}}_k \approx v_k\vec{\mathbf{t}}$, then as a consequence:

$$\mu\frac{\partial}{\partial s}S\alpha_k\left(\mathbf{V}_k\cdot\vec{\mathbf{v}}_k\right)\cdot\vec{\mathbf{t}} \approx \mu\frac{\partial}{\partial s}S\alpha_k v_k\left(\mathbf{V}_k\cdot\vec{\mathbf{t}}\right)\cdot\vec{\mathbf{t}} \approx 0 \tag{38}$$

- The $p\mathbf{I}$ is a diagonal tensor of the uniform pressure and $\vec{\mathbf{v}}_k$ is the fluid velocity vector, then:

$$p\mathbf{I}\cdot\vec{\mathbf{v}}_k = p\vec{\mathbf{v}}_k \qquad \text{and consequently} \qquad \mu\frac{\partial}{\partial s}\alpha_k S\left(p\mathbf{I}\cdot\vec{\mathbf{v}}_k\right)\cdot\vec{\mathbf{t}} = \mu\frac{\partial}{\partial s}\alpha_k Sp\left(\vec{\mathbf{v}}_k\cdot\vec{\mathbf{t}}\right) \tag{39}$$

- The vapor generation rate $\Gamma_g$ is given in Eq. (26).
- The interfacial volumetric heat flux is defined as:

$$P_i\vec{\mathbf{q}}_k\cdot\vec{\mathbf{n}}_k = -SQ_{ik} \tag{40}$$

- Considering the flux density through the interface given by equation (20) it is possible to get:

$$P_i\left(p\mathbf{I}\cdot\vec{\mathbf{v}}_k\right)\cdot\vec{\mathbf{n}}_k = P_i p\left(\vec{\mathbf{v}}_k\cdot\vec{\mathbf{n}}_k\right) = P_i\dot{m}_k\frac{p}{\rho_k} + P_i p\left(\vec{\mathbf{U}}_i\cdot\vec{\mathbf{n}}_k\right) \tag{41}$$

  where the first term on the right-hand side represents the pressure driven interface mass transfer and the second term represents the pressure driven dynamic effect of the moving interface.
- Because the viscous stress tensor is symmetric:

$$P_i\left(\mathbf{V}_k\cdot\vec{\mathbf{v}}_k\right)\cdot\vec{\mathbf{n}}_k = P_i\left(\mathbf{V}_k\cdot\vec{\mathbf{n}}_k\right)\cdot\vec{\mathbf{v}}_k \approx v_k P_i\left(\mathbf{V}_k\cdot\vec{\mathbf{n}}_k\right)\cdot\vec{\mathbf{t}} = iv_k SF_i \tag{42}$$

- The wall-to-fluid heat transfer is neglected (fast transient assumption) or the wall is adiabatic:

$$P_k\vec{\mathbf{q}}_k\cdot\vec{\mathbf{n}}_k \approx 0 \tag{43}$$

- With the flux density equation given by equation (20) it is possible to yield:

$$P_k\left(p\mathbf{I}\cdot\vec{\mathbf{v}}_k\right)\cdot\vec{\mathbf{n}}_k = P_k p\left(\vec{\mathbf{v}}_k\cdot\vec{\mathbf{n}}_k\right) = P_k\dot{m}_k\frac{p}{\rho_k} + P_k p\left(\vec{\mathbf{U}}_\Sigma\cdot\vec{\mathbf{n}}_k\right) \tag{44}$$

  where the first term on the right hand side represents the pressure driven mass flow rate through the pipe wall (equal to zero) and the second term represent pressure changes due to the deformation of the pipe wall. Deformations of the pipe cross-section are negligible for straight sections while ovalization at the elbow shall be considered (usually through a flexibility factor).

- Because the viscous stress tensor is symmetric, and because $\vec{\mathbf{v}}_k \approx v_k\vec{\mathbf{t}}$ :

$$P_k\left(\mathbf{V}_k\cdot\vec{\mathbf{v}}_k\right)\cdot\vec{\mathbf{n}}_k = P_k\left(\mathbf{V}_k\cdot\vec{\mathbf{n}}_k\right)\cdot\vec{\mathbf{v}}_k \approx v_k P_k\left(\mathbf{V}_k\cdot\vec{\mathbf{n}}_k\right)\cdot\vec{\mathbf{t}} = -v_k SF_{k,t} \tag{45}$$

- Because $\vec{\mathbf{v}}_k \approx v_k\vec{\mathbf{t}}$ , then:

$$\alpha_k S\rho_k\vec{F}_k\cdot\vec{\mathbf{v}}_k \approx \alpha_k S\rho_k v_k\vec{F}_k\cdot\vec{\mathbf{t}} = \alpha_k S\rho_k v_k F_{gx} \tag{46}$$

Then the first order partial differential equation for energy balance becomes:

$$\begin{aligned}&\frac{\partial}{\partial t}\alpha_k S\rho_k e_{tot,k} + u_x\frac{\partial}{\partial s}\alpha_k S\rho_k e_{tot,k} + \mu\frac{\partial}{\partial s}\alpha_k S\rho_k v_k e_{tot,k} + \mu\frac{\partial}{\partial s}\alpha_k Sv_k p = \\ &\frac{u_y}{R_p}\alpha_k S\rho_k e_{tot,k} - iS\Gamma_g\left(h+\frac{v_k^2}{2}\right) + SQ_{ik} + iSv_k F_i + Sv_k F_{k,gx} - v_k SF_{k,t}\end{aligned} \tag{47}$$

All differential terms are collected on the left hand side and all non-differential terms (source terms) are collected on the right hand side.

**Application of the fluid balance equations for a straight and stiff piping system.** If one assumes that deformations of the piping system are small, then the axial and lateral pipe velocities are zero ($u_x \rightarrow 0$, $u_y \rightarrow 0$), the stretching rate becomes equal to one ($\mu \rightarrow 1$). It is further possible to assume that the piping system is straight, then the Junction coupling term becomes infinitesimal ($u_y / R_p \rightarrow 0$). The Equation (27) for mass balance, the Eq. (36) for momentum balance and the Eq. (47) for energy balance then become:

$$\frac{\partial}{\partial t}S\alpha_k\rho_k + \frac{\partial}{\partial s}S\alpha_k\rho_k v_k = -iS\Gamma_g \tag{48}$$

$$\frac{\partial}{\partial t}\alpha_k S\rho_k v_k + \frac{\partial}{\partial s}\alpha_k S\rho_k v_k v_k + \alpha_k S\frac{\partial p}{\partial s} = -iS\Gamma_g v_i + iSF_i + SF_{k,gx} - SF_{k,t} \tag{49}$$

$$\frac{\partial}{\partial t}\alpha_k S\rho_k e_{tot,k} + \frac{\partial}{\partial s}\alpha_k S\rho_k v_k e_{tot,k} + \frac{\partial}{\partial s}\alpha_k Sv_k p = -iS\Gamma_g\left(h+\frac{v_k^2}{2}\right) + SQ_{ik} + iSv_k F_i + Sv_k F_{k,gx} - v_k SF_{k,t} \tag{50}$$

The system of equations written above is essentially the same system of equations as the one described in Appendix C (Eqs. (C-4) - (C-6)) as a standard two-fluid system of equations in Eulerian coordinate system applied in the WAHA code (Tiselj et al. [126]) and other codes like RELAP5, CATHARE, TRAC, TRACE, etc. There are only minor differences between the WAHA equations and Eqs. (27), (36), and (47):

- The WAHA momentum equation contains a virtual mass term CVM and an interfacial pressure term $p_i$. Both terms are differential and are added as auxiliary closure laws in the WAHA code to ensure hyperbolicity of the system in various flow regimes.
- The energy balance equation in the WAHA code contains the term $p\frac{\partial}{\partial t}\alpha_k S$. The origin of the term in the energy balance equations has been a topic of numerous debates in the past. However, the term is not important for our type of simulations and we proved that influence of this term on the results is negligible. Some textbooks like Toro [128] included this term (without given derivation), the other like Ishii and Hibiki [62] or Lemonier [82] not. According to our experiences, the term theoretically appears only in the energy equation if the existing equation is transformed into an equation with the enthalpy as basic variable instead of the total energy. The inclusion of this term simplifies the vectorial form of the system and thus simplifies the evaluation of the eigensystem.
- The source terms are the same (some terms in the energy balance equation are neglected later by analogously with the same terms in the WAHA code)

We have shown that the equations derived in Lagrangian coordinates under the assumption of a stiff and undeformable piping system naturally degenerate into standard equations derived in Eulerian coordinate system. We analyzed the differences between the standard model and the model derived with our approach and we realized that there is only one different term in the energy balance equation with negligible influence on the eigensystem. The other terms are either introduced as auxiliary closure laws or are neglected later being recognized as negligible (for instance change of the kinetic energy due to the interface mass exchange).

**New terms in the balance equations.** A discussion on the improvements that appear in the derivation of the balance equations in a Lagrangian coordinate system is given in this paragraph. The comparison of equations (27), (36), and (47) derived in deformable and arbitrarily shaped Lagrangian coordinates and equations (48), (49), and (50) applicable for simulations of FSI transients in stiff and fixed piping systems gives the following conclusions:

- There are two types of improvements: there are *new variables* introduced in standard terms and there are *new terms*.
- Every balance equation has a new differential term in the form $u_x \frac{\partial}{\partial s}...$ which can be understood as a correction of the convective term resulting from the axial pipe movement. **The new convective term is important for cases where the pipe motions are large.** Rearrangement of the equations (27), (36), and (47) yields the following form of the convective terms: $\left(u_x + \mu v_k\right)\frac{\partial}{\partial s}...$.
- All spatial derivatives in equations (27), (36), and (47) are multiplied by a scale factor $\mu$, which accounts for axial deformations (stretching) of the pipe. The scale factor is defined by equation (12). The axial deformations of the piping systems are usually very small compared to the lateral movement (several orders of magnitude), and **the stretching correction is expected to be very small**. Therefore, the value of the scale factor is expected to be close to one.
- The junction coupling term $u_y / R_p$ came in during the derivation of the convective term in the general balance equation. This term actually represents the contribution of the lateral pipe movement $u_y$ at curvatures, which is in FSI practice called the junction coupling. **The Junction coupling term is very important at curvatures**, but it is equal to zero for straight sections of pipe.

There are three major improvements that affect: (i) convection due to axial pipe motion, (ii) space derivatives due to stretching (axial pipe deformations), and (iii) source terms due to junction coupling at curvatures. All these terms become important only for some special conditions. However, for accurate description of the FSI at curvatures it is necessary to account junction coupling term only. The other two terms represent a minor improvement and are negligible for FSI in most practical cases.

# 3. Dynamics of arbitrarily shaped piping system

The piping systems considered in this dissertation are one dimensional structures ($R << L$), which are deformable and are arbitrarily shaped in the three dimensional space. The best parameter for the mathematical description of such structures is the general arc length parameter $s$, introduced and described in the previous Chapter (see Figure 2). The derivation of the appropriate partial differential equations for axial, lateral and rotational (in-plane and out-of-plane), radial and torsional dynamics is given in this Chapter. This derivation is based upon the constitutive laws and force/momentum balance equations. The wave equations and Timoshenko beam equations (for straight piping systems only) are easily obtainable by coupling of the constitutive law and force/momentum balance equations. The equations derived in the present section for a general arc length parameter $s$ yield several new terms compared to the standard approach to simulate FSI transient flows described by Wiggert, Hatfield and Stuckenbruck [143] and Tijsseling [115]. The new terms are not differential and describe local coupling mechanisms appearing at curvatures known as junction couplings. The standard approach is based upon the appropriate coupling of straight sections of the pipe, where the junction coupling is given with additional coupling relations at elbows and curvatures that act as boundary conditions.

An improvement of the new equations with respect to the standard approach is that the junction coupling at elbows and curvatures is described within the physical model, so the curvatures and elbows can be smooth, small (even due to deformations of the pipe), and arbitrary (regardless the boundary conditions). The piping systems applied in this thesis are assumed to obey the linear Hooke's law of elasticity (see Appendix E). Valentin, Phillips and Walker [131] applied a physical model with similar source terms for piping systems with constant curvature.

The considered physical models are essentially developed for simulations of the transient FSI, but they can be used also for consideration of oscillatory motions of piping systems (see for instance Section 6.1). The natural frequency of oscillations is discussed at the end of this Chapter, as it was proved by Lavooij and Tijsseling [75] that natural frequencies of oscillation indicate potential vulnerability of the piping system by the FSI transient occurrence.

## 3.1. Introduction

Recall that the natural set of parameters to describe an arbitrarily shaped and deformable piping system is a curve $C$ such as the neutral fiber of the pipe that can be described mathematically by a general parameter $s$ (Figures 1 & 2). The position of the point $P$ on a neutral fiber $C$ of the pipe represented with parameter $s$ is defined as $P = P(s,t)$. The local coordinate basis for any point $P$ on the curve is built upon the Fresnet frame $\left(\vec{\mathbf{t}},\vec{\mathbf{n}},\vec{\mathbf{b}}\right)$. The vectors of the Fresnet frame are respectively the tangent to the curve, the normal to the curve and the binormal. The vectors representing the physical state of the pipe at point $P$ written with the vectors of the Fresnet frame are given in Table 4.

*Table 4: Vectors representing physical state of the pipe at point P.*

| Description of vector | Mathematical notation |
|---|---|
| Fluid velocity | $\vec{\mathbf{v}}_k = v_k\vec{\mathbf{t}} + u_y\vec{\mathbf{n}} + u_z\vec{\mathbf{b}}$ |
| Pipe translations | $\vec{\mathbf{w}} = w_x\vec{\mathbf{t}} + w_y\vec{\mathbf{n}} + w_z\vec{\mathbf{b}}$ |
| Displacement velocity | $\vec{\mathbf{U}}_C = u_x\vec{\mathbf{t}} + u_y\vec{\mathbf{n}} + u_z\vec{\mathbf{b}}$ |
| Pipe rotations | $\vec{\mathbf{\Phi}} = \phi_x\vec{\mathbf{t}} + \phi_y\vec{\mathbf{n}} + \phi_z\vec{\mathbf{b}}$ |
| Rotation velocity | $\vec{\boldsymbol{\varphi}} = \varphi_x\vec{\mathbf{t}} + \varphi_y\vec{\mathbf{n}} + \varphi_z\vec{\mathbf{b}}$ |
| Internal forces | $\vec{\mathbf{F}} = N_x\vec{\mathbf{t}} + Q_y\vec{\mathbf{n}} + Q_z\vec{\mathbf{b}}$ |
| Internal moments | $\vec{\mathbf{M}} = M_x\vec{\mathbf{t}} + M_y\vec{\mathbf{n}} + M_z\vec{\mathbf{b}}$ |

## 3.2. Axial dynamics

**Constitutive equation of axial motion.** Spreading of the stress waves in the arbitrarily shaped piping system is described with two equations. The first equation is derived form the stress-strain Hooke's law of elasticity. The constitutive equation for the axial direction relates the axial unit strain $\varepsilon_{xx}$ to the axial stress $\sigma_{xx}$ and the lateral stress $\sigma_{yy}$, and is derived in Appendix E in Eq. (E-10):

$$\varepsilon_{xx} = \frac{1}{E}\left(\sigma_{xx} - \nu\sigma_{yy}\right) \tag{51}$$

Where $E$ denotes elasticity modulus and $\nu$ the Poisson ratio. The relationship is known as the approximation of the three-dimensional Hooke's law for two-dimensional shell structures. The axial strain $\varepsilon_{xx}$ is related to the tangential projection of the vector of displacements $\vec{\mathbf{w}}$ by the following relationship (see Appendix B for derivative rules):

$$\varepsilon_{xx} = \frac{\partial\vec{\mathbf{w}}}{\partial s}\cdot\vec{\mathbf{t}} = \frac{\partial w_x}{\partial s} - \frac{w_y}{R_p} \tag{52}$$

where the term $w_y/R_p$ describes the contribution of the lateral deformation to the axial strain at curvatures. The equation for the circumferential stress $\sigma_{yy}$ is derived as Eq. (E-13) in Appendix E:

$$\sigma_{yy} = \frac{R}{e}p \tag{53}$$

The relationship between the axial stress $\sigma_{xx}$ and the axial force $N_x$ is given as:

$$\sigma_{xx} = \frac{\vec{\mathbf{F}}}{S_t}\cdot\vec{\mathbf{t}} = \frac{N_x}{S_t} \tag{54}$$

Putting equations (52), (53), and (54) into Eq. (51) yields the constitutive equation for axial motion:

$$\frac{\partial w_x}{\partial s} - \frac{w_y}{R_p} = \frac{1}{E}\left(\frac{N_x}{S_t} - \frac{\nu R p}{e}\right) \tag{55}$$

Differentiation of the above equation with respect to the time yields the constitutive equation for axial motion of the arbitrarily shaped and deformable piping system (with $u_x = \partial w_x / \partial t$ and $u_y = \partial w_y / \partial t$ ):

$$\frac{1}{ES_t}\frac{\partial N_x}{\partial t} - \frac{\nu R}{Ee}\frac{\partial p}{\partial t} - \frac{\partial u_x}{\partial s} = -\frac{u_y}{R_p} \tag{56}$$

For straight piping sections, the radius of curvature approaches infinity and Eq. (56) gets the form that is used in standard models for FSI simulations (Eq. (14) in Wiggert, Hatfield and Stuckenbruck [143]):

$$\frac{1}{ES_t}\frac{\partial N_x}{\partial t} - \frac{\nu R}{Ee}\frac{\partial p}{\partial t} - \frac{\partial u_x}{\partial s} = 0 \tag{57}$$

**Equation of axial motion.** The second equation for the description of the axial motion of the pipe is defined as equilibrium of all forces acting on a control volume (Fig. 4) and uses the second Newton's law of motion, which states that the inertial force is equal to the product of the mass and acceleration. Summation of all forces in tangential direction on a differential element gives:

$$m_s\delta s\frac{\partial^2\vec{\mathbf{w}}}{\partial t^2}\cdot\vec{\mathbf{t}} = \frac{\partial\vec{\mathbf{F}}}{\partial s}\delta s\cdot\vec{\mathbf{t}} + \vec{\mathbf{f}}(s,t)\delta s\cdot\vec{\mathbf{t}} \tag{58}$$

where $\vec{\mathbf{F}}$ is the vector of the internal forces, $\vec{\mathbf{f}}(s,t)$ stands for the friction, body and external forces per unit length, and $m_s$ stands for total mass of the pipe per unit of length (including eventual load). The tangential projection of the differential of the internal forces yields:

$$\frac{\partial \vec{\mathbf{F}}}{\partial s} \cdot \vec{\mathbf{t}} = \frac{\partial N_x}{\partial s} - \frac{Q_y}{R_p} \tag{59}$$

In accordance with Appendix B, the projection of the temporal derivative of translations in tangential direction yields:

$$\frac{\partial \vec{\mathbf{w}}}{\partial t} \cdot \vec{\mathbf{t}} = \frac{\partial w_x}{\partial t} + (\Omega \times \vec{\mathbf{w}}) \cdot \vec{\mathbf{t}} \tag{60}$$

where the term with the rotation of the Fresnet frame $\Omega$ is considered to be small and is neglected (it becomes important only for spiral piping systems). Projection of the friction, body, and external forces in the tangential direction yields:

$$\vec{\mathbf{f}}(s,t) \cdot \vec{\mathbf{t}} = f_x(s,t) = SF_{k,t} + S_t F_{t,gx} + \frac{F_x}{\Delta s} \tag{61}$$

where an example of wall friction force $F_{k,t}$ correlation is given with Eq. (C-24) and an example of body force $F_{t,gx}$ with Eq. (C-15). Introduction of the above relationships into Eq. (58) then yields the second first order partial differential equation for axial motion of a deformable arbitrarily shaped piping system:

$$m_s \frac{\partial u_x}{\partial t} - \frac{\partial N_x}{\partial s} = -\frac{Q_y}{R_p} + SF_{k,t} + S_t F_{t,gx} + \frac{F_x}{\Delta s} \tag{62}$$

Compared to the forces induced by the water hammer pressure waves and through the Poisson forces or junction coupling mechanisms, the friction and body forces usually play a minor (negligible) role and are thus neglected in most practical applications [115, 144]. Additionally, for straight piping sections, the radius of curvature approaches infinity and Eq. (62) gets the form that is used in standard FSI models (Eq. (13) in Wiggert, Hatfield and Stuckenbruck [143]):

$$m_s \frac{\partial u_x}{\partial t} - \frac{\partial N_x}{\partial s} = 0 \tag{63}$$

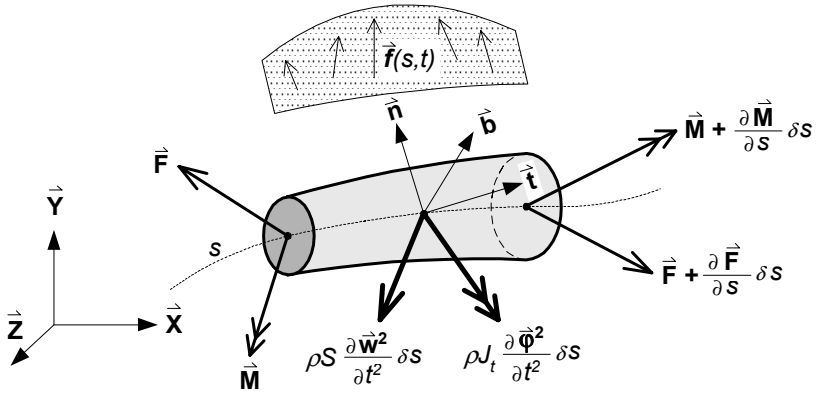


Fig. 4: Pipe section of length $\delta s$ with force and mass balance in 3D space.

## 3.3. Lateral and rotational dynamics

The lateral and rotational dynamics of the piping system are usually treated together because the standard approach in FSI computational practice is based on the general Timoshenko beam theory, which is described in Appendix F. The Timoshenko beam equation of the Timoshenko beam theory

decays into a set of four partial differential equations, two for lateral and two for rotational dynamics. The Timoshenko beam theory is well established and frequently used in civil and mechanical engineering for the evaluation of dynamics of beams. Improvement of the standard Timoshenko beam theory developed for straight sections yields equations applicable for the description of deformable piping systems of arbitrary shape. Regarding the vectors of the Fresnet frame, the term in-plane dynamics refers to the dynamics within the plane defined by vectors $\vec{\mathbf{t}}$ and $\vec{\mathbf{n}}$, with vector $\vec{\mathbf{b}}$ as normal to the plane. For general piping systems spanning in the three dimensional space, the orientation of the vector $\vec{\mathbf{b}}$ varies. However for the planar piping systems, the orientation of the vector normal to the plane becomes constant, and if defined so, also conform with the coordinate $\vec{\mathbf{Z}}$ of the general coordinate system (Fig. 4). For planar piping systems the term in-plane corresponds to the term curvature plane. Term *out-of-plane* dynamics refers to dynamics within the plane spanned with vectors $\vec{\mathbf{t}}$ and $\vec{\mathbf{b}}$, and with vector $\vec{\mathbf{n}}$ as normal to that plane. The out-of-plane dynamics becomes negligible for planar piping systems, while for three dimensional piping systems, the in-plane and out-of-plane dynamics are equally important.

### 3.3.1. In-plane dynamics

**Constitutive equation of in-plane lateral motion.** The first equation of the improved system of four Timoshenko beam partial differential equations (Appendix F) is obtained from the elementary Euler-Bernoulli theory of bending that gives the linear shear stress-strain relationship between the shear force $Q_y$ and the shear strain $\beta$:

$$\frac{Q_y}{\kappa S_t G} = -\beta \tag{64}$$

where $G = E / 2(1 + \nu)$ stands for the shear modulus and $\kappa$ for the Timoshenko shear coefficient (Appendix F). Due to the effect of the shear, the original rectangular element changes its shape to somewhat like a parallelogram with slightly curved sides. The total slope of the displacement of the beam differential element is defined as an angle of the bending rotation $\phi_z$ of the beam element minus the increase in the slope of the element due to the shear strain $\beta$:

$$\frac{\partial \vec{\mathbf{w}}}{\partial s} \cdot \vec{\mathbf{n}} = \phi_z - \beta \tag{65}$$

Using the derivative rules for the vectors of the Fresnet frame, the slope of the displacement is related to the vector of the displacements by the following relationship:

$$\frac{\partial \vec{\mathbf{w}}}{\partial s} \cdot \vec{\mathbf{n}} = \frac{\partial w_y}{\partial s} + \frac{w_x}{R_p} + \frac{w_z}{T_p} \tag{66}$$

where $R_p$ is the radius of curvature and $T_p$ is the radius of torsion of the pipe, the term $w_x / R_p$ describes contribution of the axial deformation to the change of the slope and the term $w_z / T_p$ describes the contribution of the torsional deformation to the change of the slope of the pipe. The combination of equations (64), (65), and (66), and then differentiation with the time yields the constitutive equation for the lateral direction:

$$\frac{1}{\kappa S_t G}\frac{\partial Q_y}{\partial t} - \frac{\partial u_y}{\partial s} = \frac{u_x}{R_p} + \frac{u_z}{T_p} - \varphi_z \tag{67}$$

where $u_x = \partial w_x / \partial t$ , $u_y = \partial w_y / \partial t$ and $\varphi_z = \partial \phi_z / \partial t$ are the velocity-displacement relations. All torsional terms are neglected for planar piping systems. Additionally, for straight piping sections, the radius of curvature approaches infinity and Eq. (67) gets the standard form for simulations of the FSI (Eq. (6) in Wiggert, Hatfield and Stuckenbruck [143]):

$$\frac{1}{\kappa S_t G}\frac{\partial Q_y}{\partial t}-\frac{\partial u_y}{\partial s}=-\varphi_z \tag{68}$$

**Equation of in-plane lateral motion.** The equation of lateral motion is defined as the equilibrium of all forces acting on a control volume (Fig. 4) and using the second Newton's law of motion, which states that inertial force is equal to the product of the mass and acceleration. Summation of all forces in the lateral (normal) direction on a differential element gives:

$$m_T \delta s \frac{\partial^2 \vec{\mathbf{w}}}{\partial t^2}\cdot\vec{\mathbf{n}} = \frac{\partial \vec{\mathbf{F}}}{\partial s}\delta s\cdot\vec{\mathbf{n}} + \vec{\mathbf{f}}(s,t)\delta s\cdot\vec{\mathbf{n}} \tag{69}$$

In accordance with Appendix B, the projection of the temporal derivative of translations in normal direction yields:

$$\frac{\partial \vec{\mathbf{w}}}{\partial t}\cdot\vec{\mathbf{n}} = \frac{\partial w_y}{\partial t} + (\Omega\times\vec{\mathbf{w}})\cdot\vec{\mathbf{n}} \tag{70}$$

where the term with the rotation of the Fresnet frame $\Omega$ is again small and it is neglected since it is important only for spiral piping systems. The normal projection of the differential of the forces yields:

$$\frac{\partial \vec{\mathbf{F}}}{\partial s}\cdot\vec{\mathbf{n}} = \frac{\partial Q_y}{\partial s} + \frac{N_x - Sp}{R_p} + \frac{Q_z}{T_p} \tag{71}$$

The body and external forces in the lateral direction are defined as:

$$\vec{\mathbf{f}}(s,t)\cdot\vec{\mathbf{n}} = f_y(s,t) = m_T g\cos(\gamma) - \frac{F_y}{\Delta s} \tag{72}$$

Finally, the equation of lateral motion yields (with $u_y = \partial w_y / \partial t$ ):

$$m_T\frac{\partial u_y}{\partial t} - \frac{\partial Q_y}{\partial s} = \frac{N_x - Sp}{R_p} + \frac{Q_z}{T_p} + m_T g\cos(\gamma) - \frac{F_y}{\Delta s} \tag{73}$$

For straight piping sections, the radiuses of curvature and torsion approach infinity, body forces for in-plane oscillation become negligible and if there is no external load, then Eq. (73) gets the form of the standard physical model utilized in FSI studies (Eq. (5) in Wiggert, Hatfield and Stuckenbruck [143]):

$$m_T\frac{\partial u_y}{\partial t} - \frac{\partial Q_y}{\partial s} = 0 \tag{74}$$

**Constitutive equation for in-plane rotational motion.** The constitutive equation for the rotational motion is conducted from the elementary theory of bending that gives a relationship between the bending momentum and the angle of rotation bending:

$$M_z = EI_t\frac{\partial \vec{\boldsymbol{\varphi}}}{\partial s}\cdot\vec{\mathbf{b}}\text{ , where }\quad \frac{\partial \vec{\boldsymbol{\varphi}}}{\partial s}\cdot\vec{\mathbf{b}} = \frac{\partial \phi_z}{\partial s} - \frac{\phi_y}{T_p} \tag{75}$$

Combination of the above definitions and then differentiation over the time yields the constitutive equation for in-plane rotational motion:

$$\frac{1}{EI_t}\frac{\partial M_z}{\partial t} - \frac{\partial \varphi_z}{\partial s} = -\frac{\varphi_y}{T_p} \tag{76}$$

For straight piping sections, the radius of torsion approaches infinity and Eq. (76) gets the form that is used in standard FSI simulations (Eq. (4) in Wiggert, Hatfield and Stuckenbruck [143]):

$$\frac{1}{EI_t}\frac{\partial M_z}{\partial t} - \frac{\partial \varphi_z}{\partial s} = 0 \tag{77}$$

**Equation of in-plane rotational motion.** Summation of the moments in binormal direction on a differential element in Fig. 4 gives:

$$I_t \rho_t \delta s \frac{\partial^2 \vec{\boldsymbol{\varphi}}}{\partial t^2} \cdot \vec{\mathbf{b}} = \frac{\partial \vec{\mathbf{M}}}{\partial s} \delta s \cdot \vec{\mathbf{b}} + \left( \vec{\mathbf{r}} \times \left( 2\vec{\mathbf{F}} + \frac{\partial \vec{\mathbf{F}}}{\partial s} \delta s \right) \right) \cdot \vec{\mathbf{b}} \tag{78}$$

where $\vec{\mathbf{r}} = \{\delta s/2, 0, 0\}$ is the vector length from the center of the differential element to the vector force $\vec{\mathbf{F}}$. It is perpendicular to the force vector. The last term of the above equation yields:

$$\left( \vec{\mathbf{r}} \times \left( 2\vec{\mathbf{F}} + \frac{\partial \vec{\mathbf{F}}}{\partial s} \delta s \right) \right) \cdot \vec{\mathbf{b}} = Q_y \delta s + \frac{1}{2}\frac{\partial Q}{\partial s} \delta s^2 \tag{79}$$

The differential of the lateral force (the second term on the right hand side) in Eq. (79) is usually infinitesimal and small compared to the size of the force and it is neglected.

The binormal projection of the differential of the momentum vector yields (see Appendix B):

$$\frac{\partial \vec{\mathbf{M}}}{\partial s} \cdot \vec{\mathbf{b}} = \frac{\partial M_z}{\partial s} - \frac{M_y}{T_p} \tag{80}$$

According to Appendix B, the projection of the temporal derivative of translations in binormal direction yields:

$$\frac{\partial \vec{\boldsymbol{\varphi}}}{\partial t} \cdot \vec{\mathbf{b}} = \frac{\partial \phi_z}{\partial t} + (\Omega \times \vec{\mathbf{w}}) \cdot \vec{\mathbf{b}} \tag{81}$$

where the term with the rotation of the Fresnet frame $\Omega$ is negligible for piping systems in plane. Rearrangement yields the first order partial differential equation known as the equation of rotational motion of the arbitrarily shaped deformable piping system:

$$I_t \rho_t \frac{\partial \varphi_z}{\partial t} - \frac{\partial M_z}{\partial s} = -\frac{M_y}{T_p} + Q_y \tag{82}$$

Again, for straight piping sections, the radius of torsion approaches infinity and Eq. (82) gets the form that is utilized in standard FSI physical models (Eq. (3) in Wiggert, Hatfield and Stuckenbruck [143]):

$$I_t \rho_t \frac{\partial \varphi_z}{\partial t} - \frac{\partial M_z}{\partial s} = Q_y \tag{83}$$

### 3.3.2. Out-of-plane dynamics

This section gives a brief derivation of the four partial differential equations for the description of the arbitrarily shaped 3D deformable piping system that moves out-of-curvature plane. The derivation is very similar to the derivation of equations for in-plane lateral and rotational dynamics. Major differences are stressed only, for details see analogy with the previous section. An extrapolation for the straight piping systems can be performed analogously to the previous section. An example of standard equations applied for FSI simulations can be found in Wiggert, Hatfield and Stuckenbruck [143].

**Constitutive equation of out-of-plane lateral motion.** The following relationships are applied:

$$\frac{Q_z}{\kappa S_t G} = -\beta\,, \quad \frac{\partial \vec{\mathbf{w}}}{\partial s}\cdot\vec{\mathbf{b}} = \frac{\partial w_z}{\partial s} - \frac{w_y}{T_p}\,, \text{ and } \quad \frac{\partial \vec{\mathbf{w}}}{\partial s}\cdot\vec{\mathbf{b}} = \phi_y - \beta \tag{84}$$

where $Q_z$ stands for the lateral force. The constitutive equation for out-of-plane lateral direction gives:

$$\frac{1}{\kappa S_t G}\frac{\partial Q_z}{\partial t} - \frac{\partial u_z}{\partial s} = -\frac{u_y}{T_p} - \varphi_y \tag{85}$$

**Equation of out-of-plane lateral motion.** Summation of all forces in the lateral (binormal) direction on a differential element in Fig. 4 gives:

$$m_T \delta s \frac{\partial^2 \vec{\mathbf{w}}}{\partial t^2}\cdot\vec{\mathbf{b}} = \frac{\partial \vec{\mathbf{F}}}{\partial s}\delta s\cdot\vec{\mathbf{b}} + \vec{\mathbf{f}}(s,t)\delta s\cdot\vec{\mathbf{b}} \tag{86}$$

Using relationships:

$$\frac{\partial \vec{\mathbf{w}}}{\partial t}\cdot\vec{\mathbf{b}} \approx \frac{\partial w_z}{\partial t}\,, \qquad \frac{\partial \vec{\mathbf{F}}}{\partial s}\cdot\vec{\mathbf{b}} = \frac{\partial T_z}{\partial s} - \frac{Q_y}{T_p}\,, \text{ and } \qquad \vec{\mathbf{f}}(s,t)\cdot\vec{\mathbf{b}} = f_z(s,t) = m_T g\cos(\gamma) - \frac{F_z}{\Delta s} \tag{87}$$

The equation of out-of-plane lateral motion yields:

$$m_T \frac{\partial u_z}{\partial t} - \frac{\partial T_z}{\partial s} = -\frac{Q_y}{T_p} + m_T g\cos(\gamma) - \frac{F_z}{\Delta s} \tag{88}$$

**Constitutive equation for out-of-plane rotational motion.** Using relationships:

$$M_y = EI_t \frac{\partial \vec{\boldsymbol{\varphi}}}{\partial s}\cdot\vec{\mathbf{n}}\,, \text{ and } \quad \frac{\partial \vec{\boldsymbol{\varphi}}}{\partial s}\cdot\vec{\mathbf{n}} = \frac{\partial \phi_y}{\partial s} + \frac{\phi_x}{R_p} + \frac{\phi_z}{T_p} \tag{89}$$

and differentiation over the time yields the following constitutive equation for out-of-plane rotational motion:

$$\frac{1}{EI_t}\frac{\partial M_y}{\partial t} - \frac{\partial \varphi_y}{\partial s} = \frac{\varphi_x}{R_p} - \frac{\varphi_z}{T_p} \tag{90}$$

**Equation of out-of-plane rotational motion.** Summation of the moments in normal direction $\vec{\mathbf{n}}$ on a differential element in Fig. 4 gives:

$$I_t \rho_t \delta s \frac{\partial^2 \vec{\boldsymbol{\varphi}}}{\partial t^2}\cdot\vec{\mathbf{n}} = \frac{\partial \vec{\mathbf{M}}}{\partial s}\delta s\cdot\vec{\mathbf{n}} + \left(\vec{\mathbf{r}}\times\left(2\vec{\mathbf{F}} + \frac{\partial \vec{\mathbf{F}}}{\partial s}\delta s\right)\right)\cdot\vec{\mathbf{n}} \tag{91}$$

The following relationships are applied:

$$\left(\vec{\mathbf{r}}\times\left(2\vec{\mathbf{F}} + \frac{\partial \vec{\mathbf{F}}}{\partial s}\delta s\right)\right)\cdot\vec{\mathbf{n}} \approx Q_z \delta s\,, \qquad \frac{\partial \vec{\mathbf{M}}}{\partial s}\cdot\vec{\mathbf{n}} = \frac{\partial M_y}{\partial s} + \frac{M_x}{R_p} + \frac{M_z}{T_p}\,, \text{ and } \quad \frac{\partial \vec{\boldsymbol{\varphi}}}{\partial t}\cdot\vec{\mathbf{n}} \approx \frac{\partial \phi_y}{\partial t} = \varphi_y \tag{92}$$

And the equation for out-of-plane rotational motion yields:

$$I_t \rho_t \frac{\partial \varphi_y}{\partial t} - \frac{\partial M_y}{\partial s} = \frac{M_x}{R_p} + \frac{M_z}{T_p} + Q_z \tag{93}$$

## 3.4. Radial dynamics

Walker and Phillips [134] presented a theoretical study of the propagation of a short-duration pressure pulse in a straight elastic pipe, including Poisson and junction coupling. They applied the four-equation single-phase linear FSI model for axial dynamics in straight piping systems, known as Skalak's four-equation model (see Section 4.2.1 and Skalak [104]), and introduced the following two additional equations for radial inertia forces in the pipe wall:

$$\left( \rho_t e + \frac{1}{2} \rho_f R \right) \frac{\partial u_y}{\partial t} + \frac{e}{R} \sigma_\varphi - p = 0 \tag{94}$$

$$(1 - \nu^2) \frac{\partial \sigma_\varphi}{\partial t} - \frac{E}{R} u_y - \nu E \frac{\partial u_x}{\partial s} \tag{95}$$

Derivation of radial dynamics equations can be found also in Tijsseling [115]. Schwarz [101] performed an extensive numerical study of coupled axial liquid and pipe motion in a single straight pipe with similar model to that of Walker and Phillips [115] and solved it with the Method of Characteristics. Schwarz proved that radial inertia is relatively unimportant for piping systems (high frequencies) and is thus not further considered in the present thesis.

## 3.5. Torsional dynamics

**Constitutive equation of torsional motion.** Torsional waves (around central axis of the pipe) become important at elbows in 3D structures where lateral waves via junction coupling mechanisms activate torsional and/or perpendicular lateral waves in accordance to the elbow properties like curvature and direction. Torsional waves are independent from the other equations of the physical model, the only interaction (coupling) occurs locally at geometric changes and elbows. The Euler-Bernoulli theory gives constitutive relationship between the torsional momentum $M_x$ and the angle of torsional rotation $\vec{\boldsymbol{\varphi}}$:

$$M_x = G J_t \frac{\partial \vec{\boldsymbol{\varphi}}}{\partial s} \cdot \vec{\mathbf{t}} \text{, where } \quad \frac{\partial \vec{\boldsymbol{\varphi}}}{\partial s} \cdot \vec{\mathbf{t}} = \frac{\partial \phi_x}{\partial s} - \frac{\phi_y}{R_p} \tag{96}$$

Combination of the above definitions, differentiation over the time, and introduction of the relationships $\varphi_x = \partial \phi_x / \partial t$, and $\varphi_y = \partial \phi_y / \partial t$ give the constitutive equation for torsional motion:

$$\frac{1}{G J_t} \frac{\partial M_x}{\partial t} - \frac{\partial \varphi_x}{\partial s} = - \frac{\varphi_y}{R_p} \tag{97}$$

For straight piping sections, the radius of curvature approaches infinity and Eq. (97) gets the standard form (Eq. (2) in Wiggert, Hatfield and Stuckenbruck [143]):

$$\frac{1}{G J_t} \frac{\partial M_x}{\partial t} - \frac{\partial \varphi_x}{\partial s} = 0 \tag{98}$$

**Equation of torsional motion.** Momentum balance in axial (torsional) direction on a differential element in Fig. 4 gives:

$$J_t \rho_t \delta s \frac{\partial^2 \vec{\boldsymbol{\varphi}}}{\partial t^2} \cdot \vec{\mathbf{t}} = \frac{\partial \vec{\mathbf{M}}}{\partial s} \delta s \cdot \vec{\mathbf{t}} + \left( \vec{\mathbf{r}} \times \left( 2\vec{\mathbf{F}} + \frac{\partial \vec{\mathbf{F}}}{\partial s} \delta s \right) \right) \cdot \vec{\mathbf{t}} \tag{99}$$

where $\vec{\mathbf{r}}$ is the perpendicular vector from the differential element center to the force $\vec{\mathbf{F}}$:

$$\vec{\mathbf{r}} = \left\{ \frac{\delta s}{2}, 0, 0 \right\} \quad \Rightarrow \quad \left( \vec{\mathbf{r}} \times \left( 2\vec{\mathbf{F}} + \frac{\partial \vec{\mathbf{F}}}{\partial s} \delta s \right) \right) \cdot \vec{\mathbf{t}} = 0 \cdot \vec{\mathbf{t}} = 0 \tag{100}$$

The tangential projection of the differential of the momentum vector yields (see Appendix B):

$$\frac{\partial \vec{\mathbf{M}}}{\partial s} \cdot \vec{\mathbf{t}} = \frac{\partial M_x}{\partial s} - \frac{M_y}{R_p} \tag{101}$$

In accordance with Appendix B, the projection of the temporal derivative of translations in the tangential direction yields:

$$\frac{\partial \vec{\boldsymbol{\varphi}}}{\partial t} \cdot \vec{\mathbf{t}} = \frac{\partial \phi_x}{\partial t} + (\Omega \times \vec{\mathbf{w}}) \cdot \vec{\mathbf{t}} \tag{102}$$

where the term with the rotation of the Fresnet frame $\Omega$ is small and neglected (relevant only for spiral systems). Rearrangement yields the equation of torsional motion of the arbitrarily shaped piping system:

$$\rho_t J_t \frac{\partial \varphi_x}{\partial t} - \frac{\partial M_x}{\partial s} = -\frac{M_y}{R_p} \tag{103}$$

For the straight piping sections, the radius of curvature approaches infinity and Eq. (103) gets the form that is utilized in standard FSI simulations (Eq. (1) in Wiggert, Hatfield and Stuckenbruck [143]):

$$\rho_t J_t \frac{\partial \varphi_x}{\partial t} - \frac{\partial M_x}{\partial s} = 0 \tag{104}$$

## 3.6. Natural frequency of an arbitrarily shaped piping system

FSI analyses have been very complicated, costly, time and processor consuming, therefore, there was always a wish to obtain reliable and generally accepted criteria for a quick estimation of the importance of the FSI. The only reliable criterion since, was proposed by Lavooij and Tijsseling [75] who discussed natural frequencies of oscillations and found a criterion valid for the case of rapid valve closure in a single elbow piping system. The criterion is based upon the natural frequencies of the structure, valve closure time and main time scale of the water hammer (pressure and/or stress) waves, i.e. the frequency of the dynamic load. **Lavooij and Tijsseling have shown that FSI is intense if the frequency of the dynamic load is close to the natural frequency of the pipe and if the valve closing time is shorter than the period of the dynamic load.** The natural frequency of the structure was then assigned as a potentially important indicator that points out the intensity and availability of the structure for a significant FSI.

Oscillations are actually more common in practice than dynamic transient motions during FSI occurrence, but consequences are less important and the phenomenon itself does not represent significant danger for integrity of the piping system (except fatigue of the material). Oscillatory motion is damped because it is not possible to eliminate energy losses due to the non-conservation forces like friction, viscosity, resistance etc. The theory of oscillating beams is well established, solutions are mostly based on finite element numerical method. The frequency $f$ is given in terms of the angular frequency $\omega$ ($f = \omega / 2\pi$) or in terms of the period $T$ ($f = 1 / T$). Natural frequency $f_n$ is a characteristic property of the structure and it is defined as a frequency of oscillation of the structure in the case, when the load is rapidly removed from the structure. The natural frequency is a periodic sinusoidal oscillation of an object

or quantity with constant amplitude, sometimes referred to also as a simple harmonic motion. Many physical systems undergoing small displacements, including any objects obeying Hooke's law, exhibit almost simple harmonic motion. The fundamental equation of structural dynamics is the equation of damped simple harmonic motion:

$$\frac{\partial^2 w}{\partial t^2} + \beta \frac{\partial w}{\partial t} + \omega^2 w = 0 \tag{105}$$

where $\beta$ is the damping constant, $w$ is the displacement, and $\omega$ is the angular frequency. The general solution of the equation of the damped simple harmonic motion gives:

$$w(t) = a e^{-\beta t} \sin(\omega_d t - \theta) \tag{106}$$

where $a$ stands for the amplitude of the oscillation, $\theta$ stands for the phase of oscillation, and $\omega_d$ is the frequency of the damped simple harmonic motion. Kladnik [70] gave the relationship between simple harmonic motion and damping, and the definition for the logarithmic decrement (amplitude decrease due to damping):

$$\omega_d = \sqrt{\omega^2 - \beta^2} \qquad \text{and} \qquad \Lambda = \ln \frac{e^{-\beta t}}{e^{-\beta (t+T_d)}} = \beta T_d \tag{107}$$

where $T_d$ is a period of damped simple harmonic motion.

Harris and Crede [51] discussed natural frequencies in their Shock and vibration handbook. Table 5 shows a compilation of frequently used expressions for the natural frequencies of common simple empty piping systems (or beams), where $m$ stands for a concentrated mass or load, $m_b$ stands for the total mass of the pipe and $m_u$ stands for the pipe mass per unit length. The cross-section shape in considered cases is not relevant, therefore the equations in Table 5 hold also for empty piping systems. The presence of a fluid inside the pipe influences the natural frequency in a way that is not trivially predictable and differs from case to case.

*Table 5: Angular natural frequency for some standard simple piping systems (beams) [51, 8].*

| Description | Geometry | Angular natural frequency | | |
|---|---|---|---|---|
| | | Massless beam with load | Massive beam with load | Massive beam without load |
| Fixed-free cantilever (axial) | 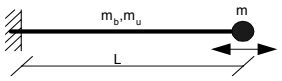 | $\omega_n = \sqrt{\frac{SE}{mL}}$ | $\omega_n = \sqrt{\frac{SE}{(m+0.333m_b)L}}$ | $\omega_n = \frac{1}{4L}\sqrt{\frac{E}{\rho_t}}$ |
| Fixed-free cantilever (lateral) | 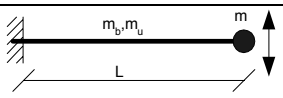 | $\omega_n = \sqrt{\frac{3EI}{mL^3}}$ | $\omega_n = \sqrt{\frac{3EI}{(m+0.23m_b)L^3}}$ | $\omega_n = 3.52\sqrt{\frac{EI}{m_u L^4}}$ |
| Pinned-pinned beam (lateral) | 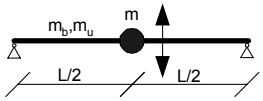 | $\omega_n = 4\sqrt{\frac{3EI}{mL^3}}$ | $\omega_n = \sqrt{\frac{48EI}{(m+0.5m_b)L^3}}$ | $\omega_n = 9.87\sqrt{\frac{EI}{m_u L^4}}$ |
| Fixed-fixed beam (lateral) | 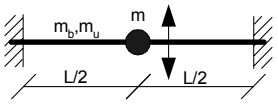 | $\omega_n = 8\sqrt{\frac{3EI}{mL^3}}$ | $\omega_n = \sqrt{\frac{196EI}{(m+0.375m_b)L^3}}$ | $\omega_n = 22.4\sqrt{\frac{EI}{m_u L^4}}$ |

Systems of equations described in Sections from 3.1 to 3.5 implicitly describe harmonic oscillations and can be used for the study of appropriate oscillations. Axial and lateral oscillations are simulated in Section 6.1, and equations from Table 5 are used for the validation of the physical model and numerical scheme. The theory of damped simple harmonic motion is used also for description of difficulties that arise due to the stiff source terms of the Timoshenko beam equations described in Section 5.4.

# 4. Physical models

The mass, momentum and energy balance equations of fluid flow derived in Section 2.3 have to be further rearranged to be applicable for implementation into the FSI physical models. First, one needs to define a set of basic variables and then, the balance equations need to be rearranged to correspond to the chosen set of basic variables. The first section of this chapter describes the conversion of the fluid balance equations into the form suitable for FSI simulation, then some fundamental thermo-fluid dynamics physical models with terms for the FSI are established. The equations of thermo-fluid and structural dynamics are then joined together into physical models that enable simulations of the FSI coupling during transient pipe flows in arbitrarily shaped deformable piping systems. Several physical models for the simulation of the thermo-fluid dynamics, structural dynamics and FSI dynamics in piping systems conveying transient flows of various complexities are presented. Some of the 'small' physical models are used as sub-models of 'larger' physical models; models that are pieced together from the sub-models are schematically indicated. The most general physical models are nonlinear. However, some test cases are calculated also with linearized systems of partial differential equations. Real water properties are applied, some of the models enable simulations of single-phase, the other imply two-phase flow models. The initial conditions are discussed at the end of this Chapter.

The following non-conservative **basic variables** are adopted in the present dissertation:

- 6 basic variables for the fluid: the phasic fluid velocities $v_g$ and $v_f$, the pressure $p$, the vapor volume fraction $\alpha$, and the phasic specific internal energies $e_g$ and $e_f$.
- 12 basic variables for the structure: the axial pipe velocity $u_x$ and the axial internal force $N_x$, the lateral pipe velocities $u_y$ and $u_z$ and the shear forces $Q_y$ and $Q_z$, the rotational velocities $\varphi_z$ and $\varphi_y$ and the bending moments $M_z$ and $M_y$, and the torsional rotation velocity $\varphi_x$ and the torsional momentum $M_x$.

The applied set of basic variables turned out to be the most practical and effective for the simulations of the FSI coupling. The basic variables are non-conservative, therefore, the balance equations written with the basic variables are written in the so-called non-conservative form. With appropriate set of variables and elimination of the source terms, the system becomes conservative. For more details on differences between conservative, non-conservative, and characteristic variables see Tiselj [122] and Hirsch [57].

A **physical model** is a closed system of first order partial differential equations developed to simulate the physics of a particular phenomenon. All physical models considered in the present thesis can be essentially written as a set of first order partial differential equations:

$$\mathbf{A}\frac{\partial \vec{\psi}}{\partial t}+\mathbf{B}\frac{\partial \vec{\psi}}{\partial s}=\vec{S} \tag{108}$$

where **A** and **B** are matrices of the vectorial system, $\vec{S}$ is vector of the sources, and $\vec{\psi}$ is vector of the basic variables. The system in vectorial form can be rewritten into diagonalized vectorial form using trivial matrix operations through the following steps:

- step 1: Equation $\mathbf{A}\frac{\partial \vec{\psi}}{\partial t}+\mathbf{B}\frac{\partial \vec{\psi}}{\partial s}=\vec{S}$ is multiplied by $\mathbf{A}^{-1}$ from the left
- step 2: Equation $\frac{\partial \vec{\psi}}{\partial t}+\mathbf{A}^{-1}\mathbf{B}\frac{\partial \vec{\psi}}{\partial s}-\mathbf{A}^{-1}\vec{S}=0$ is rewritten as $\frac{\partial \vec{\psi}}{\partial t}+\mathbf{C}\frac{\partial \vec{\psi}}{\partial s}+\vec{R}=0$
- step 3: Matrix **C** is diagonalized: $\mathbf{C} \rightarrow \mathbf{L}\,\mathbf{\Lambda}\,\mathbf{L}^{-1}$

where **C** is the Jacobian matrix of the system, $\mathbf{\Lambda}$ is the diagonal matrix of the eigenvalues and **L** is the matrix of the eigenvectors. The physical model in diagonalized vectorial form yields:

$$\frac{\partial \vec{\psi}}{\partial t}+\mathbf{L\Lambda L^{-1}}\frac{\partial \vec{\psi}}{\partial s}+\vec{R}=0 \tag{109}$$

The Jacobian matrix **C** of the hyperbolic physical model is diagonalizable with real eigenvalues. The eigenvalues represent a propagation velocities of pressure and stress waves in the considered system.

Diagonalization of the Jacobian matrix is a fundamental step toward numerical solution of the physical model.

## 4.1. Fluid balance equations with FSI

Equations (27), (36), and (47) for mass, momentum and energy balance have to be rearranged to get partial differential equations in applicable form in terms of the basic variables. The structural dynamics equations described in Chapter 3 are already given in the applicable form.

### 4.1.1. Two-phase flow with FSI

The six-equation two-fluid model of two-phase flow is made up of mass, momentum and energy balance equations for each phase. Appropriate balance equations with terms for FSI are derived below.

**Mass balance equation with FSI.** Rearrangement of the mass balance equation derived for deformable and arbitrarily shaped Lagrangian coordinates given in Eq. (27):

$$\frac{\partial}{\partial t} S\alpha_k \rho_k + u_x \frac{\partial}{\partial s} S\alpha_k \rho_k + \mu \frac{\partial}{\partial s} S\alpha_k \rho_k v_k = \frac{u_y}{R_p} S\alpha_k \rho_k - iS\Gamma_g \tag{110}$$

demands introduction of some auxiliary relationships:

- Equation of state - according to the applied set of basic variables, the density is given as function of pressure and internal energy $\rho_k = \rho_k\,(p,\, e_k)$. The differential of the density then yields (see also Appendix D and Eq. (D-1)):

$$\partial\rho_k = \left(\frac{\partial\rho_k}{\partial p}\right)_{e_k} \partial p + \left(\frac{\partial\rho_k}{\partial e_k}\right)_p \partial e_k \tag{111}$$

- The change in the cross-section area is a result of the total circumferential strain defined by the following relationship (see Appendix E for the theoretical background):

$$\partial S = 2S\partial\varepsilon_{yy} = S\frac{2R}{Ee}\left(1-\nu^2\right)\partial p - S\frac{2\nu}{ES_t}\partial N_x \tag{112}$$

After rearrangement, the two-phase mass balance equation with FSI terms, and written with the basic variables, yields:

$$\begin{aligned}
&\alpha_k\left(\left(\frac{\partial\rho_k}{\partial p}\right)_{e_k} + \rho_k\frac{2R}{Ee}\left(1-\nu^2\right)\right)\frac{\partial p}{\partial t} + \rho_k\frac{\partial\alpha_k}{\partial t} + \alpha_k\left(\frac{\partial\rho_k}{\partial u_k}\right)_p\frac{\partial e_k}{\partial t} - \alpha_k\rho_k\frac{2\nu}{ES_t}\frac{\partial N_x}{\partial t} + \\
&\alpha_k\left(\left(\frac{\partial\rho_k}{\partial p}\right)_{e_k} + \rho_k\frac{2R}{Ee}\left(1-\nu^2\right)\right)\left(u_x+\mu v_k\right)\frac{\partial p}{\partial s} + \rho_k\left(u_x+\mu v_k\right)\frac{\partial\alpha_k}{\partial s} + \\
&\alpha_k\left(\frac{\partial\rho_k}{\partial e_k}\right)_p\left(u_x+\mu v_k\right)\frac{\partial e_k}{\partial s} - \alpha_k\rho_k\frac{2\nu}{ES_t}\left(u_x+\mu v_k\right)\frac{\partial N_x}{\partial s} + \mu\alpha_k\rho_k\frac{\partial v_k}{\partial s} = \frac{u_y}{R_p}\alpha_k\rho_k - i\Gamma_g
\end{aligned} \tag{113}$$

The mass balance equation in the extended form expressed with the basic variables gives several new terms compared to the standard mass balance equation without FSI: these are terms with the pipe axial and lateral velocities $u_x$ and $u_y$, the pipe axial force $N_x$, terms with the scale factor $\mu$, and the radius of curvature $R_p$. Equation (113) is applicable only in combination with equations for axial and lateral dynamics of the piping system. For the pure fluid problems without consideration of the FSI effects, the new terms automatically fall out and the Equation (113) becomes equal to the corresponding equation in Eulerian coordinate system.

**Momentum balance equation with FSI.** The general momentum balance Eq. (36) is given as:

$$\begin{aligned}&\frac{\partial}{\partial t}\alpha_k S\rho_k v_k + u_x\frac{\partial}{\partial s}\alpha_k S\rho_k v_k + \mu\frac{\partial}{\partial s}\alpha_k S\rho_k v_k v_k + \mu\alpha_k S\frac{\partial p}{\partial s} = \\ &\frac{u_y}{R_p}\alpha_k S\rho_k v_k - iS\Gamma_g v_i + iSF_i + SF_{k,gx} - SF_{k,t}\end{aligned} \tag{114}$$

The continuity Eq. (27) is multiplied by fluid velocity $v_k$ and subtracted from the general momentum balance equation. Rearrangement yield the momentum balance equation in the non-conservative form:

$$\alpha_k\rho_k\frac{\partial v_k}{\partial t} + \alpha_k\rho_k\left(u_x + \mu v_k\right)\frac{\partial v_k}{\partial s} + \mu\alpha_k\frac{\partial p}{\partial s} = i\Gamma_g\left(v_k - v_i\right) + iF_i + F_{k,gx} - F_{k,t} \tag{115}$$

Equation (115) lost several terms compared to the same equation in the form of Eq. (36). The most important is elimination of the junction coupling source term describing coupling between the fluid dynamics and the lateral pipe dynamics at curvatures. The momentum balance equation in non-conservative form is therefore weakly affected by the FSI terms. The FSI coupling is described with terms containing scale factor $\mu$ and axial pipe velocity $u_x$.

**Internal energy balance equation with FSI.** The general energy balance equation (47) is written in terms of total energy $e_{tot,k}$:

$$\begin{aligned}&\frac{\partial}{\partial t}\alpha_k S\rho_k e_{tot,k} + u_x\frac{\partial}{\partial s}\alpha_k S\rho_k e_{tot,k} + \mu\frac{\partial}{\partial s}\alpha_k S\rho_k v_k e_{tot,k} + \mu\frac{\partial}{\partial s}\alpha_k S v_k p = \\ &\frac{u_y}{R_p}\alpha_k S\rho_k e_{tot,k} - iS\Gamma_g\left(h + \frac{v_k^2}{2}\right) + SQ_{ik} + iSv_k F_i + Sv_k F_{k,gx} - v_k SF_{k,t}\end{aligned} \tag{116}$$

The total energy and the internal energy are related through the expression $e_{tot,k} = e_k + v_k^2 / 2$, therefore, to transform Eq. (116) into the basic set of variables, the kinematic part must be eliminated from the general total energy balance equation. The kinetic energy balance equation is obtained by subtracting Eq. (115) from the Eq. (36) (both equations are appropriately multiplied by the fluid velocity). The kinetic energy balance equation is then subtracted from the energy balance equation (116). Some source terms for interface exchange of kinetic energy and the contribution of the kinetic energy are partially neglected in the internal energy balance equation, because the contribution of the kinetic energy to the total energy is much smaller than the contribution of the internal energy. Then the general internal energy balance equation becomes:

$$\frac{\partial}{\partial t}\alpha_k S\rho_k e_k + u_x\frac{\partial}{\partial s}\alpha_k S\rho_k e_k + \mu\frac{\partial}{\partial s}\alpha_k S\rho_k v_k e_k + \mu p\frac{\partial}{\partial s}\alpha_k S v_k = \frac{u_y}{R_p}\alpha_k S\rho_k e_k - iS\Gamma_g h + SQ_{ik} \tag{117}$$

Equation (117) is further rearranged. The mass balance Eq. (113) is multiplied by the internal energy and subtracted from the Eq. (117). Then the internal energy balance equation in basic variables yields:

$$\begin{aligned}&\alpha_k\rho_k\frac{\partial e_k}{\partial t} + \alpha_k\rho_k\left(u_x + \mu v_k\right)\frac{\partial e_k}{\partial s} + \mu\alpha_k p\frac{\partial v_k}{\partial s} + \mu p v_k\frac{\partial \alpha_k}{\partial s} + \mu\alpha_k v_k p\frac{2R}{Ee}\left(1 - v^2\right)\frac{\partial p}{\partial s} - \\ &\mu\alpha_k v_k p\frac{2\nu}{ES_t}\frac{\partial N_x}{\partial s} = Q_{ik} - i\Gamma_g\left(h_k - e_k\right)\end{aligned} \tag{118}$$

The Eq. (118) is applicable for both, the fluid and vapor phase using definitions from Table 3. Comparing Eq. (118) to the same equation in the form of Eq. (117) shows that the junction coupling source term describing coupling between fluid dynamics and lateral pipe dynamics at curvatures is eliminated. The FSI coupling is described with terms with stretching scale factor $\mu$ and with additional axial pipe velocity $u_x$ in convective terms.

### 4.1.2. Homogeneous equilibrium two-phase flow with FSI

The homogeneous equilibrium model (HEM) neglects the slip between phases (homogeneous model) and assumes instantaneous thermal relaxation (equilibrium model). In the HEM both phases are in thermal and mechanical equilibrium. The HEM represents an interesting improvement of the frequently used isothermal single or quasi two-phase flow model, which are limited for simulations of transients in cold water. The model includes an energy balance equation and can be used for fluids with arbitrary temperature. The model consists of three equations and excludes source terms for mass, momentum and energy non-equilibrium as relaxation is instantaneous. Equaion (113) for mass, Eq. (115) for momentum, and Eq. (118) for internal energy balance are modified by adding balance equations for both phases (example: the mass balance for the liquid is added to the mass balance equation for the gas). The following mixture variables are introduced:

$$\begin{aligned}
&\alpha + (1-\alpha) = 1 \\
&\rho_m = \alpha\rho_{g,sat} + (1-\alpha)\,\rho_{f,sat} \\
&v_m = \frac{\alpha\rho_{g,sat}v_g + (1-\alpha)\,\rho_{f,sat}v_f}{\rho_m} \\
&e_m = \frac{\alpha\rho_{g,sat}e_g + (1-\alpha)\,\rho_{f,sat}e_f}{\rho_m}
\end{aligned} \tag{119}$$

where $\rho_m$ is the mixture density, $v_m$ is the mixture velocity and $e_m$ is the mixture internal energy. Then the HEM model with terms for FSI coupling yields:

$$\begin{aligned}
&\frac{1}{c_m^2}\frac{\partial p}{\partial t} + \left(\frac{\partial \rho_m}{\partial e_m}\right)_p \frac{\partial e_m}{\partial t} - \rho_m \frac{2\nu}{ES_t}\frac{\partial N_x}{\partial t} + \frac{1}{c_m^2}\left(u_x + \mu v_m\right)\frac{\partial p}{\partial s} + \left(\frac{\partial \rho_m}{\partial e_m}\right)_p \left(u_x + \mu v_m\right)\frac{\partial e_m}{\partial s} - \\
&\rho_m \frac{2\nu}{ES_t}\left(u_x + \mu v_m\right)\frac{\partial N_x}{\partial s} + \mu\rho_m \frac{\partial v_m}{\partial s} = \frac{u_y}{R_p}\rho_m
\end{aligned} \tag{120}$$

$$\rho_m \frac{\partial v_m}{\partial t} + \rho_m\left(u_x + \mu v_m\right)\frac{\partial v_m}{\partial s} + \mu\frac{\partial p}{\partial s} = F_{m,gx} - F_{m,t} \tag{121}$$

$$\rho_m \frac{\partial e_m}{\partial t} + \rho_m\left(u_x + \mu v_m\right)\frac{\partial e_m}{\partial s} + \mu p\frac{\partial v_m}{\partial s} + \mu v_m p\frac{2R}{Ee}\left(1-v^2\right)\frac{\partial p}{\partial s} - \mu v_m p\frac{2\nu}{ES_t}\frac{\partial N_x}{\partial s} = 0 \tag{122}$$

where $c_m$ is the mixture speed of sound. Values for the vapor volume fraction $\alpha$ are from the interval *[0,1]*. At $\alpha$ = *1* single phase vapor flow is present in the system, and for $\alpha$ = *0*, the pipe contains single-phase liquid flow.

### 4.1.3. Isothermal single-phase liquid flow with FSI

The assumption of isothermal liquid flow is a very natural and important assumption for simulations of transients in single-phase water performed at room temperature. Due to the low compressibility of the liquid water the isothermal flow assumption is more or less equivalent to the adiabatic flow assumption. The flow is assumed single-phase (index *k* = *f*, and liquid volume fraction $\alpha_k$ = *1*), no interface exchange of heat, mass, and momentum. The internal energy is constant $\delta e_k$ = *0*; the internal energy balance equation is not needed. The physical model consists of two equations for mass and momentum balance. Transients with liquid of under such conditions are mainly considered by the FSI community and are also addressed in this thesis.

The speed of sound $c_{0,k}$ that is given in Eq. (D-5):

$$c_{0,f}^2 = \frac{K_S}{\rho_f} = \left(\frac{\partial p}{\partial \rho_f}\right)_S \qquad \text{for the } \textit{cold} \text{ liquid simplifies into:} \qquad c_{0,f}^2 \cong \left(\frac{\partial p}{\partial \rho_f}\right)_{e_f} \tag{123}$$

and according to the Korteweg's equation (D-4):

$$\frac{1}{c_{0,f}^2}+\rho_f\frac{2R}{Ee}\left(1-\nu^2\right)=\frac{1}{c_f^2} \tag{124}$$

Then Eq. (113) becomes the single-phase mass balance equation in deformable Lagrangian coordinates for isothermal single-phase water hammer transient:

$$\frac{1}{\rho_f c_f^2}\frac{\partial p}{\partial t}-\frac{2\nu}{ES_t}\frac{\partial N_x}{\partial t}+\left(u_x+\mu v_f\right)\frac{1}{\rho_f c_f^2}\frac{\partial p}{\partial s}-\frac{2\nu}{ES_t}\left(u_x+\mu v_f\right)\frac{\partial N_x}{\partial s}+\mu\frac{\partial v_f}{\partial s}=\frac{u_y}{R_p} \tag{125}$$

Similarly, Eq. (115) yields the single-phase momentum balance equation:

$$\rho_f\frac{\partial v_f}{\partial t}+\rho_f\left(u_x+\mu v_f\right)\frac{\partial v_f}{\partial s}+\mu\frac{\partial p}{\partial s}=F_{f,gx}-F_{f,t} \tag{126}$$

where $F_{f,gx}$ are the body forces and $F_{f,t}$ are the wall friction terms.

**Balance equations of classical water hammer.** Further simplifications of Eqs. (125) and (126) for arbitrarily shaped piping systems in Lagrangian coordinates are possible. Allievi [3,4] showed in 1903 that the convective term in the balance equations are often negligible. The convective terms, in form of $\left(u_x+\mu v_f\right)\partial\ /\partial s$, make equations nonlinear and thus make them difficult to solve numerically, i.e. the presence of the convective term enforces the use of complex numerical methods. In single-phase flows the fluid velocity $v_f$ is usually much smaller than the characteristic velocity of the traveling pressure waves in the fluid (approx. the speed of sound), and the convective terms are often negligible. Wylie and Streeter [150] denominate this assumption as the acoustic approximation. The body forces and the wall friction forces are usually much smaller than the forces of the pressure waves and can be easily neglected. If one further assumes that the pipe deformations are small, that the pipe is straight (no junction coupling) and that the pipe wall is stiff and undeformable (no Poisson coupling) then Eq. (125) becomes:

$$\frac{1}{\rho_f c_f^2}\frac{\partial p}{\partial t}+\frac{\partial v_f}{\partial s}=0 \tag{127}$$

and the Eq. (126) becomes:

$$\rho_f\frac{\partial v_f}{\partial t}+\frac{\partial p}{\partial s}=0 \tag{128}$$

which are actually the continuity and the momentum equations of the classical water hammer theory written in the introduction chapter - Eq. (2).

### 4.1.4. Isothermal quasi two-phase flow with FSI.

The isothermal quasi two-phase flow model represents a simplified upgrade of the isothermal single-phase flow for simulations of the two-phase flow transients at room temperature liquid-filled piping systems where thermal relaxation plays a negligible role. Equations (125) and (126) are essentially used for simulation of the single-phase transient. In case of cavitation, an auxiliary two-phase continuity equation for vapor volume fraction balance is considered additionally to the basic single-phase physical model. The model was developed by Kalkwijk and Kranenburg [68], Kranenburg [72] and extended by Wylie and Streeter [151], Streeter [107], Simpson [103], and Tijsseling [113]. The cavitation model is assigned as a quasi two-phase because it is based on the strong physical constraint that the absolute fluid pressure equals the saturation pressure of the vapor $p_{sat}$ during the cavitation. This is true only for isothermal systems because the vapor saturation pressure is a function of the temperature:

$$p = p_{sat} \tag{129}$$

According to Simpson [103] it is possible to apply the following two-phase continuity equation:

$$\frac{\partial \alpha}{\partial t} + \frac{\partial \alpha v_f}{\partial s} = 0 \qquad \Rightarrow \qquad \frac{\partial \alpha}{\partial t} + v_f \frac{\partial \alpha}{\partial s} + \alpha \frac{\partial v_f}{\partial s} = 0 \tag{130}$$

where $v_f$ is the fluid velocity, and $\alpha$ is the vapor volume fraction. Equation (130) simply states that the void fraction follows the bulk velocity motion i.e. changes in vapor volume fraction are considered as inertial instabilities in liquid columns. No thermal effects are considered. An alternative derivation of the continuity equation (130) for the vapor volume fraction can be conducted also by introduction of some trivial assumption into Eq (27).

The quasi two-phase flow cavitation model is implemented through the following steps:

- Inception of cavitation:
  - Cavitation starts at the instant the liquid pressure reaches the saturation pressure. The two-phase continuity Eq. (130) is activated.
  - The pressure is fixed at saturation pressure in the two-phase flow.
- During the two-phase flow:
  - The density and the speed of sound are evaluated for two-phase mixture:

$$\rho_m = \alpha \rho_{g,sat} + (1-\alpha)\, \rho_{f,sat} \tag{131}$$

$$K_S = \rho_m \left( \frac{\partial p}{\partial \rho_m} \right)_S \qquad \Rightarrow \qquad c_{0,m}^2 = \frac{K_S}{\rho_m} \tag{132}$$

  - The vapor volume fraction is evaluated through the two-phase flow continuity Eq. (130).
- End of cavitation:
  - Cavitation ends when all cavities have vanished $\alpha = 0$.
  - The two-phase continuity equation is eliminated.

## 4.2. Physical models in matrix form

### 4.2.1. Thermo-fluid dynamics physical models

This section contains physical models applicable for simulations of the thermo-fluid dynamics without consideration of the FSI. The equations are written in vectorial form given by Eq. (108):

$$\mathbf{A} \frac{\partial \vec{\psi}}{\partial t} + \mathbf{B} \frac{\partial \vec{\psi}}{\partial s} = \vec{S} \tag{133}$$

Recall that balance equations derived in a Lagrangian coordinate system degenerate into standard equations derived under assumption of Eulerian coordinates for stiff and undeformable piping system.

**Nonlinear isothermal single-phase flow model.** The two coupled isothermal single-phase flow equations in a Lagrangian coordinate system are given by Eqs. (125) and (126). The model is used for simulations of single-phase flow fluid dynamics. Considering only fluid dynamics, all terms related to the pipe axial force, pipe axial and lateral velocity, pipe deformations and curvature becomes zero and the system in vectorial form yields:

$$\mathbf{A} = \begin{bmatrix} 0 & \dfrac{1}{\rho_f c_f^2} \\ \rho_f & 0 \end{bmatrix}, \quad \mathbf{B} = \begin{bmatrix} 1 & \dfrac{v_f}{\rho_f c_f^2} \\ \rho_f v_f & 1 \end{bmatrix}, \text{ and } \vec{S} = \begin{Bmatrix} 0 \\ F_{f,gx} - F_{f,t} \end{Bmatrix} \tag{134}$$

where the vector of the basic variables is $\vec{\psi}^T = \{v_f, p\}$. Matrices of the diagonalized vectorial form read:

$$\mathbf{\Lambda} = diag\begin{Bmatrix} -c_f + v_f \\ c_f + v_f \end{Bmatrix}, \quad \mathbf{L} = \begin{bmatrix} -\dfrac{1}{c_f \rho_f} & \dfrac{1}{c_f \rho_f} \\ 1 & 1 \end{bmatrix}, \text{ and } \vec{R} = \begin{Bmatrix} \dfrac{F_{f,gx} - F_{f,t}}{\rho_f} \\ 0 \end{Bmatrix} \tag{135}$$

**Linear isothermal single-phase flow model (classical water hammer model).** If FSI coupling terms, convective terms, friction and body forces in isothermal single-phase flow model are neglected, the model becomes equal to the physical model given by the classical single-phase water hammer theory derived in Eulerian coordinates (Eqs. (127) and (128)). The vector of the basic variables is $\vec{\psi}^T = \{v_f, p\}$. The matrices **A** and **B** and the source term vector $\vec{S}$ of the vectorial form read:

$$\mathbf{A} = \begin{bmatrix} 0 & \dfrac{1}{\rho_f c_f^2} \\ \rho_f & 0 \end{bmatrix}, \quad \mathbf{B} = \begin{bmatrix} 1 & 0 \\ 0 & 1 \end{bmatrix}, \text{ and } \vec{S} = \begin{Bmatrix} 0 \\ 0 \end{Bmatrix} \tag{136}$$

where the vector of the basic variables is $\vec{\psi}^T = \{v_f, p\}$. Matrices of the diagonalized vectorial form read:

$$\mathbf{\Lambda} = diag\begin{Bmatrix} -c_f \\ c_f \end{Bmatrix}, \quad \mathbf{L} = \begin{bmatrix} -\dfrac{1}{c_f \rho_f} & \dfrac{1}{c_f \rho_f} \\ 1 & 1 \end{bmatrix}, \text{ and } \vec{R} = \begin{Bmatrix} 0 \\ 0 \end{Bmatrix} \tag{137}$$

**Nonlinear quasi-two-phase flow model.** The quasi-two-phase flow equations in the Lagrangian coordinate system are given by the isothermal single-phase Eqs. (125) and (126) and the third vapor balance Eq. (130):

$$\mathbf{A} = \begin{bmatrix} 0 & \dfrac{1}{\rho_f c_f^2} & 0 \\ \rho_f & 0 & 0 \\ 0 & 0 & 1 \end{bmatrix}, \quad \mathbf{B} = \begin{bmatrix} 1 & \dfrac{v_f}{\rho_f c_f^2} & 0 \\ \rho_f v_f & 1 & 0 \\ \alpha & 0 & v_f \end{bmatrix}, \text{ and } \vec{S} = \begin{Bmatrix} 0 \\ F_{f,gx} - F_{f,t} \\ 0 \end{Bmatrix} \tag{138}$$

where the vector of the basic variables is $\vec{\psi}^T = \{v_f, p, \alpha\}$. The model is used for simulations of quasi-two-phase flow fluid dynamics. The model is applied only in two-phase flow and according to the Allievi's [3,4] definition, the convection becomes negligible and the vapor balance equation becomes decoupled of the first two equations and does not affect the speed of sound (eigenvalues). Matrices of the diagonalized vectorial form are then the same as for nonlinear isothermal single-phase flow model, and the vapor balance equation is integrated with a separate explicit Eulerian numerical scheme.

**Linear quasi-two-phase flow model.** Analogously, the linear quasi-two-phase flow model is given with Eqs. (127), (128), and (130). The vector of the basic variables is $\vec{\psi}^T = \{v_f, p, \alpha\}$, and the matrices of the vectorial form yield:

$$\mathbf{A} = \begin{bmatrix} 0 & \dfrac{1}{\rho_f c_f^2} & 0 \\ \rho_f & 0 & 0 \\ 0 & 0 & 1 \end{bmatrix}, \quad \mathbf{B} = \begin{bmatrix} 1 & \dfrac{v_f}{\rho_f c_f^2} & 0 \\ \rho_f v_f & 1 & 0 \\ \alpha & 0 & 0 \end{bmatrix}, \text{ and } \vec{S} = \begin{Bmatrix} 0 \\ 0 \\ 0 \end{Bmatrix} \tag{139}$$

Matrices of the diagonalized vectorial form are the same as for linear isothermal single-phase flow model, and the vapor balance equation is integrated with a separate explicit Eulerian numerical scheme.

**Homogeneous equilibrium two-phase flow model.** The three-equation model consists of equations (120), (121), and (122). The model is used for simulations of two-phase flow fluid dynamics with the homogeneous equilibrium model. Considering only the fluid dynamics, all terms related to pipe axial force, pipe axial and lateral velocity, pipe deformations and curvature becomes zero and the matrices of the vectorial form read:

$$\mathbf{A}=\begin{bmatrix} \frac{1}{c_m^2} & 0 & \left(\frac{\partial \rho_m}{\partial e_m}\right)_p \\ 0 & \rho_m & 0 \\ 0 & 0 & \rho_m \end{bmatrix},\ \mathbf{B}=\begin{bmatrix} \frac{v_m}{c_m^2} & \rho_m & v_m\left(\frac{\partial \rho_m}{\partial e_m}\right)_p \\ 1 & \rho_m v_m & 0 \\ p v_m \frac{2R}{Ee}\left(1-\nu^2\right) & p & \rho_m v_m \end{bmatrix},\ \text{and}\quad \vec{S}=\begin{Bmatrix} 0 \\ F_{m,gx}-F_{m,t} \\ 0 \end{Bmatrix} \tag{140}$$

The vector of the basic variables is $\vec{\psi}^T=\{p, v_m, e_m\}$. The system is analytically diagonalizable.

**Six-equation two-fluid model of two-phase flow.** The two-phase flow balance equations defined by Equations (113), (115), and (118) for each of the phases yield a six-equation nonlinear two-phase flow physical model for simulations of two-phase flow thermo-fluid dynamics. Considering only thermo-fluid dynamics, all terms related to the pipe axial force, pipe axial and lateral velocity, pipe deformations and curvature becomes zero. The system can be written in the following vectorial form:

$$\mathbf{A}\frac{\partial \vec{\psi}}{\partial t}+\mathbf{B}\frac{\partial \vec{\psi}}{\partial s}=\vec{S}+\vec{S}_R \tag{141}$$

where the additional vector of the source terms $\vec{S}_R$ was introduced to separate the relaxation source terms from other, non-relaxation source terms. Matrices of the system **A** and **B** are given:

$$\mathbf{A}=\begin{bmatrix} -\rho_f & \frac{(1-\alpha)}{c_f^2} & 0 & 0 & (1-\alpha)\left(\frac{\partial \rho_f}{\partial e_f}\right)_p & 0 \\ \rho_g & \frac{\alpha}{c_g^2} & 0 & 0 & 0 & \alpha\left(\frac{\partial \rho_g}{\partial e_g}\right)_p \\ 0 & 0 & (1-\alpha)\rho_f + C_{vm} & -C_{vm} & 0 & 0 \\ 0 & 0 & -C_{vm} & \alpha\rho_g + C_{vm} & 0 & 0 \\ 0 & 0 & 0 & 0 & (1-\alpha)\rho_f & 0 \\ 0 & 0 & 0 & 0 & 0 & \alpha\rho_g \end{bmatrix} \tag{142}$$

$$\mathbf{B}=\begin{bmatrix} -\rho_f v_f & \frac{(1-\alpha)v_f}{c_f^2} & \alpha_f\rho_f & 0 & \alpha_f(1-\alpha)\left(\frac{\partial \rho_f}{\partial e_f}\right)_p & 0 \\ \rho_g v_g & \frac{\alpha v_g}{c_g^2} & 0 & \alpha\rho_g & 0 & \alpha v_g\left(\frac{\partial \rho_g}{\partial e_g}\right)_p \\ 0 & (1-\alpha) & (1-\alpha)\rho_f v_f + C_{vm}v_g & -C_{vm}v_f & 0 & 0 \\ 0 & \alpha & -C_{vm}v_g & \alpha\rho_g v_g + C_{vm}v_f & 0 & 0 \\ -pv_f & (1-\alpha)pv_f\frac{2R}{Ee}\left(1-\nu^2\right) & (1-\alpha)p & 0 & (1-\alpha)\rho_f v_f & 0 \\ pv_g & \alpha pv_g\frac{2R}{Ee}\left(1-\nu^2\right) & 0 & \alpha p & 0 & \alpha\rho_g v_g \end{bmatrix} \tag{143}$$

where $C_{vm}$ is the virtual mass coefficient defined in Eq. (C-22). The vector $\vec{\psi}^T=\{\alpha, p, v_f, v_g, e_f, e_g\}$ is vector of the six independent basic non-conservative variables, where $\alpha$ is the vapor volume fraction, $p$ is the fluid pressure, $v_k$ are the phasic fluid velocities, and $e_k$ are the phasic internal energies. The relaxation source terms demand a special numerical treatment and are thus written separately from the other (non-relaxation) source terms. The vectors of the relaxation and non-relaxation source terms read:

$$\vec{S}_R = \begin{Bmatrix} -\Gamma_g \\ \Gamma_g \\ \Gamma_g\left(v_f - v_i\right) + C_i \left|v_r\right| v_r \\ -\Gamma_g\left(v_g - v_i\right) - C_i \left|v_r\right| v_r \\ Q_{if} - \Gamma_g\left(h_f - e_f\right) \\ Q_{ig} + \Gamma_g\left(h_g - e_g\right) \end{Bmatrix}, \text{ and } \quad \vec{S} = \begin{Bmatrix} 0 \\ 0 \\ F_{f,gx} - F_{f,t} \\ F_{g,gx} - F_{g,t} \\ 0 \\ 0 \end{Bmatrix} \tag{144}$$

The relationships for the evaluation of the terms in the source term vector are given in Appendix C. The Jacobian matrix $\mathbf{C} = \mathbf{A}^{-1}\mathbf{B}$ of the physical model is not analytically diagonalizable, and the eigensystem is then evaluated in a special numerical procedure (EISPACK numerical library for FORTRAN - www.netlib.org).

### 4.2.2. Structural dynamics physical models

The structural dynamics physical models without FSI coupling are applied for simulations of structural oscillations, and are briefly described in the following sections.

**Axial pipe dynamics model.** Equations (56) and (62) for the straight pipe axial motion without fluid pressure term (Poisson coupling) can be written in a vectorial form as:

$$\mathbf{A}_{AXI} = \begin{bmatrix} 0 & \dfrac{1}{ES_t} \\ m_s & 0 \end{bmatrix}, \quad \mathbf{B}_{AXI} = \begin{bmatrix} -1 & 0 \\ 0 & -1 \end{bmatrix}, \text{ and } \vec{S}_{AXI} = \begin{Bmatrix} 0 \\ f_x(s,t) \end{Bmatrix} \tag{145}$$

The vector of the independent variables is $\vec{\psi}^T = \{u_x, N_x\}$. The model is utilized for simulations of the axial dynamics of straight piping systems. The matrices of the diagonalized vectorial form are given by:

$$\mathbf{\Lambda}_{AXI} = diag\begin{Bmatrix} -\sqrt{\dfrac{ES_t}{m_s}} \\ \sqrt{\dfrac{ES_t}{m_s}} \end{Bmatrix}, \quad \mathbf{L}_{AXI} = \begin{bmatrix} \dfrac{1}{\sqrt{m_s ES_t}} & -\dfrac{1}{\sqrt{m_s ES_t}} \\ 1 & 1 \end{bmatrix}, \text{ and } \vec{R}_{AXI} = \begin{Bmatrix} 0 \\ -\dfrac{f_x(s,t)}{m_s} \end{Bmatrix} \tag{146}$$

**In-plane Timoshenko beam model.** The lateral and rotational motion of the straight piping section in plane is described with Timoshenko beam equations (67), (73), (76), and (82). The vector $\vec{\psi}^T = \{u_y, Q_y, \varphi_z, M_z\}$ is a vector of four independent variables (lateral velocity and force and rotational velocity and bending momentum). Then the matrices of the system **A** and **B** and the vector of the sources $\vec{S}$ yield:

$$\mathbf{A}_{TIM,in} = \begin{bmatrix} 0 & \dfrac{1}{\kappa G S_t} & 0 & 0 \\ m_T & 0 & 0 & 0 \\ 0 & 0 & 0 & \dfrac{1}{EI_t} \\ 0 & 0 & \rho_t I_t & 0 \end{bmatrix}, \quad \mathbf{B}_{TIM,in} = \begin{bmatrix} -1 & 0 & 0 & 0 \\ 0 & -1 & 0 & 0 \\ 0 & 0 & -1 & 0 \\ 0 & 0 & 0 & -1 \end{bmatrix}, \text{ and } \vec{S}_{TIM,in} = \begin{Bmatrix} \dfrac{u_x}{R_p} + \dfrac{u_z}{T_p} - \varphi_z \\ \dfrac{N_x - Sp}{R_p} + \dfrac{T_z}{T_p} + f_y(s,t) \\ -\dfrac{\varphi_y}{T_p} \\ -\dfrac{M_y}{T_p} + Q_y \end{Bmatrix} \tag{147}$$

The Timoshenko beam equations rewritten in diagonalized vectorial form is:

$$\mathbf{\Lambda}_{TIM,in} = diag\left\{\begin{matrix} -\sqrt{\frac{\kappa G S_t}{m_T}} \\ \sqrt{\frac{\kappa G S_t}{m_T}} \\ -\sqrt{\frac{E}{\rho_t}} \\ \sqrt{\frac{E}{\rho_t}} \end{matrix}\right\}, \qquad \mathbf{L}_{TIM,in} = \begin{bmatrix} \frac{1}{\sqrt{\kappa G S_t m_T}} & -\frac{1}{\sqrt{\kappa G S_t m_T}} & 0 & 0 \\ 1 & 1 & 0 & 0 \\ 0 & 0 & \frac{1}{I_t\sqrt{\rho_t E}} & -\frac{1}{I_t\sqrt{\rho_t E}} \\ 0 & 0 & 1 & 1 \end{bmatrix} \tag{148}$$

$$\vec{R}^T_{TIM,in} = -\left\{\left(\frac{N_x - Sp}{R_p} + \frac{T_z}{T_p} + f_y(s,t)\right)\frac{1}{m_T}, \left(\frac{u_x}{R_p} + \frac{u_z}{T_p} - \varphi_z\right)\kappa G S_t, \left(-\frac{M_y}{T_p} + Q_y\right)\frac{1}{\rho_t I_t}, \left(-\frac{\varphi_y}{T_p}\right)E I_t\right\} \tag{149}$$

**Out-of-plane Timoshenko beam model.** The out-of-plane lateral and rotational motion of the straight piping section can be described by the Timoshenko beam equations (85), (88), (90), and (93). Due to the symmetry of the pipe cross-section, the matrices of the system $\mathbf{A}_{TIM,in} = \mathbf{A}_{TIM,out}$ and $\mathbf{B}_{TIM,in} = \mathbf{B}_{TIM,out}$ are actually the same as for the in-plane Timoshenko beam equations. New are the vector of four independent basic variables (binormal velocity and force and normal rotational velocity and bending momentum) $\vec{\psi}^T = \{u_z, Q_z, \varphi_y, M_y\}$, and the vector of the sources for out-of-plane bending:

$$\vec{S}^T_{TIM,out} = \left\{-\frac{u_y}{T_p} - \varphi_y,\ -\frac{Q_y}{T_p} + f_z(s,t),\ \frac{\varphi_x}{R_p} + \frac{\varphi_z}{T_p},\ \frac{M_x}{R_p} + \frac{M_z}{T_p} + Q_z\right\} \tag{150}$$

The corresponding vector in diagonalized vectorial form is given by:

$$\vec{R}^T_{TIM,out} = -\left\{\left(-\frac{Q_y}{T_p} + f_z(s,t)\right)\frac{1}{m_T}, \left(-\frac{u_y}{T_p} - \varphi_y\right)\kappa G S_t, \left(\frac{M_x}{R_p} + \frac{M_z}{T_p} + Q_z\right)\frac{1}{\rho_t I_t}, \left(\frac{\varphi_x}{R_p} + \frac{\varphi_z}{T_p}\right)E I_t\right\} \tag{151}$$

**Torsional pipe dynamics model.** Equations (97) and (103) for the pipe torsional motion, written in vectorial form, read:

$$\mathbf{A}_{TOR} = \begin{bmatrix} 0 & \frac{1}{G J_t} \\ \rho_t J_t & 0 \end{bmatrix}, \quad \mathbf{B}_{TOR} = \begin{bmatrix} -1 & 0 \\ 0 & -1 \end{bmatrix}, \text{ and } \vec{S}_{TOR} = \left\{\begin{matrix} -\frac{\varphi_y}{R_p} \\ -\frac{M_y}{R_p} \end{matrix}\right\} \tag{152}$$

The vector $\vec{\psi}^T = \{\varphi_x, M_x\}$ is the vector of the independent variables. The model is used for simulations of torsional dynamics of the piping system. The matrices of the diagonalized vectorial form read:

$$\mathbf{\Lambda}_{TOR} = diag\left\{\begin{matrix} -\sqrt{\frac{G}{\rho_t}} \\ \sqrt{\frac{G}{\rho_t}} \end{matrix}\right\}, \quad \mathbf{L}_{TOR} = \begin{bmatrix} \frac{1}{J_t\sqrt{\rho_t G}} & -\frac{1}{J_t\sqrt{\rho_t G}} \\ 1 & 1 \end{bmatrix}, \text{ and } \vec{R}_{TOR} = \left\{\begin{matrix} -\frac{M_y}{R_p}\frac{1}{\rho_t J_t} \\ -\frac{\varphi_y}{R_p} G J_t \end{matrix}\right\} \tag{153}$$

The torsional pipe dynamics equations are added and discussed. However, they are actually not applied in the present dissertation as torsion is not important for planar structures. Similar conclusion is valid also for out-of-plane Timoshenko beam equations. These models are prepared for possible application in 3D simulations of the FSI in piping systems.

### 4.2.3. FSI physical models

The equations of thermo-fluid and structural dynamics are joined together into several physical models for the simulation of the FSI coupling in arbitrarily shaped deformable piping systems conveying transient fluid flow. Several physical models of various complexities are presented.

**Nonlinear axial quasi-two-phase FSI model.** The axial quasi-two-phase FSI model is assembled from coupled equations of isothermal single-phase liquid flow (125), (126), and equations of axial beam motion (56) and (62). The model describes coupling between two-phase flow transient and axial (1D) dynamics of the straight piping systems conveying room temperature water. The matrices of the physical model are given by:

$$\mathbf{A}_{AQ2F} = \begin{bmatrix} 0 & \dfrac{1}{\rho_f c_f^2} & 0 & -\dfrac{2\nu}{ES_t} \\ \rho_f & 0 & 0 & 0 \\ 0 & 0 & m_s & 0 \\ 0 & -\dfrac{\nu R}{Ee} & 0 & \dfrac{1}{ES_t} \end{bmatrix}, \text{ and } \mathbf{B}_{AQ2F} = \begin{bmatrix} \mu & (u_x + \mu v_f)\dfrac{1}{\rho_f c_f^2} & 0 & -(u_x + \mu v_f)\dfrac{2\nu}{ES_t} \\ \rho_f (u_x + \mu v_f) & \mu & 0 & 0 \\ 0 & 0 & 0 & -1 \\ 0 & 0 & -1 & 0 \end{bmatrix} \quad (154)$$

The vector of the basic variables is $\vec{\psi}^T = \{v_f, p, u_x, N_x\}$, and the vector of the source terms is:

$$\vec{S}^T = \{0, \quad F_{f,gx} - F_{f,t}, \quad f_x(s,t), \quad 0\} \quad (155)$$

The additional equation (130) for the vapor volume fraction balance is added in two-phase flow as described in Section 4.1.4. The physical model given with Eq. (154) is utilized independently or as a sub-model of larger models defined for piping systems in 2D plane or 3D space. The Jacobian matrix **C** and the vector of the basic variables remain the same, while the source terms for 2D and 3D piping systems become:

$$\vec{S}^T_{AQ2F} = \left\{ \frac{u_y}{R_p}, \quad F_{f,gx} - F_{f,t}, \quad f_x(s,t) - \frac{Q_y}{R_p}, \quad -\frac{u_y}{R_p} \right\} \quad (156)$$

The axial FSI coupling model, defined by equation (154), source terms (156) and real water properties, is the most accurate quasi-two-phase flow FSI model for the axial movement.

**Linear axial quasi-two-phase FSI model.** Allievi [3,4] showed that the convective terms in form of $v_f \, \partial/\partial s$ are negligible. Without convective terms, the axial FSI coupling model becomes linear. In addition, the assumption of small deformations (~ stiff pipe) gives $u_x \to 0$, and $\mu \to 1$, and assumption of straight section of the pipe gives $1/R_p \to 0$. Further, the body forces and the wall friction forces are usually small compared to the forces of the pressure and stress waves, and are also frequently neglected. Taking into account the above assumptions, the linear axial FSI coupling model becomes:

$$\mathbf{A} = \begin{bmatrix} 0 & \dfrac{1}{\rho_f c_f^2} & 0 & -\dfrac{2\nu}{ES_t} \\ \rho_f & 0 & 0 & 0 \\ 0 & 0 & m_s & 0 \\ 0 & -\dfrac{\nu R}{Ee} & 0 & \dfrac{1}{ES_t} \end{bmatrix}, \quad \mathbf{B} = \begin{bmatrix} 1 & 0 & 0 & 0 \\ 0 & 1 & 0 & 0 \\ 0 & 0 & 0 & -1 \\ 0 & 0 & -1 & 0 \end{bmatrix}, \text{ and } \vec{S} = \begin{Bmatrix} 0 \\ 0 \\ 0 \\ 0 \end{Bmatrix} \quad (157)$$

The additional equation for vapor volume fraction balance appears in two-phase flow. When needed, the vector of the source terms is replaced by the vector of the source terms that considers the external forces given in Eq. (155), or by the vector of the source terms that considers the curvature of the piping system given in Eq. (156). The physical model in Eq. (157) is essentially similar to the model developed by Skalak [104] in 1956 and extensively used by Tijsseling [117]. The Skalak's system of Equations

(157) is unconditionally hyperbolic and thus diagonalizable. Tijsseling [118] and Zhang et al. [155] obtained eigenvalues from the bi-quadratic dispersion relation. They replaced the axial force differential term by the axial pipe velocity differential term in fluid continuity Equation (157):

$$-\frac{2\nu}{ES_t}\frac{\partial N_x}{\partial t} \quad \Rightarrow \quad -2\nu\frac{\partial u_x}{\partial s} \tag{158}$$

because $\sigma_{xx} = \frac{N_x}{S_t} = E\varepsilon_{xx}$, $\varepsilon_{xx} = \frac{\partial w_x}{\partial s}$, and $u_x = \frac{\partial w_x}{\partial t}$. This replacement simplifies the evaluation of the eigenvalues.

**Linear thick-walled model**. Tijsseling [118] introduced two corrections into Skalak's model for the description of the acoustic behavior of the thick-walled liquid-filled pipes. The corrected equations were defined by the cross-section integration of the axisymmetric two-dimensional basic equations. The system of equations represents an interesting improvement of the classical Skalak's theory although Tijsseling proved that these corrections are important only for very thick pipes (*R/e* < *2*). The corrections affect only matrix **A** in Eq. (157), which becomes:

$$\mathbf{A} = \begin{bmatrix} 0 & \frac{1}{K}+\frac{2R}{Ee}\psi_2 & 0 & -\frac{2\nu}{ES_t} \\ \rho_f & 0 & 0 & 0 \\ 0 & 0 & m_s & 0 \\ 0 & -\frac{\nu R}{Ee}\psi_1 & 0 & \frac{1}{ES_t} \end{bmatrix} \quad \text{where} \quad \begin{aligned} \psi_1 &= \frac{1}{1+e/2R} \\ \psi_2 &= (1-\nu^2)\left(\psi_1 + \frac{e}{R}(1+\nu)\right) \end{aligned} \tag{159}$$

**Axial HEM FSI model.** The five-equation model consists of three equations of the HEM flow model (Eqs. (120), (121), and (122)) that are coupled with two equations for axial movement (Eqs. (56) and (62)). The model is used for simulations of the coupling between the two-phase flow thermo-fluid dynamics and axial dynamics of the piping system. The matrices of the vectorial form give:

$$\mathbf{A}_{AHEM} = \begin{bmatrix} \frac{1}{c_m^2} & 0 & \left(\frac{\partial \rho_m}{\partial e_m}\right)_p & 0 & -\rho_m\frac{2\nu}{ES_t} \\ 0 & \rho_m & 0 & 0 & 0 \\ 0 & 0 & \rho_m & 0 & 0 \\ 0 & 0 & 0 & m_s & 0 \\ -\frac{\nu R}{Ee} & 0 & 0 & 0 & \frac{1}{ES_t} \end{bmatrix} \tag{160}$$

$$\mathbf{B}_{AHEM} = \begin{bmatrix} (u_x+\mu v_m)\frac{1}{c_m^2} & \mu\rho_m & (u_x+\mu v_m)\left(\frac{\partial \rho_m}{\partial e_m}\right)_p & 0 & -\rho_m(u_x+\mu v_m)\frac{2\nu}{ES_t} \\ \mu & \rho_m(u_x+\mu v_m) & 0 & 0 & 0 \\ \mu p v_m \frac{2R}{Ee}(1-\nu^2) & \mu p & \rho_m(u_x+\mu v_m) & 0 & -\mu v_m p\frac{2\nu}{ES_t} \\ 0 & 0 & 0 & 0 & -1 \\ 0 & 0 & 0 & -1 & 0 \end{bmatrix} \tag{161}$$

$$\vec{S}^T = \{0,\ F_{m,gx} - F_{m,t},\ 0,\ f_x(s,t),\ 0\} \tag{162}$$

where $m_s = S\,\rho_m + S_t\,\rho_t$, and $c_m$ is the mixture speed of sound. The vector of the basic variables is $\vec{\psi}^T = \{p, v_m, e_m, u_x, N_x\}$. The physical model is not analytically diagonalizable. This physical model is

utilized independently or as a sub-model of larger models defined for piping systems in 2D plane or 3D space. The source terms then are:

$$\vec{S}_{AHEM}^{T} = \left\{ \rho_m \frac{u_y}{R_p},\ \left(F_{m,gx} - F_{m,t}\right),\ 0,\ \left( f_x(s,t) - \frac{Q_y}{R_p} \right),\ -\frac{u_y}{R_p} \right\} \tag{163}$$

**Axial two-fluid model for FSI.** The balance equations defined by Equations (113), (115), and (118) for each of the phases yield six-equation physical model for simulations of two-phase fluid dynamics, which together with two equations for axial movement (Eqs. (56) and (62)) yield physical model for simulations of the coupling between two-phase flow thermo-fluid dynamics and axial dynamics of the piping system. The system can be written in the following slightly modified vectorial form:

$$\mathbf{A}\frac{\partial \vec{\psi}}{\partial t} + \mathbf{B}\frac{\partial \vec{\psi}}{\partial s} = \vec{S} + \vec{S}_R \tag{164}$$

where $\vec{S}_R$ stands for all relaxation source terms. The matrices of the vectorial form are:

$$\mathbf{A}_{A2F} = \begin{bmatrix} -\rho_f & (1-\alpha)K_{5,f} & 0 & 0 & (1-\alpha)K_{4.f} & 0 & 0 & -(1-\alpha)\rho_f K_2 \\ \rho_g & \alpha K_{5.g} & 0 & 0 & 0 & \alpha K_{4.g} & 0 & -\alpha\rho_g K_2 \\ 0 & 0 & (1-\alpha)\rho_f + C_{vm} & -C_{vm} & 0 & 0 & 0 & 0 \\ 0 & 0 & -C_{vm} & \alpha\rho_g + C_{vm} & 0 & 0 & 0 & 0 \\ 0 & 0 & 0 & 0 & (1-\alpha)\rho_f & 0 & 0 & 0 \\ 0 & 0 & 0 & 0 & 0 & \alpha\rho_g & 0 & 0 \\ 0 & 0 & 0 & 0 & 0 & 0 & \rho_t A_t & 0 \\ 0 & -\dfrac{\nu R}{Ee} & 0 & 0 & 0 & 0 & 0 & \dfrac{1}{ES_t} \end{bmatrix} \tag{165}$$

$$\mathbf{B}_{A2F} = \begin{bmatrix} -\rho_f K_{6.f} & \alpha_f K_{5.f} K_{6.f} & \mu\alpha_f\rho_f & 0 & \alpha_f K_{4.f} K_{6.f} & 0 & 0 & -\alpha_f\rho_f K_2 K_{6.f} \\ \rho_g K_{6.g} & \alpha K_{5.g} K_{6.g} & 0 & \mu\alpha\rho_g & 0 & \alpha K_{4.g} K_{6.g} & 0 & -\alpha\rho_g K_2 K_{6.g} \\ 0 & \mu\alpha_f & \alpha_f\rho_f K_{6.f} + C_{vm} K_{6.g} & -C_{vm} K_{6.f} & 0 & 0 & 0 & 0 \\ 0 & \mu\alpha & -C_{vm} K_{6.g} & \alpha\rho_g K_{6.g} + C_{vm} K_{6.f} & 0 & 0 & 0 & 0 \\ -\mu p v_f & \mu\alpha_f p v_f K_1 & \mu\alpha_f p & 0 & \alpha_f\rho_f K_{6,f} & 0 & 0 & -\mu\alpha_f v_f p K_2 \\ \mu p v_g & \mu\alpha p v_g K_1 & 0 & \mu\alpha p & 0 & \alpha\rho_g K_{6,g} & 0 & -\mu\alpha v_g p K_2 \\ 0 & 0 & 0 & 0 & 0 & 0 & 0 & -1 \\ 0 & 0 & 0 & 0 & 0 & 0 & -1 & 0 \end{bmatrix} \tag{166}$$

where $\alpha_f = (1 - \alpha)$ is the liquid volume fraction, $C_{vm}$ is the virtual mass coefficient defined in Eq. (C-22), and the terms $K_{i,k}$ for phase $k$ are defined in Table 6.

*Table 6: Applied connotations; $K_1$ is elastic correction in effective speed of sound, $K_2$ is contribution of the axial force and $K_3$ and $K_4$ originate in equation of state.*

| **Short form** | $K_1$ | $K_2$ | $K_{3,k}$ | $K_{4,k}$ | $K_{5,k}$ | $K_{6,k}$ |
|---|---|---|---|---|---|---|
| **Connotation** | $\dfrac{2R}{Ee}\left(1-\nu^2\right)$ | $\dfrac{2\nu}{ES_t}$ | $\left(\dfrac{\partial\rho_k}{\partial p}\right)_{e_k}$ | $\left(\dfrac{\partial\rho_k}{\partial e_k}\right)_{p}$ | $\left(K_{3,k} + \rho_k K_1\right)$ | $\left(u_x + \mu v_k\right)$ |

The vector $\vec{\psi}^T = \{\alpha, p, v_f, v_g, e_f, e_g, u_x, N_x\}$ is the vector of the eight independent basic non-conservative variables, where $\alpha$ is the vapor volume fraction, $p$ is the fluid pressure, $v_k$ are the phasic fluid velocities, $e_k$ are the phasic internal energies, and $u_x$ and $N_x$ are the axial velocity and force. The relaxation source terms require a special numerical treatment and are thus written separately from the other (non-relaxation) source terms. The vectors of non-relaxation source terms and relaxation source terms are given by:

$$\vec{S}_{A2F}=\begin{Bmatrix}0\\0\\F_{f,gx}-F_{f,t}\\F_{g,gx}-F_{g,t}\\0\\0\\f_x(s,t)\\0\end{Bmatrix},\ \text{and}\qquad \vec{S}_{R,A2F}=\begin{Bmatrix}-\Gamma_g\\\Gamma_g\\\Gamma_g\left(v_f-v_i\right)+C_i\left|v_r\right|v_r\\-\Gamma_g\left(v_g-v_i\right)-C_i\left|v_r\right|v_r\\Q_{if}-\Gamma_g\left(h_f-e_f\right)\\Q_{ig}+\Gamma_g\left(h_g-e_g\right)\\0\\0\end{Bmatrix} \tag{167}$$

This physical model is utilized independently for axial dynamics with FSI or it is used in larger models as a sub-model (if lateral force and lateral pipe velocity are considered). The source terms in 3D yield:

$$\vec{S}_{A2F}^{T}=\left\{\alpha_f\rho_f\frac{u_y}{R_p},\ \alpha\rho_g\frac{u_y}{R_p},\ F_{f,gx}-F_{f,t},\ F_{g,gx}-F_{g,t},\ 0,\ 0,\ f_x(s,t)-\frac{Q_y}{R_p},\ -\frac{u_y}{R_p}\right\} \tag{168}$$

**Nonlinear planar quasi-two-phase flow FSI model.** The nonlinear model for simulations of FSI in planar arbitrarily shaped piping systems is the fundamental model in this dissertation. The model consists of two sub models; the axial quasi-two-phase flow FSI model given with Eq. (154), and the in-plane Timoshenko beam equations (147). The model in the vectorial form is schematically written as:

$$\mathbf{A}=\begin{bmatrix}\mathbf{A}_{AQ2F} & \\ & \mathbf{A}_{TIM,in}\end{bmatrix}_{MxM},\ \mathbf{B}=\begin{bmatrix}\mathbf{B}_{AQ2F} & \\ & \mathbf{B}_{TIM,in}\end{bmatrix}_{MxM},\ \text{and}\ \vec{S}=\begin{Bmatrix}\vec{S}_{AQ2F}\\ \vec{S}_{TIM,in}\end{Bmatrix}_{1xM} \tag{169}$$

where $M = 8$ is the dimension of the matrices, matrices $\mathbf{A}_{AQ2F}$, $\mathbf{B}_{AQ2F}$ and $\vec{S}_{AQ2F}$ assemble axial quasi-two-phase flow FSI model and matrices $\vec{S}_{TIM,in}$, $\mathbf{A}_{TIM,in}$, and $\mathbf{B}_{TIM,in}$ assemble the Timoshenko beam model for in-plane bending. The matrices of the vectorial form yield the following system:

$$\mathbf{A}=\begin{bmatrix}0 & \frac{1}{\rho_f c_f^2} & 0 & -\frac{2\nu}{ES_t} & 0 & 0 & 0 & 0\\ \rho_f & 0 & 0 & 0 & 0 & 0 & 0 & 0\\ 0 & 0 & m_s & 0 & 0 & 0 & 0 & 0\\ 0 & -\frac{\nu R}{Ee} & 0 & \frac{1}{ES_t} & 0 & 0 & 0 & 0\\ 0 & 0 & 0 & 0 & 0 & \frac{1}{\kappa GS_t} & 0 & 0\\ 0 & 0 & 0 & 0 & m_T & 0 & 0 & 0\\ 0 & 0 & 0 & 0 & 0 & 0 & 0 & \frac{1}{EI_t}\\ 0 & 0 & 0 & 0 & 0 & 0 & \rho_t I_t & 0\end{bmatrix} \tag{170}$$

$$\mathbf{B}=\begin{bmatrix}\mu & \left(u_x+\mu v_f\right)\frac{1}{\rho_f c_f^2} & 0 & -\left(u_x+\mu v_f\right)\frac{2\nu}{ES_t} & 0 & 0 & 0 & 0\\ \rho_f\left(u_x+\mu v_f\right) & \mu & 0 & 0 & 0 & 0 & 0 & 0\\ 0 & 0 & 0 & -1 & 0 & 0 & 0 & 0\\ 0 & 0 & -1 & 0 & 0 & 0 & 0 & 0\\ 0 & 0 & 0 & 0 & -1 & 0 & 0 & 0\\ 0 & 0 & 0 & 0 & 0 & -1 & 0 & 0\\ 0 & 0 & 0 & 0 & 0 & 0 & -1 & 0\\ 0 & 0 & 0 & 0 & 0 & 0 & 0 & -1\end{bmatrix} \tag{171}$$

$$\vec{S}^T = \left\{ \frac{u_y}{R_p},\ F_{f,gx} - F_{f,t},\ f_x(s,t) - \frac{Q_y}{R_p},\ -\frac{u_y}{R_p},\ \frac{u_x}{R_p} + \frac{u_z}{T_p} - \varphi_z,\ \frac{N_x - Sp}{R_p} + \frac{Q_z}{T_p} + f_y(s,t),\ -\frac{\varphi_y}{T_p},\ -\frac{M_y}{T_p} + Q_y \right\} \quad (172)$$

with the vector of the basic variables $\vec{\psi}^T = \{v, p, u_x, N_x, u_y, Q_y, \varphi_z, M_z\}$ and the vapor volume fraction $\alpha$ as the independent variables in two-phase flow (additional balance equation for $\alpha$). The vector of the source terms for a straight piping section that oscillates in axial, lateral and rotational directions simplifies into:

$$\vec{S}^T = \{0,\ 0,\ 0,\ 0,\ -\varphi_z,\ 0,\ 0,\ Q_y\} \quad (173)$$

The nonlinear model is not analytically diagonalizable. The physical model consists of two decoupled sub models; therefore, the eigensystem is also decoupled and can be schematically written as:

$$\mathbf{\Lambda} = \begin{bmatrix} \mathbf{\Lambda}_{AQ2F} & \\ & \mathbf{\Lambda}_{TIM,in} \end{bmatrix}_{MxM},\ \mathbf{L} = \begin{bmatrix} \mathbf{L}_{AQ2F} & \\ & \mathbf{L}_{TIM,in} \end{bmatrix}_{MxM},\ \text{and}\ \vec{R} = \begin{Bmatrix} \vec{R}_{AQ2F} \\ \vec{R}_{TIM,in} \end{Bmatrix}_{1xM} \quad (174)$$

The first four equations have to be diagonalized numerically; the eigensystem of the last four Timoshenko beam equations is evaluated analytically using Equations (148).

**Linear planar quasi-two-phase flow FSI model.** Introduction of the linear axial FSI coupling model (157) instead of the nonlinear model given with Eq. (154) yields the linear planar quasi two-phase flow physical model:

$$\mathbf{A} = \begin{bmatrix} 0 & \frac{1}{\rho_f c_f^2} & 0 & -\frac{2\nu}{ES_t} & 0 & 0 & 0 & 0 \\ \rho_f & 0 & 0 & 0 & 0 & 0 & 0 & 0 \\ 0 & 0 & m_s & 0 & 0 & 0 & 0 & 0 \\ 0 & -\frac{\nu R}{Ee} & 0 & \frac{1}{ES_t} & 0 & 0 & 0 & 0 \\ 0 & 0 & 0 & 0 & 0 & \frac{1}{\kappa G S_t} & 0 & 0 \\ 0 & 0 & 0 & 0 & m_T & 0 & 0 & 0 \\ 0 & 0 & 0 & 0 & 0 & 0 & 0 & \frac{1}{EI_t} \\ 0 & 0 & 0 & 0 & 0 & 0 & \rho_t I_t & 0 \end{bmatrix}, \quad \text{and} \quad \mathbf{B} = \begin{bmatrix} 1 & 0 & 0 & 0 & 0 & 0 & 0 & 0 \\ 0 & 1 & 0 & 0 & 0 & 0 & 0 & 0 \\ 0 & 0 & 0 & -1 & 0 & 0 & 0 & 0 \\ 0 & 0 & -1 & 0 & 0 & 0 & 0 & 0 \\ 0 & 0 & 0 & 0 & -1 & 0 & 0 & 0 \\ 0 & 0 & 0 & 0 & 0 & -1 & 0 & 0 \\ 0 & 0 & 0 & 0 & 0 & 0 & -1 & 0 \\ 0 & 0 & 0 & 0 & 0 & 0 & 0 & -1 \end{bmatrix} \quad (175)$$

where the vector of the source terms and the vector of the basic variables remain the same as for nonlinear model of FSI in planar arbitrarily shaped piping systems given by Eq. (172).

Equation (175), together with the source terms (173) represent the model discussed and utilized by Tijsseling, Vardy and Fan [114]. Tijsseling, Vardy and Fan presented the eight-equation system that enables simulations of the FSI in two straight sections with constant properties appropriately connected at an elbow. The sections of constant properties are connected together with additional relationships (boundary conditions). Hu and Philips [59] and De Jong [29] analyzed a system similar to the one of Tijsseling, Vardy and Fan [114] in the frequency domain. The variation of the equation (175) and source terms was discussed by Valentin, Philips and Walker [131] who applied the model for a liquid-filled constantly curved pipe.

**Eigenvalues and characteristic velocities.** Diagonalization is a crucial step towards the numerical solution of the physical problem. The diagonalized matrix of eigenvalues $\mathbf{\Lambda}$ actually represents a matrix of characteristic velocities at which the pressure, stress or other waves travel along the pipe or fluid. These values are generally very close to the speed of sound in the medium. For example, the characteristic velocity of the pressure wave in the midpoint of the pipe in rod impact experiment

considered in Section 6.4 is $c_f$ = *1361.6 (1362.5) m/s*. The value in brackets is the corresponding speed of sound. Similarly, the characteristic velocity of the axial stress wave in the pipe is $c_{t,x}$ = *4617.9 (4586.9) m/s*. Typical values for characteristic velocities of the pressure waves in single-phase liquid flow lie between *1300* and *1500 m/s*, while eigenvalues in two-phase flow drops to some *10 m/s*. Typical characteristic velocities of stress waves in the piping system are:

- Axial characteristic velocities: *4500 – 5000 m/s*.
- Lateral characteristic velocities: *1700 – 1900 m/s*.
- Rotational characteristic velocities: *4400 – 4800 m/s*.
- Torsional characteristic velocities: *2800 – 3100 m/s*.

### 4.2.4. Schematic FSI physical models

**Schematic models for planar FSI.** The complex large models can be assembled from the independent sub-models, which were introduced in previous sections of this chapter. There is no need to rewrite these complex matrices. Models are given schematically and can be composed in the same way as already indicated for the nonlinear planar quasi-two-phase flow FSI model. All non-written terms in the related matrices are equal to zero. This simple approach with assembling of sub-models is possible, because the sub models are 'coupled' between each other only through nondifferential source terms and not with differential terms. The same reason enables that a diagonalized vectorial form is assembled from the sub-models. In practice that means, that some parts of the eigensystem can be evaluated numerically, while the other parts of the same physical model, can be evaluated analytically if analytical solution exists. The schematic record indicates how different models can be assembled to get the most efficient model for the particular problem.

The models of FSI in planar arbitrarily shaped piping systems can describe axial, rotational and lateral stress waves in the pipe, pressure and other waves in the fluid (according to the number of the equations for fluid). The model can be schematically written in the vectorial form as:

$$\mathbf{A}=\begin{bmatrix}\mathbf{A}_{AXI} & \\ & \mathbf{A}_{TIM,in}\end{bmatrix}_{MxM},\ \mathbf{B}=\begin{bmatrix}\mathbf{B}_{AXI} & \\ & \mathbf{B}_{TIM,in}\end{bmatrix}_{MxM},\ \text{and}\ \vec{S}=\begin{Bmatrix}\vec{S}_{AXI}\\ \vec{S}_{TIM,in}\end{Bmatrix}_{1xM} \tag{176}$$

where $\mathbf{A}_{AXI}$, $\mathbf{B}_{AXI}$ and $\vec{S}_{AXI}$ belong to any of models for axial FSI and $\vec{S}_{TIM,in}$, $\mathbf{A}_{TIM,in}$, and $\mathbf{B}_{TIM,in}$ belong to the Timoshenko beam equations for in-plane bending. The eigensystem is also decoupled and can be schematically written as:

$$\mathbf{\Lambda}=\begin{bmatrix}\mathbf{\Lambda}_{AXI} & \\ & \mathbf{\Lambda}_{TIM,in}\end{bmatrix}_{MxM},\ \mathbf{L}=\begin{bmatrix}\mathbf{L}_{AXI} & \\ & \mathbf{L}_{TIM,in}\end{bmatrix}_{MxM},\ \text{and}\ \vec{R}=\begin{Bmatrix}\vec{R}_{AXI}\\ \vec{R}_{TIM,in}\end{Bmatrix}_{1xM} \tag{177}$$

where $\mathbf{\Lambda}_{AXI}$, $\mathbf{L}_{AXI}$, and $\vec{R}_{AXI}$ belong to corresponding eigensystem for axial movement and $\mathbf{\Lambda}_{TIM,in}$, $\mathbf{L}_{TIM,in}$, and $\vec{R}_{TIM,in}$ belong to the eigensystem of in-plane Timoshenko beam equations. If *M* is the dimension of the matrices, then one can make up the following physical models according to the number of equations:

- *M = 8* and index *AXI = AQ2F*. The eight equation nonlinear physical model of FSI in planar arbitrarily shaped piping systems is the fundamental model in this thesis. It has been presented in details in section 4.2.3. The vector of the basic variables is: $\vec{\psi}^T=\{v,p,u_x,N_x,u_y,Q_y,\varphi_z,M_z\}$.
- *M = 9* and index *AXI = AHEM*. Improvement of the quasi-two-phase nonlinear four-equation model for FSI in arbitrarily shaped piping systems with the five-equation nonlinear axial Homogeneous Equilibrium Model (HEM) for two-phase flow, which is defined by Eqs. (160), (161), and (163), gives a system of nine partial differential equations where the vector of the basic variables is: $\vec{\psi}^T=\{v_m,p,e_m,u_x,N_x,u_y,Q_y,\varphi_z,M_z\}$.

- *M = 12* and index *AXI = A2F*. Further improvement with the eight-equation nonlinear axial model for two-phase flow, which is defined by Eqs. (165), (166), (167), and (168), gives a system of twelve partial differential equations with the following vector of the basic variables:
  $\vec{\psi}^T = \{\alpha, p, v_f, v_g, e_f, e_g, u_x, N_x, u_y, Q_y, \varphi_z, M_z\}$.

**Schematic models for spatial FSI.** The models of FSI for arbitrarily shaped piping systems located in the 3D space can describe axial, rotational (in-plane and out-of-plane), lateral (in-plane and out-of-plane), and torsional stress waves in the pipe and pressure and other waves in the fluid. The number of waves in the fluid depends on the number of equations for the description of the transient in the fluid. The model can be assembled from the model for axial FSI coupling, two sets of Timoshenko beam equations (for in-plane and out-of-plane), and two torsional equations for torsion in tangential axis. The model can be schematically written in the vectorial form as:

$$\mathbf{A} = \begin{bmatrix} \mathbf{A}_{AXI} & & & \\ & \mathbf{A}_{TIM,in} & & \\ & & \mathbf{A}_{TIM,out} & \\ & & & \mathbf{A}_{TOR} \end{bmatrix}_{MxM}, \quad \mathbf{B} = \begin{bmatrix} \mathbf{B}_{AXI} & & & \\ & \mathbf{B}_{TIM,in} & & \\ & & \mathbf{B}_{TIM,out} & \\ & & & \mathbf{B}_{TOR} \end{bmatrix}_{MxM}, \quad \vec{S} = \begin{Bmatrix} \vec{S}_{AXI} \\ \vec{S}_{TIM,in} \\ \vec{S}_{TIM,out} \\ \vec{S}_{TOR} \end{Bmatrix}_{1xM} \tag{178}$$

The most challenging part of the model is the appropriate application of the junction coupling terms at pipe elbows especially source terms for simulations of arbitrarily shaped piping systems.

The model is made up of four independent sub models; therefore, the eigensystem is also independent and can be schematically written as:

$$\mathbf{\Lambda} = \begin{bmatrix} \mathbf{\Lambda}_{AXI} & & & \\ & \mathbf{\Lambda}_{TIM,in} & & \\ & & \mathbf{\Lambda}_{TIM,out} & \\ & & & \mathbf{\Lambda}_{TOR} \end{bmatrix}_{MxM}, \quad \mathbf{L} = \begin{bmatrix} \mathbf{L}_{AXI} & & & \\ & \mathbf{L}_{TIM,in} & & \\ & & \mathbf{L}_{TIM,out} & \\ & & & \mathbf{L}_{TOR} \end{bmatrix}_{MxM}, \quad \vec{R} = \begin{Bmatrix} \vec{R}_{AXI} \\ \vec{R}_{TIM,in} \\ \vec{R}_{TIM,out} \\ \vec{R}_{TOR} \end{Bmatrix}_{1xM} \tag{179}$$

If *M* is the dimension of the matrices, then one can assemble the following physical models according to the number of equations:

- *M = 14* and index *AXI = AQ2F*. The quasi two-phase flow model is used for axial FSI simulations in arbitrarily shaped piping systems in 3D space. The vector of the basic variables is: $\vec{\psi}^T = \{v, p, u_x, N_x, u_y, Q_y, \varphi_z, M_z, u_z, Q_z, \varphi_y, M_y, \varphi_x, M_x\}$. By inserting any of the derived four-equation models for axial FSI coupling and various source terms one can get various fourteen-equation models. The linearization of the model yields the fourteen-equation model, which is equal to the models used by Wiggert, Hatfield and Stuckenbruck [143], Tijsseling and Lavooij [116] and Obradovič [94]. They applied the model and solved it in the time domain with the MOC method. The model was coded in FLUSTRIN FSI code [40]. Wilkinson [145] solved the same model in the frequency domain.
- *M = 15* and index *AXI = AHEM*. Improvement of the quasi-two-phase nonlinear four-equation model for FSI in arbitrarily shaped piping system with the five-equation nonlinear axial model for the two-phase flow, which is defined by Equations (160), (161), and (163), gives a system of fifteen partial differential equations where the vector of the basic variables is:
  $\vec{\psi}^T = \{v_m, p, e_m, u_x, N_x, u_y, Q_y, \varphi_z, M_z, u_z, Q_z, \varphi_y, M_y, \varphi_x, M_x\}$.
- *M = 18* and index *AXI = A2F*. Further improvement with the eight-equation nonlinear axial model for two-phase flow, which is defined by Equations (165), (166), (168), and (167), gives a system of eighteen partial differential equations. This is the most advanced two-phase flow model for simulations of transients in 3D piping systems. The vector of the basic variables is: $\vec{\psi}^T = \{\alpha, p, v_f, v_g, e_f, e_g, u_x, N_x, u_y, Q_y, \varphi_z, M_z, u_z, Q_z, \varphi_y, M_y, \varphi_x, M_x\}$.

## 4.3. Initial conditions

Initial (and boundary) conditions have to be appropriately defined to reflect real conditions at the beginning of the transient, and not to introduce additional transients/errors into the simulation. Tijsseling [118] introduced the following fundamental assumption: **the liquid-filled piping system shall be initially always in equilibrium before a transient event starts**. The system is in equilibrium if both, initial and boundary conditions are in mutual equilibrium, otherwise, an additional transient in the liquid-filled piping system can be excited. To achieve equilibrium between initial and boundary conditions it is necessary to appropriately consider basic and some non-basic variables at boundaries and geometric changes. An example of basic variable non-equilibrium at a geometric change is the axial pipe velocity at the elbow that generates new pressure and stress waves through junction coupling. An example of non-basic variable non-equilibrium initial condition is the mass of the system or the additional mass like the mass of the valve, if gravity is included into the simulation (additional flexure of the pipe/beam).

It is necessary to appropriately distinguish between **relative** and **absolute** values of basic variables. The differential equations treat relative values and the basic variables used in the differential equations are (usually) relative. To obtain absolute values of basic variables it is necessary to add the initial extension, flexure, stresses, pressures, etc. In combination with the assumption of equilibrium before the transient, the relative consideration of the basic variables exactly corresponds to the measurement. The transient in a real experimental device starts from equilibrium and therefore, the measurement gives only relative variations of basic variables, regardless the initial pressure, stress or strain distribution. The measurements are directly comparable to results obtained with simulation. Proof for the pipe and liquid:

- All stress-strain relationships used in the FSI analyses rely on the linear elastic Hooke's law and the assumption of relativeness enables exact simulations of stresses and strains if the (absolute) stresses in the pipe are below the yield stress limit. The initial stress-strain values can be set to zero.
- The initial fluid pressure (basic variable), and the external pressure are in standard FSI simulations initially equal to zero. The standard 'elastic' theory of water hammer assumes constant fluid properties and differential equations in fact follow relative pressure gradients. The solutions are sufficiently accurate within assumptions and purposes of this single-phase approach. The pressure is relative, the initial pressure is not important; the pressure history/profile can be shifted to match the measured initial pressure.
- The advanced two-phase flow water hammer theory presented and discussed in this study, rely on exact water and steam properties that depend on absolute pressure and temperature/internal energy. Because the absolute fluid pressure is usually different than the external pressure, this difference causes additional distributed and locally generated transients due to the initial non-equilibrium in the pipe wall. Distributed transient appears due to the circumferential stress that generates axial and pressure waves and locally generated transients at elbows, abrupt area changes or boundaries of the piping system. There are three options to solve this problem:
    - The initial pressure is zero; add real initial pressure to get the correct state of the fluid when water and steam properties are calculated.
    - The initial pressure is absolute; define the appropriate external pressure at elbows and boundaries of the piping system to hold the system initially in equilibrium.
    - The external and internal initial pressures are absolute; evaluate the exact initial conditions or perform steady state simulation.

The second solution was applied in our models. Regarding the distributed transient due to the circumferential stress, note that the external pressure is almost always constant during the transient and the differential of the external pressure is zero. Thus, this term vanishes from the differential equations. The external pressure term remains only at nondifferential boundary conditions and source terms.

There are four options for prescription of the equilibrium initial state:

- *Steady state initial conditions:* Tijsseling [118] derived exact definition for the initial values of the basic variables from the one-dimensional partial differential equations omitting the non-stationary terms. The relationship in compact vectorial form is known also as steady-state initial condition:

$$\mathbf{B}\frac{\partial \vec{\psi}}{\partial s} = \vec{S} \tag{180}$$

- *Constant initial conditions:* For short piping systems, and piping systems with large cross-section the friction forces are statically and/or dynamically negligible. It is assumed that phases are initially in thermal equilibrium (no heat and mass exchange). For piping systems in a horizontal plane, the gravity is omitted. Thus, the influence of the source terms is negligible in compared to the influence of the pressure and stress waves and the source terms are omitted without significant influence on the result. It is assumed (as default option in this dissertation) that the basic variables are initially constant along the pipe:

$$\mathbf{B}\frac{\partial \vec{\psi}}{\partial s} = 0 \tag{181}$$

- *Manually prescribed initial conditions:* Each simulated piping system is divided into *N* computational volumes. It is possible to prescribe initial values for each basic variable and other parameters in each computational volume separately. The additional transient due to the artificially prescribed initial state is not always negligible.
- *Initial conditions from steady state simulation:* It is possible to conduct simulation with absolute values of the basic variables and the exact external pressure ($p_{out}$ *~ 1 bar*). In this case, steady state simulation must be conducted with maximized damping to reach equilibrium faster. The calculated steady state results are then used as initial conditions for transients. This two-step procedure demands some dummy manual output/input processing, but the basic variables are absolute and exact. An alternative is to analytically evaluate the absolute initial steady state conditions with Eq. (180), but evaluation of each equilibrium variable in each computational volume can be quite demanding and time consuming, especially for piping systems with non-trivial geometry and distribution of the supports.

# 5. Numerical scheme

A general first order partial differential equation or a system of general first order partial differential equations described in Chapter 4 (physical model), together with initial conditions and boundary conditions represents an initial boundary value problem for a considered space-time computational domain:

$$\left.\begin{aligned} &\frac{\partial \psi}{\partial t} + c\frac{\partial \psi}{\partial x} = 0 \\ &\psi(x,0) = \psi_0(x) \\ &\psi(0,t) = \psi_l(t), \qquad \psi(L,t) = \psi_r(t) \end{aligned}\right\} = \text{Initial boundary value problem} \tag{182}$$

This Chapter introduces the characteristic upwind finite difference numerical method for the numerical treatment of the initial boundary value problem. The characteristic approach was used because it is based upon the propagation of the acoustic waves, which is the principal mechanism in the considered physical models for description of the transient pipe flows. The characteristic upwind numerical method has large similarities with the group of the finite volume methods for hyperbolic conservation laws. Due to consideration of the equation of state, phase changes, geometry changes etc., the characteristic velocities of the initial boundary problem are not constant with time and space. The advantage of the characteristic upwind numerical method is that it is capable to account these non-constant characteristics. The characteristic upwind method is a second order accurate high resolution total variation diminishing explicit scheme. The stiff source terms of the physical models complicate the essentially simple explicit numerical treatment and are discussed in the continuation of this Chapter. The stiff thermal or mechanical relaxation source terms in two-phase flow are treated separately from the characteristic upwind numerical method using operator splitting while the problems with the stiff source terms of Timoshenko beam equations are solved with reduced time step and additional implicit numerical iterations. Numerical errors and difficulties related to the application of the characteristic upwind numerical method for simulations of the FSI are discussed. The boundary conditions are discussed at the end.

Several numerical methods have been applied in the past for the solution of the FSI initial boundary problems, where the method of characteristics (MOC) or MOC-based methods (component synthesis, MOC-FEM) took the leading part (see Section 1.2.2). Compared to the characteristic upwind numerical method, the standard MOC is applicable for all transients where the characteristic velocities (pressure or stress wave propagation velocities) are constant or are approximated as constant in space and time.

## 5.1. Characteristic form of the physical model

Hirsch [57] and LeVeque [77, 78] recommended the explicit characteristic numerical methods for numerical solution of the hyperbolic physical models, which are based on conservation laws. The characteristic numerical methods are based upon the characteristic form of the physical model. Every hyperbolic system of partial differential equations in vectorial form, which is given schematically in Eq. (109), can be transformed into the characteristic form through multiplication by the inverse of the eigenvectors $\mathbf{L}^{-1}$ from the left to yield:

$$\mathbf{L}^{-1}\frac{\partial \vec{\psi}}{\partial t} + \mathbf{\Lambda}\mathbf{L}^{-1}\frac{\partial \vec{\psi}}{\partial s} + \mathbf{L}^{-1}\vec{R} = 0 \tag{183}$$

Then the modified characteristic variables are introduced [126]:

$$\delta\vec{\xi} = \mathbf{L}^{-1}\delta\vec{\psi} + \mathbf{\Lambda}^{-1}\mathbf{L}^{-1}\vec{R}\delta s \tag{184}$$

which gives the characteristic form of Eq. (109):

$$\frac{\partial \vec{\xi}}{\partial t} + \Lambda \frac{\partial \vec{\xi}}{\partial s} = 0 \tag{185}$$

Note that $\delta\vec{\xi}$ represents an arbitrary variation $\partial\vec{\xi} / \partial t$ and $\partial\vec{\xi} / \partial s$, and that $\partial s/\partial s = 1$. The stream wise component $s$ is a function of the time but time differential is assumed to be negligible $\partial s/\partial t \approx 0$. Exact value of the time differential term $\partial s/\partial t$ is given with Eq. (12).

## 5.2. Basic finite difference methods

The discretisation of the differential equation by finite differences gives a finite difference method, where each discrete point in the finite difference grid represents averaged values within the computational volume (pointwise approximation). This approach often gives difference methods that look very similar to the related finite volume methods (finite volume methods operate with cell averages and integral form of the conservation laws). Consequently, the extensive theory developed for finite volume methods applies also for the finite difference methods. Finite volume methods are a class of discretisation schemes that were proven as highly successful in approximating the solution of a wide variety of conservation law systems. They are extensively used in fluid mechanics, meteorology, electromagnetism, semi-conductor device simulation, models of biological processes and many other engineering areas governed by conservative systems that can be written in integral form. Barth and Ohlberger [10] analyzed and reviewed the finite volume methods. Other, more detailed description of the finite volume methods and especially characteristic upwind finite difference method and high order accurate total variation diminishing schemes are given in textbooks of LeVeque [77,78,76], Hirsch [57] and Toro [128]. The main purpose for the application of the finite difference method (instead of finite volume) in this thesis is the fact, that the physical models derived in Chapters 2, 3, and 4 cannot be written in the so-called conservative form:

$$\frac{\partial \vec{\psi}}{\partial t} + \frac{\partial \vec{f}(\vec{\psi})}{\partial x} - \vec{R} = 0 \tag{186}$$

which means that one cannot impose the Rankine-Hugoniot [77] conditions for the discontinuous solutions (shock waves) of the hyperbolic conservation laws and use them when discontinuity is encountered in the numerical solution of the equations. Thus, the direct application of the finite volume numerical methods based on the method of Godunov is not possible. However, as shown during the development of the WAHA code [126], the non-conservative hyperbolic systems can be solved quite accurately with a similar characteristic upwind finite difference numerical method that relies on less accurate treatment of the discontinuities. Numerical tests with the WAHA code have shown that shock waves in a nearly incompressible liquid obtained with a non-conservative characteristic upwind numerical scheme are extremely similar to the shock waves calculated from the Godunov-type methods that rely on the exact Rankine-Hugoniot conditions. Tiselj and Petelin [123, 124] applied the characteristic upwind finite difference method to solve the six partial differential equations of the two-phase flow and described it as an optimal scheme for the simulation of the fast transients in two-phase flow.

**First order upwind scheme.** There is a wide variety of finite difference methods that can be used to solve the characteristic equation or system of equations defined by Eq. (185). Many of the difference schemes are derived by replacing the derivatives occurring in the partial differential equations by appropriate finite difference approximation. For instance, the temporal derivative can be replaced by the first order forward-in-time approximation:

$$\frac{\partial \xi_j}{\partial t} = \frac{\xi_j^{n+1} - \xi_j^n}{\Delta t} \tag{187}$$

and the spatial derivative by the first order one-sided approximation. There are two choices:

$$\frac{\partial \xi_j}{\partial x} = \frac{\xi_j^n - \xi_{j-1}^n}{\Delta x} \qquad \text{or} \qquad \frac{\partial \xi_j}{\partial x} = \frac{\xi_{j+1}^n - \xi_j^n}{\Delta x} \tag{188}$$

Only one one-sided approximation for spatial derivative yields a useful numerical scheme. The correct choice depends on the sign of the wave propagation characteristic velocity $\lambda$ of the corresponding characteristic partial differential equation. If the eigenvalue $\lambda$ is positive, the first choice is used and the final difference scheme is called an explicit first order upwind method:

$$\xi_j^{n+1} = \xi_j^n - \lambda \frac{\Delta t}{\Delta x}\left(\xi_j^n - \xi_{j-1}^n\right) \tag{189}$$

If $\lambda$ is negative, then the analogous first order upwind difference scheme yields:

$$\xi_j^{n+1} = \xi_j^n - \lambda \frac{\Delta t}{\Delta x}\left(\xi_{j+1}^n - \xi_j^n\right) \tag{190}$$

All values at the time level *n* are known data values (prescribed or evaluated in previous time step) so the value in new time level *n+1* is evaluated explicitly.

In finite difference schemes appears a term of the form ($\lambda\ \Delta x\ /\ \Delta t$). This is a dimensionless quantity known as the Courant number; it is also known as the Courant-Friedrichs-Levy number, or a CFL number. This number represents the ratio of two speeds, namely the wave propagation speed $\lambda$ and the grid speed $\Delta x / \Delta t$ defined by the discretisation of the domain. The von-Neumann stability analysis (Toro, [128, p.167]) shows that an explicit upwind difference scheme applied for a simple hyperbolic partial differential equation is conditionally stable for:

$$0 \le \frac{\lambda}{\Delta x / \Delta t} \le 1 \qquad \Rightarrow \qquad \Delta t \ \le \ \frac{\Delta x}{\lambda} \tag{191}$$

This is the so-called *CFL* condition for stability of the explicit difference scheme (not sufficient for all explicit difference schemes) and as $\lambda$ is prescribed as external parameter, $\Delta x$ is defined by number of computational volumes and pipe length (desired accuracy), it follows that stability restriction suggests the maximal possible time step $\Delta t$. LeVeque [78] showed that the Courant-Friedrichs-Levy condition is a necessary and sufficient condition for the stability of the characteristic upwind difference scheme.

**First order upwind scheme for systems with mixed sign characteristics.** The characteristic partial differential Eq. (185) refers to the physical model (set of partial differential equations), where the sign of the characteristic velocities varies with position and time. It is necessary to perform the appropriate spatial differencing according to the sign of the characteristic speed $\lambda$ of the partial differential equation in order to obtain a useful one-sided scheme. An improvement of the upwind scheme with upwinding principle for systems of equations with characteristics of a mixed sign [49] enables appropriate splitting between the characteristics propagating to the left and to the right (superscripts – and +, respectively):

$$\vec{\xi}_j^{n+1} = \vec{\xi}_j^n - (\mathbf{\Lambda}^+)_{j-1/2}^n \left(\vec{\xi}_j^n - \vec{\xi}_{j-1}^n\right)\frac{\Delta t}{\Delta x} - (\mathbf{\Lambda}^-)_{j+1/2}^n \left(\vec{\xi}_{j+1}^n - \vec{\xi}_j^n\right)\frac{\Delta t}{\Delta x} \tag{192}$$

where $\mathbf{\Lambda}^+ = diag\left(\lambda_1^+,...,\lambda_M^+\right)$, $\mathbf{\Lambda}^- = diag\left(\lambda_1^-,...,\lambda_M^-\right)$. Subscripts *j, j+1* and *j-1* denote the grid points of the spatial discretisation defined in the middle of the each computational volume. Subscripts *j+1/2* and *j-1/2* denote the values in the midpoint of two computational volumes, $\Delta x$ denotes the length of one computational volume, superscripts *n* and *n+1* denote the time levels and $\Delta t$ denotes the time step interval between time levels *n* and *n+1*. The appropriate splitting between positive and negative waves is given through the application of the correction factors $f_p$:

$$\lambda_p^+ = \left|\lambda_p\right| \cdot f_p^+ \qquad \text{and} \qquad \lambda_p^- = \left|\lambda_p\right| \cdot f_p^- \tag{193}$$

where index *p* is running over *M* eigenvalues of the system. The correction factors $f_p$ read:

$$f_p^+ = max\left(0, \frac{\lambda_p}{|\lambda_p|}\right) \quad \text{and} \quad f_p^- = min\left(0, \frac{\lambda_p}{|\lambda_p|}\right) \tag{194}$$

The matrix $\mathbf{\Lambda}^+$ assembles all characteristics with the positive sign that travel to the right (positive characteristics) and the matrix $\mathbf{\Lambda}^-$ assembles all characteristics with negative sign that travel to the left (negative characteristics). The full matrix of characteristics $\mathbf{\Lambda}$ is correlated to partial matrices $\mathbf{\Lambda}^+$ and $\mathbf{\Lambda}^-$ at position *j-1/2* and time *n* through the relationship:

$$\mathbf{\Lambda}^n_{j-1/2} = \left(\mathbf{\Lambda}^+\right)^n_{j-1/2} + \left(\mathbf{\Lambda}^-\right)^n_{j-1/2} \tag{195}$$

**Second order Lax-Wendroff scheme.** The upwind scheme is first-order accurate and introduces numerical diffusion, yielding poor accuracy and smeared results. The method can be improved by approximating derivatives with 2nd order differences [77,78]. The basic form of these correction terms is motivated by the standard second order accurate Lax-Wendroff method. The Lax-Wendroff method for a system of partial differential equations is based upon the Taylor series expansion [78, p.100]. The first three terms (only) on the right-hand side of the Taylor series expansion where the spatial derivatives are replaced by central finite difference approximations gives the Lax-Wendroff finite difference scheme:

$$\vec{\xi}_j^{n+1} = \vec{\xi}_j^n - (\mathbf{\Lambda}^+)^n_{j-1/2}\left(\vec{\xi}^n_{j+1} - \vec{\xi}^n_{j-1}\right)\frac{\Delta t}{2\Delta x} + \left((\mathbf{\Lambda}^-)^n_{j+1/2}\right)^2\left(\vec{\xi}^n_{j-1} - 2\vec{\xi}^n_j + \vec{\xi}^n_{j+1}\right)\left(\frac{\Delta t}{2\Delta x}\right)^2 \tag{196}$$

However, the second (and higher) order methods are also not acceptable for shock wave simulations because they yield oscillations near discontinuities.

## 5.3. High resolution finite difference schemes

The term “high resolution” applies to methods that are at least second order accurate on smooth solutions and yet give well resolved, non-oscillatory discontinuities. The idea behind is to use a high order method, but to modify the method in the neighborhood of discontinuities to the monotone first order method that behaves well near discontinuities. For precise theory and derivation of the high resolution method see LeVeque [77,78], Hirsch [57] or Toro [128]. Here, a brief overview is given.

**Total variation diminishing schemes.** Hirsch [57] showed that the total variation of the nonlinear conservation law in Eq. (186), that is defined as:

$$TV = \int_{x_1}^{x_2}\left|\frac{\partial \xi}{\partial x}\right| dx \tag{197}$$

is not increasing with time. The total variation of a discrete solution at time level *n* is defined as:

$$TV\left(\xi^n\right) = \sum_{j=1}^{N}\left|\xi^n_{j+1} - \xi^n_j\right| \tag{198}$$

Total variation diminishing schemes are numerical schemes for which the total variation of the numerical solutions is not increasing (LeVeque [77,78]). Finite difference scheme to be TVD:

$$\xi_j^{n+1} = \xi_j^n - C_{j-1/2}\left(\xi_j^n - \xi_{j-1}^n\right) + D_{j+1/2}\left(\xi^n_{j+1} - \xi^n_j\right) \tag{199}$$

is total variation diminishing if the following condition holds for each *j*:

$$C_{j-1/2} \geq 0 \quad \text{and} \quad D_{j+1/2} \geq 0 \quad \text{and} \quad C_{j-1/2} + D_{j+1/2} \leq 1 \tag{200}$$

The first order upwind scheme can be written in the form of Eq. (199):

$$\xi_j^{n+1} = \xi_j^n - \frac{|\lambda| + \lambda}{2} \frac{\Delta t}{\Delta x} \left( \xi_j^n - \xi_{j-1}^n \right) + \frac{|\lambda| - \lambda}{2} \frac{\Delta t}{\Delta x} \left( \xi_{j+1}^n - \xi_j^n \right) \tag{201}$$

It is obvious that the upwind scheme is total variation diminishing. Analogously, the Lax-Wendroff scheme Eq. (196) written in the form of Eq. (199) yields:

$$\xi_j^{n+1} = \xi_j^n - \frac{\left( \lambda \Delta t / \Delta x + 1 \right) \lambda}{2} \frac{\Delta t}{\Delta x} \left( \xi_j^n - \xi_{j-1}^n \right) + \frac{\left( \lambda \Delta t / \Delta x - 1 \right) \lambda}{2} \frac{\Delta t}{\Delta x} \left( \xi_{j+1}^n - \xi_j^n \right) \tag{202}$$

The Lax-Wendroff scheme is not total variation diminishing because the CFL condition gives $D_{j+1/2} < 0$.

Hirsch [57] showed that:

- The linear total variation diminishing scheme can be only first order accurate.
- The total variation diminishing scheme for which the new value in point *j* at time level *n+1* is evaluated from three discrete points defined at time level *n*, can be only first order accurate.

Hirsch therefore showed that second order total variation diminishing schemes are only schemes where more than three points defined at time level *n* are nonlinearly applied. The possible solution is a combination of the first order upwind scheme and the Lax-Wendroff scheme:

$$\begin{aligned} \xi_j^{n+1} = \xi_j^n &- \left( \frac{|\lambda| + \lambda}{2} \left( 1 - \phi_{j-1/2} \right) + \frac{\left( \lambda \Delta t / \Delta x + 1 \right) \lambda}{2} \phi_{j-1/2} \right) \frac{\Delta t}{\Delta x} \left( \xi_j^n - \xi_{j-1}^n \right) \\ &+ \left( \frac{|\lambda| - \lambda}{2} \left( 1 - \phi_{j+1/2} \right) + \frac{\left( \lambda \Delta t / \Delta x - 1 \right) \lambda}{2} \phi_{j+1/2} \right) \frac{\Delta t}{\Delta x} \left( \xi_{j+1}^n - \xi_j^n \right) \end{aligned} \tag{203}$$

where parameters $\phi$ are flux or slope limiters. The difference scheme in Eq. (203) is total variation diminishing only if the slope limiters are appropriately defined to conform to LeVeque's conditions. In addition, only an appropriate definition of the slope limiters gives a high resolution scheme with minimized numerical dissipation and minimized oscillations.

**Slope limiters.** The slope limiters define the share of the first and second order difference schemes. The slope limiters depend on smoothness and gradient of the characteristic variable $\xi$ at considered point (volume). The slope limiter is close to *1* if the solution at time level *n* in the vicinity of the considered point is smooth and a larger part of the second order Lax-Wendroff difference scheme is applied. In vicinity of the discontinuous solutions, the slope limiter is close to *0* and a larger part of the first order upwind difference scheme is applied.

LeVeque [77,78], Hirsch [57] and Toro [128] gave several functions for the evaluation of the slope limiters and some of the most frequently used slope limiters are defined as:

- Minmod: $\phi = \max\left(0, \min\left(1, \theta\right)\right)$
- Van Leer: $\phi = \left( |\theta| + \theta \right) / \left( |\theta| + 1 \right)$
- MC: $\phi = \max\left(0, \min\left( (1+\theta)/2, 2, 2\theta \right)\right)$
- Superbee: $\phi = \max\left(0, \min\left(2\theta, 1\right), \min\left(\theta, 2\right)\right)$

Parameter $\theta$ measures the smoothness of the characteristic variable $\xi$ near the considered point. The steepest solutions are obtained with the *superbee* limiter, while the most 'smeared' solutions but still

second-order accurate, are obtained with the *minmod* limiter. Solutions obtained with the *van Leer* and *MC* limiter are between (for example see Figures 27 and 28).

The slope limiter fixed to a constant value transforms the difference scheme in Eq. (203) into one of the following basic linear difference schemes:

- first order upwind scheme: $\phi = 0$
- second order Lax-Wendroff scheme: $\phi = 1$

The smoothness of the solution can be measured in various ways. The most commonly used measure is a ratio of the gradients in consecutive points:

$$\theta_{j+1/2} = \frac{\xi_{j+1-m} - \xi_{j-m}}{\xi_{j+1} - \xi_j} = \frac{\Delta\xi_{j+1/2-m}}{\Delta\xi_{j+1/2}} \qquad \text{where} \qquad m = \lambda / |\lambda| \tag{204}$$

The sign $m$ of the characteristic $\lambda$ defines which of the adjoining gradient is chosen. The applied smoothness measure gives the difference scheme in Eq. (203) total variation diminishing property and gives second order accuracy on smooth solutions.

**High resolution characteristic upwind scheme.** The high-resolution characteristic upwind finite difference numerical method is based upon solution given by Eq. (203). Equation (203) can be rewritten in form of Eq. (192), where $\mathbf{\Lambda}^+ = diag\left(\lambda_1^+, ..., \lambda_M^+\right)$ and $\mathbf{\Lambda}^- = diag\left(\lambda_1^-, ..., \lambda_M^-\right)$ are matrices with corrected positive and negative characteristics. Each characteristic velocity is multiplied by the correction factors:

$$\lambda_p^+ = |\lambda_p| \cdot f_p^+ \qquad \text{and} \qquad \lambda_p^- = |\lambda_p| \cdot f_p^- \tag{205}$$

where the correction factors $f_p$ are defined as:

$$f_p^+ = max\left(0, \frac{\lambda_p}{|\lambda_p|}\right) + \frac{\phi_p}{2}\left(|\lambda_p|\frac{\Delta t}{\Delta x} - 1\right) \qquad \text{and} \qquad f_p^- = min\left(0, \frac{\lambda_p}{|\lambda_p|}\right) - \frac{\phi_p}{2}\left(|\lambda_p|\frac{\Delta t}{\Delta x} - 1\right) \tag{206}$$

The first term of the correction factor is the already known first-order upwind discretisation, and the second term with the slope limiter parameter $\phi_p$ is the second-order correction. The high-resolution slope limiters $\phi_p$ are calculated using one of the functions defined in the previous section and are based upon the gradients at adjoining points. If the solution is smooth, larger part of the second-order discretisation is used; otherwise larger part of the first-order discretisation is used.

It is necessary to stress that the total variation diminishing high resolution schemes are based upon the finite volume numerical method given by the integral form of the nonlinear characteristic laws and not as may be understood here, upon the finite difference scheme given by differential form of the balance equations. Nevertheless, the difference schemes for the finite volume approach and the finite difference approach are the same, and Tiselj [122] showed that less accurate and non-conservative balance equations yield results of the same accuracy as results obtained with 'exact' nonlinear conservation laws. For differences between conservative and non-conservative equations see Tiselj [122]). Despite the large differences in theoretical background of the finite volume methods and the finite difference methods, the practical appearance of both is essentially the same. LeVeque, for instance, in his textbooks [77, 78] mentions differences between methods. However in practical examples he makes no distinction between the methods. Applicability of the total variation diminishing and the high resolution for characteristic upwind difference method was extensively proved also during the development of the WAHA code [126].

The transformation of the characteristic Eq. (192) back into the basic variables yields the following finite difference scheme that was applied for simulations in the current thesis:

$$\vec{\psi}_j^{n+1} = \vec{\psi}_j^n - \mathbf{C}_{j-1/2}^+\left(\vec{\psi}_j^n - \vec{\psi}_{j-1}^n\right)\frac{\Delta t}{\Delta x} - \mathbf{C}_{j+1/2}^-\left(\vec{\psi}_{j+1}^n - \vec{\psi}_j^n\right)\frac{\Delta t}{\Delta x} - \mathbf{D}_{j-1/2}^+\vec{R}_{j-1/2}^n\Delta t - \mathbf{D}_{j+1/2}^-\vec{R}_{j+1/2}^n\Delta t \tag{207}$$

The difference scheme is explicit and the time step $\Delta t$ is defined by CFL condition defined in Eq. (191).

The construction of the matrices $\mathbf{C}^+$, $\mathbf{C}^-$, $\mathbf{D}^+$, $\mathbf{D}^-$ and source term vector $\vec{R}$ is described below. First, the Jacobian matrix **C** is defined as a product of the basic matrices of the system **A** and **B** as: $\mathbf{C} = \mathbf{A}^{-1}\mathbf{B}$. The Jacobian matrix **C** is a function of the basic variables and is defined at both boundaries of the *j-th* computational volume (boundary is midpoint of two contiguous computational volumes and is marked as position *j±1/2*):

$$\mathbf{C}_{j-1/2} = \mathbf{C}\left(\vec{\psi}^n_{j-1/2}\right) \quad \text{and} \quad \mathbf{C}_{j+1/2} = \mathbf{C}\left(\vec{\psi}^n_{j+1/2}\right) \tag{208}$$

A simple average of the basic variables is used at midpoint:

$$\vec{\psi}^n_{j-1/2} = \frac{\vec{\psi}^n_{j-1} + \vec{\psi}^n_j}{2} \quad \text{and} \quad \vec{\psi}^n_{j+1/2} = \frac{\vec{\psi}^n_j + \vec{\psi}^n_{j+1}}{2} \tag{209}$$

Gallouet and Masella [46] used this type of averaging and showed that it gives very accurate results for Euler equations. This is actually the most important property of the proposed numerical method – the properties and thus characteristic of the each PDE that describe a wave traveling along the pipe or fluid can change with time and position. That means that the proposed numerical method enables the introduction of the nonlinearities like pressure dependent density, two-phase flow, convective terms, ovalization effects, variable geometry properties etc.

An analogous simple averaging approach is used for the evaluation of the source terms and other geometric properties at midpoints:

$$\vec{R}^n_{j-1/2} = \frac{\vec{R}^n_{j-1} + \vec{R}^n_j}{2} \quad \text{and} \quad \vec{R}^n_{j+1/2} = \frac{\vec{R}^n_j + \vec{R}^n_{j+1}}{2} \tag{210}$$

Then eigensystem is evaluated at midpoint *j±1/2* from the matrix **C** as:

$$\left(\mathbf{L\Lambda L^{-1}}\right)_{j-1/2} = \mathbf{C}_{j-1/2} \quad \text{and} \quad \left(\mathbf{L\Lambda L^{-1}}\right)_{j+1/2} = \mathbf{C}_{j+1/2} \equiv \mathbf{C}_{(j-1/2)+1} \tag{211}$$

Some of the applied eigensystems are calculated analytically, the others are evaluated numerically during simulation using subroutines from the EISPACK numerical library (FORTRAN programming language). Numerical errors and difficulties encountered during the numerical evaluation of the eigensystem are discussed in Section 5.5. The eigenvalues are then multiplied by the correction factors given in Eq. (206) and positive and negative Jacobian matrices are reconstructed:

$$\mathbf{C}^+_{j-1/2} = \left(\mathbf{L\Lambda^+ L^{-1}}\right)_{j-1/2} \quad \text{and} \quad \mathbf{C}^-_{j+1/2} = \left(\mathbf{L\Lambda^- L^{-1}}\right)_{j+1/2} \tag{212}$$

The positive Jacobian matrix $\mathbf{C}^+$ corresponds to the high resolution waves that travel to the right with the positive characteristics and the negative Jacobian matrix $\mathbf{C}^-$ corresponds to the high resolution waves that travel to the left with the negative characteristics. The reconstructed positive and negative high resolution Jacobian matrices at position *j-1/2* are related with the original Jacobian matrix through the relationship:

$$\mathbf{C}_{j-1/2} \cong \mathbf{C}^+_{j-1/2} + \mathbf{C}^-_{j-1/2} \tag{213}$$

where almost equal sign $\cong$ is used because numerical evaluation of the eigensystem gives approximate values. The elements of the matrices **D** are defined as:

$$\mathbf{D}^+_{j-1/2} = \left(\mathbf{LF^+ L^{-1}}\right)_{j-1/2} \quad \text{and} \quad \mathbf{D}^-_{j+1/2} = \left(\mathbf{LF^- L^{-1}}\right)_{j+1/2} \tag{214}$$

where the diagonal matrices $\mathbf{F}^+$ and $\mathbf{F}^-$ contain correction factors defined by Eq. (206):

$$\mathbf{F}^{+}=diag\left(f_1^{+},\ldots,f_N^{+}\right) \quad \text{and} \quad \mathbf{F}^{-}=diag\left(f_1^{-},\ldots,f_N^{-}\right) \tag{215}$$

## 5.4. Source terms

The source terms can be stiff, which means that the characteristic time scale of the source terms can be much smaller than the characteristic time scale of the convective waves given by the time step defined by the CFL condition in Eq. (191). Chalabi and Qiu [23] showed that a stable finite difference method may fail to produce reasonable numerical results and may produce non-physical solutions when stiff source terms are present. Stiffness is a numerical problem and to avoid unreasonably small time steps in the default explicit characteristic upwind given by Eq. (207), additional special numerical procedures are applied. Chalabi [24], Jin and Levermore [64], LeVeque and Yee [76], Tang, Teng and Wang [109], and Papalexandris, Leonard and Dimotakis [97] used different numerical methods that are based on asymptotic or splitting techniques, while studying solutions of the systems with stiff source terms. Researchers agree that there is no generally accepted numerical approach. It has been shown that explicit schemes are less appropriate for the numerical treatment of the stiff source terms than implicit or semi-implicit methods. Tiselj and Horvat [125] used an explicit operator splitting method for integration of the stiff source terms in their six-equation two-fluid model of the two-phase flow. Their explicit procedure is stable, because the relaxation time step adapts to the stiffness of the source terms.

Stiffness of the source terms in Eq. (207) is arbitrary and varies with time and position. There are two main reasons for stiffness of the source terms in FSI simulations:

- Stiffness of the relaxation terms that appears in unrelaxed two-phase flow.
- Stiffness of the Timoshenko beam equation that appears for relatively small second moment of inertia $I_t$ (Section 3.3, Eqs. (76) and (82)).

**Operator splitting for the stiff relaxation source terms.** Stiffness of the thermal or mechanical relaxation source terms is typical problem of the two-phase flow systems. The problem is well understood, it is manageable and also practically successfully solved. In general two-phase flow up to four types of non-equilibrium can be present, each with different relaxation time and corresponding time step of relaxation:

- Different phasic pressures,
- Vapor temperature not at saturation,
- Liquid temperature not at saturation,
- Different phasic velocities (mechanical non-equilibrium).

Generally, the smallest time step of relaxation is applied. The operator splitting is formally first order accurate, but Tiselj et al. [126] reported that numerical tests showed operator splitting results are practically the same to results obtained with second order Strang splitting numerical procedure. The relaxation source terms and operator splitting numerical technique applied in this dissertation are directly adopted from the WAHA code developed by Tiselj et al. [126]. The convection with non-relaxation source terms $\vec{S}$ is treated separately from the relaxation source terms $\vec{S}_R$ in the two-step operator splitting:

$$\text{step 1:} \quad \mathbf{A}\frac{\partial\vec{\psi}}{\partial t}+\mathbf{B}\frac{\partial\vec{\psi}}{\partial s}=\vec{S} \tag{216}$$

$$\text{step 2:} \quad \mathbf{A}\frac{\partial\vec{\psi}}{\partial t}=\vec{S}_R \tag{217}$$

where $\vec{\psi}$ is a vector of the basic variables, and **A** is the corresponding matrix. The operator splitting is applied because *step 1* with convective terms and non-relaxation source terms are carried out directly with the explicit characteristic upwind finite difference method given with Eq. (207). The *step 2* is carried

out only if two-phase flow is simulated and phases are in thermal or mechanical non-equilibrium. The *step 2* of the operator splitting scheme is integrated over the convective time step $\Delta t$ with first order explicit Euler method, which allows variations of the integration time step $\Delta t_s$ (see reference [126] for details):

$$\vec{\psi}^{m+1} = \vec{\psi}^{m} + \mathbf{A}^{-1}\vec{S}_R \Delta t_s \tag{218}$$

After integration $\vec{\psi}_j^{m+1}$ is added to $\vec{\psi}_j^{n+1}$.

**Implicit iterations for the stiff source terms in Timoshenko beam equations.** Tijsseling [113] reported occasional problems with dominating source terms that impair hyperbolic character of his basic system of equations, so that MOC becomes less attractive. His numerical tests showed that trapezoidal rule is sufficient (but not the best) way for integration of the source terms. The problem was encountered also in the characteristic upwind numerical method in all systems of equations with Timoshenko beam equations. The problem of the Timoshenko beam equations can be understood if Eqs. (68) and (83) from the system of four Timoshenko beam equations for in-plane (or out-of-plane) lateral and rotational motion are rewritten without spatial derivatives:

$$\frac{1}{\kappa S_t G}\frac{\partial Q_y}{\partial t} = -\varphi_z \qquad \text{and} \qquad I_t \rho_t \frac{\partial \varphi_z}{\partial t} = Q_y \tag{219}$$

Combination of both give one of the following equations:

$$\frac{\partial^2 \varphi_z}{\partial t^2} + \frac{\kappa S_t G}{I_t \rho_t}\varphi_z = 0 \qquad \text{or} \qquad \frac{\partial^2 Q_y}{\partial t^2} + \frac{\kappa S_t G}{I_t \rho_t} Q_y = 0 \tag{220}$$

which can be recognized as the equation of simple harmonic motion (without damping) defined already by Eq. (105). We are not able to describe the physical meaning of this harmonic motion interlaced into Timoshenko beam equations. However, solving Eq. (220) with characteristic upwind numerical method in case of stiff source terms causes nonphysical amplification of the oscillations and the numerical method becomes unstable. The following general solutions are possible for stiff source terms: (i) significant reduction of the time step below the time step given with CFL condition in Eq. (191) or (ii) moderate time step reduction with introduction of implicit iterations.

The angular frequency $\omega$ in Eq. (220) is defined by the term:

$$\omega = \sqrt{\frac{\kappa S_t G}{I_t \rho_t}} \tag{221}$$

Considering the frequency of the oscillation ($f = \omega / 2\pi$), the period of oscillation ($T = 1 / f$), and the fact that every oscillation should be divided into at least 10 time steps for successful description, the computational time step enforced by stiff source terms in Timoshenko beam equations yields:

$$\Delta t_{TIM} \le \frac{2\pi}{10}\sqrt{\frac{I_t \rho_t}{\kappa S_t G}} \tag{222}$$

Equation (222) shows, that source terms in the Timoshenko beam equations become stiff for piping systems with small moment of inertia $I_t$. According to the relations between the time step $\Delta t_{TIM}$ defined by Eq. (222) and the time step $\Delta t$ defined by CFL condition in Eq. (191) one can find the following three characteristic cases that are applied in our code:

- $\Delta t_{TIM} > \Delta t$: The source terms are not stiff, the CFL time step $\Delta t$ is applied, and the applied difference scheme is explicit given with Eq. (207).
- $\Delta t > \Delta t_{TIM} > 0.1\ \Delta t$: The source terms are stiff (moderate), the time step $\Delta t_{TIM}$ is applied, and the applied difference scheme is explicit given with Eq. (207).

- $\Delta t_{TIM} < 0.1\ \Delta t$: The source terms are stiff (significantly), the time step is smaller than 0.1 $\Delta t$ and is defined manually according to previous numerical trials. An additional implicit iterations are applied.

**Implicit iterations.** For piping systems with very small cross-section (small moment of inertia $I_t$), or for long piping systems (large $\Delta x$) the oscillation time step becomes much smaller than the time step defined by the CFL condition. Implicit iterations are introduced to avoid unreasonable small time steps and therefore long simulation times. For only one iteration, the minimal time step given with $\Delta t_{TIM}$ can be more than ten times larger. The best-on-test and therefore applied numerical procedure for implicit iterations due to stiff source terms is implicit iterative method with upwind averaged source terms. The explicit difference scheme given in Eq. (207) is then rewritten in the form:

$$\vec{\psi}_j^{**} = \vec{\psi}_j^{n} - \mathbf{C}_{j-1/2}^{+}\left(\vec{\psi}_j^{*} - \vec{\psi}_{j-1}^{*}\right)\frac{\Delta t}{\Delta x} - \mathbf{C}_{j+1/2}^{-}\left(\vec{\psi}_{j+1}^{*} - \vec{\psi}_j^{*}\right)\frac{\Delta t}{\Delta x} - \mathbf{D}_{j-1/2}^{+}\vec{R}_{j-1/2}^{*}\Delta t - \mathbf{D}_{j+1/2}^{-}\vec{R}_{j+1/2}^{*}\Delta t = 0 \quad (223)$$

The first iteration starts with: $\vec{\psi}_j^{*} = \vec{\psi}_j^{n}$ . The predicted variables $\vec{\psi}_j^{**}$ are accepted and $\vec{\psi}_j^{n+1} = \vec{\psi}_j^{**}$ if:

$$\left|\frac{\vec{\psi}_j^{*} - \vec{\psi}_j^{**}}{\vec{\psi}_j^{*}}\right| \le \vec{\varepsilon} \quad (224)$$

Otherwise, the solutions are corrected/re-predicted with another iteration, using the relationship $\vec{\psi}_j^{*} = \vec{\psi}_j^{**}$ . Matrices **C** and **D** are updated for new variables $\vec{\psi}_j^{*}$ after each iteration within the time step. The acceptance criterion $\vec{\varepsilon}$ for variables of the Timoshenko beam at the end of each time step checks if the critical variable changes for given value within one time step (currently $\vec{\varepsilon}$ = 2). If so, then the time step is repeated. Maximal number of iterations is limited, because it turned out that if the number of iterations exceeds *10*, the solution usually diverges. The solution becomes convergent for smaller computational time steps, and for sufficiently small time steps the implicit iterations would not be necessary anymore.

## 5.5. Numerical errors and difficulties

**Numerical dissipation.** Tiselj and Petelin [123, 124] stated that the weak side of the first order numerical methods is the numerical dissipation, which tends to smear discontinuities on coarse grids. The numerical dissipation (also numerical diffusion, dispersion) is a consequence of the discretisation of the pure advection equation (which, by definition, is free of dissipation) with spatial and temporal difference schemes that are first order accurate. Numerical dissipation is similar to the physical diffusion (viscosity friction, heat conduction, etc.). It tends to smooth sharp gradients and it stabilizes oscillations of the numerical method. The first error term (also local truncation error) is defined as the difference between the approximate and the true solutions. The leading error term is not included in the upwind difference scheme, therefore, the explicit upwind difference scheme for positive characteristic with the leading error term can be written as:

$$\vec{\xi}_{\mathrm{j}}^{\mathrm{n+1}} = \vec{\xi}_{\mathrm{j}}^{\mathrm{n}} - \mathbf{\Lambda}\frac{\Delta t}{\Delta x}\left(\vec{\xi}_{\mathrm{j+1}}^{\mathrm{n}} - \vec{\xi}_{\mathrm{j}}^{\mathrm{n}}\right) - \mathbf{\Lambda}\frac{\Delta t}{2}(\Delta x - \mathbf{\Lambda}\Delta t)\frac{\partial^2 \vec{\xi}_j^{n}}{\partial x^2} \quad (225)$$

The error term is essentially similar to the dissipation term (second order derivative) with numerical dissipation coefficient $\varepsilon$:

$$\varepsilon = \frac{\mathbf{\Lambda}}{2}(\Delta x - \mathbf{\Lambda}\Delta t) \quad (226)$$

A positive dissipation coefficient yields a stable difference scheme. A negative dissipation coefficient increases oscillations and sharpen gradients, thus small disturbances increase. Diffusivity becomes negative if the characteristic $\lambda$ is negative (not possible - upwind) or if the time step is too big, hence, the time step must be defined according to the CFL condition in Eq. (191). The dissipation coefficient in Eq. (226) is made up of two terms ($\Delta x$ and $\Delta t$); the first with stabilizing and the second with destabilizing effect. Both of them summon and minimal numerical dissipation are obtained if the CFL time step $\Delta t$ is as close as possible to the ratio $\Delta x / \lambda$. For very small time steps the stabilizing term prevails and larger numerical dissipation is introduced into the solution.

**Stiff source terms of the Timoshenko beam equations.** Simulations show that an increasing number of implicit iterations within one time step introduces additional numerical error, which behaves like numerical dissipation. The number of implicit iterations can be controlled by application of smaller time steps. However, there is an optimal time step for which the numerical dissipation due to small time step in explicit scheme and due to the number of implicit iterations is minimal.

**Operator splitting.** The operator splitting is a source of a specific non-accuracy that behaves like numerical dissipation, and was discussed by Burman and Sainsaulieu [18], Bereux [11] and Tiselj and Horvat [125]. The problem arises for small relaxation times, where the relaxation time is a time period in which the relaxation quantity approaches to its equilibrium value. With special transformation of the equations and with appropriate complex numerical schemes described by Burman and Sainsaulieu [18], and Bereux [11], the numerical dissipation of the operator splitting method can be avoided. However, these complex procedures are not applied in this thesis.

**Numerical evaluation of the eigensystem.** A very important step in the characteristic upwind numerical procedure is the diagonalization i.e., the evaluation of the eigenvalues and eigenvectors. The eigensystem is evaluated at each time step for each computational volume. Some simple physical models are analytically solvable, but most of the physical systems discussed in this dissertation are solved numerically. The numerical evaluation of the eigensystem is introduced through the application of the subroutines from EISPACK numerical library. The simulations showed that the results obtained with the same physical model, once solved analytically and then numerically, are identical, which in turn validates the numerical approach to evaluate the eigensystem.

The numerical evaluation of the eigensystem has only one weak side: the eigenvalues and eigenvectors are sorted at output, but for the characteristic upwind numerical method, each characteristics needs to be at the same position in the diagonalized Jacobian matrix **C**. Eigensystem re-sorting is thus conducted always. Re-sorting is simple when eigenvalues are almost constant with time and position and when the eigenvalues are roughly predictable in advance. However, in two-phase flow, the eigensystem significantly changes during the simulation and the re-sorting becomes very pretentious.

**Other sources of numerical errors and difficulties.** Various numerical tests performed showed that the influence of other types of numerical errors and difficulties emerging in the code during the simulation is negligibly small:

- The basic variables in fluid equations are written in a non-conservative form. Several tests showed that non-conservation is negligible for simulations of fast transients with short duration.
- The eigensystem is partially evaluated numerically – only slight differences to analytical values are found.
- Artificially introduced relative velocities between phasic velocities and pipe axial velocity in two-phase system enable appropriate sorting of eigenvalues and cause that the system is initially not at rest. The error is small.
- Application of various techniques of extrapolation of the boundary condition influence the solution and stability of the simulation.

## 5.6. Outlook of the code

The physical model with numerical discretisation was compiled into the computer code using FORTRAN programming language. The FORTRAN files contain over 9000 lines of code. The scheme below describes the basic steps of the algorithm:

Calculate initial values (read input datafile, set initial values (see Section 4.3), set basic parameters)

**Time step loop**

Calculate boundary conditions (set values in blind volumes, see Section 5.7)

Calculate averaged basic variables in accordance with Eq. (209)

Calculate characteristic variables and slope limiters (see Section 5.3)

Calculate basic matrices and vectors (**A**, **B**, **C**, $\vec{S}$ , $\vec{R}$ , etc.)

Calculate eigensystem ( **Λ** , **L**) numerically and/or analytically

Calculate matrices $\mathbf{C}^+$, $\mathbf{C}^-$, $\mathbf{D}^+$ and $\mathbf{D}^-$

**Evaluate variables at new time level t with Eq. (**223**)**

Check for stiff source terms of the Timoshenko beam equation (accept solution or iterate Basic loop)

Check for stiff source terms due to the relaxation (two-phase flow only, relax if necessary)

Conclude time step (accept new variables, define new additional variables, outputs, etc.)

**End of time step loop**

## 5.7. Boundary conditions

Each simulated piping system or section is divided into *N* computational volumes. There are two blind volumes at the beginning and at the end of the piping system or section (Figure 5) used for prescription of the boundary conditions. The most important is the first blind volume, while the second blind volume is used only for evaluation of the gradients for calculation of the slope limiters for the second order correction. All boundary conditions fall into one of two fundamental groups of boundary conditions:

- **Fixed value**; the value at the boundary is fixed at a certain value due to boundary condition (constant tank pressure, closed end) or is prescribed through the junction coupling mechanisms.
- **Extrapolation**; the value at the boundary is extrapolated from the last few computational volumes near the boundary. Figure 6 shows principles of various techniques.

Transients are generated by time-varying boundary conditions [118]. Table 7 shows boundary conditions for some frequently used types of supports for up to eight equation models.

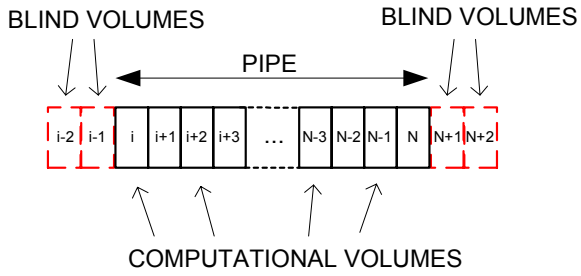


Fig. 5: Each pipe is divided into *N* computational volumes with two blind volumes at both sides of the pipe for definition of the boundary conditions.

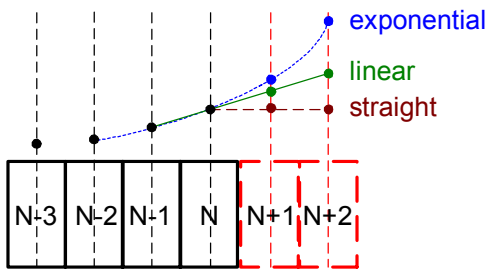


Fig. 6: Various types of extrapolation of the basic variables into blind volumes.

**Valve.** Boundary conditions in real experimental setups are not abrupt and sharp; the valve closure for example is not instantaneous. Each valve has its own closing function and time. In characteristic upwind numerical method where volume averaged values are used, the flow change function during the valve closure can be described by varying flow, fluid velocity or cross-section. The fluid velocity variation is chosen in the present dissertation and it can change according to the relationship:

$$v = u_x \pm (v_0 - u_{x0})\,\tau(t) \tag{227}$$

where $u_x$ is the axial velocity of the pipe, $u_{x0}$ is the initial velocity of the pipe, $v_f$ is the fluid velocity, $v_{f0}$ is the initial fluid velocity, ± sign depends on the pipe orientation and flow direction, and $\tau(t)$ is a given empirical closing function of time. Each type of valve has its own closing function. Tijsseling [118] presented the following equation, based on experimental measurements, for non-instantaneous ball valve closing in his experiment:

$$\tau(t) = \begin{cases} \left(1 - \dfrac{t}{t_c}\right)^{3.53} & \text{for} \quad 0 \le t \le 0.4t_c \\ 0.394\left(1 - \dfrac{t}{t_c}\right)^{1.70} & \text{for} \quad 0.4t_c \le t \le t_c \\ 0 & \text{for} \quad t_c < t \end{cases} \tag{228}$$

with $t_c$ as the valve closing time.

*Table 7: Boundary conditions for frequently used types of supports. Values represent fixed boundary condition; label E stands for boundary condition based on extrapolation.*

| Description of the BC | Boundary condition for basic variables | | | | | | | |
|---|---|---|---|---|---|---|---|---|
| | $v$ | $p$ | $u_x$ | $N_x$ | $u_y$ | $Q_y$ | $\varphi_z$ | $M_z$ |
| Open pipe, fixed pressure (tank), no support | E | $p_{tank}$ or $p_{out}$ | E | S(p-$p_{out}$) | E | 0 | E | 0 |
| Open pipe, fixed pressure (tank), roller support | E | $p_{tank}$ or $p_{out}$ | E | S(p-$p_{out}$) | 0 | E | E | 0 |
| Open pipe, fixed pressure (tank), pinned support | E | $p_{tank}$ or $p_{out}$ | 0 | E | 0 | E | E | 0 |
| Open pipe, fixed pressure (tank), clamped support | E | $p_{tank}$ or $p_{out}$ | 0. | E | 0 | E | 0 | E |
| Closed pipe (valve), no support | $u_x$ | E | E | S(p-$p_{out}$) | E | 0 | E | 0 |
| Closed pipe (valve), roller support | $u_x$ | E | E | S(p-$p_{out}$) | 0 | E | E | 0 |
| Closed pipe (valve), pinned support | 0 | E | 0 | E | 0 | E | E | 0 |
| Closed pipe (valve), clamped support | 0 | E | 0. | E | 0 | E | 0 | E |
| Closed pipe (valve), no FSI (junction coupling) | 0 | E | 0 | 0 | 0 | 0 | 0 | 0 |
| Closed pipe (valve), no support, rod impact | $u_x$ | E | E | S(p-$p_{out}$)+$Y_{rod}$($u_x$-$v_{0,rod}$) $Y_{rod} = A_{rod}\,(E_{rod}\rho_{rod})^{1/2}$ | E | 0 | E | 0 |

**Additional mass.** All measuring equipment and other objects mounted on the piping system (valve, end plug, or end cap, support accessory, etc.) influence pipe inertia. These objects can be simply included into simulation by adding their mass to the mass term in axial $m_s$ or lateral $m_T$ direction. It is possible to specify additional mass for each computational volume.

**Forces.** External forces and bending momentum at the boundary are not necessarily equal to zero. It is possible to introduce additional values through an external force term or by fixing a boundary condition in Table 7 at a certain value that is different than zero.

**Elastic support.** None of the supports is absolutely stiff. The first approximation of the elastic support is support reaction force that depends on extension or flexure of the pipe *w* and stiffness of the corresponding support *k*:

$$F_x = k_x w_x \qquad \text{and} \qquad F_y = k_y w_y \tag{229}$$

The elastic support is introduced in a similar way like external force and mass. The elastic support can be defined at any position of the piping system.

**Piping systems splitted into two or more sections.** An additional option for the boundary condition was implemented to enable splitting of the piping system into two or more straight sections with constant parameters. These constant straight sections are then coupled through appropriate boundary conditions. This option is important for comparison of our results with results obtained with standard approaches presented by Tijsseling [114]. There are two possible connections:

- Straight connection (Figure 7). The connection is used when there is a change of one parameter (for instance pipe wall thickness) of the piping system that causes change of the constant eigensystem. The values of the basic variables in two blind volumes at the beginning of the second pipe are copied from the last two computational volumes of the first pipe. Similarly the blind volumes at the end of the first pipe are copied from the first two volumes of the second pipe.
- Elbow connection (Figure 8). The connection is used to model coupling relations (junction coupling) at sharp elbow with curvature radius $\alpha$, that are given by the relationships (index *1* stands for pipe 1 and index *2* stands for pipe 2):

$$\begin{aligned}
&S_1\left(v_1 - u_{x,1}\right) = S_2\left(v_2 - u_{x,2}\right) && u_{y,1} = u_{y,2}\cos(\alpha) + u_{x,2}\sin(\alpha)\\
&p_1 = p_2 && Q_{y,1} = Q_{y,2}\cos(\alpha) - \left(S_2 p_2 - N_{x,2}\right)\sin(\alpha)\\
&u_{x,1} = u_{x,2}\cos(\alpha) - u_{y,2}\sin(\alpha) && \varphi_{z,1} = \varphi_{z,2}\\
&N_{x,1} - S_1 p_1 = \left(N_{x,2} - S_2 p_2\right)\cos(\alpha) - Q_{y,2}\cos(\alpha) && M_{z,1} = M_{z,2}
\end{aligned} \tag{230}$$

These models of the splitting were introduced only for comparisons with verified computer codes developed in the past, which use exclusively this type of coupling to describe any variation of any parameter of calculation (variable geometry, elasticity, elbow flexibility, pipe orientation (elbows), cross-section, etc.). The standard numerical methods are applicable only for linear physical models describing straight sections with constant parameters. Therefore, appropriate models were applied at straight connection to account for these variations. The characteristic upwind numerical method introduced in this thesis, enables simulations of nonlinear physical models without additional coupling models.

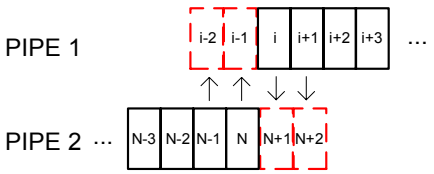


Fig. 7: Straight connection.

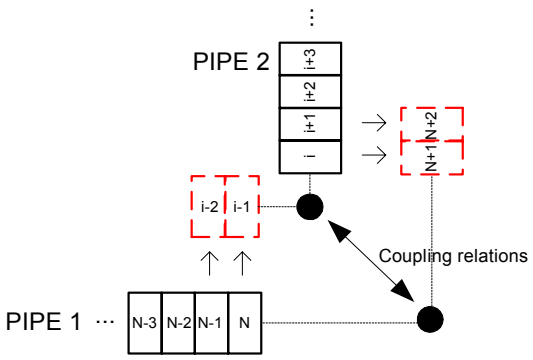


Fig. 8: Elbow connection.

# 6. Numerical examples

This Chapter describes the application and validation of the developed FSI computer codes with discussion of accompanying phenomena. Axial and lateral oscillations of a straight pipe (beam) are studied first; the results are compared to available analytical solutions. Special attention is given to the study of the natural frequency of oscillation of empty pipe and the influence of the fluid inside the pipe on the axial or lateral dynamics. Several benchmark problems for the numerical verification of the FSI codes were developed at the Delft hydraulics laboratory. Some of these benchmarks are simulated and discussed with special emphasis on the characteristic upwind numerical method and its properties. The results are compared to the MOC-based verified computer code developed by Tijsseling. At the end of this Chapter simulations of three different experiments with two-phase flow FSI are presented. The Simpson pipe experiment is essentially used to validate the quasi-two-phase flow model. The mechanisms that can be used to prevent FSI effects at elbows and pipe ends (valve) are studied. The rod impact experiment (Vardy and Fan [132]) in a straight pipe hanging on wires was used to study the single-phase flow FSI. The experimental apparatus isolates the FSI and enables the advanced study of mutual dynamics of the fluid and structure. At the end some simulations of the rod impact experiment in a hanging single-elbow piping system conveying two-phase flow are presented and discussed. Both, cavitation and the FSI are very strong. The code effectively and accurately simulates all considered experiments.

## 6.1. Axial and lateral oscillations of a pipe

**Axial oscillation of an empty pipe.** The problem of the axially oscillating empty pipe was used for verification of the structural part of the code without fluid flow. A simple straight cantilever piping system is schematically presented in Figure 9. It is simulated with axial pipe dynamics model described in Section 4.2.2. At time zero, steady axial force $F_x = 10\ kN$ starts to act on the pipe endpoint and the pipe endpoint extends and starts to oscillate around new equilibrium. The pipe is horizontal, gravity effects are excluded, the system can move in the axial direction only.

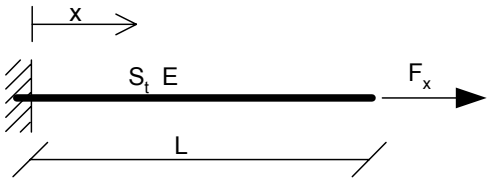


$S_t = 5.938E\text{-}4\ m^2$, $E = 200\ GPa$,
$\rho_t = 7980\ kg/m^3$, $L = 2\ m$

Fig. 9: Geometry of an empty pipe loaded with axial force $F_x$.

There is a difference between two types of loads: force and mass. The force is applied as initiator of oscillations and affects the amplitude of the oscillation, while the mass affects system's inertia and consequently affects amplitude and frequency. The mass can initiate movement only if gravity is included into simulation. The piping system loaded with the force oscillates at the natural frequency of the unloaded pipe regardless the size of the force.

A point mass, hanging on a massless spring, oscillates with sinusoidal trajectory in position/time plane. The question that arises is what would be the trajectory of the endpoint if the spring is not massless and there is no point mass? This is actually the case of the axial oscillation of a straight empty cantilever pipe loaded with an axial force. Figure 10 shows that axial oscillations of the pipe are sharp with 'saw' trace. This behavior is a consequence of the fact that each disturbance in the piping system travels along the medium with the characteristic velocity, which is very close to the speed of sound in the current medium. Precisely, the pipe endpoint starts to extend from the initial position immediately after the axial force starts to act. It moves constantly with constant velocity. At the same time, the axial stress wave is induced at the endpoint and the head of the axial stress wave travels along the pipe from the

endpoint to the support with its characteristic velocity. Each section along the pipe starts to extend only when it is reached by the axial stress wave. The pipe is fixed at support, therefore the axial stress wave reflects at the support and when traveling back to the endpoint, it turns sign of the movement (extension turns to contraction). This is an effect of the boundary condition. If the speed of sound in the pipe in axial direction is $c_t$ = *5006.3 m/s*, and the length of the pipe is $L$ = *2 m*, then the pipe's endpoint extends constantly with constant velocity for the period $t_{ext} = 2\,L / c_t$ = *0.7989 ms*. Afterwards, the pipe's endpoint starts to contract for the same period, $t_{cont} = t_{ext}$. This behavior is repeating, therefore adding $t_{cont}$ to the $t_{ext}$ gives a period of one oscillation or inversely, a frequency of oscillation $f$ = *625.9 and 625.8 Hz* obtained with simulation and from analytical solution (Table 5), respectively.

Figure 10 shows oscillations of the pipe endpoint obtained with three different approaches: (i) with our code where the pipe is divided into $N$ = *640* computational volumes, (ii) with the commercial structural dynamics code Abaqus/Explicit [1] based on Finite Element Method where the pipe is divided into $N$ = *80* computational finite elements, and (iii) with Arscott's analytical solution. Arscott [8] gave exact solution of the problem of axial oscillation without damping for the unloaded heavy spring. The solution is valid also for axially oscillating empty piping systems loaded with an axial force. The point at position $s$ oscillates with amplitude $a$ around equilibrium due to some initial disturbance in accordance with equation:

$$w_x(s,t) = \sum_{n=0}^{\infty} \frac{8a}{\pi^2} \frac{(-1)^n}{(2n+1)^2} \sin\left((2n+1)\frac{\pi s}{2L}\right) \cos\left((2n+1)\frac{\pi t}{2L}\sqrt{\frac{E}{\rho_t}}\right) \tag{231}$$

Generally, the differences between the solutions in Figure 10 are very small although detail shows small discrepancies between various results at the discontinuity in the solution. The discrepancies depend on the assumptions of the calculation. An example, how calculation assumptions affect numerical results of our code is shown in Figure 11, which shows that numerical dissipation decreases and accuracy of the solution increases for denser computational grids. The analytical solutions are usually exact, but the Arscott's analytical solution is an infinite sum, which means that the accuracy of the analytical solution depends on a number of accounted summands. The dashed blue line in Figure 10 was obtained as a sum of the first 100 summands. The sum of the first 10 summands gives much more smeared solution, comparable to the result of our code. Finally, the Abaqus/Explicit solution will be sharper (i.e. more accurate), if a larger number of finite elements is applied.

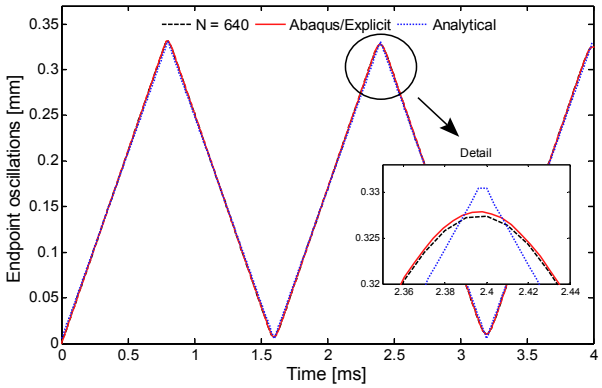


Fig. 10: Axial oscillations of the endpoint: comparison between our code, Abaqus/Explicit and analytical solution.

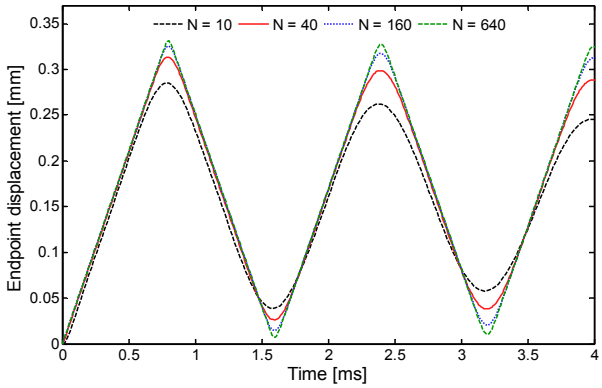


Fig. 11: Axial oscillations of the endpoint: influence of the grid refinement.

Every real natural oscillatory motion is damped as it is not possible to eliminate energy losses due to non-conservative forces. Thus, oscillations of the cantilever piping system slowly become sinusoidal as time evolves because of damping. On the other hand, there are several mechanisms that introduce numerical errors into simulation, which is known as numerical dissipation (see Section 5.5). The governing effects of the numerical dissipation and natural damping are the same – smoothened solution, damping of motion and finally equilibrium. Figure 11 shows, that one of the mechanisms that affect numerical dissipation is the number of computational volumes. As natural damping, also numerical dissipation finally stops any movement of the piping system. From basic equations of statics of structures, it is possible to evaluate the pipe endpoint equilibrium extension due to an imposed axial

force. Analytically evaluated extension is $w_x$ = *0.168 mm*, which is *0.004 mm (2.3 %)* more than simulated $w_{x,sim}$ = *0.164 mm*.

**Axial oscillation of a fluid-filled pipe.** The considered transient in a closed fluid-filled piping system is an extension of the empty pipe transient. The two-equation axial structural dynamics model applied in the previous section is upgraded with the fluid dynamics model into a four-equation axial quasi-two-phase flow FSI physical model described in Section 4.2.3. Various fluids with constant fluid properties are applied to verify the influence of the fluid on axial dynamics of the pipe. Figure 12 schematically shows geometry and properties of the pipe, and Table 8 shows properties for all applied fluids (air, water, methanol, and dichlorodifluoromethane R12). The properties are valid for fluids at room pressure ($p$ = *1 bar*, except R12 where $p$ = *7 bar*) and room temperature ($T$ = *293 K*). The thermodynamic properties of the fluid are constant during simulation, and the flow is single-phase. The closed fluid-filled cantilever pipe at rest is instantaneously loaded in axial direction with axial force $F_x$ = *10 kN*. The transient is controlled with properties of the both, the pipe and the fluid.

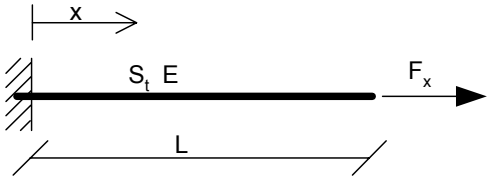


*$S_t$ = 5.938E-4 $m^2$, E = 200 GPa,*
*$\rho_t$ = 7980 $kg/m^3$, L = 2 m, S = 5.938E-4 $m^2$*

Fig. 12: Geometry of the closed fluid-filled pipe loaded with axial force $F_x$.

*Table 8: Properties of the state for the applied fluids. T = 293 K and p = 1 (7*) bar*

| Fluid | $\rho$ [kg/m3] | K [Pa] | $c_0$ [m/s] |
|---|---|---|---|
| Water | 998.2 | 2.009E9 | 1418.9 |
| Methanol | 791.1 | 0.987E9 | 1116.7 |
| R12* | 1330. | 0.379E9 | 533.6 |
| Air | 1.204 | 1.418E5 | 343.2 |

Figure 13 shows the relative pressure history near the unsupported right end for the first 5 milliseconds of the transient and Figure 14 shows pipe unsupported endpoint extension history for the same period. The stress waves in the structure travel several times faster than the pressure waves in the fluid, thus, at the beginning, all changes in the pressure appear as a consequence of the pipe movement. This is the influence of the pipe on the fluid due to the FSI coupling. If the pipe is extending, the pressure is reduced below and if the pipe is contracting, the pressure is increased above the initial 'Joukowsky' pressure. The changes in the pressure appear at the same time for all fluids because properties of the pipe are the same regardless the conveying fluid. The pressure waves in the fluid are few times slower than the stress waves in the pipe. The pressure wave in the water is the fastest among the pressure waves in applied fluids (Table 8). It travels with characteristic velocity $c_f$ = *1304 m/s* and comes back to the unsupported right end after $t$ = *3.07 ms*. This can be observed in water pressure history as disturbance. Similarly, the pressure wave in methanol travels with characteristic velocity $c_f$ = *1069 m/s* and reaches the remote end at time $t$ = *3.74 ms*. The transient shows strong coupling between the fluid and the structure.

The time history results presented in Figures 13 and 14 and equilibrium extension $w_x$ and pressure $p$ collected in Table 9 with comparison of simulation and analytical results indicate that:

- The **energy** from the loaded pipe **is transported** through FSI effects into the fluid. The fluid pressure and the amplitude of the endpoint oscillations are affected.
- The pressure rise/drop is stronger for systems with less compressible fluid.
- The endpoint oscillations are smaller for systems with less compressible fluid
- The inertia effects of the mass of the fluid (density) are not trivially related to effects of the FSI. Proof: the heaviest fluid (R12) is not the most influential.
- The intensity of the FSI in the axial direction depends on stiffness (bulk modulus) as recognized already by Casadei [22], who recommended FSI analysis if the fluid is incompressible. Several properties affect FSI transient. However, the **compressibility of the fluid is the most important**. The effects of the FSI are most evident and intense in low compressible water-filled piping system and less evident in a very compressible air-filled piping system.
- Less compressible fluids exhibit higher numerical damping (not evident from the Figures).

- Equilibrium extension is smaller in less compressible fluid.
- Equilibrium pressure change is larger in less compressible fluid.
- Comparison of simulated equilibrium to analytical solution shows high accuracy and reliability of the applied mathematical model and numerical technique.

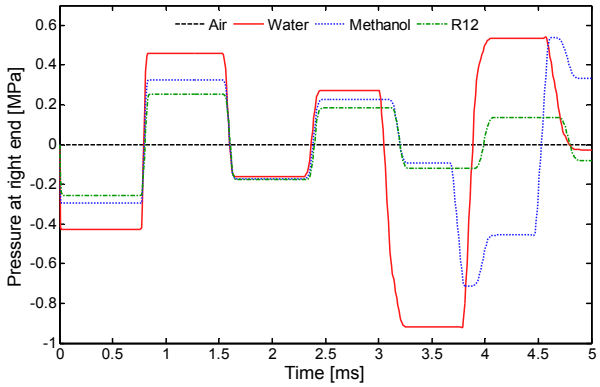


Fig. 13: Pressure history near the right end of the fluid-filled cantilever pipe due to axial force.

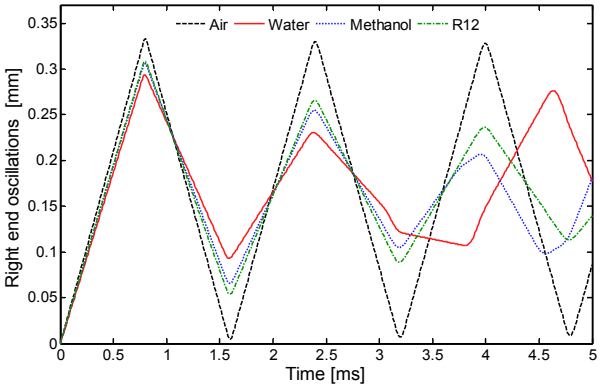


Fig. 14: Endpoint oscillation history near the right end of the fluid-filled cantilever pipe.

*Table 9: Equilibrium pipe extension and fluid pressure due to axial force.*

| Fluid | Simulation | | Analytical | | Relative difference | |
|---|---|---|---|---|---|---|
| | $w_x$ [mm] | $p$ [Pa] | $w_x$ [mm] | $p$ [Pa] | $\Delta w_x$ [%] | $\Delta p$ [%] |
| Water | 0,16635 | -56942 | 0,16658 | -56864 | -0,14 | 0,14 |
| Methanol | 0,16691 | -30280 | 0,16704 | -30405 | -0,08 | -0,41 |
| R12 | 0,16709 | -12105 | 0,16736 | -12323 | -0,16 | -1,77 |
| Air | 0,16715 | -4,5 | 0,16758 | -4,8 | -0,25 | -5,77 |

**Lateral oscillations of an empty pipe.** The response of the structure (piping system) to the lateral load, i.e. lateral oscillations of the structure, are a complicated function of the pipe stiffness, inertia, mass, distribution of the load and supports, etc. Stokey in a handbook of Harris and Crede [51] gave analytically equations for the frequencies of lateral oscillations that were developed with an exact method, with a lumped parameter solution and with a solution using Rayleigh's method (Table 5). The analytical solutions are valid for numerous combinations of vibrating beams (empty pipes), plates, masses and supports. Derivation of these analytical solutions is usually based on assumption of symmetric load and symmetric supports, which in turn actually enables analytical solution. Consequently, tables in the literature that collect natural lateral frequencies refer to idealized symmetric cases with centralized masses and are thus useless for the majority of the real structures. The simulations of cases in this section point out that our approach, where four in-plane Timoshenko beam equations are applied, give an elegant numerical way for the study of the natural frequencies of arbitrarily loaded and asymmetrically supported piping systems. All pipes in Figures from 15 to 20 are empty and have the same properties: cross-section area $S_t$ = *5.938E-4* $m^2$, moment of inertia (second moment of area) $I_t$ = *2.952E-5* $m^4$, Young elasticity modulus $E$ = *200 GPa*, density $\rho_t$ = *7980* $kg/m^3$ and length $L$ = *2 m*. The transient is induced at time zero, when the gravity and/or external load start to act on the piping system. The simple structure starts to oscillate in lateral direction with more or less sinusoidal trajectory.

Figure 15 shows the oscillations of the midpoint of a pinned-pinned pipe loaded with centric force $F_y$ = *100 N* and the comparison to the case with equivalent mass $m$. The natural frequency of the oscillations of the pipe loaded with a force is equal to the frequency of the unloaded pipe $f$ = *43.7 (43.5) Hz*, and is decreased when the pipe is loaded with an additional centric mass $f_{cm}$ = *24.8 (24.5) Hz*. First values are obtained with simulation while values inside brackets are obtained from analytical expressions. Figure 16 shows a comparison of oscillations of a pipe with centric and eccentric masses. In the case with an eccentric mass the frequency is increased to $f_{sim,ecm}$ = *28.5 Hz*, and the amplitude and the ultimate bending of the midpoint is slightly decreased. Figure 17 shows an example of oscillations of the right endpoint of the piping system with arbitrary supports and masses. The oscillation of any point along the

pipe is a complicated function of the load, pipe stiffness and supports. The analytical solution for the eccentric mass case and the case with arbitrary supports and loads does not exist.

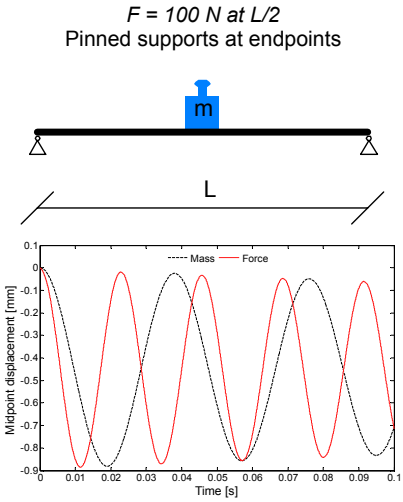


Fig. 15: Geometry and lateral oscillation of the midpoint for the pipe with centric force and equivalent mass.

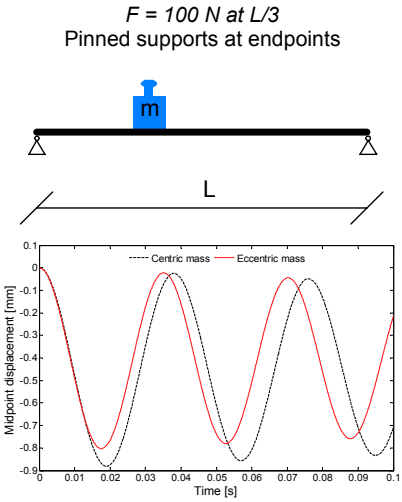


Fig. 16: Geometry and lateral oscillation of the midpoint for the pipe with centric and eccentric mass.

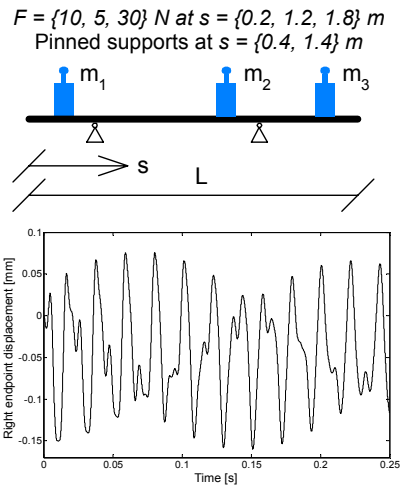


Fig. 17: Geometry and right endpoint oscillation for arbitrarily supported and loaded pipe.

The additional mass $m$ is included into the simulation as external load through differential term with $m_T$ in Eq. (73). If the additional mass $m$ (usually $m > m_T$ ) is concentrated in a single volume then the abrupt jump in the mass represents a singularity in the eigensystem that locally increases the numerical dissipation. Table 10 shows that a simulation gives more accurate results for the cases with denser grid and the cases where the mass is distributed over more computational volumes. The analysis was performed with centric mass oscillating pipe problem depicted in Fig. 15.

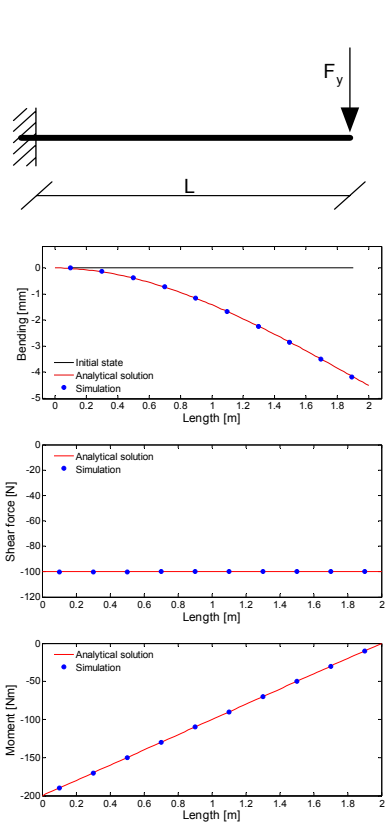


Fig. 18: Bending, shear force and momentum in cantilever pipe due to static force at endpoint.

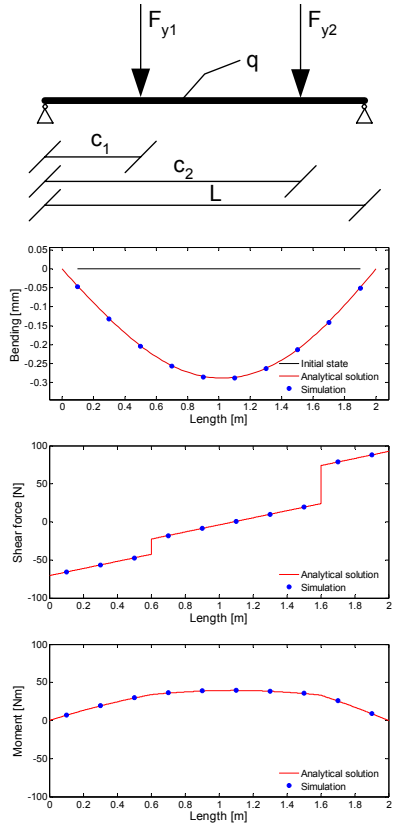


Fig. 19: Bending, shear force and momentum in pipe due to static forces and gravity.

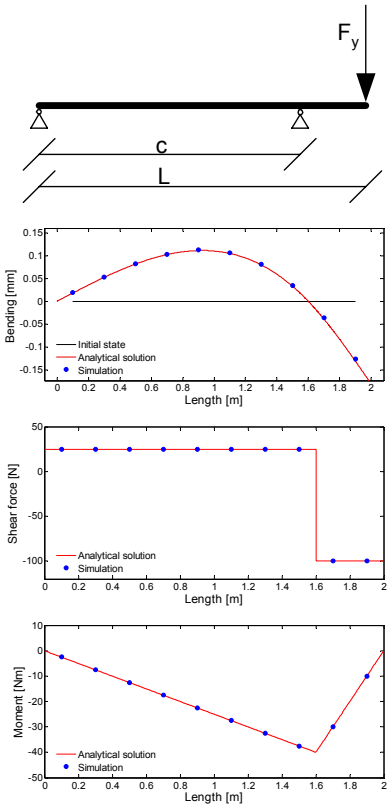


Fig. 20: Bending, shear force and momentum in cantilever pipe due to static force at endpoint.

*Table 10: Accuracy of the simulation depends on the grid and number of computational volumes over which the mass is distributed.*

| Grid density [comp. volumes] | Mass distribution [comp. volumes] | Frequency [Hz] |
|---|---|---|
| 10 | 1 | 31.5 |
| 30 | 3 | 26.3 |
| 90 | 1 | 36.9 |
| 90 | 3 | 26.8 |
| 90 | 9 | 25.1 |
| 270 | 27 | 24.8 |
| **Analytical solution:** | | **24.5** |

Additional examples are presented in Figures 18, 19, and 20 (diagrams are grouped in columns). The pipes are loaded with forces at various positions ($c = c_2 = 1.6\ m$, and $c_1 = 0.6\ m$). The external lateral force for the cases of Figs. 18 and 20 is equal to $F_y = 100\ N$ and the beam in Fig. 19 is loaded with two eccentric lateral forces, $F_{y1} = 20\ N$ and $F_{y2} = 50\ N$, and distributed mass $q = 46.51\ N/m$. The natural frequency of oscillation of the (unloaded) cantilever pipe in Fig. 18 is $f = 16.0\ (15.6)\ Hz$, and the natural frequency of the midpoint of the (unloaded) pipe in Fig. 19 oscillates with frequency $f = 43.5\ (44.1)\ Hz$. Each movement is damped until the equilibrium is reached. Figures 18, 19, and 20 show equilibrium bending, shear force and bending momentum and all simulated variables (blue dots) perfectly match with analytical solution depicted with red continuous line. One should note, that the achievement of the equilibrium is not a consequence of the physical damping, but due to the numerical damping.

**Lateral oscillations of a fluid-filled pipe.** The planar eight-equation quasi-two-phase flow FSI physical model described in Section 4.2.3 is applied to verify the influence of various fluids on lateral dynamics of the pipe. The geometry and geometric properties are the same as for the structure in Figure 15, the piping system is closed at both ends, pressurized, and filled with four different fluids (properties in Table 8). The system is initially at rest, relative changes in pressure and displacements of the midpoint are traced.

The case where the pipe is not loaded with an external load is considered first. Various fluids have various densities and therefore the total mass of the piping system per unit of length is different for different fluids. At time zero, the gravity starts to act on the piping system and the structure starts to oscillate. Figure 21 shows that for lateral dynamics, the heaviest fluid yields to the largest amplitude and the smallest frequency of oscillation. The structural oscillations through FSI coupling induce oscillations of the pressure in the midpoint however, the pressure changes due to oscillations are actually negligible. It is possible to see that the frequency of the pressure waves is few times larger than the frequency of the lateral movement, which in turn prevents the appearance of significant FSI effects in the lateral direction.

Figure 22 shows a case similar to the previous one with one exception. There is no gravity field, the transient is initiated by the action of the lateral force $F_y = 100\ N$ in the midpoint. Then the amplitude is equal for all fluids, because different density of different fluids (mass) affect only the frequency of the oscillations. The heaviest fluid R12 has the largest period of oscillation. The pressure history shows that the frequency of pressure pulsations is much shorter than the frequency of structural dynamics, the heaviest fluid experiences the highest pressure peaks, and the pressure pulsations are actually negligible.

The study of the lateral dynamics in fluid-filled piping system with FSI yields to the following conclusions:

- **FSI is very weak** in lateral dynamics of structures.
- The most **important** FSI parameter for oscillation in the lateral direction is the **density** of the fluid (mass).
- The total pipe volume change is very small for lateral dynamics, therefore, the **pressure changes** in the fluid **are negligible**.
- With consideration of the gravity: the denser fluid decreases the natural frequency of the oscillation and increases the amplitude.

- Without consideration of the gravity: the denser fluid decreases the natural frequency of the oscillation while the amplitude is not affected.

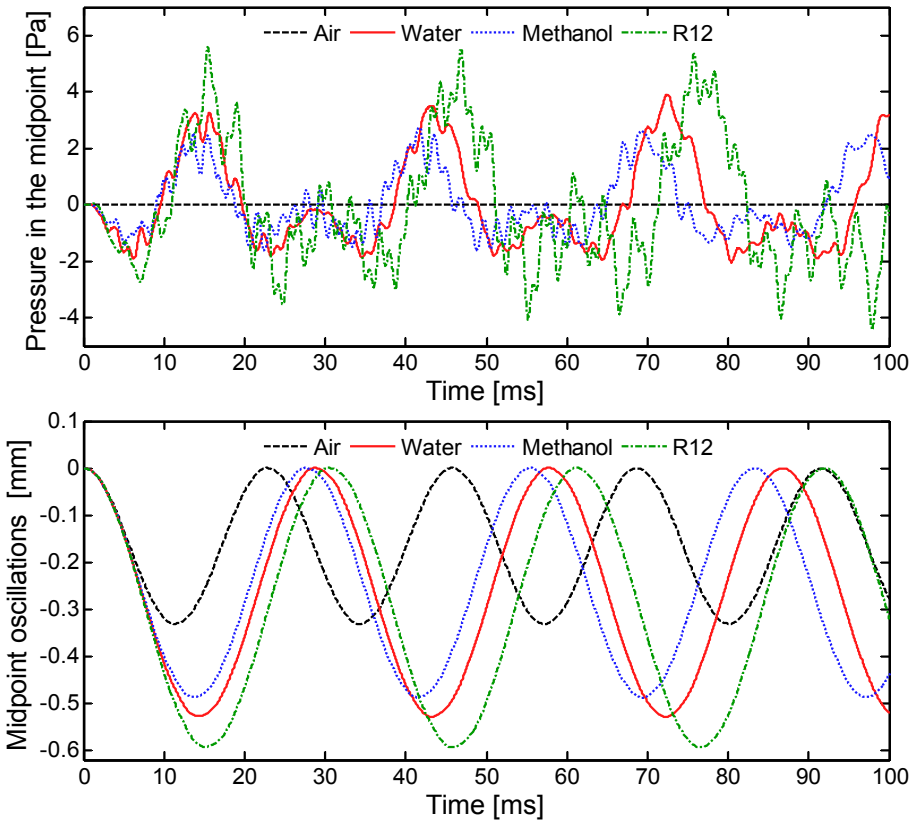


Fig. 21: Pressure and oscillation history in the midpoint of the piping system filled with various fluids. The transient is initiated by introduction of the gravity forces.

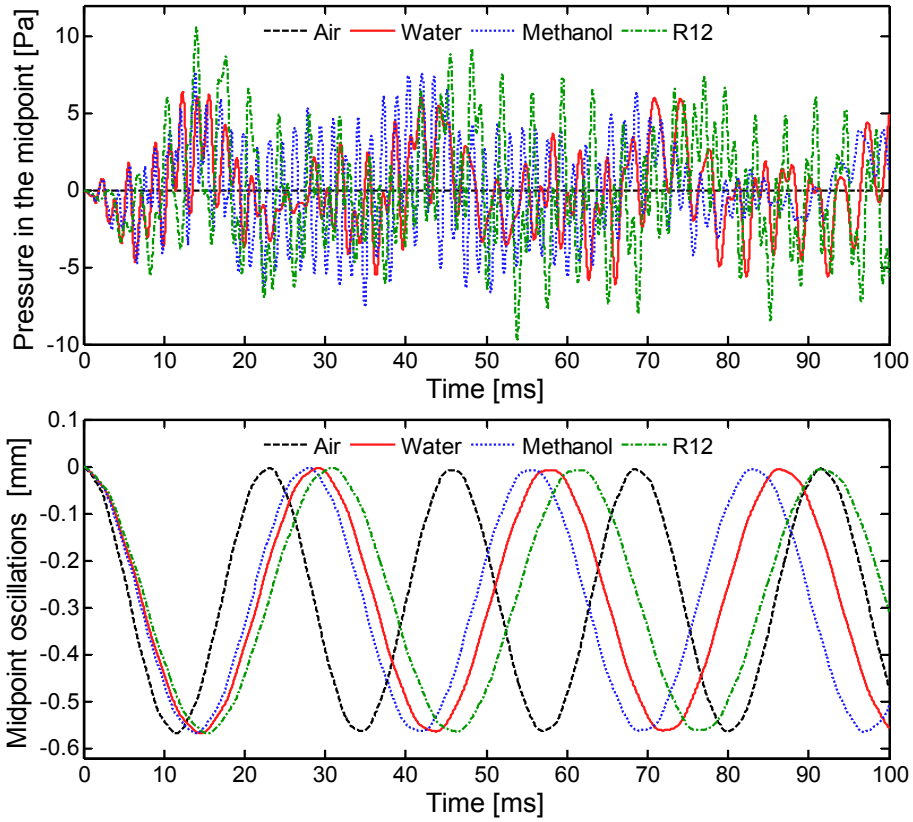


Fig. 22: Pressure and oscillation history in the midpoint of the piping system filled with various fluids. The structure is loaded with lateral force (no gravity considered).

## 6.2. Delft hydraulic benchmark problems

All developed FSI computer codes and the underlying mathematical models and numerical methods, have to be extensively tested. For this purpose Tijsseling [113] adopted several benchmark problems, known as Delft hydraulics benchmark (DHB) problems A to F. These benchmark problems are based on an inventory of field cases and were defined in consultation with prof. Wiggert. The DHB problems are:

- DHB problem A: 20 m straight pipe with free massless valve.
- DHB problem B: 20 m straight pipe with fixed valve.
- DHB problem C: 330 m straight pipe with free massless valve.
- DHB problem D: 330 m L-shaped pipeline, free bend 20 m away from fixed valve.
- DHB problem E: 330 m L-shaped pipeline, fixed bend 20 m away from fixed valve.
- DHB problem F: 330 m system with four bends.

### 6.2.1. Delft hydraulic benchmark problems A and B

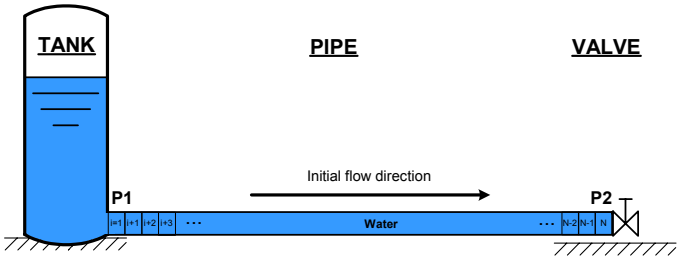


Fig. 23: Numerical model of the DHB problem A (valve is free) and B (valve is fixed).

*Table 11: Piping system and water properties for DHB problems A and B.*

| Piping system | Water |
|---|---|
| $L = 20$ m | $\rho_f = 1000$ kg/m$^3$ |
| $R = 0.3985$ m | $K = 2.1$ GPa |
| $e = 0.008$ m | $p = p_{tank} = 0$ bar |
| $E = 210$ GPa | $v = 1$ m/s |
| $\rho_t = 7900$ kg/m$^3$ | $T = 20$ °C |
| $\nu = 0.3$ | |

The DHB problems A and B refer to a simple straight tank-pipe-valve system depicted in Fig. 23. The pipe with properties described in Table 11 is filled with water at room temperature. The transient is initiated in the fluid by the instantaneous closure of the valve, which rapidly stops the steady-state water flow. The valve is massless and free for case A and fixed for case B. The results were obtained with application of the linear four-equation physical model for simulations of axial quasi-two-phase flow FSI coupling and are compared to the results obtained with the validated computer code of Tijsseling [113] **s1ax01**. The *s1ax01* is based upon a linear physical model with constant characteristics for axial FSI coupling and is solved with the method of characteristics (for details see Lavooij and Tijsseling [75], Wylie and Streeter [150], or Tijsseling [117, 113]). Recall that the method of characteristics (MOC) actually provides the analytical solutions of FSI problems based on several assumptions that have to be introduced into the physical model: the transient is single-phase, the pipe is uniform, straight, with constant material properties, the state properties of the fluid are constant, all parameters that introduce damping are eliminated, and the source terms are set to zero. These assumptions mean the linearization of the leading partial differential equations. In addition, Wylie and Streeter [150] stated that the numerical error of MOC is partly eliminated by initial tuning of (constant) densities to appropriately adjust wave speeds to conform into equidistantly spaced grid points in distance-time plane (Lavooij and Tijsseling [75, 117]).

To be comparable to the MOC results, all, although non-realistic assumptions were implemented into our physical model and consequently, all advantages of our approach were lost. However, the results enable a direct comparison between the method of characteristics and the characteristic upwind numerical method and thus the validation of the proposed numerical scheme. Figures 24 and 25 show the fluid pressure, the pipe axial force, and the pipe axial velocity histories obtained for the DHB problems A and B at position P2 that is located as close as possible to the valve. The simulation with both approaches yields practically the same results however, detail shows that the results obtained with the method of characteristics are slightly sharper. The differences are attributed to:

- **Numerical dissipation.** The numerical dissipation that comes with the characteristic upwind method smoothens the discontinuities in the results. The numerical dissipation cannot be

eliminated, but it can be minimized (the applied number of computational volumes $N = 400$, the optimal time step is reduced by factor $0.2$, and the Superbee limiter is applied). The amount of numerical dissipation contributes the largest part into differences between methods.

- **Position of the measurement.** The MOC gives values that are valid for a position exactly at the end of the pipe (point), while the characteristic upwind method, with computational volumes, gives an averaged value over the whole computational volume (volume average). The practical representation of the slightly shifted and averaged measuring position again reduces the sharpness of discontinuities, which is an effect similar to the numerical dissipation.

One can conclude that Figures 24 and 25 validate the characteristic upwind numerical method since the simulation perfectly matches the results obtained with the verified MOC method.

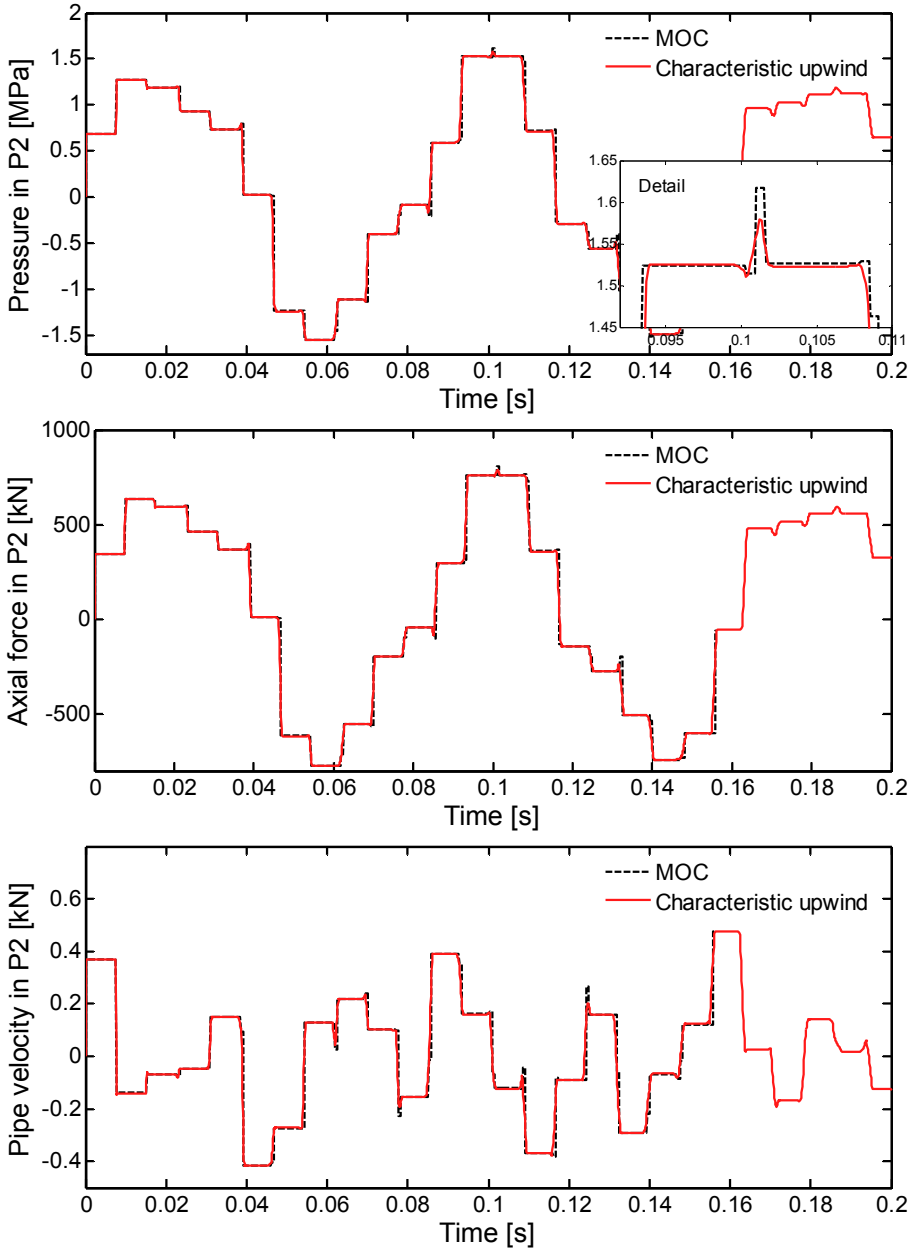


Fig. 24: DHB problem A: time history of basic variables at position P2.

Figure 26 shows the pressure history in P2 for the first 4 seconds of the transient without consideration of the damping. The results for the DHB problem B exhibit the secondary frequency of pressure oscillations, which appears due to the Poisson coupling mechanism of the FSI. It is also evident that the maximal pressure peak near the valve is not achieved immediately after the valve closure, but it appears as transient evolves. **The maximal pressure and therefore the maximal load of the fluid on the structure are not obtainable without appropriate FSI simulation.** It is necessary to stress, that

simulations were performed without consideration of any of the damping mechanisms. Damping in real experiments is always significant and affects the pressure history.

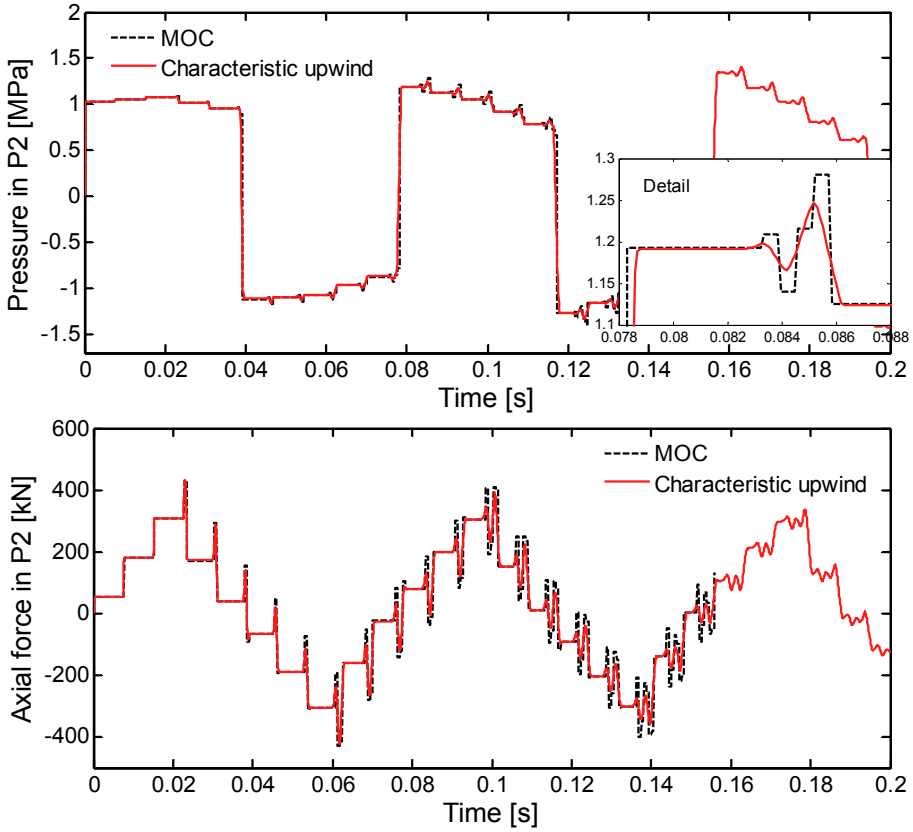


Fig. 25: DHB problem B – time history of basic variables at position P2.

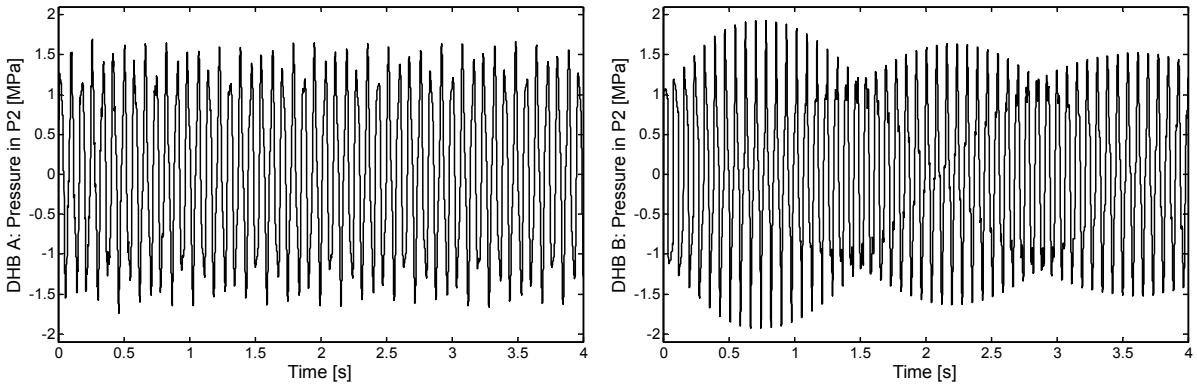


Fig. 26: DHB problems A and B – Pressure history in P2 for the first 4 seconds of the transient.

**Minimization of the numerical dissipation.** The numerical dissipation of the applied numerical method is relatively small and manageable i.e. it is possible to control the amount of the numerical dissipation by various parameters of the simulation. One of the possible mechanisms are slope limiters given in Section 5.3. Figures 27 and 28 show that each limiter has a different influence on the sharpness of the result. The sharpest results are obtained with the Superbee limiter, the most diffusive (smearest) solutions, but still 2$^{nd}$ order accurate, are obtained with the Minmod limiter, while the solutions with Van Leer and MC limiters lie between the sharpest and the smearest results. All results obtained with application of limiters are second order accurate on smooth solutions (see first order solution Figs. 27 and 28). The best results were obtained with the Superbee limiter but this limiter, especially in some more complex two-phase simulations, sometimes introduces nonstability into the simulation. The use of the Superbee limiter is recommended in single-phase flow but should be used with caution in two-phase flow.

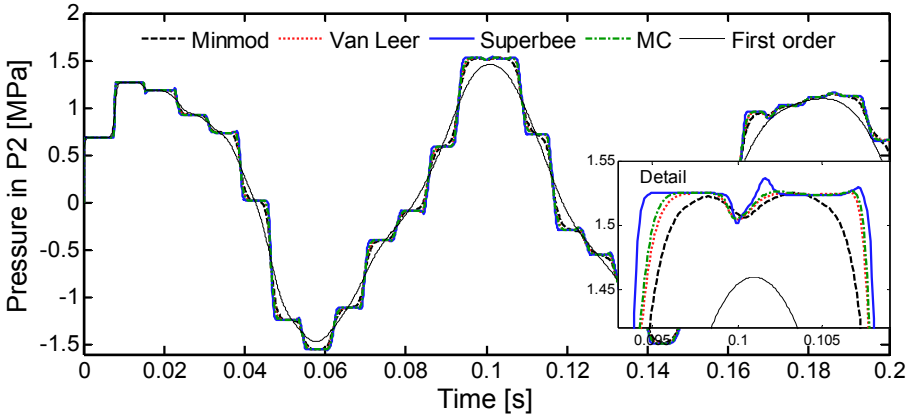


Fig. 27: DHB problem A: pressure time history in P2 with study slope limiters.

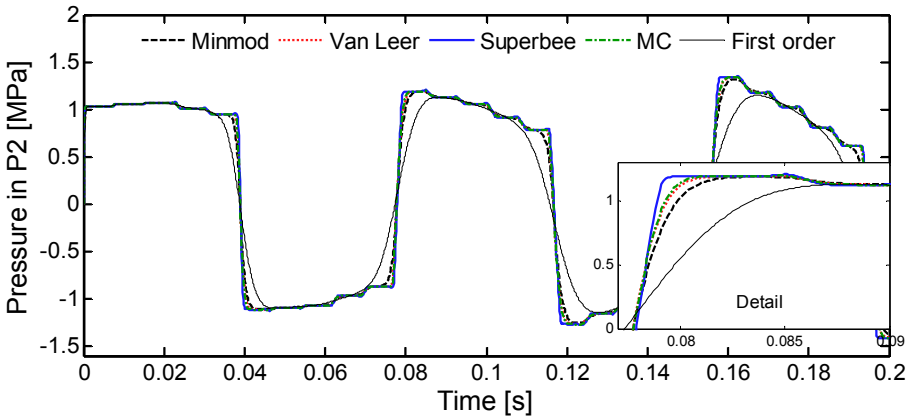


Fig. 28: DHB problem B: pressure time history in P2 with study of slope limiters.

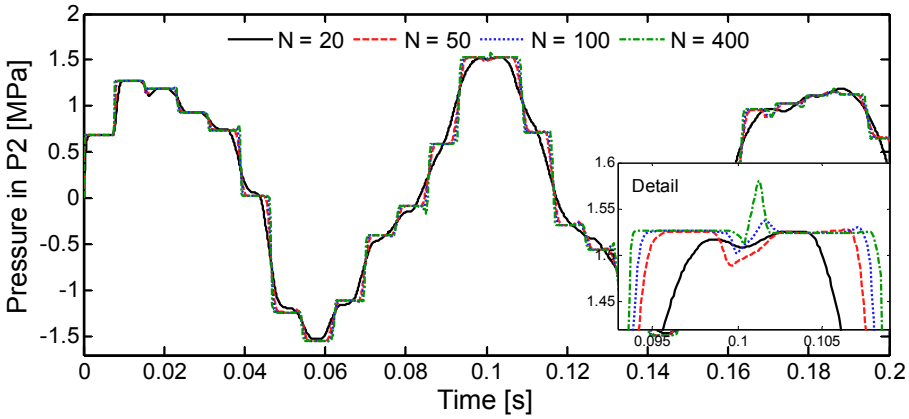


Fig. 29: DHB problem A: pressure time history in P2 with study of grid refinement.

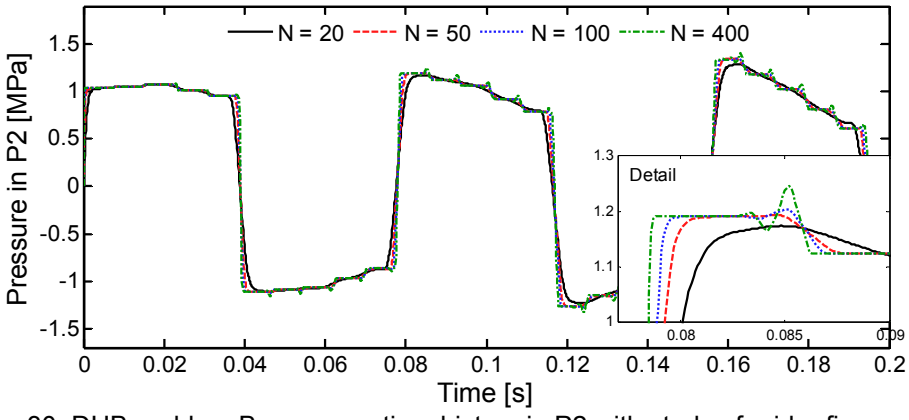


Fig. 30: DHB problem B: pressure time history in P2 with study of grid refinement.

The second mechanism that affects numerical dissipation is the nodalization of the computational domain. The importance of this mechanism is shown by a very trivial grid refinement study in Figs. 29 and 30. The sharpest results are obtained with *N = 400* computational volumes however, *N = 50* computational volumes are sufficient for fast and accurate simulation. The case with *50* computational volumes took one minute of calculation time on Pentium IV 3.0 GHz processor.

**FSI coupling mechanisms.** There are two major coupling mechanisms for the description of the FSI: the distributed Poisson coupling and the local junction coupling. Figures 31 and 32 show the importance of the coupling mechanisms, because both the Poisson and the junction coupling mechanisms must be accounted for accurate results. The valve in DHB problem B in Fig. 32 is fixed, which prevents junction coupling, thus the case "No Poisson coupling" is equal to the case "No FSI" (valid only for the straight pipe). The DHB problem A pressure history is equal to the DHB problem B pressure history if FSI is not considered. The simulation without the FSI is denominated as standard water hammer simulation, and rather simple box-like pressure histories near the valve are observed due to rapid valve closure (Figures 31, 32, and C-2) in non-cavitating flow. The standard water hammer pressure history at the valve and the first few moments in pressure history at the valve due to the junction coupling mechanism can be reconstructed with Joukowsky's equation, which defines the pressure rise/drop due to the disturbance in the flow velocity (see also Appendix C):

$$\Delta p = \rho_f c_f \Delta v_f \qquad \text{where} \qquad \Delta v_f = v_{f,before} - v_{f,after} \tag{232}$$

where $c_f$ is the speed of sound, $\rho_f$ is the density of the fluid, and $\Delta v_f$ is the flow velocity change with $v_{f,before}$ as the fluid velocity before and $v_{f,after}$ as the fluid velocity after the disturbance of the flow. Figures 31 and 32 show that for standard water hammer simulations without consideration of the FSI, the fluid velocity after the valve closure is zero ($v_{f,after} = 0$) and a typical box-like pressure history is obtained. The continuous (black) line on Figure 31 shows that with consideration of the FSI, just after the valve closure, the fluid pressure rise is smaller than for the no FSI case, while few milliseconds later, the continuous line increases above the standard solution (see the same effects in Figs. 13 and 36). The discrepancies from the standard solution are explained using Joukowsky's theory: at the beginning, the flow is not entirely stopped although the valve is closed, because the pipe starts to extend. Therefore, $v_{f,after} = u_x$, where $u_x$ is the axial velocity of the pipe (valve). Consequently, the pressure near the valve remains lower than that of the fixed valve. The induced axial stress wave travels along the pipe and reflects at the tank as discussed in Section 6.1. When the reflected stress wave reaches the valve again, the valve starts to move in the opposite direction with velocity $v_{f,after} = -u_x$, which corresponds to the case of reversed flow. The fluid is additionally compressed, and the pressure near the valve increases above the no FSI case. The initially simple FSI phenomenon becomes much more complicated as time evolves.

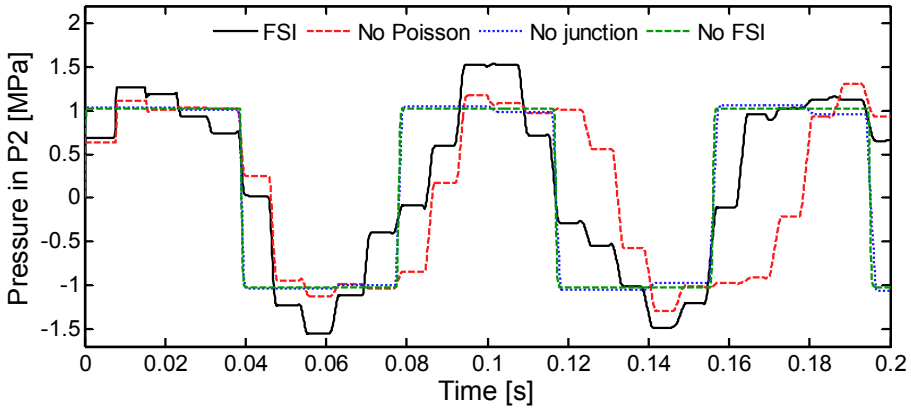


Fig. 31: DHB problem A: pressure time history with study of the FSI coupling mechanisms.

Figure 32 shows DHB case B with a fixed valve where only the Poisson coupling mechanism appears. The pressure gradually increases and later on decreases. This is the effect of the Poisson coupling mechanism. After the valve closure, the pressure rise through the Poisson coupling swells the cross-section of the pipe and generates a new stress wave. The stress wave that travels along the pipe

approximately three times faster than water hammer wave, swells the pipe cross-section and therefore reduces the pressure. This pressure reduction is known as precursor wave. The pressure reduction changes sign at the tank and becomes a pressure increase, and this can be observed on the pressure history near the valve. This effect becomes more intense as time evolves. It is possible to conclude that **simulations of an FSI are not possible without appropriate consideration of the Poisson and junction coupling mechanisms**.

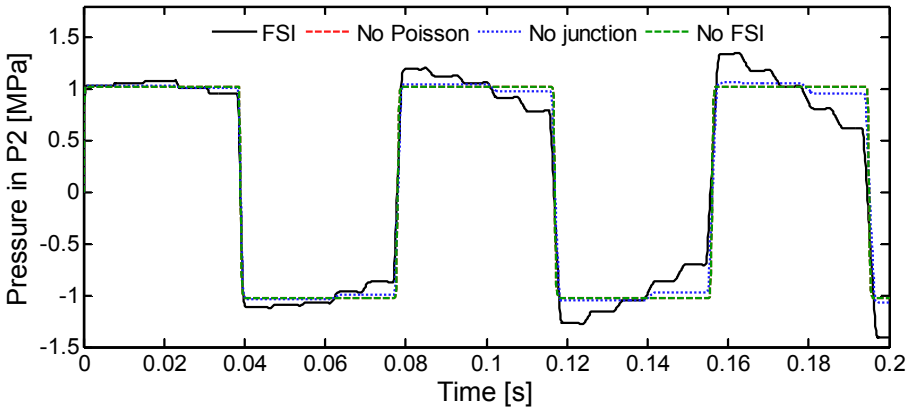


Fig. 32: DHB problem B: pressure time history with study of the FSI coupling mechanisms.

**Precursor and successor wave.** At the moment of the valve closure in the straight axial system, an axial stress wave and a pressure wave are generated that travel along the pipe at the corresponding characteristic velocity. The axial stress waves travel approximately 3 times faster than pressure waves, and due to the axial extension of the pipe, throughout Poisson effect, cause contraction of the pipe cross-section. Consequently, the pressure is raised. This pressure rise travels along the pipe with the same speed as the axial stress wave in the pipe, so it is faster than other pressure waves in the fluid. This pressure disturbance wave is known as the precursor wave, and can be observed as a small pressure disturbance that travels in front of the pressure wave in the fluid during the transient. It is most evident at the beginning of the FSI transient (Figure 33), while later on, the pressure longitudinal profile becomes rather complicated and the precursor waves are not traceable anymore. The precursor waves are very evident in DHB case B, where only Poisson coupling mechanism is considered. The less famous counterpart of the precursor wave can be observed in the axial force longitudinal cross-section. At the position of the pressure wave, a small disturbance in the axial force is evident. This disturbance appears because the pressure wave swells the pipe and the pipe starts to contract throughout the Poisson coupling mechanism. In analogy to the precursor wave, this wave can be denominated as a successor wave. The successor wave travels in the pipe wall with the characteristic velocity of the pressure waves in the fluid.

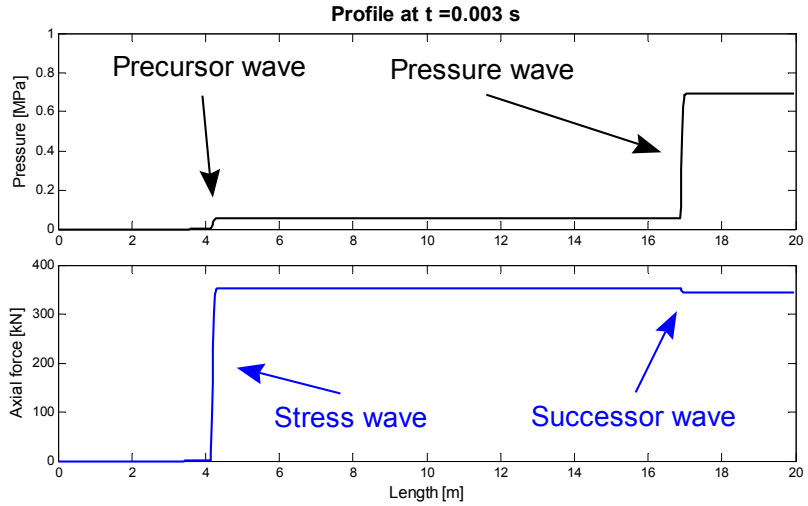


Fig. 33: DHB problem A: Pressure and axial force longitudinal profile at time *t = 3 ms* with indication of the precursor and successor wave.

Common characteristics of the precursor and successor waves are, that they are both observed in one medium, while they are a consequence of the transient in the other medium. The propagation velocity of the transient wave in the first medium is equal to the characteristic velocity of the transient in the second medium. **The precursor and successor waves can be described only with appropriate consideration of the Poisson coupling mechanism.**

### 6.2.2. Delft hydraulic benchmark problems C, D and E

The Delft hydraulic benchmark (DHB) problems C, D and E are an extension of the DHB problems A and B. The piping system is longer, and it contains an additional 90° elbow in cases D and E. The material properties are collected in Table 12, the geometrical model for DHB problem C is sketched in Fig. 34 and the model for DHB problems D and E is sketched in Fig. 35. The DHB problems D and E are similar except the elbow that is located 20 meter away from the valve is not supported in case D, while it is fixed in case E. The valve is massless and free for case C and fixed for cases D and E. The piping system is initially filled with water at room temperature. The transient is initiated at time zero when the valve is instantaneously closed and the steady-state water flow is stopped. The flow is single-phase. The fluid thermodynamic state properties are assumed constant. The simulations were performed with the eight-equation linear quasi-two-phase flow model for FSI in arbitrarily shaped planar piping systems.

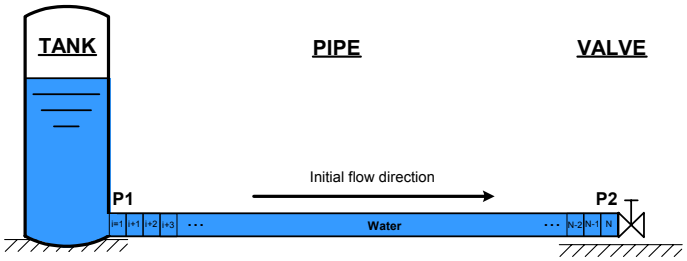


Fig. 34: Numerical model of the DHB problem C.

*Table 12: Piping system and water properties for DHB problems C, D and E.*

| Piping system | Water |
|---|---|
| $L = 330$ m | $\rho_f = 880$ kg/m$^3$ |
| $R = 0.1032$ m | $K = 1.55$ GPa |
| $e = 0.00635$ m | $p = p_{tank} = 0$ bar |
| $E = 210$ GPa | $v = 4$ m/s |
| $\rho_t = 7900$ kg/m$^3$ | $T = 20$ °C |
| $\nu = 0.3$ | |

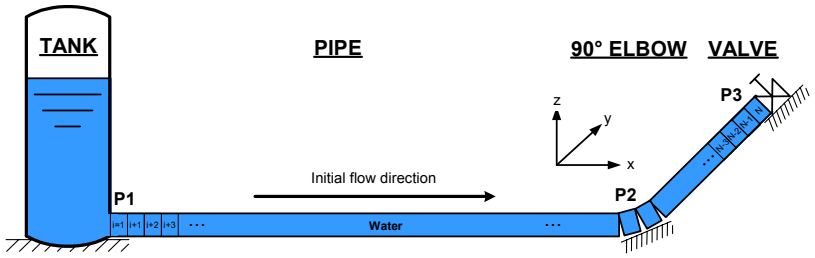


Fig. 35: Numerical model of the DHB problem D (**free** elbow 20 m away from the fixed valve) and E (**fixed** elbow 20 m away from the fixed valve).

The results for the DHB problem C obtained with the simulations are compared to the results obtained with the verified computer code **s1ax01** of Tijsseling [113, 117]. The physical model and assumptions applied in our code have been defined in a way to enable direct comparison of numerical methods (MOC vs. Characteristic upwind) without additional influences. The difference compared to the analysis of Section 6.2.1 is that eight-equation model is applied. Figure 36 shows some most important basic variables and comparisons to the results of the MOC. Numerical dissipation and non-equal measuring position contribute to some small discrepancies. However, the agreement between simulation with our code and verified MOC is perfect, which again, validates the application of the high resolution characteristic upwind numerical method.

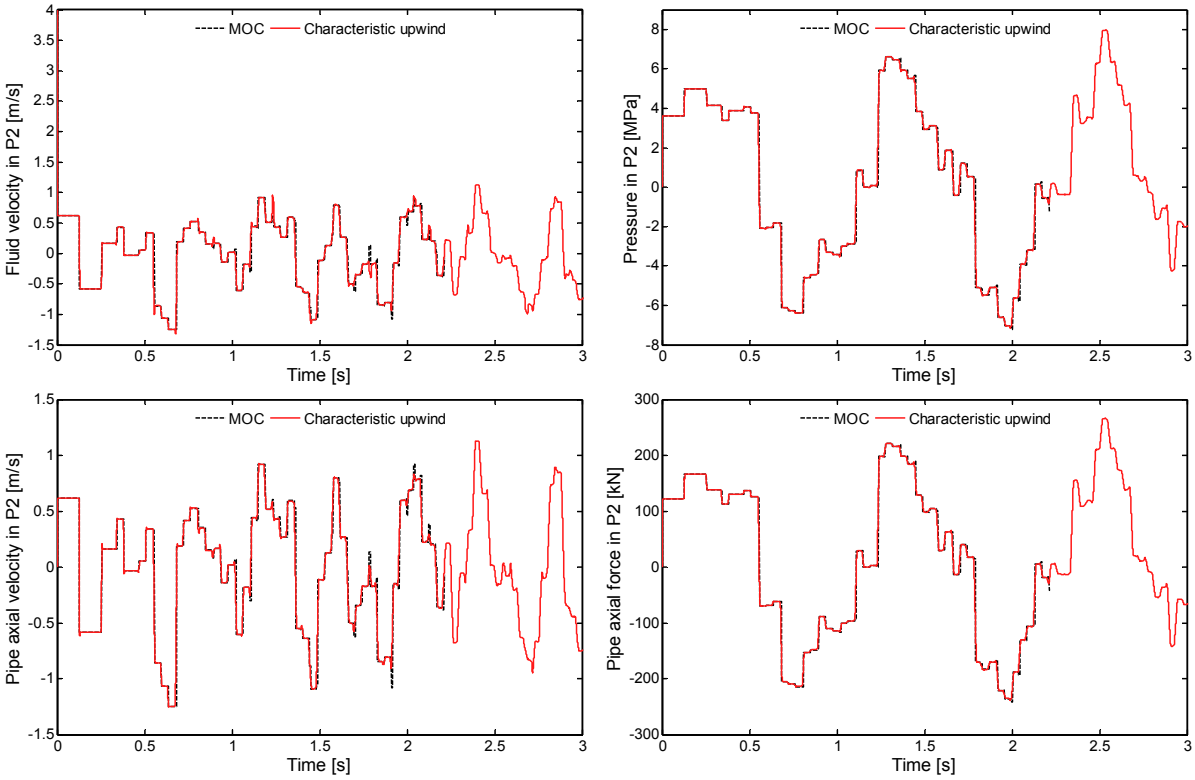


Fig. 36: DHB problem C: History of basic variables in position P2 – comparison between MOC and characteristic upwind numerical method.

**Junction coupling at valve.** Figure 37 shows a comparison for three variations of the DHB problem C precisely, the no FSI case is compared to the case with fixed valve (Poisson coupling mechanism only) and the case with free valve (Poisson and junction coupling mechanisms). Figure 37 shows that significantly higher pressures in the considered transient were recorded for the case with free valve, which means that the junction coupling mechanism at the valve plays a very important role. This confirms the generally accepted rule, which states that FSI is more intense in weakly or wrongly supported piping systems. It is possible to conclude that **fast operating valves should be adequately supported** in order to minimize FSI and transfer of energy from the pipe into the fluid.

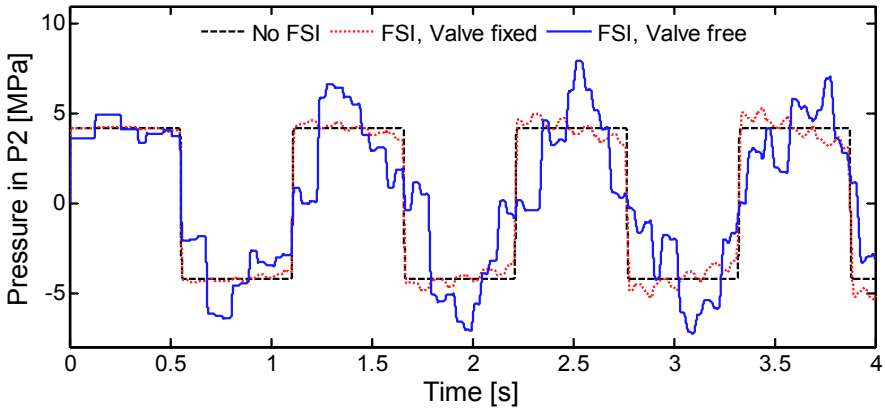


Fig. 37: Comparison of pressure histories in straight pipe (DHB C) near the valve for cases without FSI, with FSI with fixed valve and with FSI with free valve.

**Junction coupling at an elbow.** The simulation results of the DHB problems D (elbow is free) and E (elbow is fixed) are compared with the results of the simulation of the DHB problem C (straight pipe). Figure 38 shows the pressure histories close to the valve. The valve is fixed and closed instantaneously in all considered cases. It is possible to see that the highest pressure peaks (more than 50% higher)

were obtained for the case where the elbow was free. This again confirms the general rule, which states that the piping system has to be sufficiently supported to prevent development of the FSI coupling. **Every elbow of the piping system has to be adequately supported.** Comparison of the case with straight pipe and pipe with fixed elbow gives another interesting conclusion: the pressure history for case with fixed elbow (DHB problem E) is essentially the same as the pressure history for the case with straight pipe (DHB problem C, fixed valve). We can conclude that during the FSI pipe transient the **piping system with fixed elbows behaves similarly as the straight piping system**.

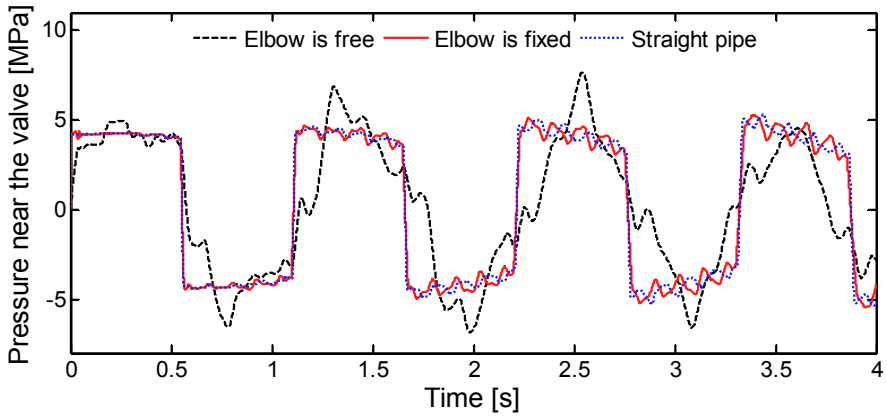


Fig. 38: Comparison of pressure histories in position as close as possible to the valve for cases with free and fixed elbow (DHB D & E) and for case without elbow (DHB C).

Elbows are one of the most common parts of the piping systems, and simulations (and experiences) show that they should be adequately supported. Of course, this is not a trivial task. In the piping systems of a nuclear power plant for example, the thermal extensions of the primary coolant loop piping system lead to up to 20 centimeter extensions/contractions. Fixed supports would impose gigantic loads. The general solution was found in **snubbers** (mechanical shock arrestors). The snubber allows thermal displacements with velocities lower than threshold velocity (few cm/s), during the water hammer transient occurrences (or plant transients, earthquakes, etc.), velocities of displacements increase over the threshold and the snubber blocks any movement. For example there are approximately 2300 snubbers mounted to support various piping systems in nuclear power plant Krško.

## 6.3. Valve closure experiment in single elbow pipe

Simpson [103] in 1986 conducted a series of 9 experiments during his Ph.D. research where he experimentally and numerically studied cavitation in single-elbow piping system. The valve closure experiment in the single elbow pipe, also known as Simpson's pipe column separation water hammer experiment [103], became one of the fundamental benchmarks for two-phase flow computer codes because of the simple geometry, initial conditions and clear water hammer initiating mechanism. The valve closure experiment in the single elbow pipe was applied in this dissertation for verification of the quasi-two-phase flow model and to study the influence of the FSI on two-phase flow transients. The simulated results were obtained with the eight-equation quasi-two-phase flow physical model for FSI in planar arbitrarily shaped piping systems, which was solved with the characteristic upwind numerical method. The quasi-two-phase flow model was applied for simulation of the column separation. The results of the simulations were compared to the experimental measurements.

Simpson varied the initial velocity of the steady state fluid to affect the appearance of the two-phase flow and the severity of the water hammer and cavitation. The other initial parameters were held as constant as possible during the execution of the experiments. The matrix with initial conditions for various experiments is presented in Table 13. The transient in initially steady state tank-pipe-valve system (Fig. 40) is induced by instantaneous ball valve closure. The ball valve is closed by hand to avoid the amount of pipe movement and vibration resulting from the fast closure of the valve. The hand operation of the valve leads to longer closing times and smooth and non-standard flow diminishing functions of the ball valve. For the simulation of all experiments we assumed that the fluid temperature is $T_f = 297\ K$, the

valve closing function is defined by Eq. (228), and the applied uniform valve closing time is $t_c$ = *10 ms*. The piping system in Fig. 40 is *36* meters long with one *90°* elbow at *12.5* meter, and the section from *12.5* to *36* meters is slightly inclined ($\gamma$ = *2.44°*). The experimental apparatus is fixed with brackets to the wall at approximately *2.5* meters interval and at additional three points: at the tank, at the elbow and at the valve. Simpson [103] claims that two brackets rigidly support the elbow and any movement of the elbow during the transient is expected to be negligible. Because of the fixed supports that are located at the crucial parts of the piping system, it is expected that the junction coupling FSI mechanism will be negligible.

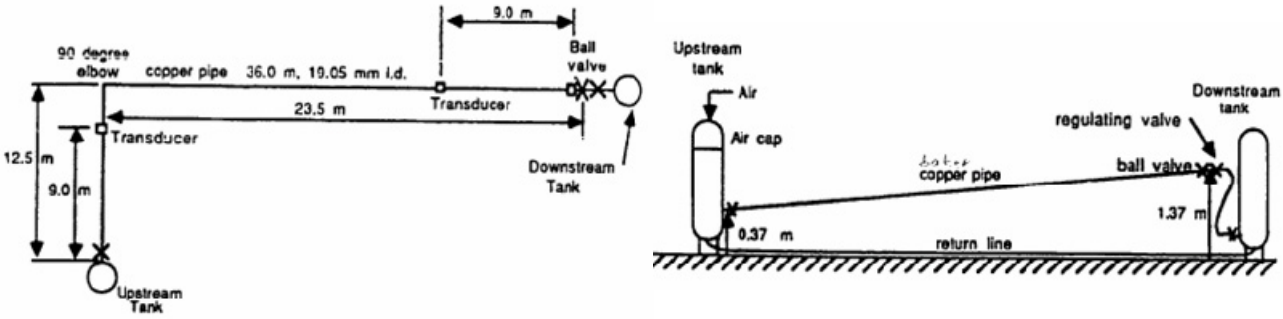


Fig. 39: Plane (left) and side (right) schematic view (not to scale) of experimental apparatus of the valve closure experiment in the single elbow pipe [103].

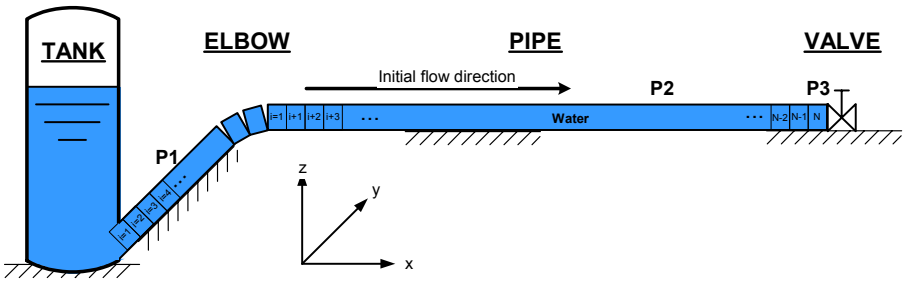


Fig. 40: Numerical model for experimental apparatus of the valve closure experiment in the single elbow pipe.

*Table 13: Matrix of initial conditions for experimental runs.*

| Label | Fluid velocity [m/s] | Tank and pipe pressure [bar] | Valve closing time [ms] | Fluid temperature [K] | Wall friction coeff. | Cavitation |
|---|---|---|---|---|---|---|
| Exp 1 | 0.239 | 3.369 | 29 | 297.1 | 0.0325 | No |
| Exp 2 | 0.332 | 3.281 | 35 | 297.6 | 0.0315 | Yes |
| Exp 3 | 0.401 | 3.281 | 17 | 296.5 | 0.0290 | Yes |
| Exp 4 | 0.466 | 3.259 | 34 | 296.5 | 0.0280 | Yes |
| Exp 5 | 0.507 | 3.244 | 25 | 296.5 | 0.0280 | Yes |
| Exp 6 | 0.596 | 3.265 | 29 | 297.1 | 0.0270 | Yes |
| Exp 7 | 0.696 | 3.233 | 25 | 297.1 | 0.0260 | Yes |
| Exp 8 | 0.938 | 3.196 | 35 | 297.1 | 0.0240 | Yes |
| Exp 9 | 1.125 | 3.118 | 43 | 297.1 | 0.0230 | Yes |

*Table 14: Material properties of experimental apparatus ($T_f$ = 297 °K).*

| Material | Elasticity modulus [Pa] | Poisson ratio | Density [kg/m$^3$] | Inner pipe radius [m] | Pipe wall thickness [m] | Effective speed of sound in fluid [m/s] |
|---|---|---|---|---|---|---|
| Copper | 1.19E11 | 0.34 | 8920 | 9.525E-3 | 1.588E-3 | 1355 |
| Alloy | 0.75E11 | 0.25 | | | | 1280 |

The material properties of the piping system are described in Table 14. Simpson [103, p.97] stated that the applied pipe was made of copper and consideration of the copper material properties and pipe geometry properties results in the following effective speed of sound in fluid: $c_f$ = *1355 m/s*. Simpson performed a spectral analysis of all experimental data and as a result he obtained an effective speed of sound equal to $c_{f,real}$ = *1280 m/s*, which was actually applied in his numerical studies. Simpson didn't give any explanation for the discrepancy between the real and theoretical values for effective speed of sound. Kovač [71] showed that the Young modulus and other material properties depend on orientation of the crystals and therefore properties of a monocrystal material significantly changes compared to a policrystal material. It is possible that orientation of the copper crystals was affected during the manufacturing of the pipe. Another possible reason can be, if instead of the pure copper, a copper alloy was used as pipe material. Simulations showed that the properties for the undefined alloy give very good agreement with the experimental results. The alloy elasticity modulus was calculated backwards from the Korteweg's equation (D-9), and the Poisson ratio was estimated based on comparisons between the experiment and simulation. A material with such properties was not found in the literature; we will denominate it in this dissertation as Alloy.

The fluid pressure was measured along the pipe at three positions that are described in Table 15. In addition, the pressure in the tank was measured (manually) with a Mercury manometer. Other variables were not measured.

*Table 15: Position of the measuring equipment and elbow.*

| Label | Position [m] | Volume No. | Variable | Equipment |
|---|---|---|---|---|
| Tank | 0.00 | 0 | Pressure | Mercury manometer |
| P1 | 9.00 | 25 | Pressure | Pressure transducer |
| Elbow | 12.50 | 35 | | |
| P2 | 27.00 | 75 | Pressure | Pressure transducer |
| P3 | 36.00 | 100 | Pressure | Pressure transducer |

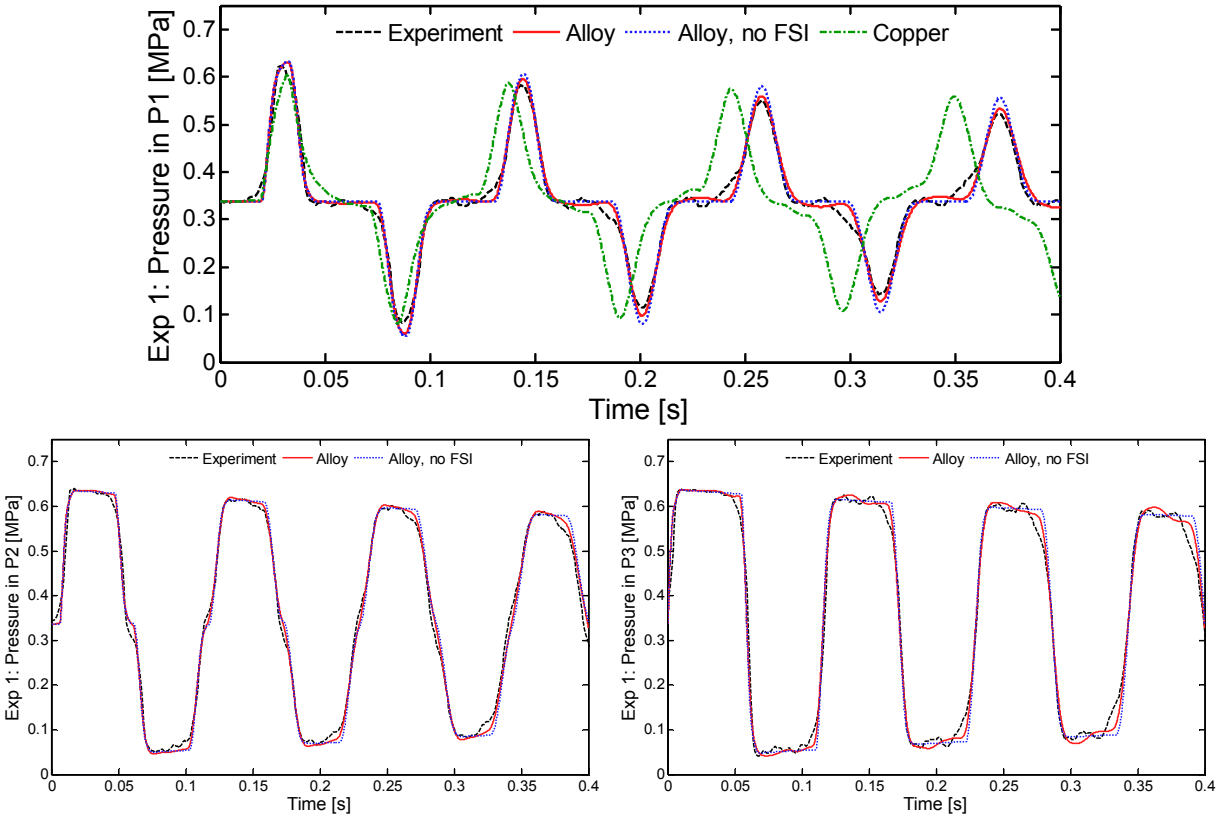


Fig. 41: Pressure history at positions P1, P2 and P3 for single-phase Exp 1. Comparison between experiment and simulation with consideration of the Copper or Alloy material properties.

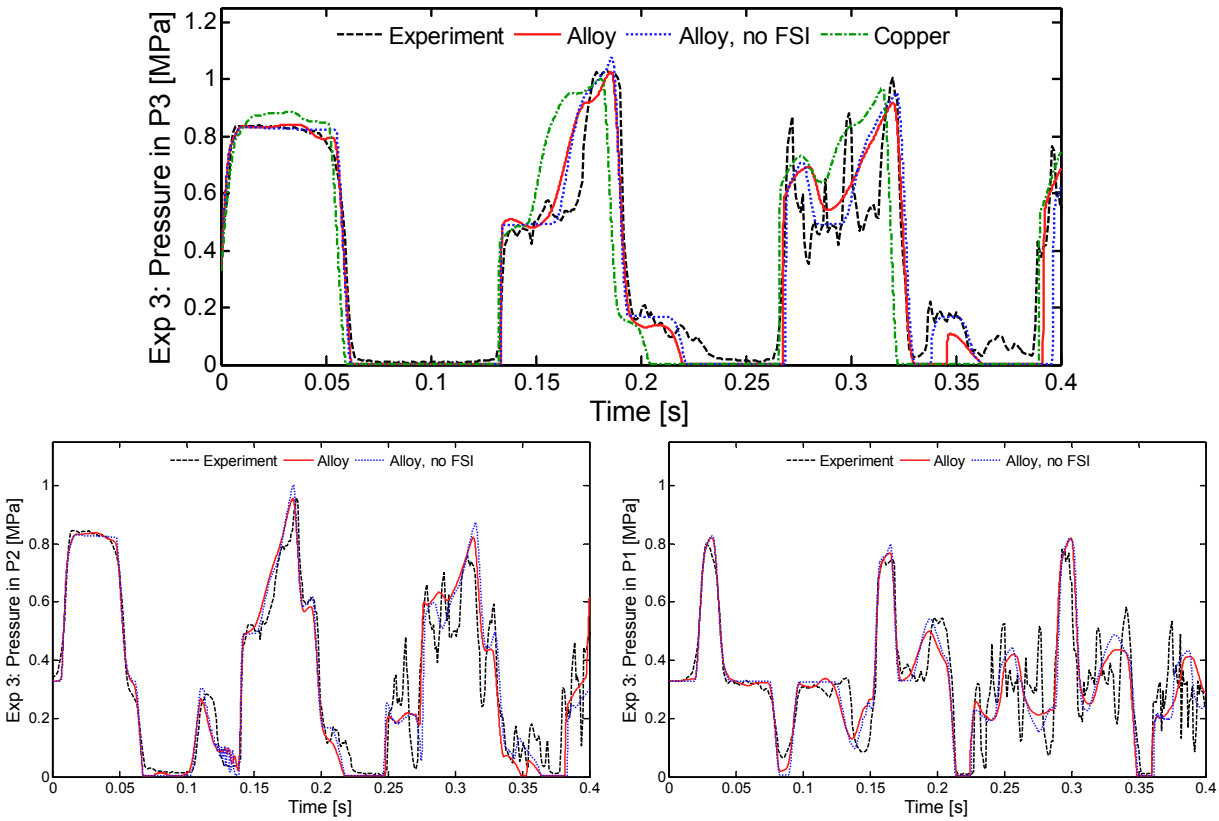


Fig. 42: Pressure history at positions P1, P2 and P3 for moderate cavitation Exp 3. Comparison between experiment and simulation with consideration of the Copper or Alloy material properties.

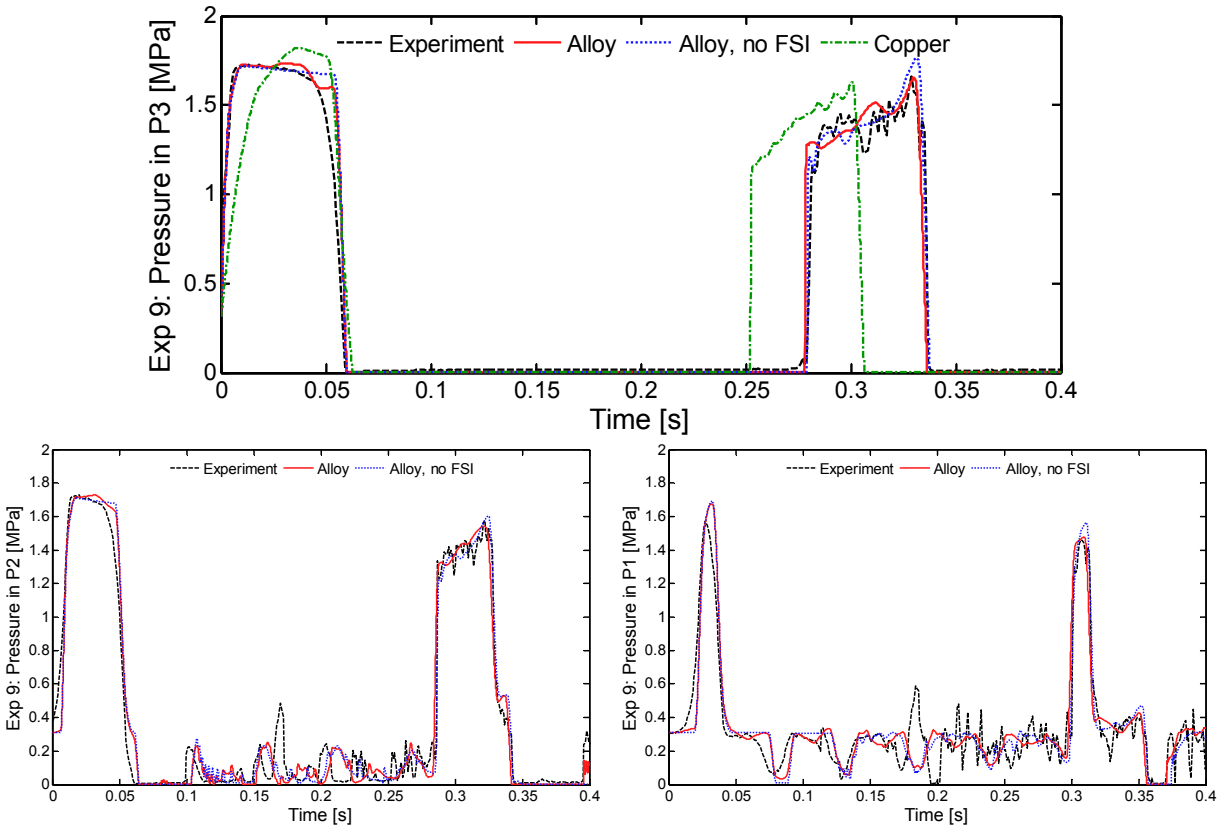


Fig. 43: Pressure history at positions P1, P2 and P3 for severe cavitation Exp 9. Comparison between experiment and simulation with consideration of the Copper or Alloy material properties.

Figures 41, 42, and 43 show a pressure history comparison between the simulation and the measurement at various locations along the pipe, for three representative experiments (Single phase experiment Exp 1, experiment Exp 3 with moderate cavitation and experiment Exp 9 with severe cavitation). The continuous (red) line was obtained with the assumption of the alloy material properties (Table 14), the dotted (blue) line stands for default copper material properties, and the dash-dotted (green) line stands for Alloy but without consideration of the FSI coupling mechanisms. The simulation with imaginary Alloy material properties perfectly match with the experiment in all cases. It is also possible to see, that the results for Alloy with and without consideration of the FSI are almost identical. This points to the fact, that sufficiently supported piping system, like Simpson pipe is, prevents junction coupling FSI during the column separation water hammer transient. The pipe has a small cross-section and a relatively small radius over thickness ratio ($R/e = 5.9$) and consequently the Poisson coupling is present but it is so weak, that it can be easily neglected. The simulations show that **the influence of the FSI coupling is negligible for the Simpson pipe experiment**. These findings are further supported by Figures from 44 to 47.

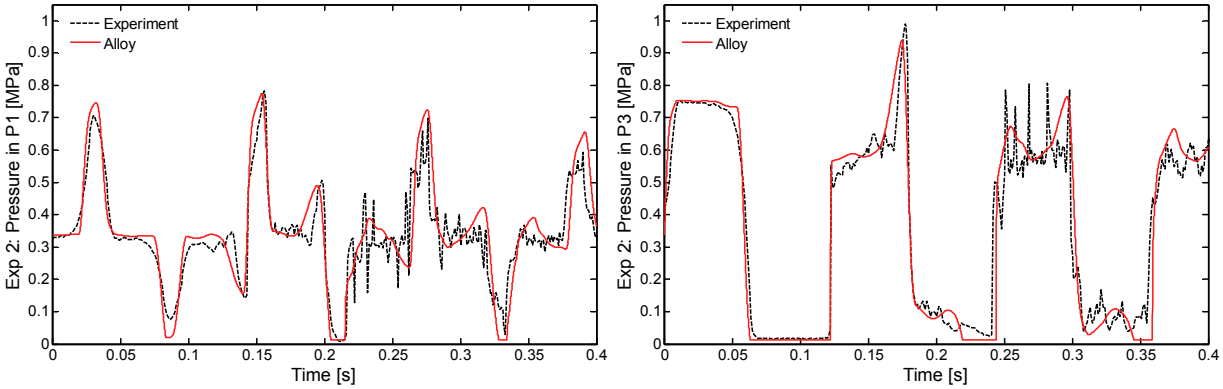


Fig. 44: Pressure history at positions P1 and P3 for Exp 2.

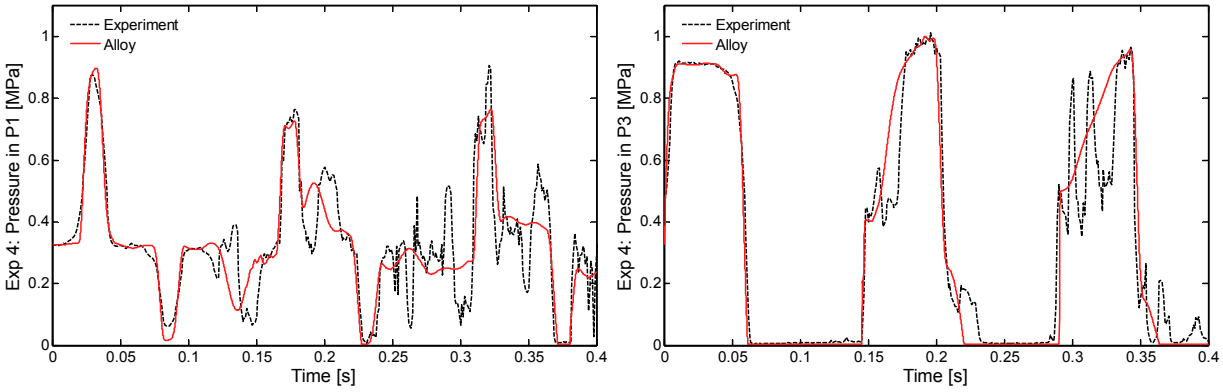


Fig. 45: Pressure history at positions P1 and P3 for Exp 4.

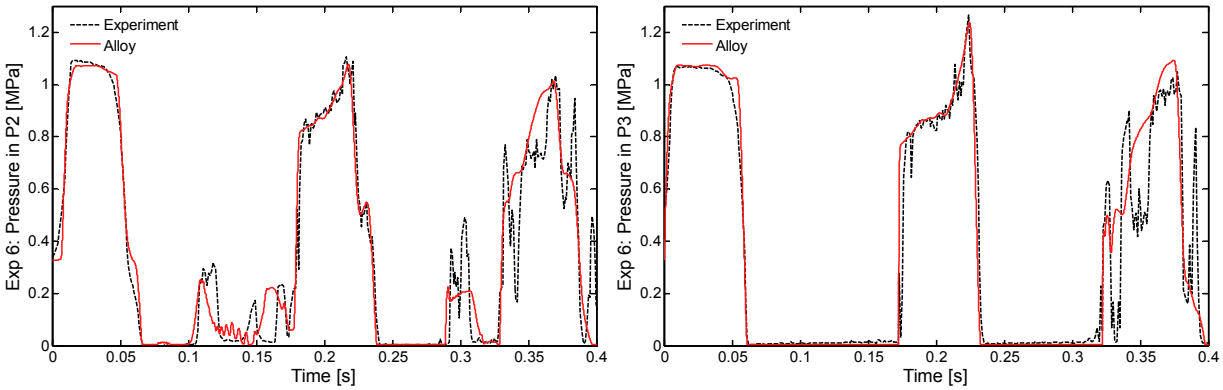


Fig. 46: Pressure history at positions P2 and P3 for Exp 6.

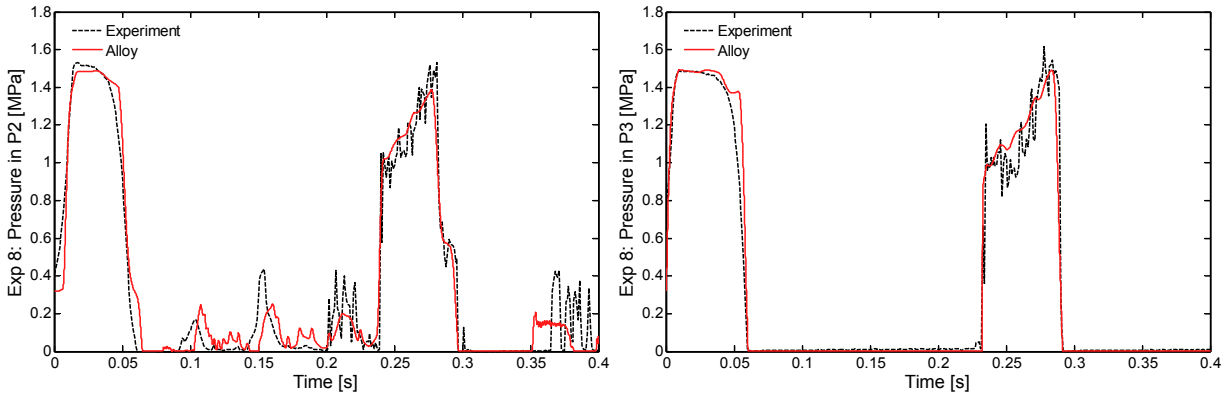


Fig. 47: Pressure history at positions P2 and P3 for Exp 8.

**Quasi-two-phase flow model.** Gale and Tiselj [43] described their simulations of the Simpson's pipe experiment with the six-equation two-fluid WAHA code (Tiselj et al. [126]) and showed that one does not need a complete two-fluid model for successful simulation of the column separation water hammer. Especially at low temperatures, flashing and condensation of the steam are not governed by the heat and mass transfer between the phases, but by dynamics of the liquid column. Thus, modeling of the transient in water at room temperature usually does not require energy equations (Bergant et al. [12]) and simplified cavitation models can be applied.

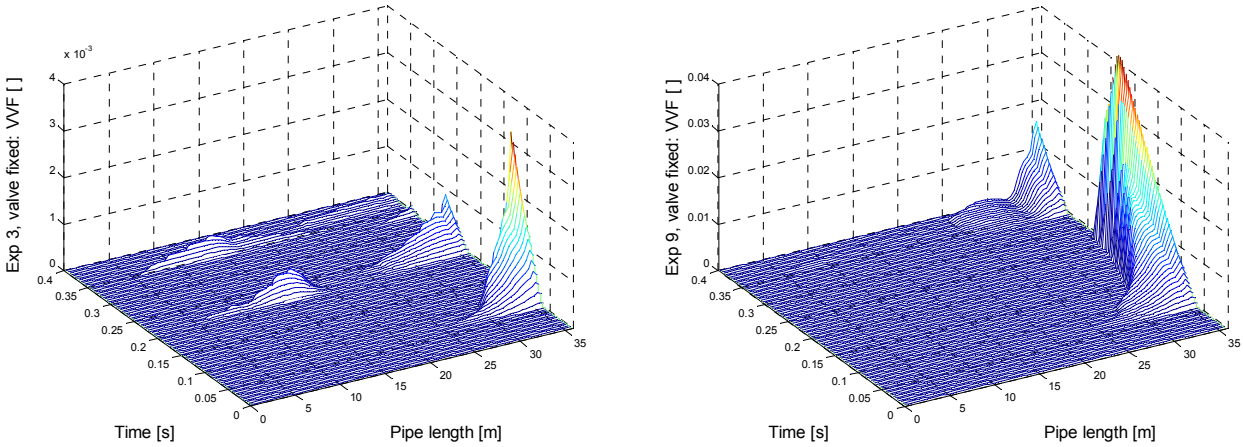


Fig. 48: Vapor volume fraction in time-space plane for the case with fixed valve (Exp 3 and 9).

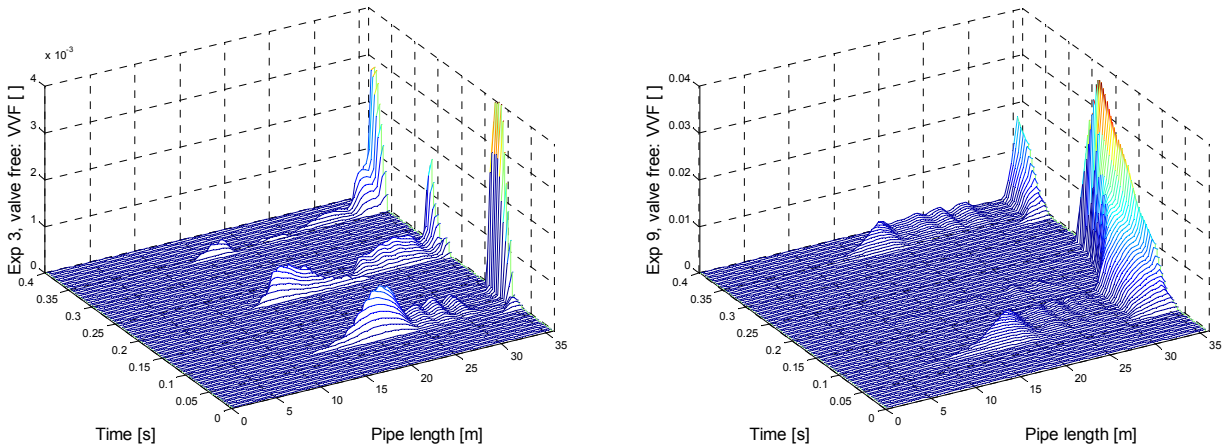


Fig. 49: Vapor volume fraction in time-space plane for the case with free valve – with FSI (Exp 3 and 9).

Figures from 41 to 47 show and validate at the same time, that a relatively **simple quasi-two-phase flow model describes the column separation type of the two-phase flow in water at room temperature with great accuracy**. The duration of the cavitating flow in pressure history is exactly simulated, while it cannot be anticipated, that simulation will catch all small disturbances in a measured pressure history. Figure 48 shows the distribution of the vapor volume fraction in the time-space plane for two cases: moderate cavitation (Exp 3) and severe cavitation (Exp 9). In both cases, the initial cavitating area extends over larger sections of the pipe and later on appears also in the middle of the pipe. Figure 50 shows the vapor volume fraction (VVF) history in the closest volume to the valve. The growth of the vapor bubble is made up of two phases: the first phase where the vapor bubble grows and the second phase, shorter, where the vapor bubble collapses. The simulation shows that the length of the cavitation phase, vapor generation gradient, and amount of the generated vapor linearly depend on the initial fluid velocity. This is actually a property of the chosen quasi-two-phase flow model. The variable initial fluid velocity in lesser extent influences the length of the cavitating area and to a larger extent influences the amount of the generated vapor. The total amount of the vapor is exactly predicted with our code, while it is difficult to discuss or validate the distribution of the vapor without comparison to the experiment.

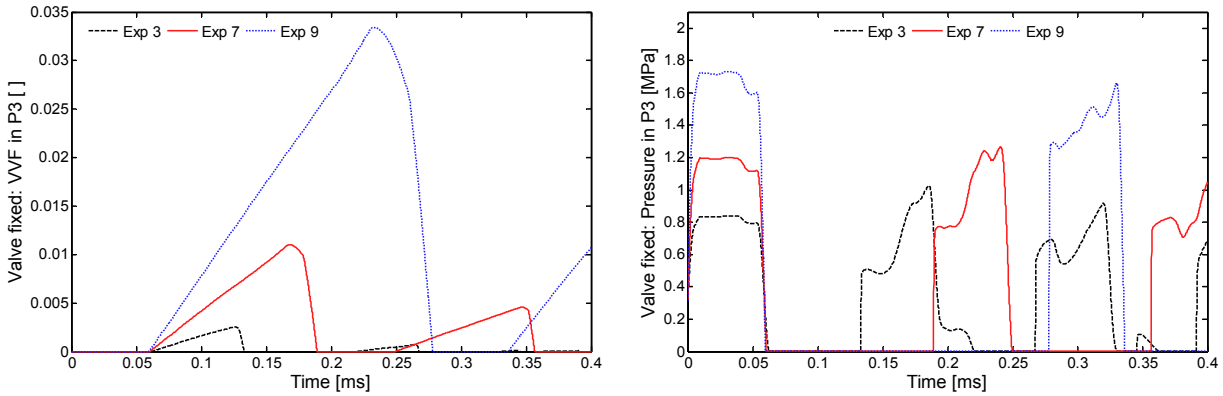


Fig. 50: VVF and pressure history at position P3 for the case with fixed valve.

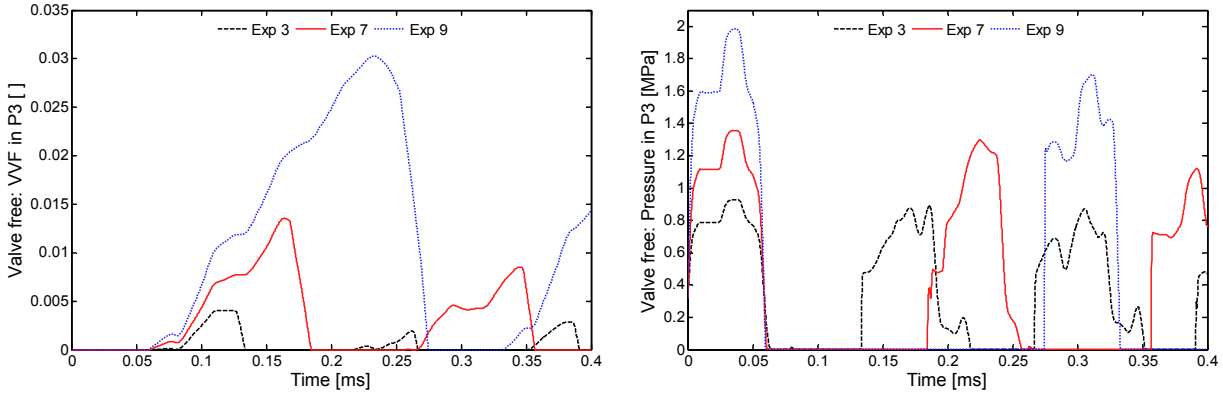


Fig. 51: VVF and pressure history at position P3 for the case with free valve – with FSI.

**FSI coupling mechanisms and cavitation.** The Simpson pipe experimental apparatus is relatively strongly supported and thus enables only development of the Poisson coupling FSI mechanism. To include the junction coupling mechanism into the transient, the simulations were repeated with a free valve and released supports in the axial direction. The results with the free valve and the junction coupling are presented in Figures 49 and 51 and some interesting differences in histories of basic variables can be found. Figure 51 shows that junction coupling affects the vapor generation rate. The vapor is generated faster or slower depending on the relative velocity between the pipe (valve) and the fluid. Figures 48 and 49 show the vapor volume fraction in the time-space plane. The vapor is distributed along larger sections of the pipe for the cases with the free valve than for the cases with a fixed valve, especially at the beginning of the transient pipe flow. The reason for the appearance of the additional distributed cavitation is FSI coupling, namely, significant axial stresses are generated at the valve through junction coupling, and as stress waves travel along the pipe, through Poisson coupling

generates additional pressure waves in the fluid denoted precursor waves. The precursor waves are added to the basic pressure waves and in case that two 'negative' waves are added, the pressure may occasionally drop below saturation and the cavitation starts. Tijsseling [113] denoted this type of cavitation as the **Poisson coupling induced cavitation**. As distributed cavitation may appear anywhere along the pipe according to the pressure profile, the Poisson coupling induced cavitation appears only as a consequence of the (negative) precursor waves. As time evolves, cavitation generates more and more pressure waves that travel along the piping system and add to the complexity of the pressure profile. In such cases, the precursor waves become more and more hidden and less important. Therefore, the Poisson coupling induced cavitation can be detected probably only at the beginning of the transient.

## 6.4. Rod impact experiments in hanging piping systems

Vardy and Fan [132] studied Fluid-Structure Interaction without cavitation in liquid-filled piping systems. An extensive series of high-quality measurements was carried out on four different piping systems in a test rig built in the Hydraulics Laboratory at the University of Dundee (UK). The interaction between the fluid and the structure in these piping systems is very strong. The piping systems are suspended by long, thin, vertical steel wires from the ceiling, and can move freely in a nearly horizontal plane. All piping systems are filled with pressurized tap water. The impact rod is used to simultaneously initiate stress waves in the pipe wall and pressure waves in the water by the axial impact of the rod on the left free end of the piping system. The experiments on the wired piping systems were carried out with intention to reduce all influences of the complex initial and boundary conditions, which usually affect the transient. The hanging experimental apparatus actually isolates the effects of the fluid-structure interaction in the case of axial wave propagation. Compared to the standard tank-pipe-valve system, the following unwanted influences were eliminated:

- Influence of the initial steady-state distribution of the fluid properties (pressure, temperature, velocity, density, etc.).
- Influence of the closing valve (closing time, closing function, induced vibrations).
- Influence of the boundary conditions and supports of the piping system.

Therefore, the only measured input in the simulation is the impact rod velocity that is theoretically equal to (with very small deviation in practice):

$$v_{0,rod} = \sqrt{2gh_{rod}} \tag{233}$$

where $h_{rod}$ is the elevation of the rod in raised position.

In his dissertation, Tijsseling [113] studied the cavitation and developed a computer code based on the method of characteristics for simulations of cavitation during FSI occurrence. At the test rig of Vardy and Fan [132] in the Hydraulics Laboratory at the University of Dundee, Tijsseling performed an additional set of experiments with reduced initial pressure in the piping system and thus included cavitation. Tijsseling [39, 113] stated that, at the time of his investigation, the FSI experiments with cavitation were the only well-documented experiments in which FSI and cavitation occur simultaneously and are both significant. Tijsseling provided several experimental data measured during a two-phase rod impact experiment and published them at his web site dedicated to the FSI phenomenon (www.win.tue.nl/fsi/). These experiments quickly became fundamental benchmarks for the FSI two-phase flow codes. The single-phase rod impact experiment in a straight pipe performed by Vardy and Fan and the two-phase flow rod impact experiment in a single elbow pipe performed by Tijsseling are simulated and discussed in the following subsections of this Section.

### 6.4.1. Rod impact experiment in a straight pipe

The rod impact experiment in the straight piping system consists of a stainless steel pipe closed at both ends with an end plug and an end cap (mass $m_1$ and $m_2$). The piping system presented in Figure 52 is filled with pressurized tap water and suspended by two long (about *3.3 m*) thin, vertical steel wires from the ceiling. The impact rod is used to simultaneously initiate a transient by the axial impact of the rod on

the left free end of the piping system. The impact rod and the piping system are separated when the contact force becomes tensile, which happens *2* milliseconds after the strike. The material properties and the initial conditions of the considered piping system, water and impact rod are collected in Table 16. Friction and gravity effects are unimportant and were not considered. The measured initial flexure of the pipe caused by its weight is less than *0.2 mm* relative to the suspension points, which are situated about *0.95 m* from the pipe ends. The experiment was simulated with the four-equation axial quasi-two-phase flow FSI coupling model.

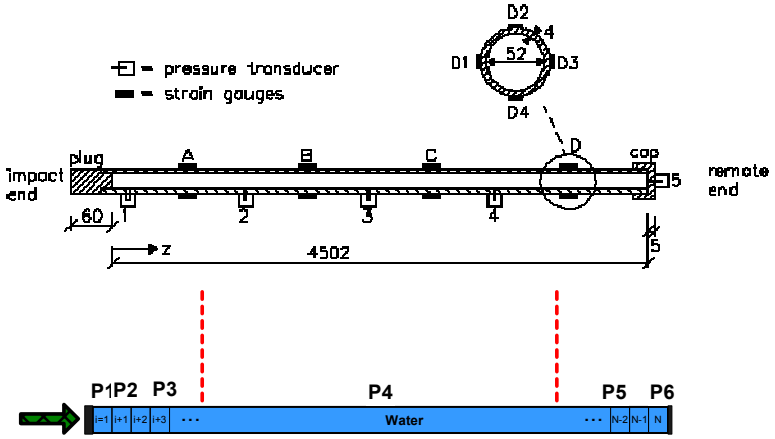


Fig. 52: Sketch of experimental apparatus of the rod impact experiment from Tijsseling [113] (above), and nodalization of the piping system for simulation (below).

Vardy and Fan [132] actually performed several single-phase experiments with variable initial pressure and velocity of the impact rod. The pipe in the considered experiment is pressurized with an initial pressure $p = 20$ *bar*, which is sufficiently high to prevent cavitation during the transient. Wiggert and Tijsseling [144] stressed that the underlying theory is almost linear for single-phase transients, thus, pressure, velocities and strains are linearly proportional to the impact velocity of the rod. The comparison of the measurement and simulation for one particular impact velocity are considered to be sufficient due to linearity.

*Table 16: Material and state properties of the piping system, water and impact rod.*

| Piping system | Water | Impact rod |
|---|---|---|
| $L = 4.502$ *m* | $\rho_f = 999$ *kg/m*$^3$ | $L_{rod} = 5.006$ *m* |
| $R = 0.02601$ *m* | $K = 2.14$ *GPa* | $R_{rod} = 0.02537$ *m* |
| $e = 0.003945$ *m* | $p = 20$ *bar* | $E_{rod} = 200$ *GPa* |
| $E = 168$ *GPa* | $v = 0$ *m/s* | $\rho_{rod} = 7848$ *kg/m*$^3$ |
| $\rho_t = 7985$ *kg/m*$^3$ | $T = 20$ °*C* | $v_{0,rod} = 0.739$ *m/s* |
| $\nu = 0.29$ | | $Y_{rod} = 80109.7$ *kg/s* |
| $m_{1,2} = 1.2866 / 0.2925$ *kg* | | |

The piping system was extensively instrumented [39, 132, 113]. Table 17 shows a summary of the instrumentation used to obtain data used for comparisons with results of simulation. The axial force was not directly measured but it is related to the averaged axial strain (measured at 4 positions around the circumference) and pressure throughout relationship:

$$N_x = \left( ES_t\varepsilon_x + \nu S_t \frac{R}{e} p \right) \qquad \text{where} \qquad \varepsilon_x = (\varepsilon_{x,1} + \varepsilon_{x,2} + \varepsilon_{x,3} + \varepsilon_{x,4}) / 4 \tag{234}$$

The experimental data obtained during the rod impact experiments are very valuable, because of the simple and clear geometry and transient initiating mechanism. In comparison to the Simpson pipe experiment, the rod impact experimental data exhibit a higher level of interaction between the fluid and the structure. The numerical reproduction of the results without consideration of the Poisson and junction coupling mechanisms is not possible. These experiments therefore serve as an excellent

benchmark for any numerical simulation that considers the FSI phenomenon. Figure 53 shows a comparison between the experimental measurement and simulation with our code for all available measured variables (pressure in P1, P4, P6, axial force in P5 and axial pipe velocity in P2). The agreement is excellent.

*Table 17: Position of the measuring equipment from the impact (left) end.*

| Label | Position [m] | Variable | Equipment |
|---|---|---|---|
| P1 | 0.0195 | Pressure | Piezoelectric pressure transducer |
| P2 | 0.0465 | Axial velocity | Laser-Doppler vibrometer |
| P3 | 0.5740 | Axial strain | Strain gauges (4 records) |
| P4 | 2.2510 | Pressure | Piezoelectric pressure transducer |
| P5 | 3.9440 | Axial strain | Strain gauges (4 records) |
| P6 | 4.5020 | Pressure | Piezoelectric pressure transducer |

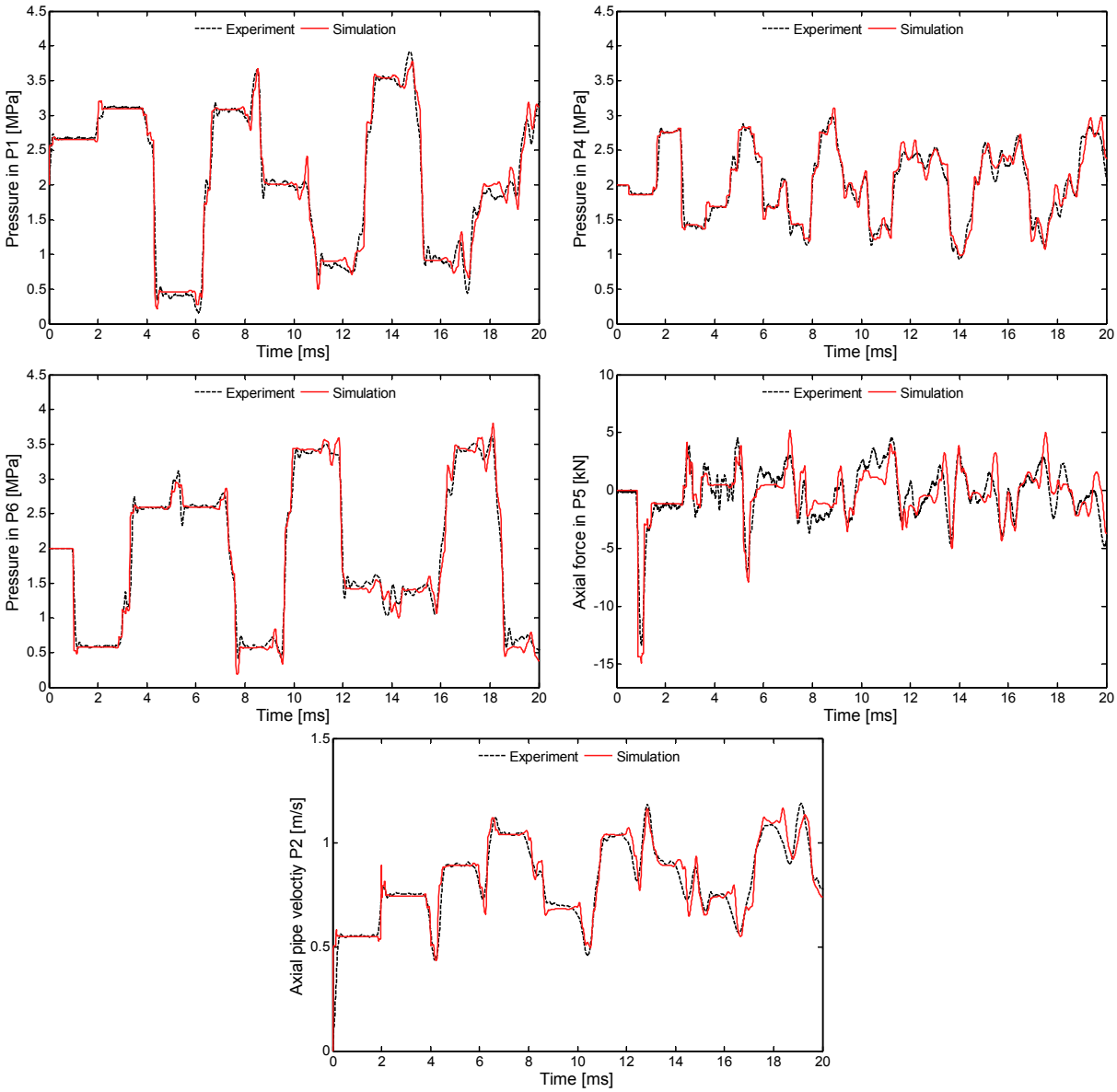


Fig. 53: History of measured basic variables (pressure in P1, P4, and P6, axial force in P5, and axial pipe velocity in P2). Comparison between the experiment and simulation.

The good agreement between the numerical simulations and the measurements allows us to display and explain the physical phenomena in the relatively simple experiment with the help of a comprehensive computer output. Figure 54 very illustratively shows the basic variables in the time-space plane. From the aspect of the integrity of the structure, the most important variables are pressure

and axial force. Figure 54 shows that the pressure is strongly correlated with the axial pipe velocity. The direction of movement of the pipe actually determine the pressure profile. If the pipe moves to the right, the pressure at the right end is low and the pressure at the left end is high. Therefore, the high pressure always appears in a pair with low pressure (like the children's swing). The pipe is not loaded with the pressure in the middle of the pipe (axis of the swing). Timing and position of the maximal pressure is not known in advance, all what is certain is, that the maximal pressure will appear in the vicinity of the left or right end. The largest compressive axial force appears just after the strike of the impact rod. When the stress wave travels along the pipe for the first time and reflects from the remote end, it shares energy with the fluid through the junction coupling and the axial force becomes much more moderate. In addition, the energy from the impact partly transforms into kinematic energy (movement) of the piping system. The largest compressive axial force appears at the beginning of the transient along the whole pipe, while the largest tensile axial force appears as transient evolves at arbitrary time and position. Similar analyses can be performed for other parameters of the simulation.

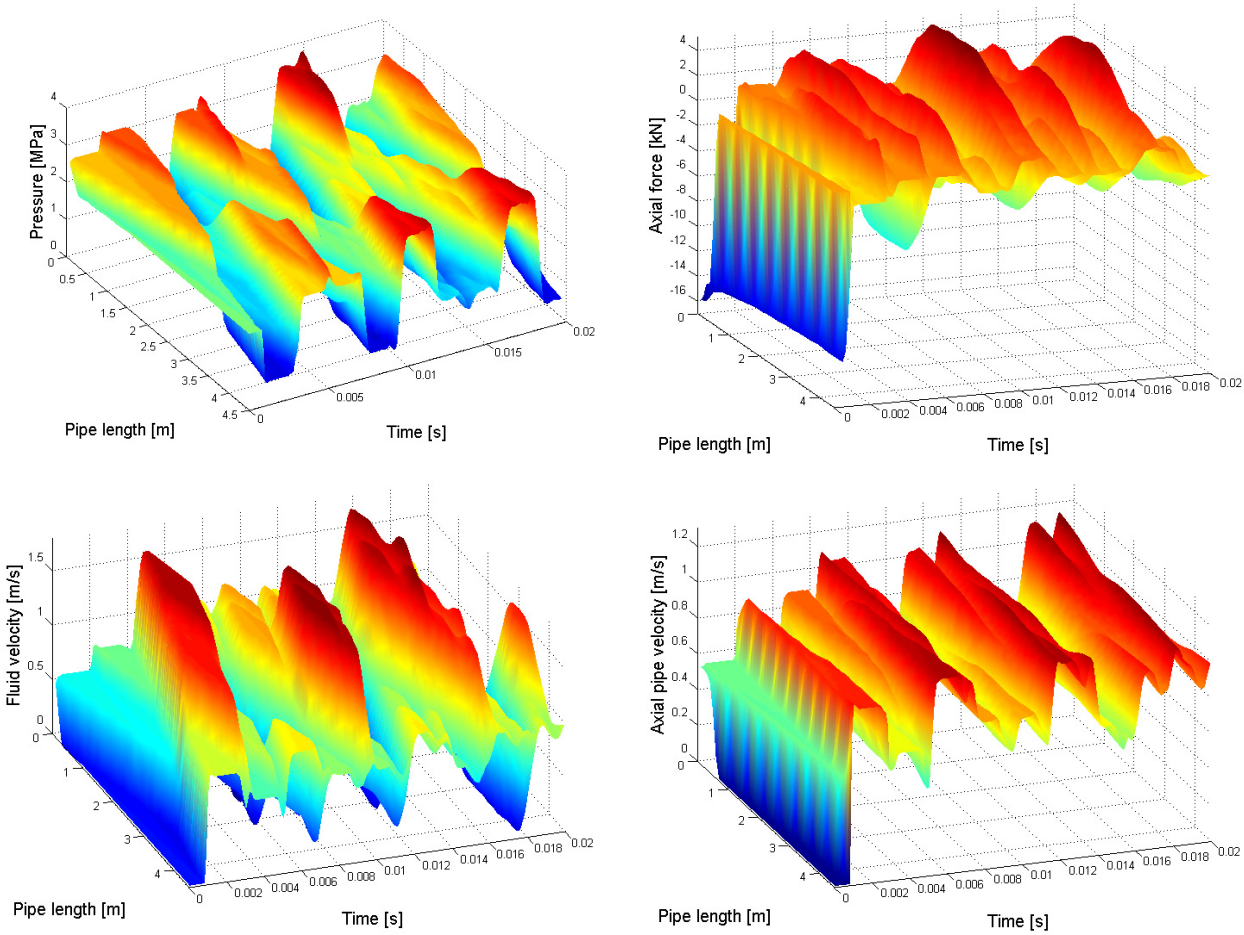


Fig. 54: Basic variables in time – space plane.

**Generation of new waves in the piping system.** The absolute value of the pressure or axial force at any time and any position is a superposition of all stress and pressure waves that travel along the pipe at current instance. The superposition is initially simple, made up of only few waves (example: after the rod impact, the precursor wave is added to the pressure wave), but it becomes quite complicated as time evolves. Each pressure (stress) wave through the junction coupling at geometric singularities generates new stress (pressure) wave, therefore, the number of stress and pressure waves in the piping systems is rapidly increasing with time. More precisely, the pressure and the stress wave are generated simultaneously at the impact end (left), therefore the faster stress wave is the first that reaches the remote end (right) of the pipe (Figure 54). The stress wave pushes the remote end away from the liquid so that the pressure drops and a new negative pressure wave is generated. The new pressure wave travels backwards and when it meets the forthcoming pressure wave, they are added together (the

precursor wave is also added). Afterwards, the first pressure wave reaches the remote end and reflects from the end cap. The end cap is pushed further away, the pressure is raised and a new tensile stress wave is generated. Only the first reflection of the pressure and the stress wave at remote end was described above but in general, any reflection of any wave through the junction coupling generates new waves.

**Linear and nonlinear physical models.** The general form of a one dimensional nonlinear system of conservation laws is given as:

$$\frac{\partial \vec{\psi}}{\partial t} + \frac{\partial \mathbf{f}(\vec{\psi}, x, t)}{\partial s} = 0 \tag{235}$$

Linearization of the nonlinear system with application of the Jacobian matrix **C** yields equation in the following vectorial form:

$$\frac{\partial \vec{\psi}}{\partial t} + \mathbf{C}(\vec{\psi}, x, t)\frac{\partial \vec{\psi}}{\partial s} = 0 \tag{236}$$

The system of equations written in form of Eq. (236) is still nonlinear however, LeVeque [77] called it quasilinear because it resembles a linear system. The balance equations for the fluid developed in Chapter 2 are nonlinear. Moreover, every set of partial differential equations considered in this dissertation can be written in vectorial form by equation (236) with corresponding Jacobian matrix. The character (dependency) of the Jacobian matrix is very important for the selection of the numerical method. The following systems are possible:

- Linear system with constant coefficients: $\frac{\partial \vec{\psi}}{\partial t} + \mathbf{C}\frac{\partial \vec{\psi}}{\partial s} = 0$
- Linear system with variable coefficients: $\frac{\partial \vec{\psi}}{\partial t} + \mathbf{C}(x, t)\frac{\partial \vec{\psi}}{\partial s} = 0$
- Nonlinear system: $\frac{\partial \vec{\psi}}{\partial t} + \mathbf{C}(\vec{\psi}, x, t)\frac{\partial \vec{\psi}}{\partial s} = 0$

The linear model with constant coefficients is the only acceptable form that can be solved with the method of characteristics, because these systems have constant eigenvalues with time and position, and such systems are mostly used by the FSI community. The model is also known as a standard physical model, and the solution with the method of characteristics is known as a standard FSI procedure. The novelty of our approach introduced in this dissertation is application of the characteristic upwind numerical scheme, which provides numerical solutions of nonlinear systems and linear systems with variable coefficients in space and time. The ability of the characteristic upwind numerical method to solve nonlinear systems is an advantage of great practical importance because it enables application of advanced physical models. Figure 55 shows eigenvalues history in P6 for case with linear constant coefficient system (labeled Linear-const.), which is compared to the system with real water properties (labeled Linear-var.), and to the system with included convective terms (labeled Nonlinear). Figure 56 left shows eigenvalue profiles at time *t = 10 ms*, where constant coefficient system is compared to the case where masses of the end cap and end plug are taken into account. Figure 56 right shows a similar comparison, where real water properties are used. Figures 55 and 56 show, that the **characteristic velocities (eigenvalues) that appear in simulations of experimental (real) cases are not constant**. They change with time and position however, Figure 57 shows that for the single-phase rod impact experiment in the straight piping system, consideration of advanced physical models yields relatively small differences to the results obtained with standard linear constant coefficient system. The solution with nonlinear matrix C (labeled Nonlinear) is actually identical to the linear constant matrix C (labeled Linear-const.) due to the acoustic approximation ($v_f << c_f$). The advanced physical models become much more important for accurate simulations of the two-phase flow FSI transients, for simulations of FSI transients in piping systems of more complicated geometry or for simulations of transients where the fluid velocity is not small (convection).

Improvements of the physical model that affect character of the Jacobian matrix and that were applied in dissertation consist in taking into account the convective terms, exact fluid thermodynamic properties (density, compressibility, speed of sound, etc.), various geometric changes like cross-section changes, variable pipe wall thickness, elbows, flexibility due ovalization, masses and loads, elastic supports, etc. Several examples of use of these improvements with discussion on advantages are given in the following sections.

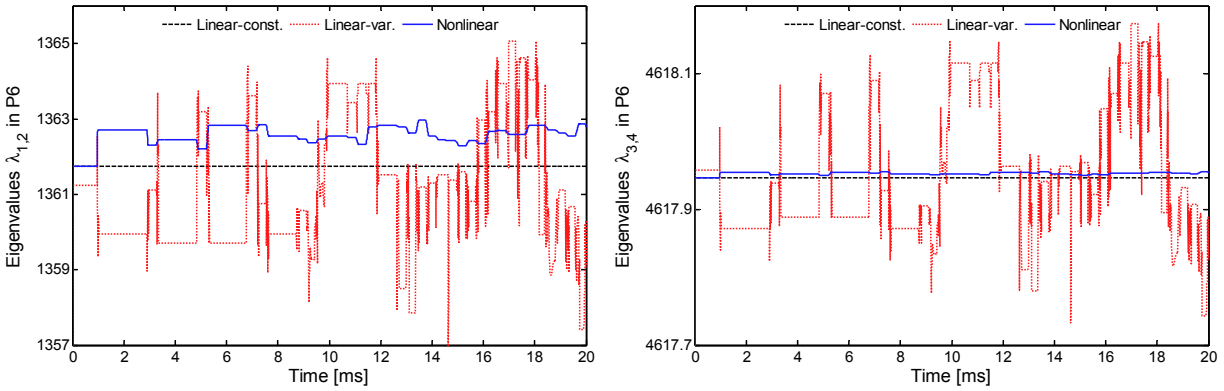


Fig. 55: History of eigenvalues in P6 obtained with various systems of equations.

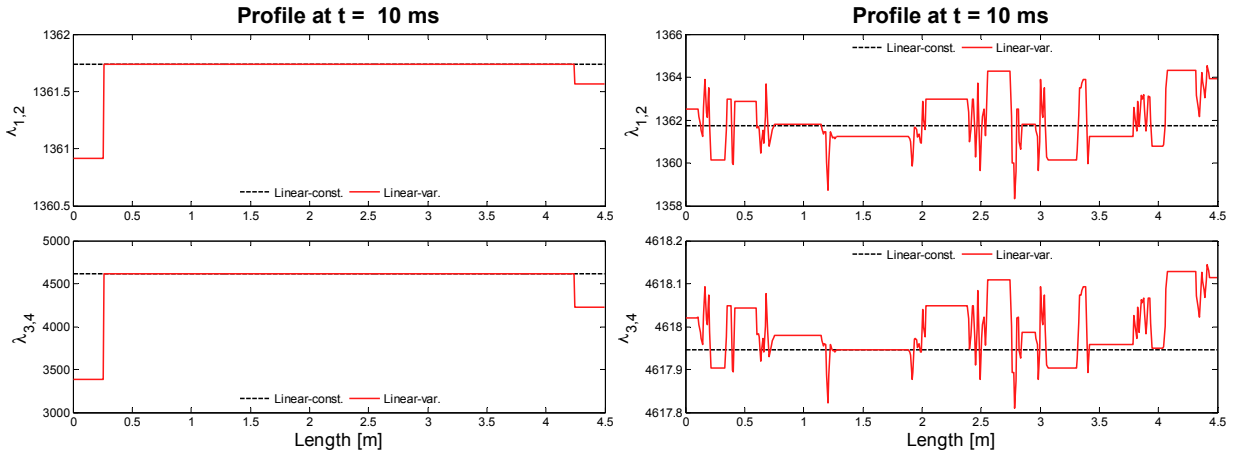


Fig. 56: Eigenvalues profiles obtained with various systems of equation.

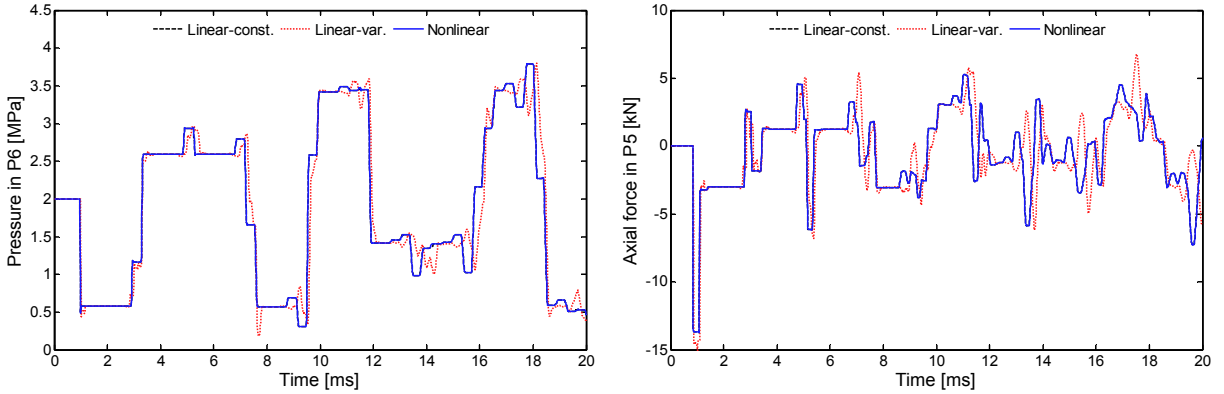


Fig. 57: Pressure history in P6 and axial force history in P5 obtained with various systems of equations.

**Mass of the end cap and end plug.** An external load that is mounted on the pipe (end cap, end plug, and other objects with mass) affects inertia of the piping system, and therefore also the eigensystem itself. The eigenvalues of such system are not constant in space (Figure 56 left) but they are still constant in time. Figure 56 shows that the eigenvalues for the rod impact experiment are reduced at the

beginning and at the end of the experimental apparatus due to the end plug/cap mass, which is numerically distributed over the first/last few volumes. The effect of the mass of the end plug can be physically compared to the mass hanging on the spring. A heavier mass gives a longer period of natural oscillation and smaller natural frequency and the characteristic velocity is therefore reduced to account for this effects. Consideration of the end mass noticeable improves accuracy of results, therefore all results in Figure 53 were obtained with consideration of the additional mass of the piping system (differences are indicated in Figure 57).

**Friction and thick-walled model.** Figure 58 shows the wall friction forces, obtained with a constant Darcy-Weisbach factor $f = 0.01$. The influence of the wall friction force is negligible for the considered experiment (small relative velocity between fluid and pipe wall) although it turned out that the friction forces are important for accurate simulation of the Simpson's pipe experiment (see Table 13). The thick-walled model described by Eq. (159) affects the characteristic velocities of the pressure/stress waves. The characteristic velocity of the pressure wave in the fluid is reduced to $c_f = 1350.6\ (1361.7)\ m/s$ and the characteristic velocity of the stress wave in the pipe is reduced to $c_{t,x} = 4615.2\ (4617.9)\ m/s$. Values in brackets were obtained with the default (thin-walled) model. Figure 59 shows that the reduction of the characteristic velocities of the pressure wave in thick-walled model affects the course of the transient.

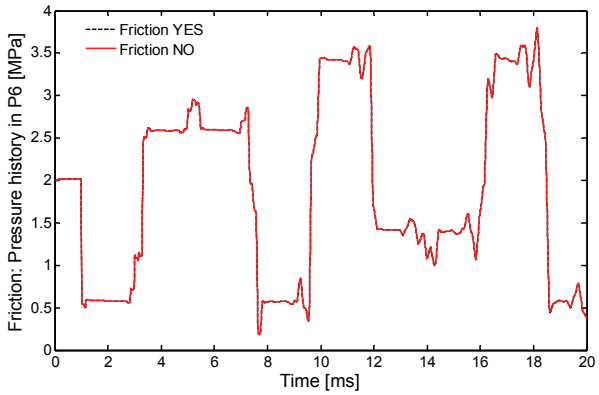


Fig. 58: Pressure history in P6 – wall friction forces are negligible.

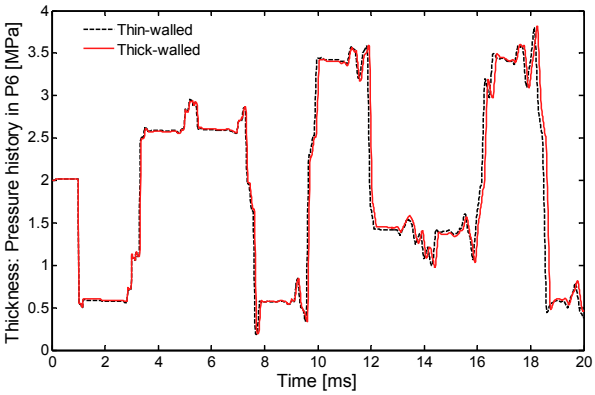


Fig. 59: Pressure history in P6 – influence of the thick-walled model.

**Processor time consumption.** The number of waves in the piping system is rapidly increasing with time and this may become quite processor demanding for certain numerical methods like method of characteristics where each wave (characteristics) needs to be detected and traced with time. The advantage of the characteristic upwind numerical method is that the processor time consumption during the simulation is constant regardless the number of pressure, stress and other waves in the system. Actually, only the relaxation in the two-phase flow (see WAHA manual [126]) or eventually the implicit iterations for the solution of the stiff source terms can slow down the simulation.

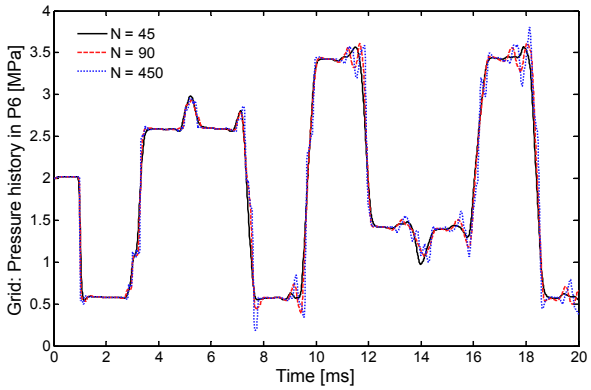


Fig. 60: Pressure history in P6 – grid refinement study.

Figure 54 shows the results obtained with the numerical model that contains 45 computational volumes. The simulation itself on a Pentium IV 3.0 GHz processor lasts 50 seconds (extensive output to files and screen). The grid refinement study in Figure 60 shows that results are almost independent of the grid. The rough grid with *N = 45 volumes* is sufficiently dense and accurate since the results obtained on a denser grid with *N = 90* and *N = 450* computational volumes are not essentially better. The total computational time spent was 30 seconds (reduced output to file) on a P IV 3.0 GHz computer for the rough case and 2 minutes and 50 minutes for the cases with 90 and 450 volumes, respectively.

### 6.4.2. Rod impact experiment in a single elbow pipe

The rod impact experiment in a single elbow piping system is the second piping system of the experimental work of Vardy and Fan [132] who studied Fluid-Structure Interaction in wire hanging liquid-filled piping systems. Tijsseling [39, 113] improved the set of initially single-phase experiments with two-phase flow experiments. A detailed description of the experiments is given by Tijsseling, Vardy and Fan [114]. Figure 61 shows the geometry of the single elbow piping system that is hanging on three steel wires. The system consists of a stainless steel pipe closed at both ends with an end plug and an end cap (mass $m_1$ and $m_2$) and is filled with pressurized tap water. All geometry and state properties for the piping system, water and impact rod are collected in Table 18. The appearance of the two-phase flow depends on the initial pressure in the system, while the other parameters are held constant as much as possible. The transient starts when the impact rod axially strikes the left end of the piping system.

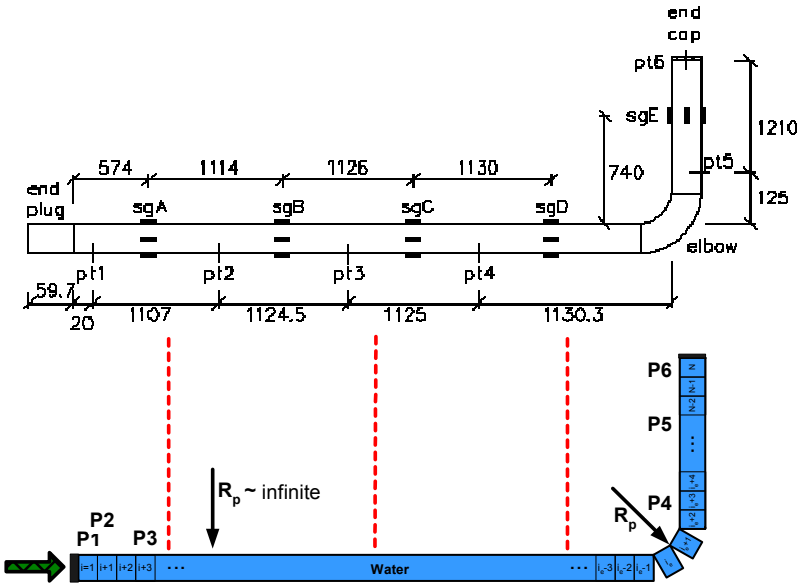


Fig. 61: Sketch of the experimental apparatus from Vardy and Fan [114] (above), and numerical model of the rod impact experiment in single-elbow piping system (below).

*Table 18: Material and state properties of the piping system, water and impact rod.*

| Piping system | Water | Impact rod |
|---|---|---|
| L = 4.51 + 1.34 m | v = 0 m/s | $L_{rod}$ = 5.006 m |
| R = 0.02601 m | K = 2.14 GPa | $R_{rod}$ = 0.02537 m |
| e = 0.003945 m | $p_{1F}$ = 2.0 MPa | $E_{rod}$ = 200 GPa |
| E = 168 GPa | $p_{2F}$ = 0.30, 0.67, 0.87, 1.08, 1.24 MPa | $Y_{rod}$ = 80109.7 kg/s |
| $\rho_t$ = 7985 kg/m$^3$ | T = 20 °C | $v_{0,rod}$ = 0.809 m/s |
| $\nu$ = 0.29 | $\rho_f$ = 999 kg/m$^3$ | $\rho_{rod}$ = 7848 kg/m$^3$ |
| $m_{1,2}$ = 1.312 / 0.3258 kg | | |

Tijsseling [113] and Tijsseling, Vardy and Fan [114] described the extensive instrumentation that was mounted on the piping system to collect data from the experiment. Table 19 shows only a summary of the instrumentation applied in the present dissertation. The axial force is related to the averaged axial strain and pressure, and the bending momentum is related to the top and bottom axial stresses:

$$N_x = \left( ES_t \varepsilon_x + \nu S_t \frac{R}{e} p \right), \qquad \text{and} \qquad M_z = \frac{EI_t}{R+e} \frac{\left( \varepsilon_{x,1} + \varepsilon_{x,3} \right)}{2} \tag{237}$$

*Table 19: Applied measuring equipment and position measured from the impact end.*

| Label | Position [m] | Variable | Equipment |
|---|---|---|---|
| P1 | 0.0195 | Pressure | Piezoelectric pressure transducer |
| P2 | 0.0465 | Axial velocity | Laser-Doppler vibrometer |
| P3 | 0.5740 | Axial strain | Strain gauges (4 records) |
| P4 | 4.6400 | Pressure | Piezoelectric pressure transducer |
| P5 | 5.2500 | Axial strain | Strain gauges (4 records) |
| P6 | 5.8500 | Pressure | Piezoelectric pressure transducer |

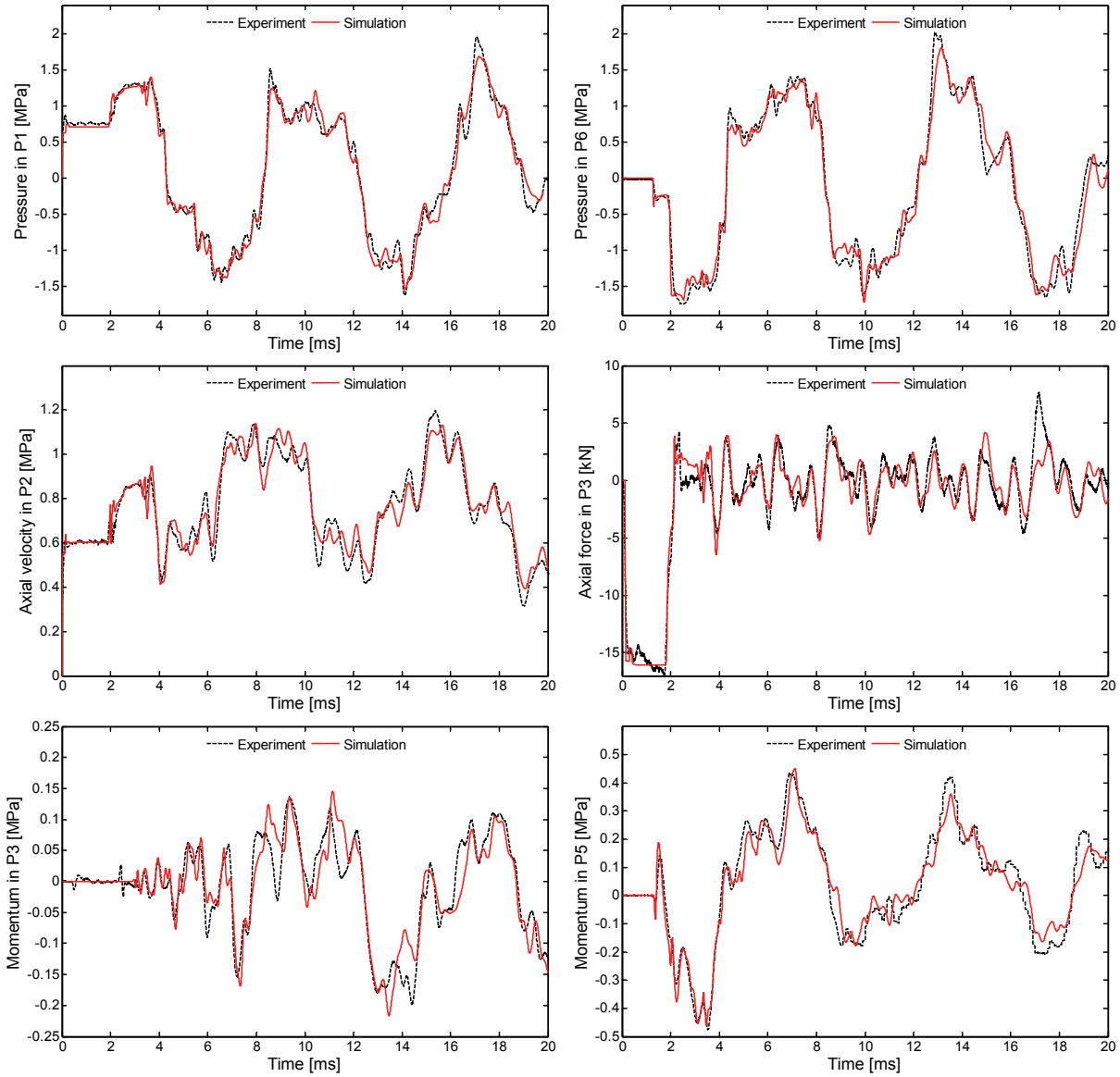


Fig. 62: Histories of measured basic variables (pressure in P1 and P6, axial force in P5, and axial pipe velocity in P2 and momentum in P3 and P5). Comparison between the experiment and simulation.

**Single-phase transient.** A single phase transient with an initial pressure *p = 20 bar* was considered first. The end masses and the flexibility factor of the elbow improve the accuracy of the simulation and were taken into account. Figure 62 shows a comparison between the experiment and the simulation for all available measured variables. The general agreement is very good for all variables; small

discrepancies are attributed to the complex 3D phenomena at the elbow which are linearized and solved with the 1D physical model. Figure 63 gives an additional illustrating overview of timing and position of extreme values of basic variables in the time-space plane.

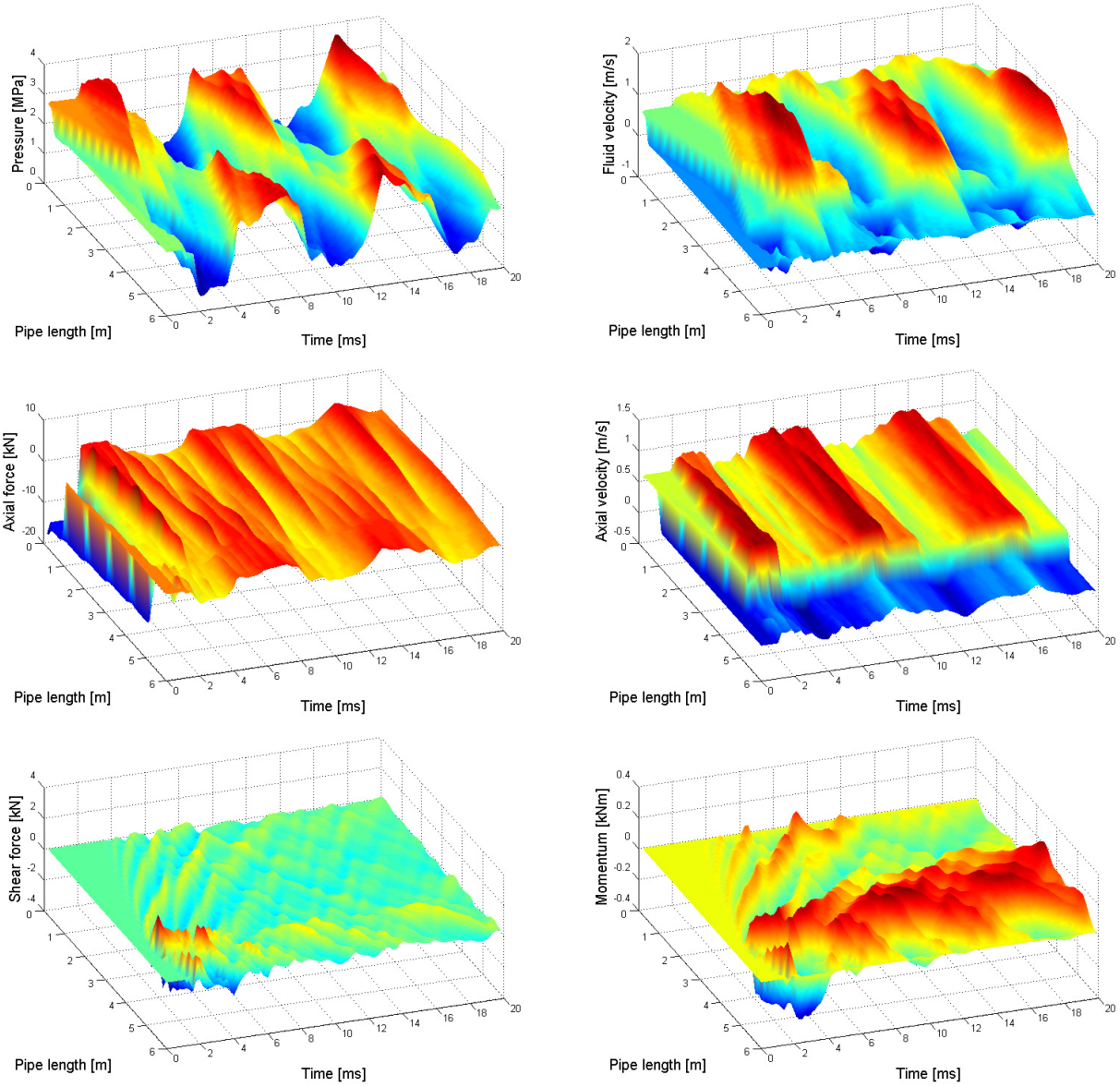


Fig. 63: Basic variables in time-space plane.

**Flexibility factor – ovalization of the elbow.** In 1911, Von Karman [133] explained the complex behavior of an elbow under in-plane bending. He identified the ovalization of the circular cross-section of the pipe under the bending. Von Karman showed that using simplifying assumptions, the elbow is much more flexible than an equivalent straight pipe and that more complex stress distribution is induced. He introduced the concept of a **flexibility factor** and **stress intensification factor** that compares the flexibility under bending and the maximum stress to those of an equivalent straight pipe. Dodge and Moore [33] reported that ovalization gives the elbows an elastic flexibility that is 5 to 20 times more than the flexibility of the same size straight pipe. The flexibility of the elbow is accompanied by stresses and strains that are typically 3 to 12 times those of a straight pipe under the same load. The Von Karman's concept essentially remains unchanged in today's state of the art piping design and analysis software as specified by various design codes and standards [84, 9]. The effect of ovalization is taken into account as a reduction of the moment of inertia of the pipe's cross-section for flexibility factor *k*. In accordance to the ASME code (ASME, B&PVC, Class 1 components, NB-3686) the flexibility factor yields:

$$k = \frac{1.65R^2}{eR_p}\left[\frac{1}{1+6\frac{p}{E}\left(\frac{R}{e}\right)^{7/3}\left(\frac{R_p}{R}\right)^{1/3}}\right] \tag{238}$$

where $R_p$ stands for the radius of curvature of the elbow, $R$ stands for the internal radius of the pipe, and $e$ stands for the thickness of the pipe. In addition, the following conditions must hold: $R_p/R < 1.7$, centerline length $R_p\ \alpha > 2\ R$, and there are no flanges or stiffeners on the elbow. The presented equation for the flexibility factor without part in square brackets is the most commonly used short form; the part in square brackets is a correction for the strengthening effect of the internal pressure.

Figure 64 (upper left) shows the flexibility factor along the piping system for the rod impact experiment. The flexibility factor is different than at the elbow (or any other curved sections of the piping system). The introduction of the flexibility factor influences the eigensystem of the Jacobian matrix. Although the eigenvalues are still constant with time and position, the flexibility factor influences the corresponding eigenvectors **L** of the Timoshenko beam equations (148):

$$\mathbf{L}_{TIM} = \begin{bmatrix} \ddots & \vdots & \vdots \\ \cdots & -\dfrac{k}{\sqrt{\rho_t E I_t^2}} & \dfrac{k}{\sqrt{\rho_t E I_t^2}} \\ \cdots & 1 & 1 \end{bmatrix} \tag{239}$$

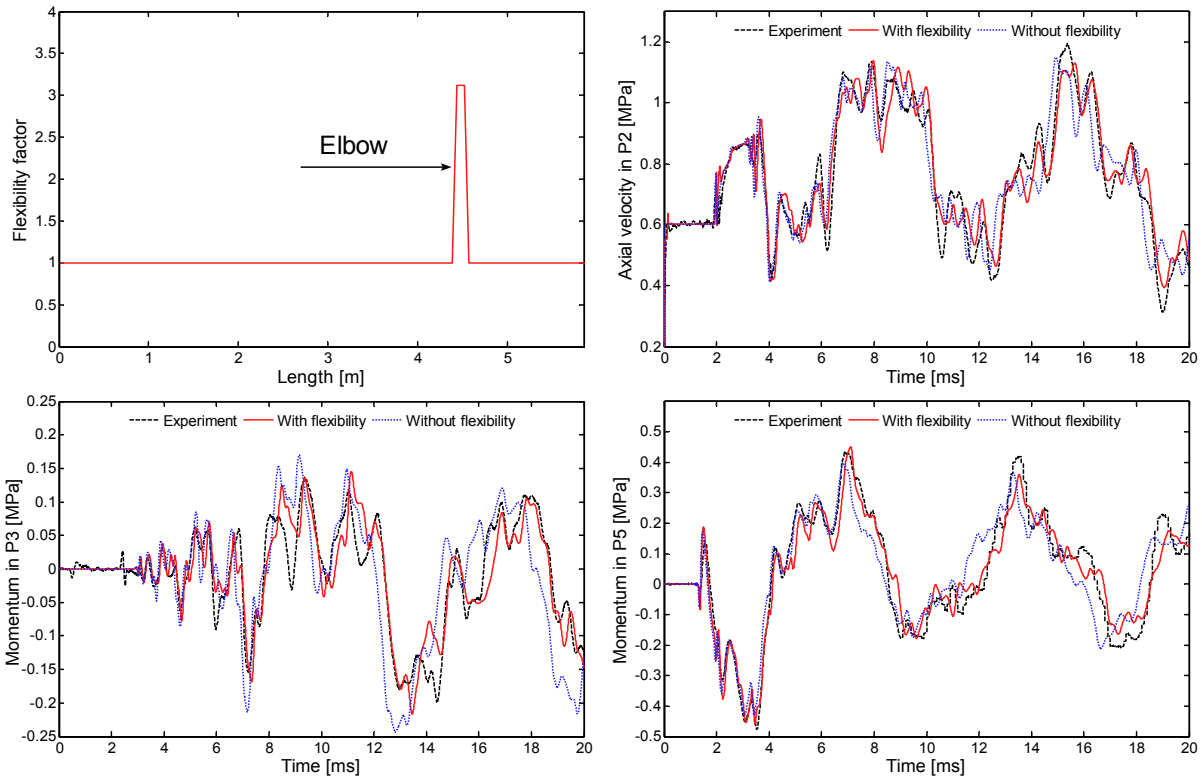


Fig. 64: Flexibility factor profile and histories of some basic variables: comparison with and without consideration of the flexibility factor.

Figure 64 shows that the history of various variables fits better to the measurement if the flexibility of the elbow is taken into account. The reduction of the flexibility at the elbow decelerates traveling waves in comparison to the simulation without flexibility factor. The ability to take into account different flexibility factors in the same computational section is one of the advantages of the Godunov numerical method. DeYong [29] and Kannapan [69] also utilized flexibility factors to account effects of the elbow ovalization during their simulations of the FSI in piping systems.

**Reinforcement of the elbow.** The ASME Boiling and Pressure Vessel code (NB-3641) recommends a minimum wall thickness prior to the bending. For sharp elbows ($R_p < 3R$) the code suggests an increase of the thickness for *25%* compared to the straight section. Introduction of this recommendation into the computational model causes the system to become linear with variable coefficients in space. Figure 65 shows the pipe wall profile with a thicker pipe wall at the elbow and the corresponding eigenvalues profile. Figure 66 shows that the different thickness affects the history of all variables and that the influence on the pressure history is smaller than the influence on the momentum history. The elbow of the experimental apparatus in the rod impact experiment was not reinforced, thus the simulations obtained with the reinforced pipe at the elbow are less accurate compared to the measurement.

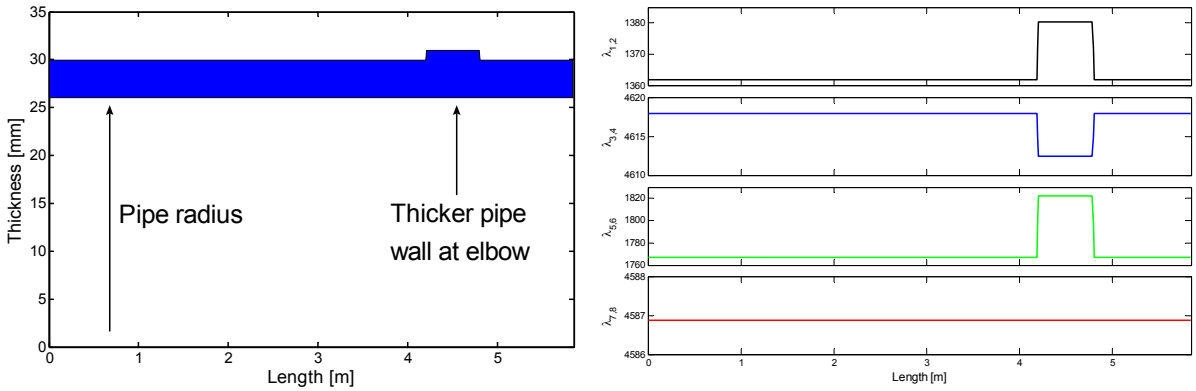


Fig. 65: Pipe wall profile with thicker wall at elbow and eigenvalues profile.

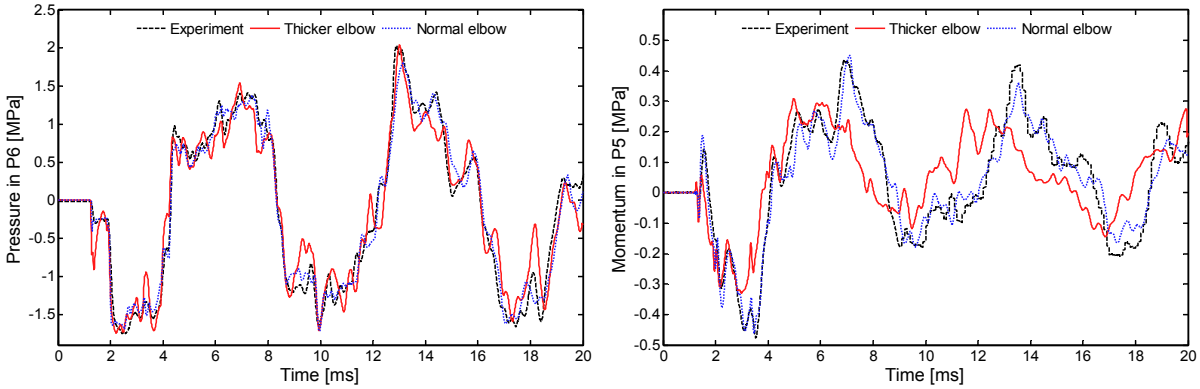


Fig. 66: Pressure and momentum histories for simulation with normal and reinforced pipe wall.

**Water properties.** The water properties are evaluated from the water tables in special subroutine, with temperature and pressure as inputs to the subroutine, and density and specific internal energy as outputs of the subroutine. The water properties are evaluated for each computational volume at each time step. Figure 67 shows that the temperature of the fluid affects the pressure and momentum histories because the temperature through the water properties affects the characteristic velocity (speed of sound) of the pressure waves. The influence of the temperature on the basic structural variables (velocity of the pipe, internal forces, momentum, etc.) is indirect, and therefore less evident. Table 20 shows that the speed of sound in a six kelvins colder fluid is *20 m/s* lower compared to the speed of sound at room temperature. **Small changes in density and temperature have considerable influence on the speed of sound.** The speed of sound is fundamental parameter in FSI simulations, therefore it is recommended to perform simulations with exact water properties, and when unavoidable, to be cautious and exact when defining constant water properties in order to estimate the speed of sound as close to reality as possible. Exact temperature should be measured and reported as an important initial condition.

The temperature of the fluid in the (isothermal) eight equation planar quasi-two-phase flow FSI physical model is constant during the simulation (no energy balance equation included), and the experiments presented so far show, that this assumption is accurate for all transients at room temperature. The

temperature changes due to thermal relaxation in such transients are actually small and duration of the transients is so short that exchanges of heat through the pipe walls are negligible.

*Table 20: State properties of the fluid (water).*

| Parameter | Constant values | T = 293 K | T = 287 K |
|---|---|---|---|
| Density [kg/m$^3$] | 999.00 | 999.12 | 1000.16 |
| Bulk modulus [GPa] | 2.1400E9 | 2.1887E9 | 2.1401E9 |
| Speed of sound [m/s] | 1463.6 | 1480.1 | 1462.8 |

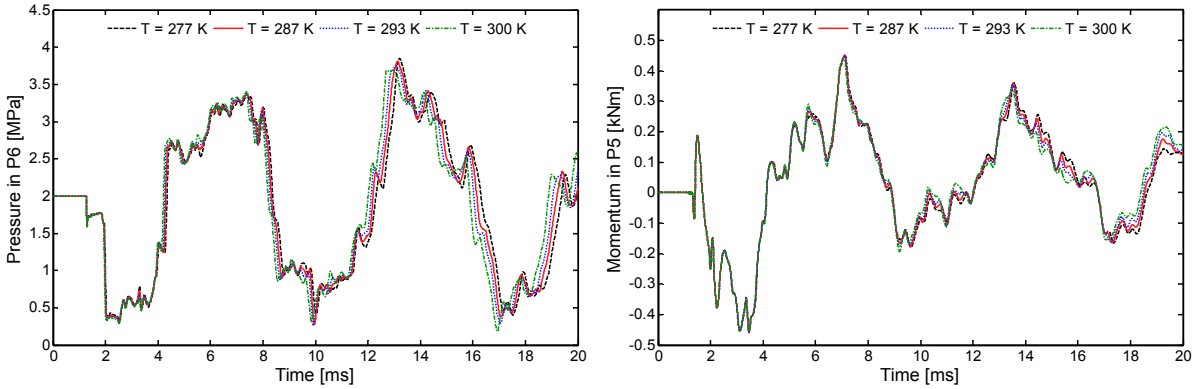


Fig. 67: Pressure and momentum time histories for fluid with variable initial temperature.

Tijsseling et al. [115] reported that they conducted the rod impact experiments at room temperature (it is assumed that room temperature is *T = 293 K*). Tijsseling [113] performed also numerical simulation of the experiment with constant water properties (MOC method), and got a very good agreement between simulation and experiment. The same experiment was simulated with our model, once with Tijsseling's constant fluid properties and then with accurate water properties. The simulations yield the following conclusions:

- The agreement between the simulation, the experiment and the results of Tijsseling is very good (Fig. 62).
- The results of simulation obtained with accurate and constant water properties are almost identical (Fig. 57, linear-cons. vs. linear-var.). The improvement of real water properties over constant water properties represents a minor improvement for simulations of single-phase transients in cold water. However, it becomes very important for two-phase flow transients or transients in warm and hot water.
- The best agreement with the experiment was obtained for the fluid temperature *T = 287 K*. This temperature was then applied for all simulations of considered rod impact experiments. The applied temperature is six kelvins lower than the presupposed 'room' temperature. However, the decision is justified by the accuracy of the results and by the fact that exact temperature of the water in the rod impact experimental apparatus is not available.

**Von Mises stress.** The Von Mises stress or simply the Mises stress is a scalar function of the deviatoric components of the stress tensor that gives an appreciation of the overall magnitude of the shear components of the tensor. This allows the onset and amount of plastic deformation under triaxial loading to be predicted from the results of a simple uniaxial tensile test. It is most applicable to ductile materials. In three-dimension, the Mises stress can be expressed as:

$$\sigma_v = \sqrt{\frac{\left((\sigma_1-\sigma_2)^2+(\sigma_2-\sigma_3)^2+(\sigma_3-\sigma_1)^2\right)}{2}} \tag{240}$$

where $\sigma_1$, $\sigma_2$, and $\sigma_3$ are the principal stresses. In one-dimension, this reduces to the uniaxial stress. In terms of a local coordinate system, the Von Mises stress can be expressed as:

$$\sigma_v = \frac{1}{\sqrt{2}}\sqrt{\left(\sigma_{xx}-\sigma_{yy}\right)^2+\left(\sigma_{yy}-\sigma_{zz}\right)^2+\left(\sigma_{zz}-\sigma_{xx}\right)^2+6\left(\sigma_{xy}^2+\sigma_{yz}^2+\sigma_{zx}^2\right)} \quad (241)$$

Von Mises yield criterion for the onset of yield in ductile materials was first formulated by Maxwell [41] in 1865 but is generally attributed to Von Mises in 1913. Von Mises yield criterion can be interpreted physically in terms of the maximum distortion strain energy, which states that yielding in three-dimension occurs when the distortion strain energy reaches that required for yielding in uniaxial loading. Mathematically, this is expressed as: $\sigma_v \leq \sigma_y$. In the two-dimensional stress space (shell, pipe wall, $\sigma_3 = 0$) shown in Fig. 68, the yield criterion represents the interior of an ellipse. **Stress states $\sigma_1$ and $\sigma_2$ not touching the boundary of the ellipse produce only elastic deformation.** Figure 68 shows also Tresca's maximum shear stress criterion (dashed line labeled Maximum shear). This criterion is more conservative than Von Mises's criterion since it lies inside the von Mises ellipse.

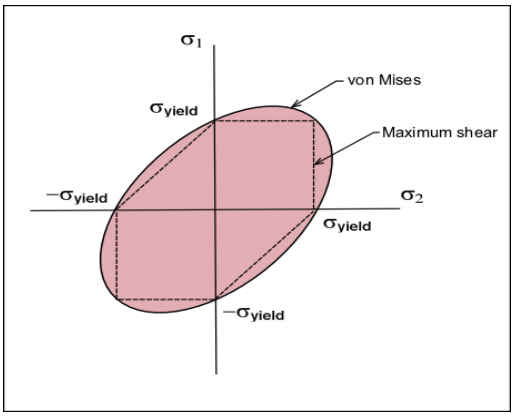


Fig. 68: Von Mises yield criterion for two dimensional stress space.

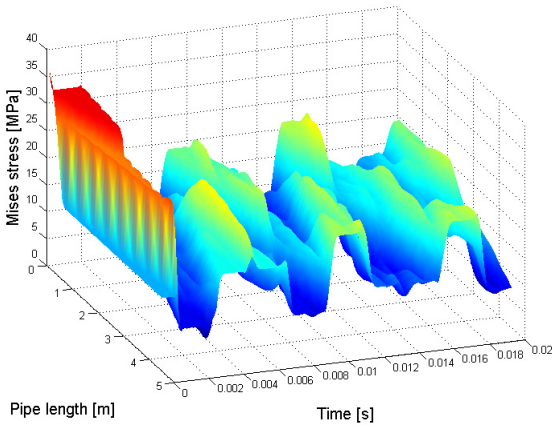


Fig. 69: Von Mises stress scalar function in time-space plane for rod impact experiment in straight piping system.

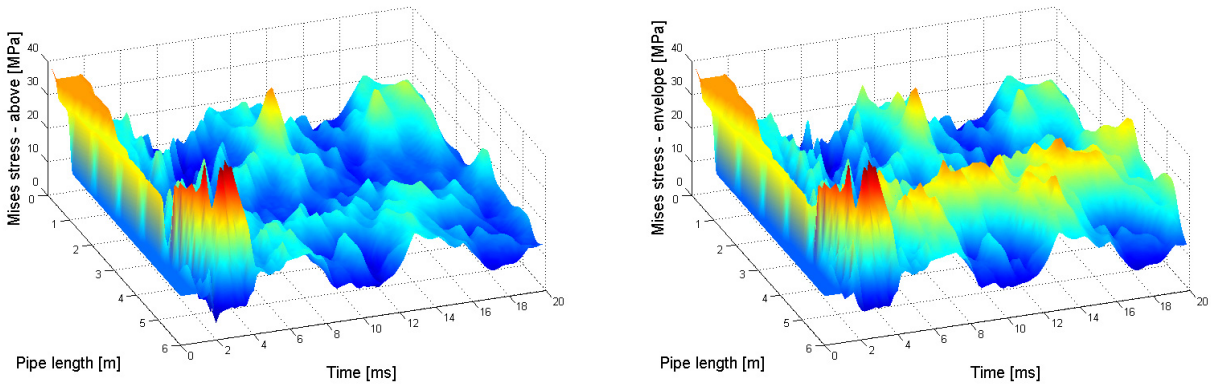


Fig. 70: Von Mises stress in time-space plane in the upper part of the pipe and the cross-section envelope for rod impact experiment in single elbow piping system.

Figure 70 shows the appearance of the maximal Mises stress in the upper part of the pipe and the envelope of the Mises stress for the whole cross-section of the piping system. It is evident that the critical section of the pipe with the maximal load is the section in the vicinity of the elbow at the beginning of the transient. The maximal stresses are less than $\sigma_{v,max} < 50\ MPa$ (typical yield stress for stainless steel is some $\sigma_y = 250\ MPa$), and the duration of the maximal stresses is very short – pulsations. If the pipe resists for the first five milliseconds, then the integrity of the piping system is not jeopardized. Figure 69 shows the von Mises stress for the rod impact experiment in the straight piping system described in previous section. It is possible to see, that the maximal stresses ($\sigma_{v,max} < 35\ MPa$) are achieved at the beginning of the transient during the strike of the impact rod. If the pipe resists impact strike, then there is no need to worry about the integrity of the piping system.

**Two-phase flow experiments.** The quasi-two-phase flow model was verified with the Simpson pipe experiment. The FSI coupling mechanisms have been verified for numerous geometries of the pipe

conveying single-phase transients. Finally, the study in this section compares the experimental data and the simulation in piping systems where cavitation and FSI occur simultaneously and are both significant. The considered transients presented in Figs. form 71 to 74 cannot be reproduced without consideration of the coupling mechanisms and without consideration of the appropriate two-phase flow model.

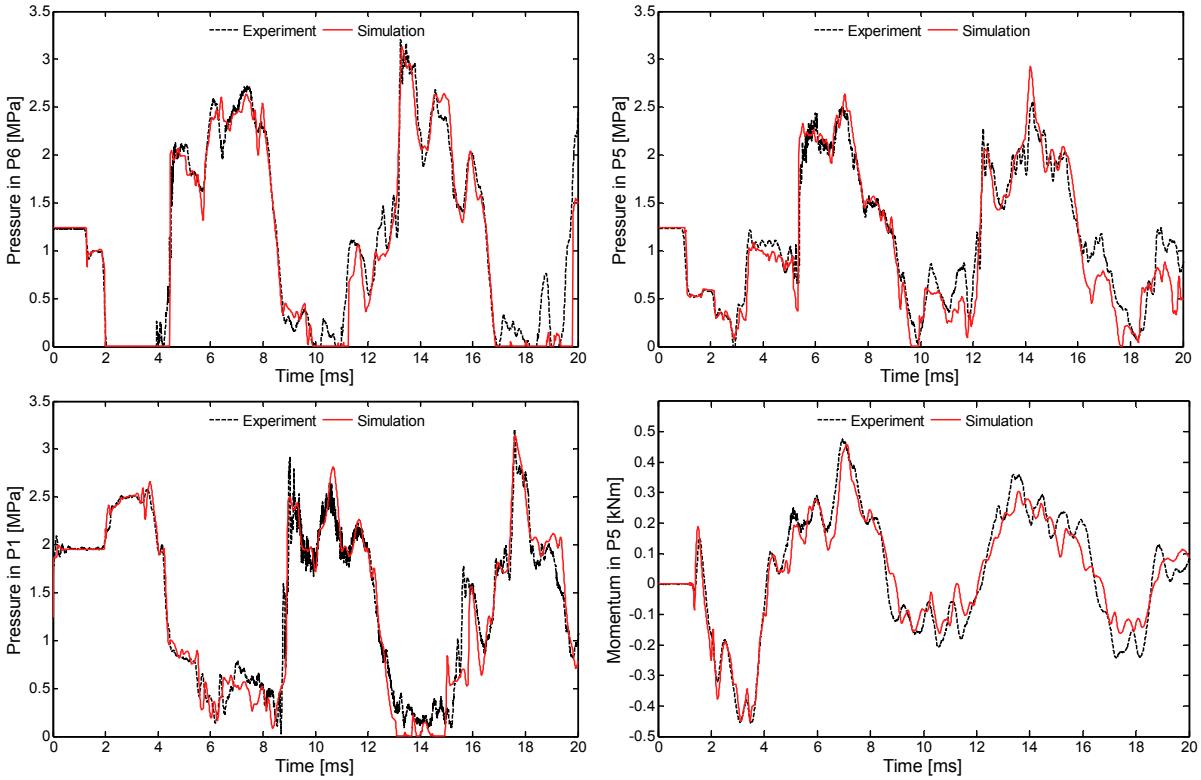


Fig. 71: Histories of basic variables ($p_{2F}$ = *1.24 MPa*): measurement vs. simulation.

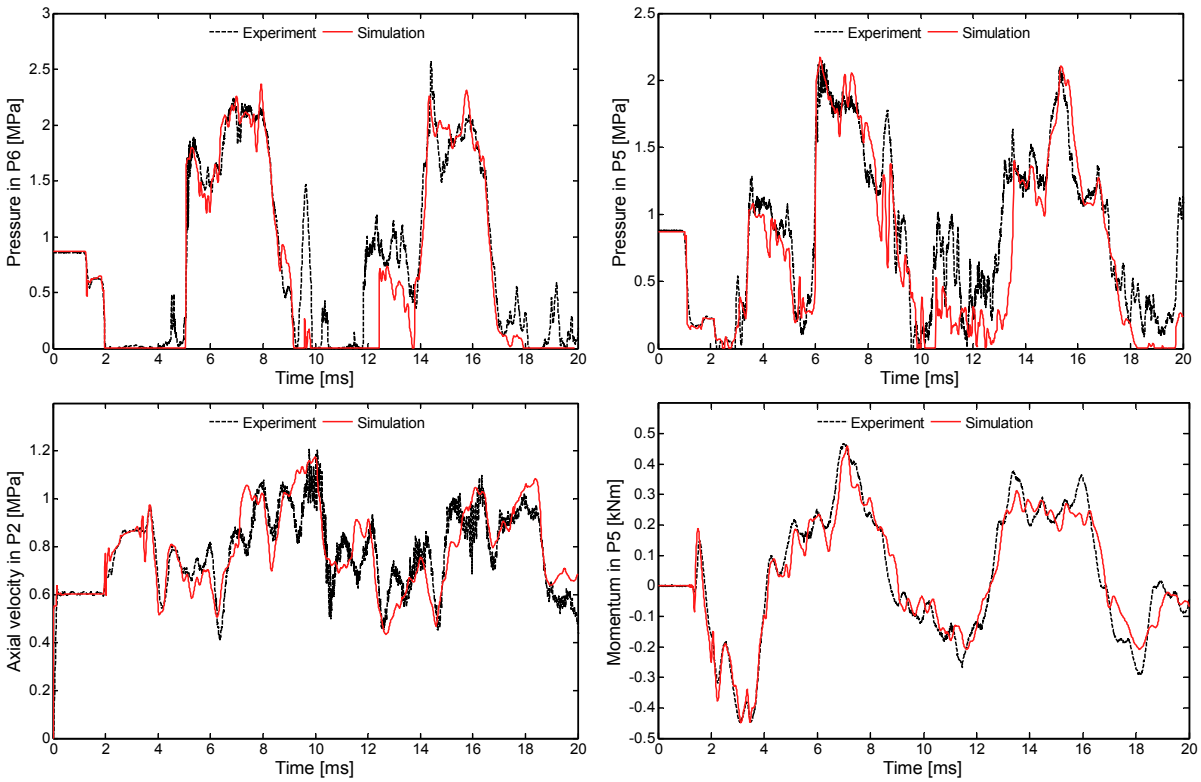


Fig. 72: Histories of basic variables ($p_{2F}$ = *0.87 MPa*): measurement vs. simulation.

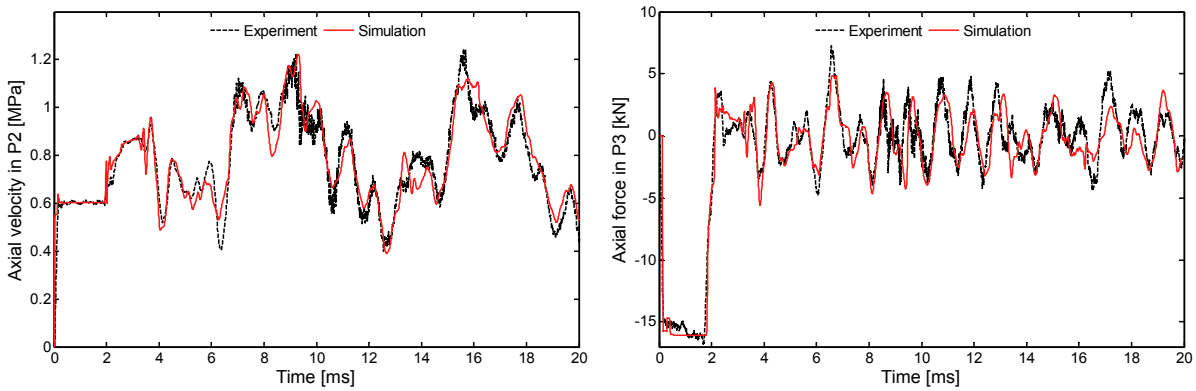


Fig. 73: Histories of basic variables ($p_{2F}$ = *1.08 MPa*): measurement vs. simulation.

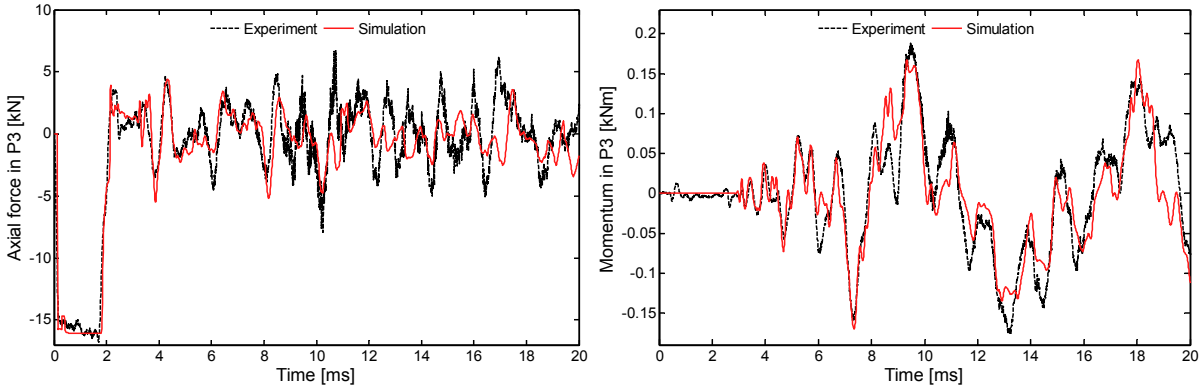


Fig. 74: Histories of basic variables ($p_{2F}$ = *0.69 MPa*): measurement vs. simulation.

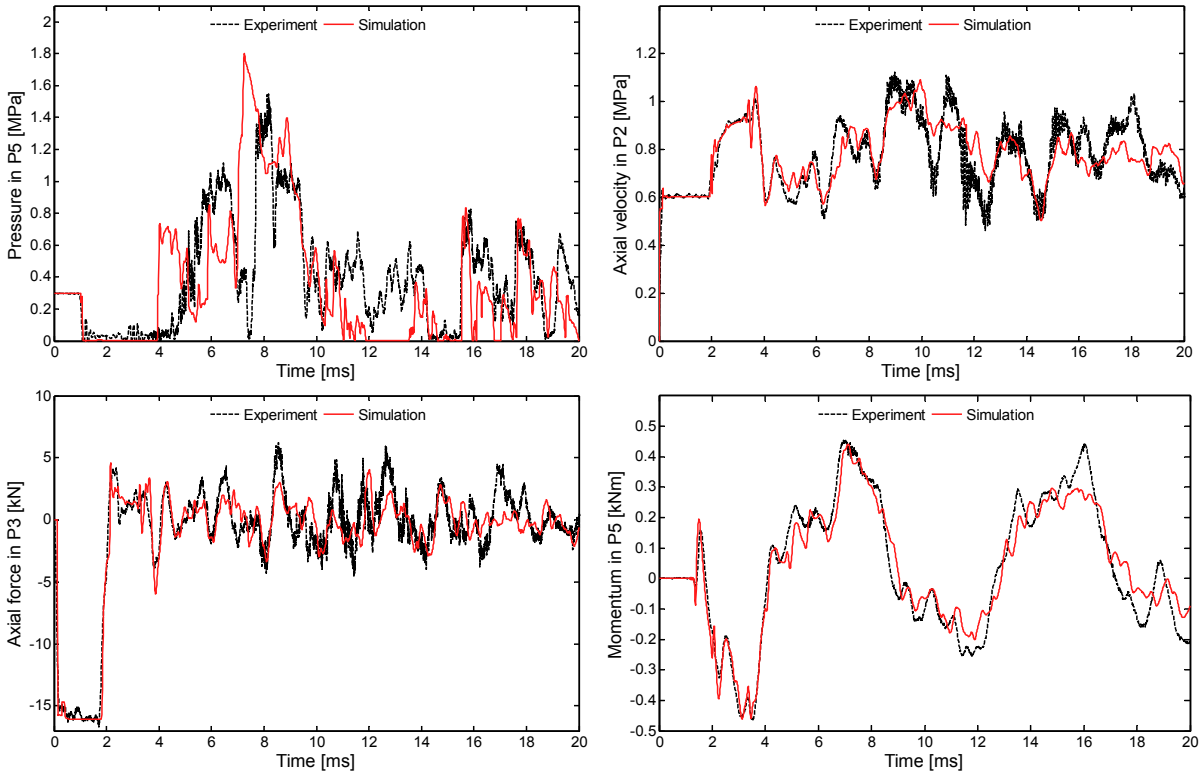


Fig. 75: Histories of basic variables ($p_{2F}$ = *0.30 MPa*): measurement vs. simulation.

The simulation was performed with the eight-equation nonlinear model for FSI in a planar arbitrarily shaped piping system with consideration of real water properties and quasi-two-phase flow model. The available experimental data have been applied for comparison with simulation in Figures 71 to 74. The

overall agreement found between the experimental and numerical results is good in view of the complexity of the phenomena. The magnitude and timing of the extreme pressures, the axial velocities, the extreme axial forces and the extreme bending moments are predicted accurately. Discrepancies between numerical and experimental results are attributed to (i) the use of a simple quasi-two-phase flow model of two-phase flow, which is not able to describe cross-section specific localized cavitation at elbow, (ii) the experimental uncertainty (Tijsseling et al. [113] showed that reproducibility of the experiments is generally good, although discrepancies rise for flows with stronger cavitation), (iii) other standard errors, discussed in previous sections, which come with applied numerical method and physical model.

Although an advanced physical models and an advanced numerical method are applied, the overall agreement between the numerical and experimental results is only slightly better compared to the results obtained by Tijsseling et al. [113]. This points to the fact that Tijsseling et al. in their simplified approach, included in physical model all fundamental terms that are essential for the description of the FSI phenomenon coupled with cavitating flow. However, the results presented in this thesis show that all improvements of our physical model and numerical method, give more accurate results and enable significantly more advanced analyses and simulations. While the approach based on the method of characteristics, already reached its limit, our approach enables the inclusion of numerous additional improvements.

**Generation and distribution of vapor**. Figure 76 shows the comparison of the vapor volume fraction with (left) and without (right) consideration of the FSI for the experiment with moderate cavitation and analogously Figure 77 for the case with severe cavitation. In the cases with FSI, the amount of generated vapor is slightly larger however, the overall generation and distribution with and without FSI are almost the same.

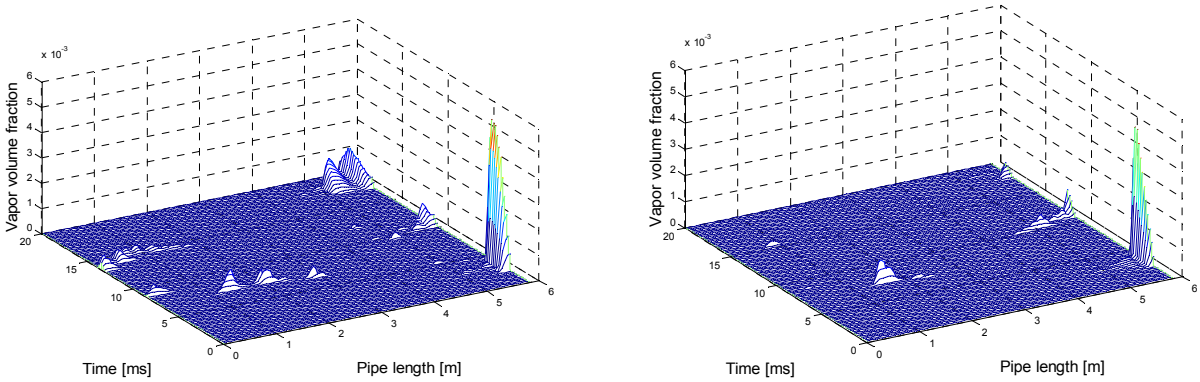


Fig. 76: Vapor volume fraction in time-space plane for moderate ($p_{2F}$ = *1.08 MPa*) cavitation, with (left) and without (right) consideration of the FSI effects.

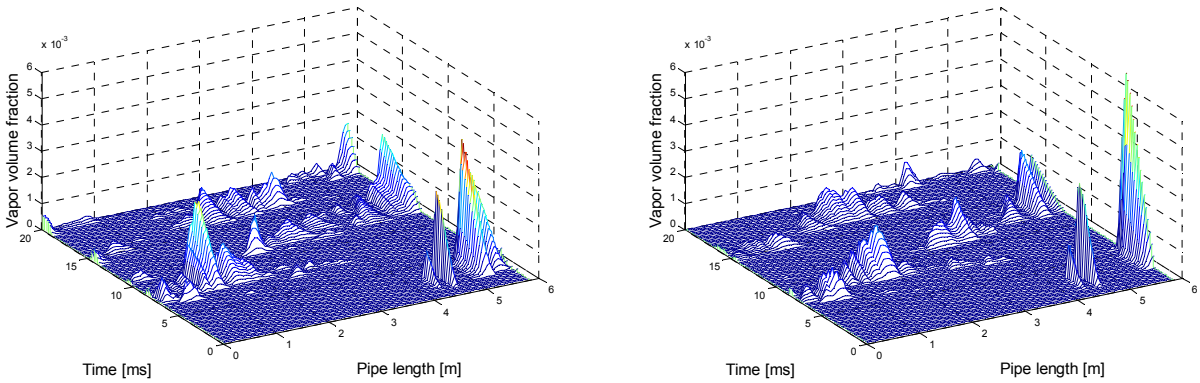


Fig. 77: Vapor volume fraction in time-space plane for severe ($p_{2F}$ = *0.3 MPa*) cavitation, with (left) and without (right) consideration of the FSI effects.

**Von Mises stress in two-phase flow.** Comparison of Figures 70 and 78 show that the severity of the cavitation does not influence the overall stress situation in the piping system. The maximal stresses appear at the same position and the temporal distribution is approximately the same. The moderate cavitation case exhibits only one anticipated effect (higher stress) that comes due to different initial pressure. Because all parameters of the simulation, except the initial pressure, are held constant, the maximal stresses are shifted for contribution of the initial pressure. Consequently, the maximal absolute stresses are encountered in single-phase flow, because of the maximal contribution of the initial pressure. It is possible to conclude that the **appearance of the two-phase flow, regardless to the intensity of the cavitation, does not reduce the relative maximal stresses in the piping system**. The statement that two-phase flow isolates and prevents FSI is wrong. FSI is strong even in compressible two-phase flow.

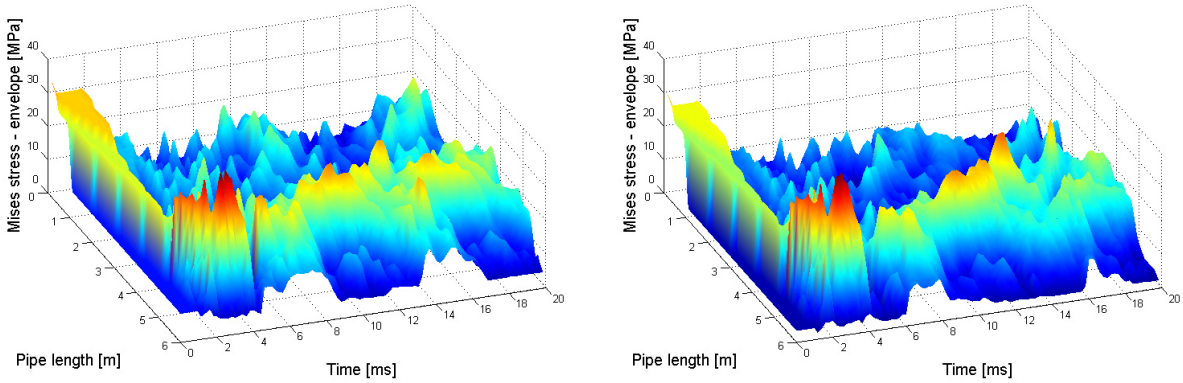


Fig. 78: Von Mises stress envelope in time-space plane for moderate (left, $p_{2F}$ = *1.08 MPa*) and severe (right, $p_{2F}$ = *0.3 MPa*) cavitation.

# 7. Conclusions

Fluid-Structure Interaction (FSI) during a transient in a fluid is an important phenomenon that affects dynamics and integrity of many piping systems. The FSI coupling is strong in soft piping systems conveying less compressible single or two-phase fluids, and is weak in stiff and fully supported piping systems. The integrity of soft piping systems is jeopardized during the FSI occurrence, while the stiff piping systems are costly and are jeopardized by thermal loads. Exchange of energy between the fluid and the structure during the FSI transient occurrence is thus a very important issue and should be predicted (and controlled) as precisely as possible. There are no simple criteria for the estimation of the FSI coupling importance for a general piping system; therefore, several physical and computational approaches have been developed in the past. The approaches that are based on modeling of the FSI coupling phenomena with a single physical model for the thermo-fluid and structural dynamics, and that are solved with an appropriate numerical method, turned out to be the best way for design of new piping systems, for modifications and improvements of the existing piping systems and for analyses of the past accidents. New and more accurate concepts for derivation of advanced physical models, coupling of physical sub-models, and new more accurate numerical algorithm are founded in this dissertation.

The one dimensional general balance equation of thermo-fluid dynamics is derived in arbitrarily shaped, moving and deformable Lagrangian coordinates. The general balance equation is then applied for the derivation of the mass, momentum and energy balance equations of the two-phase flow. The mass, momentum and energy balance equations are used for the construction of the six-equation two-fluid model of the two-phase flow intended for simulations of the two-phase flow transients with FSI. Analogously, the single-phase flow model and the simplified two-phase flow models namely, the homogeneous equilibrium model and the quasi-two-phase flow model, are derived. The Lagrangian derivation yields several new terms in the balance equations compared to the equivalent equations derived in the standard Eulerian coordinate system or compared to the generally accepted fluid dynamics models applied for simulations of the FSI. These terms are terms for local junction coupling FSI mechanism at curvatures and distributed Poisson coupling FSI mechanism, terms with axial force of the pipe and axial and lateral velocity of the pipe, terms accounting for deformations and curvature of the pipe. Accurate thermodynamic states of the fluid are evaluated from the realistic water properties. It is shown that assuming stiff, straight and fixed pipe, the balance equations naturally degenerate into the standard equations derived in the Eulerian frame.

The one dimensional physical models for axial, rotational, lateral and torsional structural dynamics are derived for arbitrarily shaped piping systems described with a general arc length parameter. Several new terms appear compared to the standard physical models of the beam theory, namely, terms accounting for the junction coupling FSI mechanism at curvatures, and distributed Poisson and friction coupling FSI mechanisms. Considering the assumption of a straight piping system, the models for arbitrarily shaped piping systems degenerate into the standard models for straight piping systems. The equations for rotational and lateral movement of the straight piping systems correspond to the equations of the Timoshenko beam theory. The physical models are valid for phenomena in piping systems where longitudinal and lateral frequencies of vibration prevail over circumferential vibration of the pipe wall (low-frequency or long wavelength assumption). The high-frequency phenomena are negligible for the fluid transient and also for the FSI and are thus neglected.

The physical models for thermo-fluid dynamics are grouped with the physical models for structural dynamics into various models of various complexities. They range from the two-equation single-phase flow model to the eighteen-equation model for two-phase flow FSI simulations in arbitrarily shaped and deformable piping systems lying in a 3D space. The fundamental physical model of this dissertation is the eight-equation quasi-two-phase flow FSI model for arbitrarily shaped piping systems in a 2D plane. The equations that make up these physical models are first order nonlinear partial differential equations. The majority of the physical models are hyperbolic by default i.e. the Jacobian matrix of the physical model is diagonalizable, while in order to assure hyperbolicity of all physical models that imply the six-equation two-fluid model of the two-phase flow, a differential virtual mass term is introduced. Analytical solutions for diagonalization exist only for the simple physical models; numerical diagonalization is performed for all other physical models. The eigensystem at output of the numerical diagonalization is

sorted from the largest eigenvalue towards the smallest, therefore additional sorting of the eigensystem is performed at the end of each diagonalization. The sorting is trivial for physical models containing single-phase flow, quasi-two-phase flow, or homogeneous equilibrium two-phase flow, while it becomes quite complicated for the physical models containing the six-equation two-fluid model of a two-phase flow.

The high resolution characteristic upwind finite difference numerical scheme is applied. The term high resolution applies to methods that are at least second order accurate on smooth solutions and yet give well resolved, non-oscillatory discontinuities by modifying the method in the neighborhood of a discontinuity to a monotone first order method. The numerical scheme for the convective terms is explicit: the results exhibit second order accuracy. The stiff source terms of the Timoshenko beam equations are solved by implicit iterations and the stiff relaxation source terms are integrated with the two-step operator splitting approach. The most important property of the numerical method is that it operates with piecewise constant characteristics of the nonlinear physical models. This enables the introduction of numerous improvements like consideration of realistic water properties, consideration of curvatures of the piping system, consideration of geometry changes (cross-section area, pipe wall thickness, material properties, etc.), consideration of the distributed cavitation, consideration of the external loads and masses, friction terms based on Reynolds number, reinforcement of the pipe wall, etc. All these phenomena cannot be addressed with methods dealing with linear equations like the method of characteristics. The weakest point of the characteristic upwind numerical method is the numerical dissipation, which tends to smoothen the solutions at discontinuities. However, the numerical dissipation can be minimized by an appropriate definition of the slope limiter and by increasing the number of computational volumes per unit of length. The numerical method is proclaimed as effective since the average processor time spent for simulation is few minutes, and the most accurate solutions presented in this dissertation took less than one hour on personal computer Pentium IV with 3.0 GHz processor.

The accuracy of the characteristic upwind numerical method is verified by comparison with the results obtained by the method of characteristics. The physical model used was linearized and simplified to match the same assumptions that are used in standard physical models (linear constant coefficient system, no source terms). The agreement is almost perfect, small differences between the characteristic upwind numerical method and the method of characteristics refer to numerical dissipation.

The analytical verification of the results validated the code for the evaluation of the natural frequency of oscillation for arbitrarily supported and loaded piping systems. The code exhibits high accuracy for the non-standard evaluation (simulation with increased damping) of equilibrium values – deflection, internal forces, bending momentum, and other variables, which are used in static calculations in civil engineering. The analysis of the axial and lateral oscillations points out that intensity of the FSI in the axial direction strongly depends on compressibility of the fluid while the intensity of the FSI in the lateral direction is negligible. The most important parameter for lateral oscillations is the mass of the fluid.

Precursor and successor waves are simulated, their origin, appearance and significance for the FSI transient pipe flow is explained. While precursor waves are rather well known and frequently mentioned in the literature, their counterpart, successor waves, are usually neglected; their existence was not traced in the literature by the author yet. Precursor waves under certain circumstances cause the formation of the Poisson coupling induced cavitation. The phenomenon is explained and discussed.

The quasi two-phase flow model is verified by means of experiments for the case with moderate and severe cavitation in a very stiff piping system. The quasi two-phase flow is utilized for the simulation of the rod impact experiment, where FSI coupling is very strong and isolated from the surroundings. Agreement between the experiment and the simulation is remarkable.

The stiffness of a piping system at elbows is reduced due to ovalization of the elbow. The standard model, based on a flexibility factor, is integrated into the computer code. The accuracy of the simulation is increased for the cases with unsupported and flexible elbow.

The 3D stress tensor is represented with scalar values based on the approach established by Von Mises. The Von Mises stress plotted in the time-space plane is one of the most important engineering results of the FSI coupling simulations. It gives timing and position of the maximal stresses in the pipe. The simulations of the pipe with an elbow show that the position and the height of the maximal stresses

are unpredictable without appropriate FSI simulation, and that the duration of the maximal stresses is short – pulsations.

The good agreement between the numerical simulations and the measurements allows explaining the physical phenomena in the relatively simple experimental setups with the help of extensive computer output. Many lessons can be learned from it. It clarifies the phenomenon, when significant cavitation and pipe motion due to water hammer occur simultaneously. Simulations of the FSI coupling transient pipe flow are not possible without consideration of the local junction coupling mechanism and distributed Poisson coupling mechanism. In view of possible transient pipe flows, the junction coupling can be prevented by fixing elbows and/or valves, and the Poisson coupling can be prevented with thick walled pipes. However, none of the solutions to prevent FSI is reasonable. FSI must be allowed to occur, because exchange of energy between the fluid and the structure is in most of the cases beneficial for the integrity of the piping system. Exchange of energy during the FSI must be controlled, and this is not possible without appropriate computer simulations.

The developed advanced physical models and the applied characteristic upwind numerical method have been compiled into the computer code, which is the most prominent practical outcome of the present dissertation. The code is assigned as verified since it was successfully applied for simulation of numerous phenomena related to the FSI and cavitation, and can be now used for simulations of practical cases. There are two possibilities for further research and development. The first is the application of the six-equation two-fluid model of the two-phase flow into the current eight-equation model. The second possibility is a further extension of the equations for 3D space so that it would be possible to simulate arbitrary structures in 3D. It is necessary to stress, that the abovementioned improvements mainly concern computer programming skills, while the firm theoretical background has been established within the scope of the current work. On the other hand, the lessons learned and the advanced physical models derived can be implemented also into the WAHA code, which will improve the WAHA for simulations of the FSI.

# References


[1] Abaqus Documentation, Ver. 6.4-1.

[2] Abbot, M.B., Basco, D.R., 1989, Computational Fluid Dynamics: An introduction for Engineers, John Wiley and Sons, Inc., Harlow, England

[3] Allievi, L., 1903, Teoria generale del moto perturbato dell'acqua ani tubi in pressione, Ann. Soc. Ing. Arch. Ithaliana, (French translation by Alleivi, 1904, Revue de mechanique).

[4] Allievi, L., 1913, Teoria del copo d'ariete, Atti Collegio Ing. Arch, (English translation by Halmos, E.E., 1929, The theory of water hammer, Trans. ASME).

[5] Anderson, A., 2000, Celebrations and challenges - water hammer at the start of the 20th and 21st centuries, Proc. of the 8th International Conference on Pressure Surges, BHR Group, 317-322.

[6] Ansys Documentation

[7] Antes, H., 2003, Fundamental solution and integral equations for Timoshenko beams, Computers and Structures, 81: 383-396.

[8] Arscott, F. M., 1955, The oscillation of a heavy spring, The Mathematical Gazette, 39 328: 126-131.

[9] ASME Boiler & Pressure Vessel Code, 1998, Section III, Division 1, Class 1 components.

[10] Barth, T., Ohlberger, M., 2004, Finite Volume Methods: foundations and analysis, Encyclopedia of Computational Mechanics, John Wiley & Sons, Ltd.

[11] Bereux, F., 1996, Zero-relaxation limit versus operator splitting for two-phase fluid flow computations, Computer Methods in Applied Mechanics and Engineering, 133: 93-124.

[12] Bergant, A., Simpson, A. R., Tijsseling, A. S., 2006, Water hammer with column separation: A historical review, Journal of Fluids and Structures, 22 2: 135-171.

[13] Bestion, D., 1990, The Physical closure laws in the CATHARE code, Nuclear Engineering and Design, 124, pp. 229-245.

[14] Bettinali, F., Molinaro, P., Ciccotelli, M., Micelotta, A., 1991, Transient analysis in piping networks including fluid-structure interaction and cavitation effects, Trans. of SMiRT11, Paper K35/5: 565-570.

[15] Boure, A., 1975, On a Unified Presentation of the Non-Equilibrium Two-Phase Flow Models, Proc. of ASME Symp., New York.

[16] Brennen, C. E., 1995, Cavitation and Bubble Dynamics, Oxford University Press.

[17] Burell, M. J., Enix, D., Lerchel, E., Miro, J., Techendorff, V., Wolferth, K., The Thermal-Hydraulic Code ATHLET for Analysis of PWR and BWR Systems, Fourth Int. Meeting on Nuclear Reactor Therma-Hydraulics, NURETH-4, Proceedings, Vol 2: 1234-1239.

[18] Burman, E., Sainsaulieu, L., 1995, Numerical analysis of two operator splitting methods for and hyperbolic system of conservation laws with stiff relaxation terms, Computer Methods in Applied Mechanics and Engineering, 128: 291-314.

[19] Burmann, W., 1975, “Water Hammer in Coaxial Pipe Systems”, ASCE Journal of the Hydraulics Division, 101, pp. 699-715.

[20] Carlson, K.E., Riemke, R.A., Rouhani, S.Z., Shumway, R.W., Weaver, W.L., 1990, RELAP5/MOD3 Code Manual,Vol. 1-7, NUREG/CR-5535, EG&G Idaho, Idaho Falls.

[21] Carpenter, R. C., 1893, Experiments on Waterhammer, Trans. of ASME, 15.

[22] Casadei, F., Halleux, J. P., Sala, A., Chille, F., 2001, “Transient Fluid-Structure Interaction Algorithms for Large Industrial Applications“, Computer Methods in Applied Mechanics and Engineering, 190, pp. 3081-3110.

[23] Chalabi, A., Qiu, Y., 2000, “Relaxation Schemes for Hyperbolic Conservation Laws With Stiff Source Terms: Application to Reacting Euler Equations”, Journal of Scientific Computating, 15(4), pp. 395-416.

[24] Chalabi, A., 1999, “Convergence of Relaxation Schemes for Hyperbolic Conservation Laws with Stiff Source Terms”, Mathematics of Computation, 68 (227), pp. 955-970.

[25] Clough, R. W., Penzien, J., 2003, Dynamics of Structures, Third edition, Computers & Structures, Inc.

[26] Coutris, N., 1993, Balance equations for fluid lines, sheets, filaments and membranes, International Journal of Multiphase Flow, 19 4: 611-637.

[27] Cowper, G. R., 1966, The shear coefficient in Timoshenko's beam theory, Journal of Applied Mechanics, 33: 335-340. Timoshenko beam

[28] Davis, J. L., 1988, Wave Propagation in Solids and Fluids, Springer-Verlag, New York Inc.

[29] De Jong, C. A. F., 1994, "Analysis of Pulsations and Vibrations in Fluid-Filled Pipe Systems", PhD. Thesis, Eindhoven University of Technology, Department of Mechanical Engineering, Eindhoven, The Netherlands.

[30] Debenedetti, P. G., 1996, Metastable liquids, Concepts and Principles, Princeton University Press.

[31] Delhaye, J. M., Achard, J. L., 1976, On the Averaging Operators Introduced in Two-Phase Flow Modeling, Proc. CSNI Specialist Mtg. on Transient Two-Phase Flow, Toronto.

[32] Delhaye, J. M., Giot, M., Riethmuller, M. L., 1981, Thermo hydraulics of two-phase flow systems for industrial design and nuclear engineering, Hemisphere and McGraw-Hill.

[33] Dodge, W.G., Moore, S.E., 1972, "Stress Indices and Flexibility Factors for Moment Loadings on Elbows and Curved Pipes," Welding Research Council Bulletin, 179.

[34] Downar-Zapolski, P., Bilicki, Z., Bolle, L., Franco, J., 1996, The non-equilibrium relaxation model for one-dimensional flashing liquid flow, International Journal of Multiphase Flow, 22 3: 473-483.

[35] Drew, D. A., Cheng, L., Lahey, R. T., 1979, The analysis of virtual mass effects in two-phase flow, International Journal of Multiphase Flow, 5: 232-242.

[36] Drew, D., Lahey, R. T., 1979, Application of General Constitutive Principles to the Derivation of the Multidimensional Two-Phase Flow Equations, International Journal of Multiphase Flow, 5 (4): 243-264.

[37] Elansary, A. S., Contractor, D. N., 1994, "Valve Closure: Method for Controlling Transients", Journal of Pressure Vessel Technology, Transactions of the ASME 116 (4), pp. 437-442.

[38] Erath, W., Nowotny, B., Maetz, J., 1999, "Modeling the FSI Produced by a Water Hammer During Shutdown of High-Pressure Pumps", Nuclear Engineering and Design, 193, pp. 283-296.

[39 Fan, D., Tijsseling, A. S., 1992 "Fluid-Structure Interaction with Cavitation in Transient Pipe Flows", Journal of Fluids Engineering, Transactions of the ASME, 114, pp. 286-274.

[40] FLUSTRIN, 1990, Manual, ver. 1, Delft Hydraulics.

[41] Ford, H., Alexander, J. M., 1963, Advanced Mechanics of Materials, Longman, London.

[42] Frizell, J. P., 1898, Pressures Resulting From Changes of Velocity of Water in Pipes, Trans. Am. Soc. Civ. Eng., 39: 1-18.

[43] Gale, J., Tiselj, I., 2004, WAHA (WAter HAmmer) Computer Code, Proc. of the 9th International Conference on Pressure Surges.

[44] Gale, J., Tiselj, I., 2005, "Applicability of the Godunov's Method for Fundamental Four-Equation FSI Model", Proc. of Int. Conf.: Nuclear Energy for New Europe 2005.

[45] Gale, J., Tiselj, I., 2008, Godunov's method for simulations of fluid-structure interaction in piping systems, ASME Journal of Pressure Vessel Technology (final manuscript approved).

[46] Gallouet, T., Massela, J. M., 1996, "A Rough Godunov Scheme", C.R.A.S. Paris, 323, pp. 77-84.

[47] Ghidaoui, M. S., Zhao, M., McInnis, D. A., Axworthy, D. H., 2005, A Review of Water Hammer Theory and Practice, Applied Mechanics Reviews, 58: 49-76.

[48] Giot, M., Prasser, H. M., Castrillo, F., Dudlik, A., Ezsol, G., Jeschke, J., Lemonnier, H., Rubbers, A., Tiselj, I., Van Hoove, W., Potapov, S., 2003, "Two-Phase Flow Water Hammer Transients and Induced Loads on Materials and Structures of Nuclear Power Plants (WAHALoads)", FISA 2003, EU research in reactor safety, pp. 523-528.

[49] Godunov, S. K., 1959, Mat. Sb., 47: p. 271.

[50] Goncalves, P. J. P., Brennan, M. J., Elliot, S. J., 2007, Numerical evaluation of high-order modes of vibration in uniform Euler-Bernoulli beams, Journal of Sound and Vibration, 301: 1035-1039.

[51] Harris, C. M., Crede, C. E., 1976, Shock and vibration handbook, McGraw-Hill book company, 2nd edition.

[52] Harvey, A. H., Peskin, A. P., Klein, S. A., 2004, "NIST Standard Reference Database 10," NIST/ASME Steam properties, Ver. 2.21, US Department of Commerce.

[53] Heinsbroek, A. G. T. J., Kruisbrink, A. C. H., 1993, "Fluid-Structure Interaction in Non-Rigid Pipe Systems - Large Scale Validation Experiments", Transactions of SMiRT12, pp. 211-216.

[54] Heinsbroek, A. G. T. J., Tijsseling, A. S., 1993, Fluid-Structure Interaction in non-rigid pipeline systems - a numerical investigation II, Proc. of SMiRT 12, J08/2.

[55] Heinsbroek, A. G. T. J., 1997, "Fluid-Structure Interactions in Non-Rigid Pipe Systems", Nuclear Engineering and Design, 172, pp. 123-135.

[56] Hetsroni, G, 1982, Handbook of multiphase systems, McGraw Hill.

[57] Hirsch, C., 1988, Numerical Computation of Internal and External Flows, Vol 1-2, John Wiley & Sons.

[58] Holmboe, E. L., Rouleau, W. T., 1967, The effect of viscous shear on transients in liquid lines, ASME Journal of Basic Engineering, 89: 174-180.

[59] Hu, C. K., Phillips, J. W., 1981,"Pulse Propagation in Fluid-Filled Elastic Curved Tubes", ASME Journal of Pressure Vessel Technology, 103, pp. 43-49.

[60] Hutchinson, J. R., 2001, Shear coefficients for Timoshenko beam theory, ASME Journal of Applied Mechanics, 68: 87-92.

[61] Ishii, M., 1975, Thermodynamics of Two-Phase Flow, Eyrolles, Paris.

[62] Ishii, M., Hibiki, T., 2006, Termo-Fluid Dynamics of Two-Phase Flow, Springer Science+Business Media, Inc.

[63] Jaeger, C., 1933, Theorie Generale du Coup de Belier, Dunod, Paris.

[64] Jin, S., Levermore, D., 1996, "Numerical Schemes for Hyperbolic Conservation Laws with Stiff Relaxation Terms", Journal of computational physics, 126 (1), pp. 449-467.

[65] Jones, S. E., Wood, D. J., 1972, The effect of axial boundary motion on pressure surge generation, ASME Journal of Basic Engineering, 94: 441-446.

[66] Joukowsky, N. E., 1900, On the hydraulic hammer in water supply pipes, Memories of the Imperial Academy Society of St. Petersburg , Series 8, 9(5), (in German) English translation, partly by o Simin: Proc. Am. Water Works Assoc. 24, pp.341-424: 1-71.

[67] Joung, I., Shin, Y. S., 1985, "A New Model on Transient Wave Propagation in Fluid-Filled Tubes", ASME Proc. of the Pressure Vessels and Piping Conference, 98(7), pp. 275-281.

[68] Kalkwijk, J. P. T., Kranenburg, C., 1971, Cavitation in horizontal pipelines due to water hammer, ASCE Journal of the Hydraulics Division, 97 No. HY10: 1585-1605.

[69] Kannappan, H., 1986, Introduction to pipe stress analysis, John Willey & Sons.

[70] Kladnik, R., 1991, Visokošolska Fizika (in slovene), 1. del, mehanski in toplotni pojavi, DZS, Ljubljana.

[71] Kovač, M., 2004, Influence of microstructure on development of large deformations in reactor pressure vessel steel, Ph.D. thesis, University of Ljubljana, Faculty of mathematics and physics.

[72] Kranenburg, C., 1972, The effect of free gas on cavitation in piplines induced by water hammer, Proc. of the 1st Int. Conf. on Pressure Surges, BHRA, Canterbury, UK, Paper C4: 41-52.

[73] Kries, J. von, 1883, On the relations between pressure and velocity, which exist in the wave-like motion in elastic tubes, Festschrift der 56. Versammlung deutscher Naturforscher und Arzte (in German).

[74] Kucienska, B., 2004, Friction Relaxation Model for Fast Transient Flows, PhD dissertation.

[75] Lavooij, C. S. W., Tijsseling, A. S., 1991, "Fluid-Structure Interaction in Liquid-Filled Piping Systems", Journal of Fluids and Structures, 5, pp. 573-595.

[76] Le Veque, R. J., Yee. H.C., 1990, "A Study of Numerical Methods for Hyperbolic Conservation Laws with Stiff Source Terms", Journal of computational physics, 86(1), pp. 187-210.

[77] Le Veque, R. J., 1992, Numerical Methods for Conservation Laws, Second edition, Birkhauser verlag, Basel.

[78] Le Veque, R. J., 2002, Finite volume method for hyperbolic problems, Cambridge University Press, Cambridge.

[79] Lee, U., Kim, J., 1999, "Dynamics of Branched Pipeline Systems Conveying Internal Unsteady Flow", ASME Journal of Vibration Acoustics, 121, pp. 114-121.

[80] Lemmon, E. W., McLinden, M. O., Friend, D. G., 2003, Thermophysical Properties of Fluid Systems, NIST Chemistry WebBook, NIST Standard Reference Database , 69.

[81] Lemonnier, H., 2002, An attempt to apply the homogeneous relaxation model to the WAHALoads benchmark tests with interaction with the mechanical structure, CEA-T3.3-D61-200302.

[82] Lemonnier, H., 2002, Two-fluid 1D-averaged model equations for a pipe undergoing arbitrary motions, CEA-T3.3-D61-301002.

[83] Leslie, D. J., Vardy, A. E., 2001, Practical guidelines for fluid-structure interaction in pipelines: a review, Proc. of the 10th international meeting of the work group on the behavior of hydraulic machinery under steady oscillatory conditions. See also web site of PHMSA office for pipeline safety: http://ops.dot.gov/stats/LQ_SUM.HTM

[84] Lubis, A., Boyle, J. T., 2004, "The Pressure Reduction Effect in Smooth Piping Elbows – Revisited", International Journal of Pressure Vessels and Piping, 81, pp. 119-125.

[85] Macchelli, A., Melchiorri, C., 2005, Modeling and control of the Timoshenko beam. The distributed port Hamiltonian approach, SIAM Journal on Control and Optimization, 43 2: 743-767.

[86] Menabrea, L. F., 1885, Note sur les effects de choc de l'eau dans les conduites, C.R. Hebd. Seances Acad. Sci, 47 Jul-Dec: 221-224.

[87] Mendez-Sanches, R. A., Morales, A., Flores, J., 2005, Experimental check on the accuracy of Timoshenko's beam theory, Journal of Sound and Vibration, 279: 508-512.

[88] Mills, A. F., 1999, Heat Transfer, second edition, Prentice-Hall, Inc.

[89] Moody, F. J., 1990, Introduction to Unsteady Thermo fluid Mechanics, John Wiley & Sons, Inc.

[90] MpCCI, Technical reference, Ver. 3.0.

[91] Muller, W. Ch., 1987, Uncoupled and coupled analysis of a large HDR pipe, Transactions of SMiRT9, Vol. F: 31-36.

[92] Naguleswaran, S., 2002, Vibration of an Euler-Bernoulli beam on elastic end supports and with up to three step changes in cross-section, Int. Journal of Mechanical Sciences, 44: 2541-2555.

[93] Naguleswaran, S., 2004, Transverse vibration of an uniform Euler-Bernoulli beam under linearly varying axial force, Journal of Sound and Vibration, 275: 47-57.

[94] Obradović, P., 1990, "Fluid-Structure Interactions: an Accident which has Demonstrated the Necessity for FSI Analysis", Transactions of the 15th IAHR Symposium on Hydraulic Machinery and Cavitation, Paper J2.

[95] Païdoussis, M.P., 1998, Fluid-Structure Interactions - Slender structures and axial flow, Volume 1, Academic Press, San Diego.

[96] Païdoussis, M.P., 2004, Fluid-Structure Interactions - Slender structures and axial flow, Volume 2, Elsevier Academic Press, London.

[97] Papalexandris, M. V., Leonard, A., Dimotakis, P. E., 1997, "Unsplit Schemes for Hyperbolic Conservation Laws with Source Terms in One Space Dimension", Journal of computational physics, 134(1), pp. 31-61.

[98] Parmakian, J., 1955, Water-Hammer Analysis, Prentice-Hall Englewood Cliffs, N.J. (Dover Reprint, 1963).

[99] Regetz, J. D., 1960, An experimental determination of the dynamic response of a long hydraulic line, National Aeronautics and Space Administration, Technical note D-576.

[100] Rich, G., 1951, Hydraulic transients, 1st edition, McGraw-Hill, New York (Dover reprint).

[101] Schwarz, W., 1978, "Waterhammer Calculations Taking into Account the Radial and Longitudinal Displacements of the Pipe Wall", Ph.D thesis, Institut fur Wasserbau, Universitat Stuttgart (in German).

[102] Sha, W. T., Soo, S. L., 1979, On the effect of $p\nabla\alpha$ term in multiphase mechanics, International Journal of Multiphase Flow, 5 2: 153-158.

[103] Simpson, A. R., 1986, Large water hammer pressures due to column separation in sloping pipes, Ph.D thesis, The University of Michigan, Department of Civil Engineering.

[104] Skalak, R., 1956, "An Extension of the Theory of Waterhammer", Trans. of the ASME, 78, pp. 105-116.

[105] Stadtke, H., Bestion, D., 2002, State-of-the-Art and Limitations of Present Nuclear Thermal Hydraulic Codes and Models, Eurofastnet, Astar, Deliverable D1.

[106] Streeter, V. L., Lai, C., 1963, Waterhammer Analysis Including Fluid Friction, TransTrans. Am. Soc. Civ. Eng., 128: 1491-1524.

[107] Streeter, V. L., 1983, Transient cavitating pipe flow, ASCE Journal of Hydraulic Engineering, 109, No. HY11: 1408-1423.

[108] Svingen, B., 1996, Fluid Structure Interaction in Piping Systems, PhD thesis, The Norwegian University of Science and Technology, Faculty of Mechanical Engineering.

[109] Tang, T., Teng, Z.-H., Wang, J., 2001, "Convergence Analysis of Relaxation Schemes for Conservation Laws with Stiff Source Terms", Methods and Applications of Analysis, 8(4), pp. 667-680.

[110] Taylor, S. T., Yau, S. C. B., 2003, Boundary control of a rotating Timoshenko beam, ANZIAM - Australian & New Zealand Industrial and Applied Mathematics Journal, 44 E: 143-184.

[111] Tentarelli, S. C., 1990, Propagation of noise and vibration in complex hydraulic tubing systems, Ph.D thesis, Department of Mechanical Engineering, Lehigh University.

[112] Tijsseling, A. S., Fan, D., 1991, The response of liquid-filled pipes to vapor cavity collapse, Transactions of SMiRT11, 183-188.

[113] Tijsseling, A. S., 1993, Fluid-structure interaction in case of waterhammer with cavitation, Ph.D thesis, Delft University of Technology, Faculty of Civil Engineering.

[114] Tijsseling, A. S., Vardy, A. E., Fan, D., 1996, "Fluid-Structure Interaction and Cavitation in Single-Elbow Pipe System", Journal of Fluids and Structures, 10, pp. 395-420.

[115] Tijsseling, A. S., 1996, "Fluid-Structure Interaction in Liquid-Filled Pipe Systems: A Review", Journal of Fluids and Structures, 10, pp. 109-146.

[116] Tijsseling, A. S., Lavooij, C. S. W., 1997, "Water hammer with fluid-structure interaction", Applied Scientific Research, 47, pp. 273-285.

[117] Tijsseling, A. S., 2003, "Exact Solution of Linear Hyperbolic Four-Equation System in Axial Liquid-Pipe Vibration", Journal of Fluids and Structures, 18, pp. 179-196.

[118] Tijsseling, A. S., 2007, Water hammer with fluid-structure interaction in thick-walled pipes, Computers and Structures, 85: 844-851.

[119] Timoshenko, S. P., Young, D. Y., 1961, Vibration problems in engineering, 3rd edition, D. van Nostrand, New York, 329-331.

[120] Timoshenko, S. P., 1921, On the correction for shear of the differential equation for trasverse vibrations of prismatic bars, Philosophical Magazine, 41: 744-746.

[121] Tiselj, I., Cizelj, L., 1993, Stresses in the steam generator U tubes during large loss of coolant accident, IJS Report, IJS-DP-6766, Confidential.

[122] Tiselj, I., 1997, Sheme drugega reda natančnosti za dvofluidne modele dvofaznega toka (in Slovene), Second order accurate schemes for two-fluid models of two-phase flow, Ph.D disertation, Faculty of mathematics and physics, University of Ljubljana.

[123] Tiselj, I., Petelin, S., 1997, "Modeling of Two-Phase Flow with Second-Order Accurate Scheme", Journal of computational physics, 136, pp. 503-521.

[124] Tiselj, I., Petelin, S., 1998, First and Second-order Accurate Schemes for Two-Fluid Models, ASME Journal of Fluids Engineering, 120: 363-368.

[125] Tiselj, I., Horvat, A., 2002, "Accuracy of the Operator Splitting Technique for Two-Phase Flow with Stiff Source Terms", Proceedings of ASME FEDSM02, 2002 ASME FED Summer Meeting.

[126] Tiselj, I., Černe, G., Horvat, A., Gale, J., Parzer, I., Giot, M., Seynhaeve, J. M., Kucienska, B., Lemonnier, H., 2004, "WAHA3 Code Manual", WAHALoads project deliverable D10, Ljubljana, Download: http://www.rcp.ijs.si/jgale/WAHA.pdf.

[127] Tiselj, I., Gale, J., 2008 (accepted), Numerical integration of unsteady friction models in pipe flow simulations, Journal of Hydraulic Research.

[128] Toro, E. F., 1999, Rieman Solvers and Numerical Methods for Fluid Dynamics, A practical introduction, 2nd edition, Springer.

[129] Trac-M/FORTRAN90 Theory Manual, 2001, NUREG/CR-6724.

[130] Trapp, J. A., Ransom, V. H., 1982, A Choked-Flow Calculation Criterion for Nonhomogeneous, Nonequilibrium, Two-Phase Flow, International Journal of Multiphase Flow, 8 6: 669-681.

[131] Valentin, R. A., Phillips, J. W., Walker, J. S., 1979, "Reflection and Transmission of Fluid Transients at an Elbow", Transactions of SMiRT5, Paper B 2-6.

[132] Vardy, A. E., Fan, D., 1986, Water hammer in a closed tube, Proc. of the 5th International Conference on Pressure Surges BHRA, 123-137.

[133] Von Karman, 1911, "Ueber die Formanderung dunnwandiger Rohre", Zeitschrift des Vereines deutscher Ingenieure, 55(2), pp. 1889-1895.

[134] Walker, J. S., Phillips, J. W., 1977, "Pulse Propagation in Fluid-Filled Tubes", Journal of Applied Mechanics, 44, pp. 31-35.

[135] Warsi, Z. U. A., 1998, Fluid Dynamics, Theoretical and Computational Approaches, 2nd edition, CRC Press.

[136] Weber, W., 1866, Theorie der durch Wasser oder andere incompressible Flussigkeiten in elastischen Rohren fortgepflanzten Wellen (Theory of waves propagation in water or in other incompressible liquids contained in elastic tubes), Berichte uber die Verhandlungen der Koniglichen Sachsischen Gesellschaft der Wissenschaften zu Leipzig, Germany, Mathematical-Physical Section, 18 (in German): 353-357.

[137] Weber, E.-H., 1850, Ueber die Anwendung die Wellenlehre vom Kreislaufe des Blutes und insbesondere auf die Pulslehre (On the application of wave theory to the circulation of blood and particular on the pulse), Berichte uber die Verhandlungen der Koniglichen Sachsischen Gesellschaft der Wissenschaften zu Leipzig, Germany, Mathematical-Physical Section, 2 (in German): 164-204.

[138] Westinghouse Technology Advanced Manual R-504P, Rev 0296

[139] Weston, E. B., 1885, Description of Some Experiments Made on the Providence, RI Water Works to Ascertain the Force of Water Ram in pipes, Trans. Am. Soc. Civ. Eng., 14: 238.

[140] Wiedermann, A. H., 1982, An elastic-plastic pipe response model for small thickness to diameter ratio pipes in water hammer analysis, ASME-PVP, Fluid Transients and Fluid-Structure Interaction, 64: 116-126.

[141] Wiggert, D. C., Otwell, R. S., Hatfield, F. J., 1985, "The Effect of Elbow Restraint on Pressure Transients", Journal of Fluids Engineering, Transactions of the ASME, 107, pp. 402-406.

[142] Wiggert, D. C., 1986, "Coupled Transient Flow and Structural Motion in Liquid-Filled Piping Systems: A Survey", Proc. of the ASME Pressure Vessels in Piping Conference, Paper 86-PVP-4.

[143] Wiggert, D. C., Hatfield, F. J., Stuckenbruck, S., 1987, "Analysis of Liquid and Structural Transients in Piping by the Method of Characteristics", ASME Journal of Fluids Engineering, 109, pp. 161-165.

[144] Wiggert, D. C., Tijsseling, A. S., 2001, "Fluid transients and fluid-structure interaction in flexible liquid-filled piping", ASME Applied Mechanical Review, 54(5), pp. 455-481.

[145] Wilkinson, D. H., 1978, "Acoustic and Mechanical Vibrations in Liquid-Filled Pipework Systems", Proc. of the BNES International Conference on Vibration in Nuclear Plant, pp. 863-878.

[146] Wood, F. M., 1937, The Application of the Heaviside's Operational Calculus to the Solution of Problems in Waterhammer, Trans. ASME, 59: 707-713.

[147] Wood, D. J., 1968, A study of the response of coupled liquid flow-structural systems subjected to periodic disturbances, ASME Journal of Basic Engineering, 90: 532-540.

[148] Wood, D. J., 1969, Influence of line motion on waterhammer pressures, ASCE Journal of the Hydraulics Division, 95: 941-959.

[149] Wood, D. J., Chao, S. P., 1971, Effect of pipeline junctions on waterhammer surges, ASCE Transportation Engineering Journal, 97: 441-456.

[150] Wylie, E. B., Streeter, V. L., 1978, Fluid Transients, McGraw - Hill International Book Company, New York.

[151] Wylie, E. B., Streeter, V. L., 1978, Column separation in horizontal pipelines, Proc. of the Joint Symp. on Design and Operation of Fluid Machinery, IAHR, ASME,ASCE, Colorado State university, Fort Collins, USA, 1: 3-13.

[152] Young, T., 1802, On the velocity of sound, Journal of the Royal Institution of Great Britain, 1: 214-216.

[153] Young, T., 1808, Hydraulic investigations, subservient to an intended Croonian lecture on the motion of the blood, Philosophical Transactions of the Royal Society (London), 98: 164-186.

[154] Youngdahl, C. K., Kot, C. A., Valentin, R. A., 1980, Pressure transient analysis in piping systems including the effects of plastic deformation and cavitation, ASME Journal of Pressure Vessel Technology, 102: 49-55.

[155] Zhang, L., Tijsseling, A. S., Vardy, A. E., 1999, “FSI Analysis of Liquid-Filled Pipes”, Journal of Sound and Vibration, 224(1), pp. 69-99.

[156] Zhang, X., Huang, S., Wang, Y., 1994, “The FEM of Fluid Structure Interaction in Piping Pressure Transients”, Proc. of the First International Conference on Flow Interaction, pp. 532-535.

# Appendix A. Gauss theorem and Leibniz rule

A natural set of parameters to describe a pipeline or the fluid domain inside that pipeline consists in a line such as the neutral fiber of the pipe and a cross-section sliding on this line (see Figure A-1). The sliding section on the line generates a domain that Coutris [26] denominates a fluid filament. The fluid filament is thus defined by the inner space of a moving and deforming pipe of circular cross-section. The derivations of the Gauss theorem and the Leibniz rule for a fluid filament of arbitrary cross-section are based on extensive theoretical discussions by Lemonnier [82], Delhaye [32] and Coutris [26] and exceed the scope and purpose of the present work. The interested reader can find the derivation in the above references. The purpose of this section is to define the Leibniz rule and the Gauss theorem for a fluid filament of arbitrary cross-section.

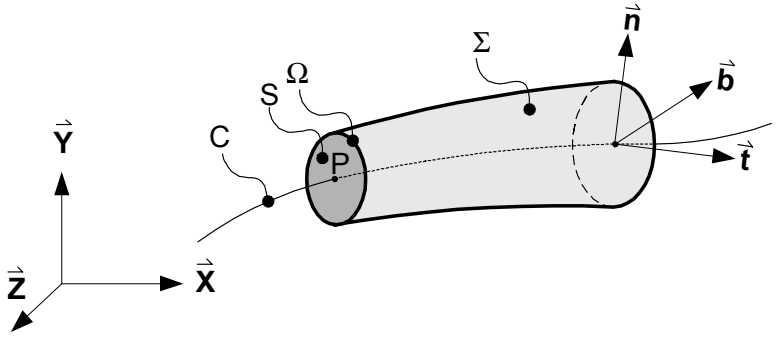


Fig. A-1: A fluid filament generated by the motion of the section *S* limited by circle $\Omega$, the center of which is *P* and lies on the curve *C*.

**The Gauss theorem for a filament of arbitrary cross-section.** Let us described the divergence theorem of vector calculus more commonly known in the older literature as the Gauss theorem. Let *V* be the region in space with boundary *S*. Then the volume integral of the divergence $\nabla\cdot$ **B** of an arbitrary vector or tensor **B** over V and the surface integral of **B** over the boundary *S* of *V* are related by:

$$\int_V \nabla\cdot\mathbf{B}dV = \int_S \mathbf{B}\cdot d\vec{\mathbf{S}} \tag{A-1}$$

Coutris [26, Eq. C5] mentioned in a footnote that the limiting form of the Gauss theorem holds for arbitrary cross-sections. Lemonnier [82] proved this statement. Following Coutris, the starting point is the Gauss theorem applied to a finite and arbitrary portion of a filament (see Figure A-1) limited by two end sections $S_1$ and $S_2$, and the lateral surface of the filament $\Sigma$. The Gauss theorem applied to **B** on *V* is given by:

$$\int_V \nabla\cdot\mathbf{B}dV = \int_\Sigma \mathbf{B}\cdot\vec{\mathbf{n}}_\Sigma dS + \int_{S_1} \mathbf{B}\cdot\vec{\mathbf{n}}_1 dS + \int_{S_2} \mathbf{B}\cdot\vec{\mathbf{n}}_2 dS \tag{A-2}$$

where $\vec{\mathbf{n}}$ is the unit vector normal to *V* pointing outwards the volume and where the subscripts *1*, *2*, and $\Sigma$ refers respectively to surfaces $S_1$, $S_2$, and $\Sigma$. After derivation given by Lemonnier [82], the limiting form of the Gauss theorem, within the Fresnet frame, yields:

$$\int_{S(P,t)} \nabla\cdot\mathbf{B}\lambda dS = \frac{\partial}{\partial s_0}\int_{S(P,t)} \mathbf{B}\cdot\vec{\mathbf{t}}dS + \int_{\Omega(P,t)} \frac{\mathbf{B}\cdot\vec{\mathbf{n}}_\Sigma}{\vec{\mathbf{n}}_\Sigma\cdot\vec{\mathbf{n}}_\Omega}\lambda d\Omega \tag{A-3}$$

where $\lambda$ is the geometrical factor, and $\vec{\mathbf{n}}_\Omega$ is the normal unit vector to the section perimeter and pointing outwards *S*. This equation is very similar to that of Delhaye [32] related to fixed and straight pipes. The main difference arises from the geometrical factor $\lambda = 1 - y/R$ accounting for the lesser weight of points of the cross-section lying closer to the center of the curvature of the neutral fiber of the pipe.

**The Leibniz integral rule for a filament of arbitrary cross-section.** The Leibniz integral rule gives a formula for the differentiation of a definite integral whose limits are functions of the differential variable:

$$\frac{\partial}{\partial t}\int_{a(t)}^{b(t)} f(x,t)dx = \int_{a(t)}^{b(t)} \frac{\partial f}{\partial t}dx + f\left(b(t),t\right)\frac{\partial b}{\partial t} - f\left(a(t),t\right)\frac{\partial a}{\partial t} \tag{A-4}$$

It is sometimes known as the integration under the integral sign. According to the derivation of Lemonnier [82], the Leibniz integral rule for arbitrarily shaped fluid filaments yields (see also [26, Eq. C7]):

$$\begin{aligned}&\int_{S(P,t)} \frac{\partial f}{\partial t}\lambda dS = \frac{\partial}{\partial t}\int_{S(P,t)} f\lambda dS + \\ &\frac{\partial \vec{\mathbf{U}}_C}{\partial s_0}\cdot\vec{\mathbf{t}}\int_{S(P,t)} f\lambda dS + \left(\vec{\mathbf{U}}_C\cdot\vec{\mathbf{t}}\right)\frac{\partial}{\partial s_0}\int_{S(P,t)} f\lambda dS - \frac{\partial}{\partial s_0}\int_{S(P,t)} f\left(\vec{\mathbf{U}}_S\cdot\vec{\mathbf{t}}\right)dS - \int_{\Omega(P,t)} f\frac{\vec{\mathbf{U}}_\Sigma\cdot\vec{\mathbf{n}}_\Sigma}{\vec{\mathbf{n}}_\Sigma\cdot\vec{\mathbf{n}}_\Omega}\lambda dl\end{aligned} \tag{A-5}$$

where $\vec{\mathbf{t}}$ is the vector tangent of the Fresnet frame, $\vec{\mathbf{U}}_\Sigma$ is the displacement velocity of the lateral surface (pipe wall), $\vec{\mathbf{U}}_S$ is the displacement velocity of the section *S* and $\vec{\mathbf{U}}_C$ is the velocity vector of a point *P* attached to the line *C*. The derivation of the Leibniz rule can be found in Lemonnier [82]. When compared with the analogous equation of Delhaye [32] for fixed and straight pipes, Equation (A-5) shows many new terms. New are the second and the third term on the left hand side and they are related respectively to the stretching of *C* and the motion of the center of the cross-section *S* on *C*. The new term on the right hand side is the second term, which is relative to the motion of the cross-section *S*. It is naturally encountered when the balance equations are written on a section translating with respect to the frame of reference.

**Identity for the pressure.** An identity for the pressure is derived from the Gauss theorem. It is a classical transformation in the two-fluid model (Hetsroni, [56]) to collect terms involving the pressure on the interface and pipe boundary and to substitute them with the average of the pressure gradient on the section. This identity is still valid in the case of a moving and deformable pipe. Its derivation is a consequence of the limiting form of the Gauss theorem, that is formally valid also for tensors. Lemonnier [82] derived and proved the following relationship:

$$\tilde{S}_k\nabla p_k = \frac{\partial}{\partial s_0}\tilde{S}_k p_k\frac{\vec{\mathbf{t}}}{\lambda} + \int_{\Omega(P,t)}\frac{p_k\cdot\vec{\mathbf{n}}_\Sigma}{\vec{\mathbf{n}}_\Sigma\cdot\vec{\mathbf{n}}_{k\Omega}}\lambda dl + \int_{\Omega_k(P,t)}\frac{p_k\cdot\vec{\mathbf{n}}_\Sigma}{\vec{\mathbf{n}}_\Sigma\cdot\vec{\mathbf{n}}_{k\Omega}}\lambda dl \tag{A-6}$$

# Appendix B. Derivation rules for vectors in Fresnet frame

This appendix gives an overview of the time and space derivatives of vectors in the Fresnet frame $(\vec{\mathbf{t}},\vec{\mathbf{n}},\vec{\mathbf{b}})$ basis. The results are expressed as functions of the derivatives of the vector components. Let $\vec{\mathbf{B}}$ be an arbitrary vector in the $(\vec{\mathbf{t}},\vec{\mathbf{n}},\vec{\mathbf{b}})$ basis given by:

$$\vec{\mathbf{B}} = B_t\vec{\mathbf{t}} + B_n\vec{\mathbf{n}} + B_b\vec{\mathbf{b}} \tag{B-1}$$

**Time derivatives.** The time derivative of $\vec{\mathbf{B}}$ is given by:

$$\frac{\partial\vec{\mathbf{B}}}{\partial t} = \frac{\partial B_t}{\partial t}\vec{\mathbf{t}} + \frac{\partial B_n}{\partial t}\vec{\mathbf{n}} + \frac{\partial B_b}{\partial t}\vec{\mathbf{b}} + B_t\frac{\partial\vec{\mathbf{t}}}{\partial t} + B_n\frac{\partial\vec{\mathbf{n}}}{\partial t} + B_b\frac{\partial\vec{\mathbf{b}}}{\partial t} \tag{B-2}$$

moreover, since $(\vec{\mathbf{t}},\vec{\mathbf{n}},\vec{\mathbf{b}})$ is a rigid frame:

$$\frac{\partial\vec{\mathbf{t}}}{\partial t} = \vec{\Omega}\times\vec{\mathbf{t}}\text{, and} \qquad \frac{\partial\vec{\mathbf{n}}}{\partial t} = \vec{\Omega}\times\vec{\mathbf{n}}\text{, and} \qquad \frac{\partial\vec{\mathbf{b}}}{\partial t} = \vec{\Omega}\times\vec{\mathbf{b}} \tag{B-3}$$

where $\vec{\Omega}$ is the angular velocity of rotation of the $(\vec{\mathbf{t}},\vec{\mathbf{n}},\vec{\mathbf{b}})$ frame. As a result:

$$\frac{\partial\vec{\mathbf{B}}}{\partial t} = \frac{\partial B_t}{\partial t}\vec{\mathbf{t}} + \frac{\partial B_n}{\partial t}\vec{\mathbf{n}} + \frac{\partial B_b}{\partial t}\vec{\mathbf{b}} + B_t\vec{\Omega}\times\vec{\mathbf{t}} + B_n\vec{\Omega}\times\vec{\mathbf{n}} + B_b\vec{\Omega}\times\vec{\mathbf{b}} \tag{B-4}$$

therefore:

$$\frac{\partial\vec{\mathbf{B}}}{\partial t} = \frac{\partial B_t}{\partial t}\vec{\mathbf{t}} + \frac{\partial B_n}{\partial t}\vec{\mathbf{n}} + \frac{\partial B_b}{\partial t}\vec{\mathbf{b}} + \vec{\Omega}\times\vec{\mathbf{B}} \tag{B-5}$$

The components of the time derivative are then given by:

$$\vec{\mathbf{t}}\cdot\frac{\partial\vec{\mathbf{B}}}{\partial t} = \frac{\partial B_t}{\partial t} + \vec{\mathbf{t}}\cdot\left(\vec{\Omega}\times\vec{\mathbf{B}}\right) \tag{B-6}$$

$$\vec{\mathbf{n}}\cdot\frac{\partial\vec{\mathbf{B}}}{\partial t} = \frac{\partial B_t}{\partial t} + \vec{\mathbf{n}}\cdot\left(\vec{\Omega}\times\vec{\mathbf{B}}\right) \tag{B-7}$$

$$\vec{\mathbf{b}}\cdot\frac{\partial\vec{\mathbf{B}}}{\partial t} = \frac{\partial B_t}{\partial t} + \vec{\mathbf{b}}\cdot\left(\vec{\Omega}\times\vec{\mathbf{B}}\right) \tag{B-8}$$

**Space derivatives.** The balance equations encompass derivatives of vectors with respect to the arc length. By using the components of $\vec{\mathbf{B}}$ it yields:

$$\frac{\partial\vec{\mathbf{B}}}{\partial s} = \frac{\partial}{\partial s}\left(B_t\vec{\mathbf{t}} + B_n\vec{\mathbf{n}} + B_b\vec{\mathbf{b}}\right) \tag{B-9}$$

Expanding the terms and using the derivative rules for the vectors of the Fresnet frame:

$$\frac{d\vec{\mathbf{t}}}{ds} = \frac{\vec{\mathbf{n}}}{R_p}\text{,} \qquad \frac{d\vec{\mathbf{n}}}{ds} = -\frac{\vec{\mathbf{t}}}{R_p} - \frac{\vec{\mathbf{b}}}{T_p}\text{,} \quad \text{and} \qquad \frac{d\vec{\mathbf{b}}}{ds} = \frac{\vec{\mathbf{n}}}{T_p} \tag{B-10}$$

the space derivative of $\vec{\mathbf{B}}$ yields:

$$\frac{\partial \vec{\mathbf{B}}}{\partial s} = \vec{\mathbf{t}} \frac{\partial B_t}{\partial s} + B_t \left( \frac{\vec{\mathbf{n}}}{R_p} \right) + \vec{\mathbf{n}} \frac{\partial B_n}{\partial s} + B_n \left( -\frac{\vec{\mathbf{t}}}{R_p} - \frac{\vec{\mathbf{b}}}{T_p} \right) + \vec{\mathbf{b}} \frac{\partial B_b}{\partial s} + B_b \left( \frac{\vec{\mathbf{n}}}{T_p} \right) \tag{B-11}$$

Collecting the terms together yields:

$$\frac{\partial \vec{\mathbf{B}}}{\partial s} = \vec{\mathbf{t}} \left( \frac{\partial B_t}{\partial s} - \frac{B_n}{R_p} \right) + \vec{\mathbf{n}} \left( \frac{\partial B_n}{\partial s} + \frac{B_t}{R_p} + \frac{B_b}{T_p} \right) + \vec{\mathbf{b}} \left( \frac{\partial B_b}{\partial s} - \frac{B_n}{T_p} \right) \tag{B-12}$$

Finally the projections of these derivatives are:

$$\vec{\mathbf{t}} \cdot \frac{\partial \vec{\mathbf{B}}}{\partial s} = \frac{\partial B_t}{\partial s} - \frac{B_n}{R_p} \tag{B-13}$$

$$\vec{\mathbf{n}} \cdot \frac{\partial \vec{\mathbf{B}}}{\partial s} = \frac{\partial B_n}{\partial s} + \frac{B_t}{R_p} + \frac{B_b}{T_p} \tag{B-14}$$

$$\vec{\mathbf{b}} \cdot \frac{\partial \vec{\mathbf{B}}}{\partial s} = \frac{\partial B_b}{\partial s} - \frac{B_n}{T_p} \tag{B-15}$$

# Appendix C. Thermo-fluid dynamics equations in Eulerian coordinates

This appendix gives a short insight into the standard 1D thermo-fluid dynamics models that are based on the equations derived in Eulerian coordinates. The Eulerian coordinates are fixed in space. Typical single and two-phase flow water hammer models in Eulerian coordinates together with the results of a simple water-hammer experiment are given.

## C.1. Single-phase flow equations

The research of single-phase water hammer has a long tradition. Blaise Pascal in the 1600s contributed to some of the initial theory to this field, Bernoulli (1738) and Euler established the general equations of hydrodynamics (see also Menabrea [86], Young [152,153], brothers Weber [137,136], Weston [139], Carpenter [21], and Frizell [42]). Joukowsky [66] in 1898 developed the fundamental equation of the single-phase water hammer that relates the pressure changes $\Delta p$ to the velocity changes $\Delta v_k$ in the fluid:

$$\Delta p = \rho_k c_k \Delta v_k \qquad \text{where} \qquad \Delta v_f = v_{f,before} - v_{f,after} \tag{C-1}$$

where $\rho_k$ is the fluid density and $c_k$ is the speed of sound in fluid $k$. The equation was developed from the momentum jump condition (conservation law) under the special case where the flow velocity is negligible compared to the speed of sound. Equation (C-1) is commonly known as the **Joukowsky equation**, sometimes **Joukowsky-Frizell** or the **Allievi equation**. Although the water hammer equations were fully established by the 1960s (Allievi [3,4], Jaeger [63], Wood [146], Rich [100], Parmakian [98], Streeter and Lai [106], Wylie and Streeter [150], etc.), these equations have since been analyzed, discussed, redefined and elucidated in numerous classical texts [47]. The full single-phase water hammer equations with convective terms, gravity and friction terms are defined as:

$$\frac{1}{\rho_f c_f^2}\frac{\partial p}{\partial t} + v_f \frac{1}{\rho_f c_f^2}\frac{\partial p}{\partial x} + \frac{\partial v_f}{\partial x} = 0 \tag{C-2}$$

$$\rho_f \frac{\partial v_f}{\partial t} + \rho_f v_f \frac{\partial v_f}{\partial x} + \frac{\partial p}{\partial x} = \rho_f g \sin(\alpha) - \rho_f f_{wf} \frac{v_r |v_r|}{4R} \tag{C-3}$$

These equations constitute the fundamental equations for 1D water hammer problems and contain all the physics necessary to model wave propagation in complex single-phase fluid-filled piping systems. The standard single-phase water hammer theory correctly predicts extreme pressures and wave periods, but it usually fails in accurately calculating damping and dispersion of wave fronts [150]. The reason is a number of effects that are not taken into account in the standard theory (dissolved and free air, solidified sediment deposit at the pipe walls, unsteady friction and unsteady minor losses, non-elastic behavior of the pipe wall material, etc.). Another omitted effect is FSI in all possible ways.

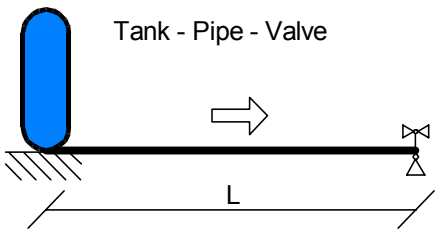


*v = 0.4 m/s, p = 3.42bar, $\rho_f$ = 997.6 kg/m$^3$, K = 2.18E9 Pa*
*$S_t$ = 2.84E-4 m$^2$, E = 0 and 120 GPa, L = 36 m.*

Fig. C-1: Geometry of the simple Tank-Pipe-Valve system. The valve is rapidly closed at time zero.

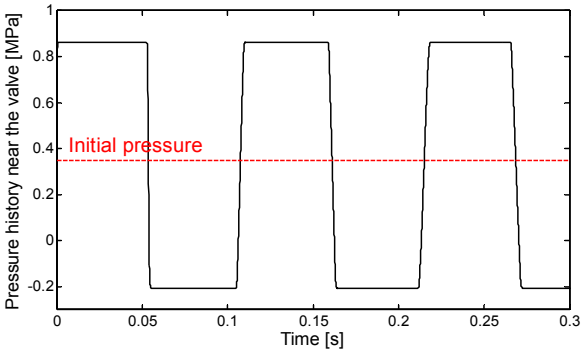


Fig. C-2: Pressure history near the valve.

Figure C-2 shows a typical single-phase flow pressure history near the valve in a Tank-Pipe-Valve system due to instantaneous valve closure. Equations (C-2) and (C-3) were applied without source terms, thus FSI, damping, body forces, friction, and two-phase flow effects were excluded. The pressure rise above and drop below the initial pressure equals the Joukowsky equation prediction (C-1). The duration of one pressure peak is exactly $t_1 = 2\ L / c_f$.

## C.2. Two-phase flow equations

**Physical models and basics.** Ishii and Hibiki [62] stressed that two-phase flow thermo-fluid dynamics is an order of a one magnitude more complicated subject than that of the single-phase flow due to the existence of a moving and deformable interface and its interactions with the phases. Significant efforts have been made in recent years to develop accurate general two-phase formulations, mechanistic models for interfacial transfer and interfacial structures, and computational methods to solve these predictive models. Standard two-phase flow models are classified according to the number of partial differential equations that constitute the model. Table C-1 shows some of the most important models.

*Table C-1: Typical two-phase flow models.*

| Number of eqs. | Description | Vector of basic variables | Notes |
|---|---|---|---|
| 2 | Single-phase water hammer equations | $\vec{\psi}=\{p, v_f\}$ | |
| 3 | Homogeneous Equilibrium Model (HEM). Thermal and mechanical equilibrium. | $\vec{\psi}=\{\rho_m, \rho_m v_m, \rho_m e_m\}$ | Theoretically important, interesting for FSI. |
| | Inhomogeneous model without heat transfer | $\vec{\psi}=\{\alpha, v_g, v_f\}$ | |
| 4 | Drift-flux model - one phase in saturation (usually vapor). | $\vec{\psi}=\{\rho_m, \rho_g, \rho_m v_m, \rho_m e_m\}$ | |
| 5 | Thermal non-equilibrium, mechanical equilibrium. | $\vec{\psi}=\{\rho_g, \rho_f, \rho_m v_m, \rho_f e_f, \rho_g e_g\}$ | Not used in practice |
| | One phase in saturation, the other in non-equilibrium, mechanical non-equilibrium | $\vec{\psi}=\{\rho_g, \rho_f, \rho_g v_g, \rho_f v_f, \rho_m e_m\}$ | |
| 6 | Thermal and mechanical non-equilibrium. Both pressures equal. | $\vec{\psi}=\{\rho_f, \rho_g, \rho_f v_f, \rho_g v_g, \rho_f e_f, \rho_g e_g\}$ | Main model in nuclear thermal-hydraulics computer codes. |
| 7 | Thermal and mechanical non-equilibrium. Non-equal pressures $X = p_2$ | $\vec{\psi}=\{\rho_f, \rho_g, \rho_f v_f, \rho_g v_g, \rho_f e_f, \rho_g e_g, X\}$ | Two-pressure model |
| | Transport equation for interfacial area concentration $X = a_{gf}$ | | |
| | Transport equation for concentration of non-condensable gas $X = \alpha_g$ | | |
| 8 | Multi-field models | Annular flow: the same phase is modeled with a separate conservation equation for the liquid film at the wall and a separate equation for the droplets in the core. | |
| | Multi-group models | Bubbly flow: bubble size spectra divided into various classes. Each class of bubbles treated with a separate balance equation. | |

The most frequently used **six-equation two-fluid model** is formulated by considering each phase separately. The model is described in every classical work concerning multiphase flows including Ishii and Hibiki [62], Moody [89], Toro [128], Warsi [135], and also researchers like Lemonnier [82] or Tiselj et al. [126] who also integrated the model into the WAHA (WAterHAmmer) computer code. The six-equation two-fluid model of the two-phase flow is derived from Navier-Stokes's system and is expressed in terms of conservation equations governing the balance of mass, momentum, and energy for each phase. The two-phase flow field equations describing the conservation principles require additional constitutive relations or balance equations (also **closure relations**) for mass, momentum and energy transfers from the $k^{th}$-phase to the interface. Closure relations encompass the turbulence effects for momentum and energy lost with averaging as well as for interfacial exchanges for mass, momentum and energy transfer. The interfacial transfer rates can be considered as the product of the interfacial flux and the available interfacial area. In the two-phase flow analysis, the void fraction and distribution of the

interface area represent the two fundamental geometrical parameters, which are closely related to the corresponding flow regime. The 1D application of the two-phase models is used for simulations of transients in piping systems whenever pipe's radius over pipe's length ratio is small. The closure relations replace various information that are lost with the averaging made to get the 1D model. The computer power still limits the utilization of the full 3D models for simulations of processes. Ishii and Hibiki [62] classify two-phase flows according to the structure of the interface into the following major groups called **flow regimes** or patterns:

- Separated flows: Film flow, annular flow, jet flow.
- Mixed or transitional flows; Cap, slug or churn turbulent flow, Bubbly annular flow, Droplet annular flow, Bubbly droplet annular flow.
- Dispersed flows: Bubbly flow, Droplet flow, Particulate flow.

Flow regime maps are coded in computer programs with various levels of complexity: from a very detailed flow regime map applied in the RELAP5 code [20] to less detailed applied in the CATHARE code [13]. The standard method using the flow regime transition criteria and the flow regime-dependent closure relations is limited by the fact that closure relations are mainly based on experimental measurements and are thus valid only for certain (steady state) conditions and certain flow regimes. The uncertainty of such correlations and conditions for the transition between flow regimes is even higher during the fast transients, which are considered in this study.

**Typical six-equation two-phase flow model.** A typical 1D six-equation two-phase flow model in the field of nuclear pipeline thermo-fluid dynamics is given in this section. The described two-fluid model of the two-phase flow belongs to the WAHA [126] code and it similar to the models of RELAP5 [20], Cathare [13], Trac and Trace [129] computer codes. The basic equations are the mass, momentum and energy balances for the liquid and the vapor, with terms for pipe elasticity and without terms for wall-to-fluid heat transfer. The continuity, momentum and internal energy balance equations used in the WAHA code are (equations are derived in Eulerian coordinates):

$$\frac{\partial}{\partial t}\alpha_k S\rho_k + \frac{\partial}{\partial x}\alpha_k S\rho_k v_k = -iS\Gamma_g \tag{C-4}$$

$$\frac{\partial}{\partial t}\alpha_k S\rho_k v_k + \frac{\partial}{\partial x}\alpha_k S\rho_k v_k^2 + \alpha_k S\frac{\partial p}{\partial x} - iS\cdot CVM + Sp_i\frac{\partial \alpha_k}{\partial x} = iSF_i + SF_{k,gx} - SF_{k,t} - iS\Gamma_g v_i \tag{C-5}$$

$$\frac{\partial}{\partial t}\alpha_k S\rho_k e_{tot,k} + \frac{\partial}{\partial x}\alpha_k S\rho_k e_{tot,k}v_k + p\frac{\partial}{\partial t}\alpha_k S + \frac{\partial}{\partial x}\alpha_k Spv_k = SQ_{ik} - iS\Gamma_g(h_k^* + v_k^2/2) + Sv_k F_{k,gx} \tag{C-6}$$

Where $e_{tot,k} = e_k + v_k^2/2$ is the total specific phasic energy, $h_k = e_k + p/\rho_k$ is the specific phasic enthalpy, $\alpha_k$ is the phasic volume fraction, $\Gamma_g$ is the vapor generation rate, $i$ is the phase factor, $Q_{ik}$ is the phasic volumetric heat flux, $F_i$ is the interface drag force, $p_i$ is the interfacial pressure term, $F_{k,t}$ is the phasic wall friction, $F_{k,gx}$ is the phasic gravity force in axial direction, and $CVM$ is the virtual mass term. The $p_i$ and $CVM$ terms were added to ensure hyperbolicity of the system of equations, which is required by the numerical method. The equations can be applied for the fluid and vapor phase using the definitions in Table C-2. For more details on this model see the WAHA code manual [126].

*Table C-2: Application of the WAHA code equations for fluid and vapor phase or mixture.*

| Property | index *k* | vapor volume fraction $\alpha_k$ | phase factor *i* |
|---|---|---|---|
| Fluid | *f* | 1 - $\alpha$ | 1 |
| Vapor | *g* | $\alpha$ | -1 |

Figure C-3 shows the geometry and initial conditions for a water hammer transient that is initiated in steady state flow by rapid valve closure. Figure C-4 shows the single and two-phase pressure histories near the valve that are compared to the experiment. Table C-1 contains a brief description of various two-phase flow models. Two of them, the six-equation model of WAHA code and the three-equation

HEM model, are compared in Figure C-5. Figure C-6 shows the importance of an accurate specification of the flow regime and the corresponding flow regime dependent closure terms in two-phase flow codes.

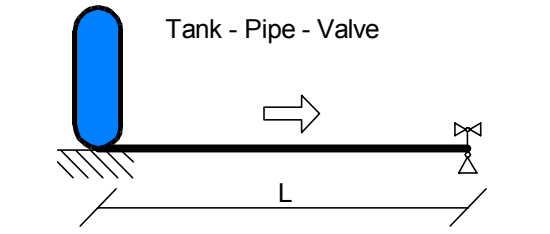


*v = 0.4 m/s, p = 3.42bar, $\rho_f$ = 997.6 kg/m$^3$, K = 2.18E9 Pa*
*$S_t$ = 2.84E-4 m$^2$, E = 120 GPa, L = 36 m.*

Fig. C-3: Geometry of the Simpson pipe [103] experiment; the valve is rapidly closed.

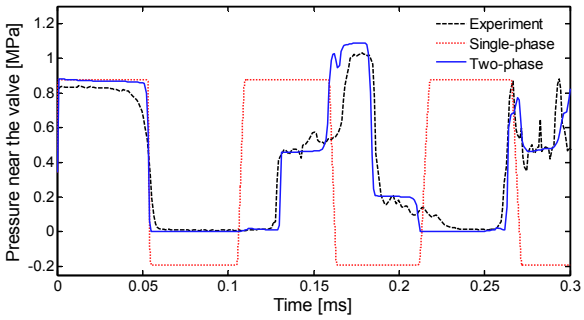


Fig. C-4: Pressure history near the valve: two-phase code accurately describes transient.

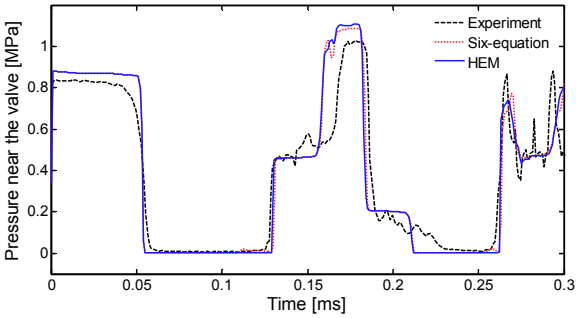


Fig. C-5: Pressure history near the valve: comparison between six-equation WAHA code and HEM model.

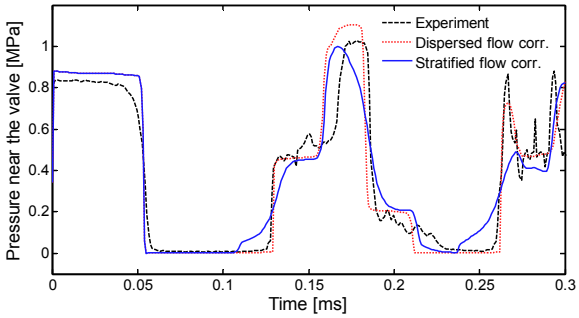


Fig. C-6: Pressure history near the valve: flow regime dependent closure terms are important.

The transition between the single and two-phase flow in the six-equation two-phase flow model starts when the pressure of the single-phase liquid drops below the saturation pressure or when the vapor volume fraction exceeds the numerical uncertainty criterion. The relaxation source terms i.e. heat, mass and energy transfers are calculated only in two-phase flows. The transition back to single-phase flow starts when the vapor volume fraction becomes zero.

The phenomenon of single to two-phase flow transition represents one of the crucial differences between the 'standard' numerical simulations of single-phase flows (CFD) and the numerical simulations of the multi-phase flows (CMFD - Computational Multi-Fluid Dynamics). The transition from single to two-phase flow emerges inside the particular computational volume as a consequence of the **thermo-dynamical instability** in the single-phase flow or as a consequence of the **convection** of two-phase flow from a contiguous volume. The Navier-Stokes equations are sufficient to describe single-phase flow with a three-equation model and, when equipped with appropriate closure relations at the interface, also two-phase flow with (usually) six-equation model. But the problem that arises in transition modeling is that the Navier-Stokes equations are not sufficient to describe the transition from single to two-phase flow, where for example bubbles are being generated in the single-phase liquid due to the cavitation. The applied model describes single-phase flow with six equations where the second, non-existing phase is virtually present with a residual volume fraction ($\alpha_{rez} = 10^{-10}$). As eigenvalues and eigenvectors are defined also in the volumes with single-phase, this approach automatically solves the problem with convection of the two-phase into the volume previously filled with the single-phase.

## C.3. Closure relationships for six-equation two-fluid model

The mass, momentum and internal energy balance equations contain several undefined source terms which are given in this section. The modeling of the interface heat, mass and momentum exchange, wall friction forces, body forces, etc. in various physical models relies on the empirically derived, (usually)

nondifferential correlations that are usually flow-regime dependent. Our experiences with transient flow modeling show, that a very simple flow regime map with only one flow regime that corresponds to the dispersed bubbly flow is sufficient for accurate simulations of the FSI transient flow. The closure relations were directly extracted from the WAHA code [126] and are briefly described below. More details are given in the WAHA code manual.

**Water properties.** Whenever realistic water properties are evaluated, an additional equation of state for each phase is needed. The equation of state for phase *k* is defined by Eq. (111) and Eq. (D-1). The derivatives on the right hand side of the Eq. (111) are determined by the water property subroutines that are based on the ASME steam tables. Water properties are pre-tabulated and saved in ASCII file for *400* pressures: *-95 bar* < p < *1000 bar* and *500* temperatures: *273 K* < T < *1638 K*. The equation of state relationships are obtained with a three-point interpolation.

**Phase-to-interface mass flux.** The mass transfer (vapor generation rate $\Gamma_g$) is calculated as:

$$\Gamma_g = -\frac{Q_{if} + Q_{ig}}{h_g^* - h_f^*} \tag{C-7}$$

where $h_k$* are specific phasic enthalpies ($h_k = e_k + p / \rho_k$) and $Q_{ik}$ are fluid-to-interface heat fluxes. The specific enthalpies are defined as:

$$\begin{aligned} h_f^* &= h_f \quad \text{and} \quad h_g^* = h_{g,sat} \quad \text{if} \quad \Gamma_g > 0 \\ h_f^* &= h_{f,sat} \quad \text{and} \quad h_g^* = h_g \quad \text{if} \quad \Gamma_g < 0 \end{aligned} \tag{C-8}$$

**Phase-to-interface heat flux.** The fluid-to-interface volumetric heat fluxes are calculated as:

$$Q_{ik} = H_{ik}(T_S - T_k) \qquad k = f, g \tag{C-9}$$

where $H_{ik}$ are the heat transfer coefficients. In WAHA, for the dispersed flow the vapor generation rate is calculated with the Homogeneous Relaxation Model (HRM) proposed by Downar-Zapolski et al. [34], and modified by Lemonnier [81]:

$$\Gamma_g = -\rho_m \frac{X - X_{sat}}{\theta} \tag{C-10}$$

where $X$ is the vapor quality, $X_{sat}$ is the saturation quality and $\theta$ is the relaxation time correlation:

$$X = \frac{\alpha\rho_g}{\rho_m} \text{ and } X_{sat} = \frac{h_m - h_{f,sat}}{h_{g,sat} - h_{f,sat}} \text{ and } \theta = \max \begin{cases} 10^{-8} \\ 6.51 \cdot 10^{-4} \alpha_w^{-0.257} \left| \dfrac{\Delta p}{p_{sat}} \right|^{-2.24} & \text{if} \quad p \le 10^6 Pa \\ 3.84 \cdot 10^{-7} \alpha_w^{-0.540} \left| \dfrac{\Delta p}{p_c - p_{sat}} \right|^{-1.76} & \text{if} \quad p > 10^6 Pa \end{cases} \tag{C-11}$$

where $p_c$ = *221.2 bar* is the critical pressure, $\Delta p$ = *max(1000 Pa,* $|p_s - p|$*)*, $p_s$ is the saturation pressure and $\alpha_w = \max(10^{-6}, \alpha)$.

The vapor heat transfer coefficient $H_{ig}$ is assumed to be extremely large to bring the vapor in equilibrium at a given pressure (similar in the RELAP5 code for dispersed flows):

$$H_{ig} = \min\left[ 10^6 \cdot \frac{\max(\alpha, 10^{-5})}{\max(\alpha, 10^{-9})}(1+\eta\cdot(100+25\cdot\eta)),\quad \max\left(1, -\frac{\Gamma_g\left(h_g^* - h_f^*\right)}{T_S - T_g}\right)\right] \tag{C-12}$$

where $\eta = \left|\max(-2, T_S - T_g)\right|$. The fluid volumetric heat transfer coefficient is then deduced as:

$$H_{if} = \frac{-H_{ig}\left(T_S - T_g\right) - \Gamma_g\left(h_g^* - h_f^*\right)}{(T_S - T_f)} \tag{C-13}$$

In most of the other flow regimes $H_{if}$ and $H_{ig}$ are calculated first, and $\Gamma$ follows from the heat fluxes $Q_{if}$ and $Q_{ig}$.

**Body forces.** The body forces per unit volume due to gravity in a pipe with inclination angle $\gamma$ and considering void fraction, direction and density of the material are defined as:

fluid *k*: $F_{k,gx} = \alpha_k \rho_k\, g \sin(\gamma)$ and $F_{k,gy} = \alpha_k \rho_k\, g \cos(\gamma)$ (C-14)

pipe: $F_{t,gx} = \rho_t\, g \sin(\gamma)$ and $F_{t,gy} = \rho_t\, g \cos(\gamma)$ (C-15)

**Phase-to-interface momentum flux.** The interface friction force is defined as:

$$F_i = C_i \left|v_r\right| v_r + CVM \qquad v_r = v_g - v_f \tag{C-16}$$

In WAHA, for the dispersed flow regime, the interfacial friction coefficient $C_i$ in the momentum equations is calculated from correlations, which are valid for two-component and/or two-phase flow (similar to the RELAP5 model):

$$C_i = \frac{1}{8}\rho_f C_D a_{gf} \tag{C-17}$$

where $C_D$ is the drag coefficient of the slug and $a_{gf}$ is the interfacial area concentration:

$$C_D = 24(1 + 0.1\,\mathrm{Re}^{0.75})/\mathrm{Re} \qquad \text{and} \qquad a_{gf} = 3.6\alpha_{bub}/d_0 \tag{C-18}$$

where *Re* is the Reynolds number, $\alpha_{bub}$ is the modified vapor volume fraction, and $d_0$ is the average bubble diameter, that are defined as:

$$\mathrm{Re} = \frac{(We\cdot\sigma)(1-\alpha)}{\mu_f\sqrt{v_{fg}^2}} \quad \text{and} \quad \alpha_{bub} = \max(\min(\alpha, 0.5), 10^{-5}) \quad \text{and} \quad d_0 = \frac{(We\cdot\sigma)}{\rho_f\, v_{fg}^2} \tag{C-19}$$

The term $\mu_f$ is the liquid viscosity, $(We\cdot\sigma)$ is the product of the critical Weber number and surface tension and $v_{fg}^2$ is the modified relative velocity:

$$(We\cdot\sigma) = \max(5\cdot\sigma,\ 10^{-10}) \qquad \text{and} \qquad v_{fg}^2 = \max\left(v_r^2,\ \frac{(We\cdot\sigma)}{\rho_f \min(D, 0.005\alpha_{bub}^{1/3})}\right) \tag{C-20}$$

**Virtual mass term.** The virtual mass term *CVM* is discussed by Drew et al. [35]. The main purpose of the virtual mass term *CVM* is to ensure hyperbolicity of the six-equation two-phase flow equations, thus only absolute velocities are taken into account in the derivatives of the following equation:

$$CVM = C_{vm}\left(\frac{\partial v_g}{\partial t} + \left(\mu v_f + u_x\right)\frac{\partial v_g}{\partial x} - \frac{\partial v_f}{\partial t} - \left(\mu v_g + u_x\right)\frac{\partial v_f}{\partial x}\right) \tag{C-21}$$

where *Cvm* is the virtual mass coefficient similar to one used in the RELAP5 [20]. It is defined as:

$$C_{VM} = \rho_m \alpha(1-\alpha)\begin{cases} \frac{1}{2}\cdot\frac{1+2\alpha}{1-a} & \alpha \le 0.4 \\ 1.5 - 10(\alpha - 0.4)(\alpha - 0.6) & 0.4 < \alpha \le 0.6 \\ \sqrt{\left(\frac{3-2\alpha}{2\alpha}\right)^2 + \frac{(1-\alpha)(2\alpha-1)}{(1-\alpha+\alpha\rho_g/\rho_f)^2}} & \alpha > 0.6 \end{cases} \tag{C-22}$$

The applied virtual mass term does not ensure unconditional hyperbolicity. Tiselj [122] reported that complex eigenvalues may appear for very large relative velocities in comparison to the mixture speed of sound ($|v_r| > 0.3\, c_m$). However these are extremely rare occasions, not relevant in realistic two-phase flows.

**The wall friction.** The pressure losses due to the wall friction within a given length of a pipe *L* are defined by the Darcy-Weisbach equation (Wylie and Streeter [150]):

$$\Delta p = \rho_k f_{k,t} \frac{v_r |v_r|}{4R} L \tag{C-23}$$

where $v_r = v_k - u_x$. The wall friction force per unit volume is defined as a product of shear stress and contact surface area: $F_{k,t} = \tau_{k,t} S_\Sigma / SL$ and the force balance on a differential pipe section in steady state flow is defined as: $\Delta p S = \tau_{k,t} S_\Sigma$. Then the friction force per unit volume is:

$$F_{k,t} = \frac{\tau_{k,t} S_\Sigma}{SL} = \rho_k f_{k,t} \frac{v_r |v_r|}{4R} \tag{C-24}$$

Much research is currently focused on transient friction (Tiselj and Gale [127], Kucienska [74]).

# Appendix D. Equation of state

The main properties of the fluid are the thermodynamic functions of state and are defined by the equation of state. Consideration of the accurate thermodynamic state properties of the fluid is essential for accurate simulations of single-phase and two-phase flow transients, therefore, the Navier-Stokes system of equations for each phase is supplemented with an additional closure relationship - corresponding equation of state. Fundamentals are briefly described in this appendix.

## D.1. Compressibility and speed of sound

According to the set of applied basic variables in this thesis the density of the fluid $k$ is written as a function of pressure and internal energy $\rho_k = \rho_k (p, e_k)$. The differential **equation of state** is:

$$\partial\rho_k = \left(\frac{\partial\rho_k}{\partial p}\right)_{e_k} \partial p + \left(\frac{\partial\rho_k}{\partial e_k}\right)_p \partial e_k \tag{D-1}$$

where $e_k$ is the phasic specific internal energy, $p$ is the pressure, $\rho_k$ is the density of the fluid.

The single-phase liquid transient pipe flow is under certain circumstances almost isothermal ($\Delta T \sim 0$) where also $\Delta e_k \sim 0$. Such circumstances are encountered during transient pipe flow with 'room' temperature water. This is generally the case in this work. Then the equation of state simplifies into:

$$\partial\rho_k \cong \left(\frac{\partial\rho_k}{\partial p}\right)_{e_k} \partial p \tag{D-2}$$

The **compressibility** $\beta$ is a measure of the relative volume change of a fluid $k$ as a response to a pressure change:

$$\beta_{T \text{ or } S} = -\frac{1}{V}\left(\frac{\partial V}{\partial p}\right)_{T \text{ or } S} \equiv \frac{1}{\rho_k}\left(\frac{\partial\rho_k}{\partial p}\right)_{T \text{ or } S} \tag{D-3}$$

where $V$ is the volume, index $T$ stands for the isothermal compressibility (const. temperature $T$), and $S$ stands for the adiabatic compressibility (const. entropy $S$). Figure D-1 shows, that differences between isothermal and adiabatic compressibility are small, but not negligible.

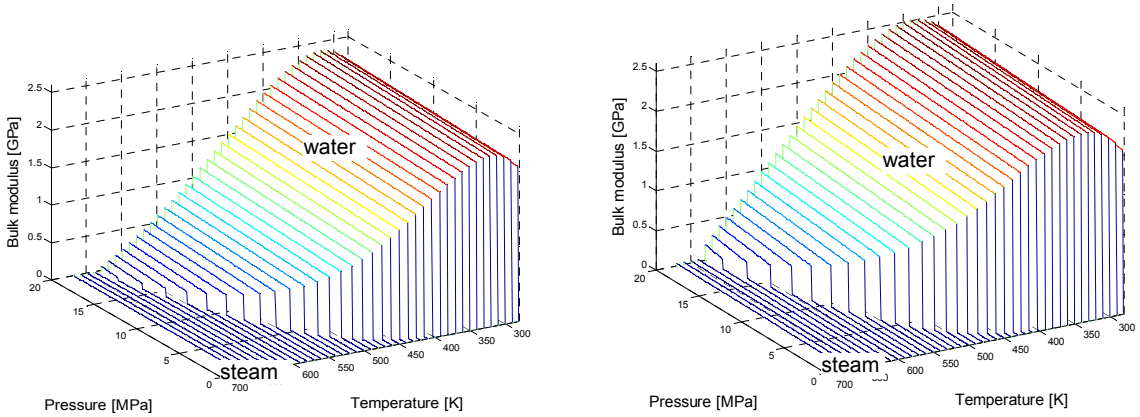


Fig. D-1: Isothermal (left) and adiabatic (right) bulk modulus for water - NIST water properties [80].

The inverse of the compressibility is the **bulk modulus** $K$. The bulk modulus of a fluid essentially measures the resistance of the fluid to uniform compression. It is a thermodynamic quantity therefore the bulk modulus varies with variable thermodynamic state (Fig. D-1). The bulk modulus is defined as the pressure increase needed to affect a given relative decrease in volume.

$$K_{T \text{ or } S} = \frac{1}{\beta_{T \text{ or } S}} = \rho_f \left( \frac{\partial p}{\partial \rho_k} \right)_{T \text{ or } S} \tag{D-4}$$

The adiabatic bulk modulus and the density of a material determine the **speed of sound** $c_0$ of a fluid $k$:

$$c_{0,k}^2 = \frac{K_S}{\rho_k} = \left( \frac{\partial p}{\partial \rho_k} \right)_S = \left( \frac{\partial p}{\partial \rho_k} \right)_{e_k} - \frac{p}{\rho_k^2} \frac{\left( \frac{\partial \rho_k}{\partial e_k} \right)_p}{\left( \frac{\partial \rho_k}{\partial p} \right)_{e_k}} \tag{D-5}$$

Figure D-2 gives the speed of sound in water in a pressure-temperature diagram. The sharp discontinuity appears near the transition from water into steam phase. The speed of sound in single-phase water or steam flow is well defined, while the speed of sound in two-phase flow is a complex flow function. The speed of sound in two-phase water hammer flows can be obtained by substituting the effective bulk modulus of elasticity $K_e$ and the effective density $\rho_e$ in place of $K$ and $\rho_k$ in the equation for the speed of sound (D-5) in single-phase flow. The effective quantities $K_e$ and $\rho_e$ are obtained by the weighted average of the bulk modulus and density of each component, where the partial volumes are the weights. Tiselj [122] derived the following relationship for the speed of sound in two-phase flow, which is valid for the WAHA code described in Appendix C with consideration of the virtual mass term:

$$c_{2F}^2 = \frac{\rho_f \rho_g}{\frac{\alpha \rho_f}{c_g^2} + \frac{(1-\alpha)\rho_g}{c_f^2}} \cdot \frac{C_{vm}\rho_m + \alpha \rho_f + (1-\alpha)\rho_g}{C_{vm}\rho_m^2 + \rho_f \rho_g} \tag{D-6}$$

where $c_g$ and $c_f$ are the (effective) speeds of sound in gas and liquid, respectively.

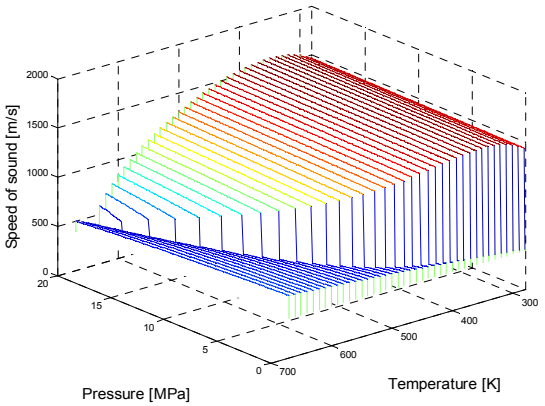


Fig. D-2: The speed of sound water according to the NIST water properties [80].

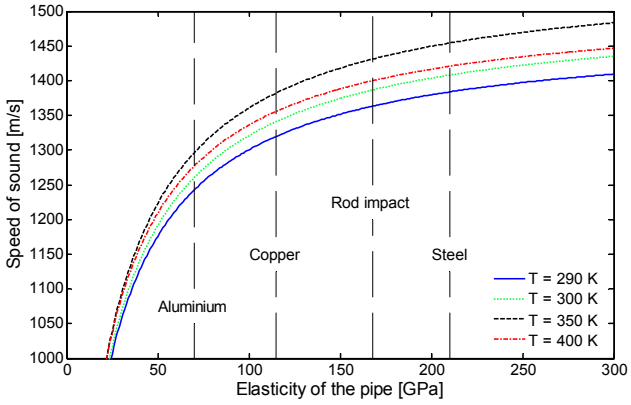


Fig. D-3: The effective speed of sound in water conducted by elastic pipe.

Tijsseling [115] in the standard FSI approach applied the following assumption of compressible material with constant density and bulk modulus. The properties of the fluid are evaluated at the beginning of the transient from the initial state. The temporal derivative of density is replaced by the temporal derivative of the pressure given by relationship (D-2):

$$\partial \rho_k \cong \left( \frac{\partial \rho_k}{\partial p} \right)_{e_k} \partial p \qquad \text{where} \qquad \left( \frac{\partial \rho_k}{\partial p} \right)_{e_k} = \frac{\rho_k}{K_S} = const. \tag{D-7}$$

The theory of water hammer based on the assumption of constant fluid properties is sometimes called the **elastic water hammer theory** according to the analogy with Hooke's linear elasticity theory for solids.

## D.2. Effective speed of sound

The standard water hammer and the FSI theory consider the correction of the speed of sound in a fluid as a consequence of the pipe elasticity. The effective speed of sound in an elastic conduit is given by [66,150]:

$$\frac{1}{c_f^2} = \frac{1}{c_{0,f}^2} + \text{correction} = \left(\frac{\partial \rho_f}{\partial p}\right)_S + \frac{\rho_f}{S}\frac{\partial S}{\partial p} \tag{D-8}$$

where variable *S* stands for the cross-section area and index *S* stands for the adiabatic process. The speed of sound in a compressible fluid within a rigid pipe is obtained by setting $\partial S/\partial p = 0$, and the speed of sound in an incompressible fluid within an extremely flexible pipe is obtained by setting $\left(\partial \rho_f / \partial p\right)_S = 0$.

Korteweg [150] in 1878 introduced the fluid properties through the state equation (D-4) and used the elastic theory of continuum mechanics to evaluate the correction term. Korteweg developed the relationship for the effective speed of sound and improved it with terms for the Poisson coupling (axial stresses and inertia are considered) and a term to account for the propagation of stress waves along the pipe:

$$\frac{1}{c_f^2} = \left(\frac{\partial \rho_f}{\partial p}\right)_S + \frac{2R}{Ee}\psi\rho_f = \frac{\rho_f}{K} + \frac{2R}{Ee}\psi\rho_f = \frac{\rho_f}{K'} \qquad \text{where} \qquad \frac{1}{K'} = \frac{1}{K} + \frac{2R}{Ee}\psi \tag{D-9}$$

where $\psi$ is the multiplication factor that depends on geometry and support conditions. Wylie and Streeter [150] find the following options for the multiplication factor (see Appendix E for details):

- $\psi = 1 - \nu/2$ for a pipe anchored at its upstream end only.
- $\psi = 1 - \nu^2$ for a pipe anchored throughout from axial movement.
- $\psi = 1$ for a pipe anchored with expansion joints throughout.

Korteweg indicated that his theory is valid for long wavelengths with respect to the pipe diameter. Figure D-3 shows the effective speed of sound as a function of elasticity modulus *E* of the piping system for various initial temperatures of the fluid according to Korteweg's equation.

# Appendix E. Hooke's law of elasticity

**Hooke's law for uniaxial strain**. Hooke's law of elasticity is an approximation that states that the amount by which a structure is deformed (the strain) is linearly related to the force causing the deformation (the stress). The materials for which Hooke's law is a useful approximation are known as linear-elastic or "Hookean" materials. The most commonly encountered form of the Hooke law is the spring equation, which relates the force exerted by a spring *F* to the distance *w* it is stretched by a spring constant *k*:

$$F = k\,w \tag{E-1}$$

It can be rewritten in a form valid for Hookean materials under certain loading conditions:

$$\sigma = E\varepsilon \tag{E-2}$$

where *E* is the modulus of elasticity, $\sigma$ the axial stress causing the deformation, and $\varepsilon$ strain is the ratio of the change caused by the stress to the original state of the object. The modulus of elasticity is a measure of the stiffness of a given material.

The modulus of elasticity in uniaxial tension, also known as Young's modulus *E*, is the ratio of stress to strain on the loading plane along the loading direction:

$$E = \frac{\sigma_{ii}}{\varepsilon_{ii}} \qquad \text{i = x,y,z} \tag{E-3}$$

Other moduli describe the material response to other kinds of stress. The shear modulus *G* describes the response to shear and is related to the elasticity modulus by the relationship:

$$G = \frac{E}{2(1+\nu)} \tag{E-4}$$

where $\nu$ is the Poisson ratio. When a sample of material is stretched in one direction, it tends to get thinner in the other two directions. The Poisson ratio $\nu$ is a measure of this tendency. Tensile deformation is considered as positive and compressive deformation is considered as negative:

$$\nu = -\frac{\text{transverse unit strain}}{\text{longitudinal unit strain}} = -\frac{\varepsilon_{yy}}{\varepsilon_{xx}} \tag{E-5}$$

The Poisson ratio for most metals falls between 0.25 and 0.35. Materials with a Poisson ratio of exactly 0.5 (rubber) are incompressible, since the sum of all their strains leads to a zero volume change. Cork, on the other hand, has a Poisson ratio close to zero.

The Young elasticity modulus and the density of a material determine the speed of sound in the solid material (the wall of the piping system) in the axial direction $c_t$ (longitudinal waves):

$$c_t = \sqrt{\frac{E}{\rho_t}} \tag{E-6}$$

**General form of Hooke's law for 3D isotropic material**. Most metallic alloys are considered isotropic, where by definition the material properties are independent of the direction. Such materials have only 2 independent variables, Young elasticity modulus and Poisson ratio. Hooke's law for isotropic materials in compliance matrix form is given by:

$$\begin{bmatrix}\varepsilon_{xx}\\ \varepsilon_{yy}\\ \varepsilon_{zz}\\ \varepsilon_{yz}\\ \varepsilon_{zx}\\ \varepsilon_{xy}\end{bmatrix} = \frac{1}{E}\begin{bmatrix}1 & -\nu & -\nu & 0 & 0 & 0\\ -\nu & 1 & -\nu & 0 & 0 & 0\\ -\nu & -\nu & 1 & 0 & 0 & 0\\ 0 & 0 & 0 & 1+\nu & 0 & 0\\ 0 & 0 & 0 & 0 & 1+\nu & 0\\ 0 & 0 & 0 & 0 & 0 & 1+\nu\end{bmatrix}\begin{bmatrix}\sigma_{xx}\\ \sigma_{yy}\\ \sigma_{zz}\\ \sigma_{yz}\\ \sigma_{zx}\\ \sigma_{xy}\end{bmatrix} \tag{E-7}$$

where $\varepsilon_{ij}$ are the strains and $\sigma_{ii}$ and $\tau_{ij}$ are the corresponding stresses depicted in Fig. E-1. The stiffness matrix is equal to the inverse of the compliance matrix, and is given by:

$$\begin{bmatrix}\sigma_{xx}\\ \sigma_{yy}\\ \sigma_{zz}\\ \sigma_{yz}\\ \sigma_{zx}\\ \sigma_{xy}\end{bmatrix} = \frac{E}{(1+\nu)(1-2\nu)}\begin{bmatrix}1-\nu & \nu & \nu & 0 & 0 & 0\\ \nu & 1-\nu & \nu & 0 & 0 & 0\\ \nu & \nu & 1-\nu & 0 & 0 & 0\\ 0 & 0 & 0 & 1-2\nu & 0 & 0\\ 0 & 0 & 0 & 0 & 1-2\nu & 0\\ 0 & 0 & 0 & 0 & 0 & 1-2\nu\end{bmatrix}\begin{bmatrix}\varepsilon_{xx}\\ \varepsilon_{yy}\\ \varepsilon_{zz}\\ \varepsilon_{yz}\\ \varepsilon_{zx}\\ \varepsilon_{xy}\end{bmatrix} \tag{E-8}$$

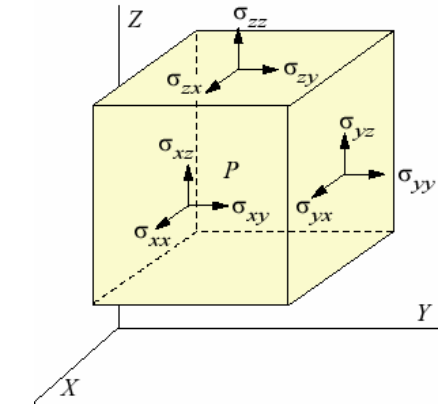


$$\sigma = \begin{vmatrix}\sigma_{xx} & \sigma_{xy} & \sigma_{xz}\\ \sigma_{yx} & \sigma_{yy} & \sigma_{yz}\\ \sigma_{zx} & \sigma_{zy} & \sigma_{zz}\end{vmatrix}$$

Fig. E-1: Infinitesimal cube with stress vectors and the corresponding stress tensor.

**Application of Hooke's law for piping systems**. The wall of the piping system can be treated as a 2D shell structure ($\sigma_{zz} = \sigma_{zx} = \sigma_{yz} = 0$). An approximation of the three-dimensional Hooke law for a two-dimensional structure gives:

$$\begin{bmatrix}\varepsilon_{xx}\\ \varepsilon_{yy}\\ \varepsilon_{xy}\end{bmatrix} = \frac{1}{E}\begin{bmatrix}1 & -\nu & 0\\ -\nu & 1 & 0\\ 0 & 0 & 1+\nu\end{bmatrix}\begin{bmatrix}\sigma_{xx}\\ \sigma_{yy}\\ \sigma_{xy}\end{bmatrix} \tag{E-9}$$

which can be rewritten in an explicit form as:

$$\varepsilon_{xx} = \frac{1}{E}\left(\sigma_{xx} - \nu\sigma_{yy}\right) \tag{E-10}$$

$$\varepsilon_{yy} = \frac{1}{E}\left(\sigma_{yy} - \nu\sigma_{xx}\right) \tag{E-11}$$

where $\sigma_{xx}$ is the axial stress, and $\sigma_{yy}$ is the circumferential stress.

**Application of Hooke's law for evaluation of the cross-section area change**. Wylie and Streeter [150] defined the relationship for the change of cross-section area of the pipe as a result of the circumferential strain. It is given as:

$$\partial S = 2S\partial\varepsilon_{yy} \tag{E-12}$$

The 2D circumferential strain for a pipe wall is given by Eq. (E-11). The circumferential stress appears as a consequence of the internal and external pressures and is given by:

$$\sigma_{yy} = \frac{Rp - (R+e)\,p_{out}}{e} \cong \frac{R}{e}p \tag{E-13}$$

where $R$ is the inner radius of the pipe, $e$ is the pipe thickness, $p$ is the internal pressure (fluid), and $p_{out}$ is the external pressure. Approximation of $p_{out} = 0$ can be usually made because the external pressure is constant with time and position (derivative is zero), in addition the experimental measurements are always relative: therefore the external pressure is usually neglected.

The axial stress $\sigma_{xx}$ can vary according to the support situation, and this in turn yields various definitions of the total circumferential strain. Wylie and Streeter [150] recognized the following support situations for a thin-walled pipeline:

- The pipe anchored only at one end (example: closed piping system is fixed at one end only):

$$\sigma_{xx} = \frac{\sigma_{yy}}{2} \qquad \text{and (E-11) gives:} \qquad \varepsilon_{yy} = \frac{R}{Ee}p\left(1 - \frac{\nu}{2}\right) \tag{E-14}$$

- The pipe anchored throughout against axial movement (example: closed piping system is fixed at both ends, $\varepsilon_{xx} = 0$ ):

$$\sigma_{xx} = \nu\sigma_{yy} \qquad \text{and (E-11) gives:} \qquad \varepsilon_{yy} = \frac{R}{Ee}p\left(1 - \nu^2\right) \tag{E-15}$$

- The pipe anchored with expansion joints throughout (example: open piping system is free at both ends):

$$\sigma_{xx} = 0 \qquad \text{and (E-11) gives:} \qquad \varepsilon_{yy} = \frac{R}{Ee}p \tag{E-16}$$

- The pipe is anchored throughout against axial movement and loaded with axial force (example: closed piping system is fixed at both ends, $\varepsilon_{xx} = 0$ , and loaded with an additional axial force $N_x$):

$$\sigma_{xx} = \nu\sigma_{yy} + \sigma_{N_x} \qquad \text{and (E-11) gives:} \qquad \varepsilon_{yy} = \frac{R}{Ee}p\left(1 - \nu^2\right) - \frac{\nu N_x}{ES_t} \tag{E-17}$$

The Eq. (E-17) where the pipe is anchored throughout against axial movement and loaded with axial force actually corresponds to the case encountered in numerical simulations of the FSI transient pipe flow. The piping section is divided into computational volumes and each computational volume is anchored between two contiguous computational volumes and loaded with an axial force. So, the change in cross-section area that is influenced by the total circumferential strain, and is defined by Eq. (E-12) gives:

$$\partial S = 2S\partial\varepsilon_{yy} = S\frac{2R}{Ee}\left(1 - \nu^2\right)\partial p - S\frac{2\nu}{ES_t}\partial N_x \tag{E-18}$$

# Appendix F. Timoshenko's beam theory

Lateral and rotational motion of piping sections can be described with a Timoshenko beam equation (Taylor and Yau [110], Mendez, Sanches, Morales and Flores [87]), which can be decomposed into a system of four linear first order partial differential equations. Timoshenko's beam theory (TBT) constitutes an improvement over the Euler-Bernoulli theory in that it incorporates shear deformation and rotation inertia effects. These improvements of the Euler-Bernoulli theory make the system of four partial differential equations hyperbolic, which is a fundamental condition for the application of the upwind characteristic numerical method. The importance of the shear deformation and rotatory inertia in the description of the response of beams is well documented (Timoshenko and Young [119]) and first improved theory was given by Timoshenko [120] already in 1921. Antes [7] demonstrated that the Euler-Bernoulli theory is a special case of TBT, and that the difference depends on the geometry and is in general very small for static problems. The four Timoshenko beam equations are (see also Section 3.3):

$$\frac{1}{\kappa S_t G}\frac{\partial Q_y}{\partial t}-\frac{\partial u_y}{\partial s}=-\varphi_z \tag{F-1}$$

$$m_T\frac{\partial u_y}{\partial t}-\frac{\partial Q_y}{\partial s}=f_y(s,t) \tag{F-2}$$

$$\frac{1}{EI_t}\frac{\partial M_z}{\partial t}-\frac{\partial \varphi_z}{\partial s}=0 \tag{F-3}$$

$$I_t\rho_t\frac{\partial \varphi_z}{\partial t}-\frac{\partial M_z}{\partial s}=Q_y \tag{F-4}$$

where, $\varphi_z$ is the pipe rotation velocity, $u_y$ is the pipe displacement velocity, $Q_y$ is the lateral force, $M_z$ is the momentum, $E$ is the Young elasticity modulus, $G$ is the shear modulus, $I_t$ is the moment of inertia, $S_t$ is the pipe wall cross-section area, $\rho_t$ is the pipe wall density, $\kappa$ is the Timoshenko shear coefficient, $m_T$ stands for total mass, and $f_y(s,t)$ stands for the external and body forces. The system of four Timoshenko's beam equations is free of distributed coupling and therefore independent from axial stresses, extensions and fluid transient. The system of Timoshenko beam equations can be coupled to the axial and fluid dynamics locally through junction coupling mechanisms (see Section 3.3 for appropriate derivation). Considering $u_y = \partial w_y / \partial t$ and $\varphi_z = \partial \phi_z / \partial t$, and eliminating momentum and lateral force, the two coupled equations are obtained (Taylor and Yau [110], Antes [7] and Macchelli and Melchiorri [85]):

$$m_T\frac{\partial^2 w_y}{\partial t^2}-\kappa G S_t\frac{\partial}{\partial s}\left(\frac{\partial w_y}{\partial s}-\phi_z\right)=f_y(s,t) \tag{F-5}$$

$$I_t\rho_t\frac{\partial^2 \phi_z}{\partial t^2}-EI_t\frac{\partial^2 \phi_z}{\partial s^2}-\kappa G S_t\left(\frac{\partial w_y}{\partial s}-\phi_z\right)=0 \tag{F-6}$$

After elimination of the rotational displacement the fundamental Timoshenko beam equation gives

$$\frac{EI_t}{m_T}\frac{\partial^4 w_y}{\partial s^4}+\frac{I_t\rho_t}{\kappa G S_t}\frac{\partial^4 w_y}{\partial t^4}-\left(\frac{I_t\rho_t}{m_T}+\frac{I_t E}{\kappa G S_t}\right)\frac{\partial^4 w_y}{\partial s^2\partial t^2}+\frac{\partial^2 w_y}{\partial t^2}= \frac{f_y(s,t)}{m_T}+\frac{I_t\rho_t}{\kappa G S_t m_T}\frac{\partial^2 f_y(s,t)}{\partial t^2}-\frac{EI_t}{\kappa G S_t m_T}\frac{\partial^2 f_y(s,t)}{\partial s^2} \tag{F-7}$$

The left hand part of the equation consists of four terms having the units of force per mass or acceleration. There are terms involving bending momentum, rotational motion, shear force, and

translational motion on the left side of the equation and terms with axially distributed forces on the right side of the equation, respectively. When the shear and rotational terms in (F-7) are small and disregarded, and when there are no external load, the equation becomes the equation of motion of the Euler-Bernoulli beam (Nanguleswaran [92 and 93], Goncalves, Brennan and Elliot [50]):

$$\frac{EI_t}{\rho_t S_t}\frac{\partial^4 w_y}{\partial s^4} + \frac{\partial^2 w_y}{\partial t^2} = 0 \tag{F-8}$$

**Timoshenko's shear coefficient**. The Timoshenko shear coefficient $\kappa$ is defined as the average shear stress on beam cross-section over the shear stress at the neutral axis. The value depends on the shape of the cross-section, and, as pointed out by Cowper [27], on the material's Poisson ratio $\nu$ and on the considered frequency range (only for dynamic problems). Hence, different approximations exist that typically give values between *0.5* and *0.6* for a hollow circular cross-section. Hutchinson [60] defined the precise expression of the Timoshenko shear coefficient valid for pipes:

$$\kappa = \frac{6\left(R^2 + b^2\right)^2 (1+\nu)^2}{7\mathrm{R}^4 + 34\mathrm{R}^2 b^2 + 7\mathrm{b}^4 + \nu\left(12\mathrm{R}^4 + 48\mathrm{R}^2 b^2 + 12\mathrm{b}^4\right) + \nu^2\left(4\mathrm{R}^4 + 16\mathrm{R}^2 b^2 + 4\mathrm{b}^4\right)} \tag{F-9}$$

where $b = R + e$ is outer radius of the pipe. For a thick walled pipe Cowper [27] proposed:

$$\kappa = \frac{6(1+\nu)\left(1+m^2\right)^2}{(7+6\nu)\left(1+m^2\right)^2 + (20+12\nu)m^2} \qquad \text{with} \qquad m = \frac{1}{1+\dfrac{e}{R}} \tag{F-10}$$

For a thin walled pipe $m$ tends to *1* and a simpler and most frequently used definition for the shear coefficient independent of geometry is given by [27]:

$$\kappa = \frac{2(1+\nu)}{4+3\nu} \tag{F-11}$$

The definitions of the Timoshenko shear coefficient are valid for long wavelengths and low frequencies, since they are based on a quasi-static shear-stress distribution. For short wavelengths, the Timoshenko shear coefficient $\kappa$ becomes frequency dependent [113].

# Appendix G. Sklopitev linijske konstrukcije in dvofaznega toka tekočine med hitrimi prehodnimi pojavi - povzetek v slovenskem jeziku

## G.1. Uvod

ITK - Interakcija med tekočino in konstrukcijo (ang.: FSI – Fluid-Structure Interaction) je splošen pojem za opis izmenjave (kinetične) energije med gibajočo tekočino in deformabilno konstrukcijo. Količina izmenjane energije je v veliki meri odvisna od gibkosti in deformabilnosti konstrukcije in upora, ki ga le ta nudi toku tekočine (nanj vplivajo geometrijske in materialne lastnosti konstrukcije, podpore, zunanje obremenitve, itd.). Prav tako je količina izmenjane energije odvisna od tekočine, t.j. od gradientov in amplitude tlačnih valov, hitrostnega polja in od lastnosti stanja tekočine, predvsem stisljivosti. ITK se pojavlja v konstrukcijah, ki so potopljene v tekočino, v konstrukcijah v katerih se pretaka tekočina in v kombinaciji obeh vrst konstrukcij. Področje, ki ga zajema ITK je zelo obširno, od aeronavtike, gradbeništva, (procesnega) strojništva, kemične in naftne industrije, in mnogih drugih področij, do končno glasbil in človeškega telesa.

V disertaciji smo se osredotočili na majhen del področja ITK: na dolge (1D) tanke votle konstrukcije v katerih se pretaka tekočina, t.j. cevovode. Cevovodi in cevni sistemi omogočajo transport velikemu spektru tekočin, od vode, kemikalij, nafte, plina, ipd., hkrati pa v nekaterih primerih zagotavljajo varnostno funkcijo (na primer v jedrski elektrarni – hlajenje sredice reaktorja). Tlačni sunki in mehanske vibracije cevovoda med hitrim prehodnim pojavom lahko zmanjšajo varnost in kvaliteto funkcije, ki jo opravlja cevovod. Odpoved cevovoda ima lahko katastrofalne posledice, lahko povzroči poškodbe in smrti ljudi, ekonomsko škodo, okoljske posledice, odpoved ali vibracije cevovoda in hrup. Tijsseling [113] pravi, da ITK ni splošno priznan pojav, čeprav znatno prispeva k določenim odpovedim cevovodov, kot sta na primer utrujanje ali korozija cevovoda.

Raziskave ITK v cevovodih so relativno mlada veja znanosti, še posebno dvosmerna sklopitev konstrukcije in tekočine in raziskave z dvofazno tekočino, čeprav prve hidravlične raziskave vodnega udara segajo daleč nazaj v 18 stoletje (najbrž pa še mnogo dlje, saj so markantne vodne sisteme gradili že Egipčani in Rimljani). Svingen [108] je klasificiral delo, ki se izvaja na področju ITK in delo, ki ga je še potrebno opraviti, na naslednje 4 točke:

- Eksperimentalne **preiskave**, ki omogočajo širjenje baze podatkov in tako omogočajo izdelavo vedno boljših računalniških programov in povečujejo poznavanje in znanje o pojavu ITK.
- Izpeljava **fizikalnih modelov** in uporaba naprednih **numeričnih shem** prevedenih v učinkovite in zanesljive računalniške programe za raziskovalno in praktično inženirsko delo.
- Priprava **smernic** temelječih na eksperimentih, terenskih izkušnjah in računalniških programih, ki omogočajo prepoznavanje pomembnosti ITK in izdelavo točnejših računskih analiz.
- Določitev **projektantskih kriterijev** za cevovode, s katerimi se je v večini primerov mogoče na preprost način izogniti nepotrebnim posledicam ITK med hitrimi prehodnimi pojavi.

Raziskovalno delo predstavljeno v pričujoči disertaciji se neposredno nanaša na drugo točko, izpeljava naprednih fizikalnih modelov in vpeljava zmogljivejše numerične sheme. Prva točka (eksperimentalne raziskave) je uporabljena za validacijo računalniškega programa, medtem ko tretja in četrta točka logično sledita iz analize rezultatov.

V nadaljevanju povzetka v slovenskem jeziku, so na kratko navedeni osnovni koraki in najpomembnejši rezultati in dosežki, ki so sicer podrobneje opisani v angleškem delu besedila.

**Namen in cilji disertacije.** Disertacija je orientirana k modeliranju interakcije med tekočino in konstrukcijo med eno ali dvofaznim hitrim prehodnim pojavom v cevovodu. Obsežne raziskave in publikacije prof. Tijsselinga [112 - 118] predstavljajo tako imenovani *stat-of-the-art* v svetu modeliranja ITK. Skoraj izključno se uporabljajo linearni hiperbolični sistemi parcialnih diferencialnih enačb prvega

reda, ki v enem modelu opisujejo tako tekočino kot konstrukcijo. Tijsseling in ostala skupnost raziskovalcev uporablja izključno metodo karakteristik (MK). Z MK se lahko rešuje le linearne modele s konstantnimi karakterističnimi hitrostmi, kar že v osnovi izključuje uporabo nelinearnih fizikalnih modelov oziroma izboljšav obstoječih fizikalnih modelov z nelinearnimi členi. Identifikacija omejitev metode karakteristik sugerira osnovni namen pričujoče disertacije, ki je, vpeljati in preveriti numerično metodo, ki omogoča reševanje nelinearnih sistemov diferencialnih enačb. Na podlagi bogatih izkušenj, pridobljenih v času razvoja računalniškega programa WAHA [126] (namenjen je simulacijam termo-hidrodinamike v tekočini med hitrim prehodnim pojavom v popolnoma togem cevovodu brez ITK), in dejstva da se take numerične metode v zadnjem desetletju pogosto uspešno uporabljajo za reševanje inženirskih problemov [44,45,125,127], smo uporabili karakteristično privetrno shemo visoke resolucije drugega reda natančnosti. Drugi pomembni cilji disertacije so (i) izpeljati nelinearne ravnovesne enačbe za tekočino v Lagrangejevem koordinatnem sistemu, (ii) izpeljati enačbe za opis dinamike poljubno ukrivljenega cevovoda, (iii) izpeljati ustrezne fizikalne modele za simulacije ITK, in (iv) izdelati učinkovit in zanesljiv računalniški program za simulacije ITK.

**Originalni prispevek.** Pričujoča disertacija vsebuje več pomembnih originalnih prispevkov k področju modeliranja interakcije med tekočino in konstrukcijo v cevnih sistemih napolnjenih z eno ali dvofazno tekočino med hitrim prehodnim pojavom. Rezultati raziskav so objavljeni v reviji Journal of Pressure Vessel Technology (Gale in Tiselj [45]). Naše raziskave so privedle do naslednji originalnih prispevkov:

1. Izpeljani so ustrezni nelinearni več-enačbni fizikalni modeli za točnejše simulacije pojava ITK med dvofaznim hitrim prehodnim pojavom v poljubno ukrivljenih in deformabilnih cevovodih.
   - Splošna ravnovesna enačba tekočine je izpeljana v premičnem, deformabilnem in poljubno ukrivljenem Lagrangejevem koordinatnem sistemu in uporabljena za izpeljavo ravnovesne enačbe za maso, gibalno količino in energijo. Iz teh enačb so sestavljeni tudi osnovni modeli (termo) dinamike tekočine: šest-enačbni model dvofaznega toka, tri-enačbni model homogenega ravnovesnega toka (HEM model) in dvo-enačbni model kvazi-dvofaznega toka.
   - Izpeljan je fizikalni model za opis osne, prečne, rotacijske in torzijske dinamike poljubno ukrivljenega cevovoda napolnjenega s tekočino.
   - Izpeljani so različno kompleksni fizikalni modeli za opis ITK, sestavljeni iz fizikalnih modelov za tekočino in konstrukcijo.
2. Uporabljena in preverjena je karakteristična privetrna numerična shema visoke resolucije, ki temelji na metodi končnih razlik, ter izpeljana numerična rešitev za stabilno integracijo togih členov v enačbah Timoshenkovega nosilca.
3. Izpeljan in preverjen je računalniški program za simulacije hitrih prehodnih pojavov v dvofazni tekočini v cevovodu ob upoštevanju prispevka ITK. Različne izboljšave in modeli so integrirani v program in uspešno uporabljeni v simulacijah (točne lastnosti vode, faktor upogljivosti kolena, debelostenski model, zunanje sile, obremenitve, elastične podpore, napetosti po von Misesu, model tanka, ventila, ipd.).

## G.2. Ravnovesne enačbe v Lagrangejevem koordinatnem sistemu

Standardne enačbe za opis termodinamike tekočin so izpeljane v Eulerjevem koordinatnem sistemu (dodatek Appendix C). Eulerjeve koordinate so fiksne v prostoru, medtem ko so Lagrangejeve koordinate fiksirane na določen odsek premikajočega se in deformabilnega cevovoda. Lemonnier [82] pravi, da je izpeljava ravnovesnih enačb iz Eulerjevega k.s. v Lagrangejev k.s. obvezna za točen opis termodinamike tekočine v premikajočih se in deformabilnih cevovodih, še posebej, če so premiki cevovoda znatni. Najpomembnejši korak pri transformaciji enačb v Lagrangejev k.s. je povprečenje ravnovesnih enačb preko prečnega preseka cevovoda, ter nato izpeljava in ustrezna uporaba Gausovega (divergenčnega) teorema in Leibnizovega integralskega pravila. Vpeljan je nov splošni parameter $s$ s katerim je enoznačno opisana poljubna krivulja v prostoru. Krivulja predstavlja nevtralno os cevovoda oz. delčka tekočine, ki je predstavljen na sliki G-1.

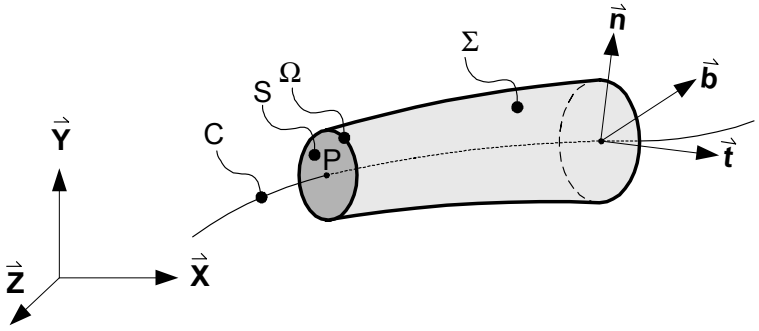


Slika G-1: Delec tekočine, ki ga omejujeta dva prečna prereza $S_1$ in $S_2$ ter ploskev $\Sigma$, ki nastane, če ploskev $S$ z obodom $\Omega$ in centralno točko $P$, drsi po krivulji $C$. Gibanje oboda $\Omega$ generira ploskev $\Sigma$, ki predstavlja steno cevovoda. Krivuljo $C$ opišemo s splošnim parametrom krožnega loka $s$.

**Splošna ohranitvena enačba.** Vsaka posamezna faza oziroma enofazni delec tekočine omejen z jasnimi mejami oziroma stenami cevovoda, se matematično opiše s sistemom Navier-Stokesovih enačb, ki vsebuje kontinuitetno, gibalno in energijsko enačbo. Navier-Stokesove enačbe so podrobneje obravnavane v mnogih knjigah (Moody [89], Ishii in Hibiki [62], Davis [28], Warsi [135], ipd.). Uporabili smo ravnovesne enačbe v najsplošnejši obliki (Ishii in Hibiki [62]):

$$\frac{\partial}{\partial t}\rho_k\psi_k + \nabla\cdot\left(\rho_k\vec{\mathbf{v}}_k\psi_k\right) + \nabla\cdot\mathbf{J}_k - \rho_k\phi_k = 0 \qquad \text{(G-1)}$$

kjer je $\rho_k$ gostota tekočine $k$ ($k$ = $f$ za kapljevine in $k$ = $g$ za pare), $\vec{\mathbf{v}}_k$ je vektor hitrosti tekočine, ostale spremenljivke pa so definirane v tabeli G-1. S pomočjo tabele G-1 lahko izpeljemo ustrezno kontinuitetno, gibalno in energijsko enačbo iz splošne ravnovesne enačbe.

*Tabela G-1: Spremenljivke v splošni ohranitveni enačbi.*

| **Ravnovesje** | $\psi_k$ | $\mathbf{J}_k$ | $\phi_k$ |
|---|---|---|---|
| Mase | 1 | 0 | 0 |
| Gibalne količine | $\vec{\mathbf{v}}_k$ | $p\mathbf{I} - \mathbf{V}_k$ | $\vec{F}_g$ |
| Totalne energije | $e_{tot,k} = e_k + 0.5v_k^2$ | $\vec{\mathbf{q}}_k + \left(p\mathbf{I} - \mathbf{V}_k\right)\cdot\vec{\mathbf{v}}_k$ | $\vec{F}_g\cdot\vec{\mathbf{v}}_k$ |

**Splošna 1D ohranitvena enačba v Lagrangejevem koordinatne sistemu.** Po izpeljavi, podrobneje opisani v angleškem delu, dobimo naslednjo splošno ravnovesno enačbo v Lagrangejevih koordinatah:

$$\frac{\partial}{\partial t}S\alpha_k\rho_k\psi_k + u_x\frac{\partial}{\partial s}S\alpha_k\rho_k\psi_k + \mu\frac{\partial}{\partial s}S\alpha_k\rho_k v_k\psi_k + \mu\frac{\partial}{\partial s}S\alpha_k\mathbf{J}_k\cdot\vec{\mathbf{t}} - \frac{u_y}{R_p}S\alpha_k\rho_k\psi_k + P_i\left(\dot{m}_k\psi_k + \mathbf{J}_k\cdot\vec{\mathbf{n}}_k\right) + P_k\left(\mathbf{J}_k\cdot\vec{\mathbf{n}}_k\right) - S\alpha_k\rho_k\phi_k = 0 \qquad \text{(G-2)}$$

Splošna ravnovesna enačba v Lagrangejevih enačbah se lahko uporabi za poljubno tekočino $k$, pravila za aplikacijo na posamezno fazo pa so definirana v tabeli G-1.

*Tabela G-2: Uporaba splošne ravnovesne enačbe v Lagrangejevih koordinatah za poljubno fazo k.*

| **Faza** | **Indeks *k*** | **Volumski delež pare $\alpha_k$** | **Fazni faktor *i*** |
|---|---|---|---|
| Kapljevina | *f* | 1 - $\alpha$ | 1 |
| Para | *g* | $\alpha$ | -1 |

**Kontinuitetna, gibalna in energijska ohranitvena enačba.** Če v splošno ohranitveno enačbo vstavimo relacije $\psi_k = 1;\quad \mathbf{J}_k = 0;\quad \phi_k = 0$ definirane v tabeli G-1 in nastavek modela generacije pare, dobimo splošno kontinuitetno enačbo:

$$\frac{\partial}{\partial t} S\alpha_k \rho_k + u_x \frac{\partial}{\partial s} S\alpha_k \rho_k + \mu \frac{\partial}{\partial s} S\alpha_k \rho_k v_k = \frac{u_y}{R_p} S\alpha_k \rho_k - iS\Gamma_g \tag{G-3}$$

v kateri so vsi diferencialni členi zbrani na levi strani, nediferencialni členi pa so zbrani na desni strani enačbe. Na podoben način s pomočjo tabele G-1 in mnogih dodatnih zvez in relacij, izpeljemo tudi splošno gibalno in energijsko enačbo:

$$\begin{aligned} &\frac{\partial}{\partial t} \alpha_k S\rho_k v_k + u_x \frac{\partial}{\partial s} \alpha_k S\rho_k v_k + \mu \frac{\partial}{\partial s} \alpha_k S\rho_k v_k v_k + \mu\alpha_k S \frac{\partial p}{\partial s} = \\ &\frac{u_y}{R_p} \alpha_k S\rho_k v_k - iS\Gamma_g v_i + iSF_i + SF_{k,gx} - SF_{k,t} \end{aligned} \tag{G-4}$$

$$\begin{aligned} &\frac{\partial}{\partial t} \alpha_k S\rho_k e_{tot,k} + u_x \frac{\partial}{\partial s} \alpha_k S\rho_k e_{tot,k} + \mu \frac{\partial}{\partial s} \alpha_k S\rho_k v_k e_{tot,k} + \mu \frac{\partial}{\partial s} \alpha_k S v_k p = \\ &\frac{u_y}{R_p} \alpha_k S\rho_k e_{tot,k} - iS\Gamma_g \left( h + \frac{v_k^2}{2} \right) + SQ_{ik} + iSv_k F_i + Sv_k F_{k,gx} - v_k SF_{k,t} \end{aligned} \tag{G-5}$$

**Aplikacija enačb za raven in tog cevovod.** Ob predpostavki, da je cevovod raven, nepremičen in popolnoma tog, postaneta osna in prečna hitrost cevi enaki nič ($u_x = 0$, $u_y = 0$), koeficient raztezanja postane enak ena ($\mu = 1$), člen z radijem ukrivljenosti pa postane enak nič ($u_y / R_p \rightarrow 0$). Splošna kontinuitetna enačba, gibalna enačba in energijska enačba se poenostavijo:

$$\frac{\partial}{\partial t} S\alpha_k \rho_k + \frac{\partial}{\partial s} S\alpha_k \rho_k v_k = -iS\Gamma_g \tag{G-6}$$

$$\frac{\partial}{\partial t} \alpha_k S\rho_k v_k + \frac{\partial}{\partial s} \alpha_k S\rho_k v_k v_k + \alpha_k S \frac{\partial p}{\partial s} = -iS\Gamma_g v_i + iSF_i + SF_{k,gx} - SF_{k,t} \tag{G-7}$$

$$\frac{\partial}{\partial t} \alpha_k S\rho_k e_{tot,k} + \frac{\partial}{\partial s} \alpha_k S\rho_k v_k e_{tot,k} + \frac{\partial}{\partial s} \alpha_k S v_k p = -iS\Gamma_g \left( h + \frac{v_k^2}{2} \right) + SQ_{ik} + iSv_k F_i + Sv_k F_{k,gx} - v_k SF_{k,t} \tag{G-8}$$

Enačbe dejansko predstavljajo standardne ravnovesne enačbe zapisane v Eulerjevem koordinatnem sistemu, ki je razen člena $p \frac{\partial}{\partial t} \alpha_k S$ z zanemarljivim vplivom na lastne vrednosti sistema, popolnoma enak enačbam uporabljenim na primer pri izpeljavi šest-enačbnega dvotekočinskega modela termo-hidrodinamike med hitrimi prehodnimi pojavi, znanega pod imenom računalniški program WAHA (Tiselj et al. [126]). Enačbe programa WAHA so povzete v dodatku Appendix C.

**Novi členi v ravnovesnih enačbah.** Primerjava enačb (G-3), (G-4) in (G-5), zapisanih v Lagrangejevih koordinatah, z enačbami (G-6), (G-7) in (G-8), zapisanimi v Eulerjevih koordinatah pokaže, da se v novih enačbah pojavijo novi členi in nove spremenljivke:

- V ravnovesnih enačbah se pojavi nov diferencialni člen oblike $u_x \frac{\partial}{\partial s}...$ oz. $\left(u_x + \mu v_k\right) \frac{\partial}{\partial s}...$, ki predstavlja popravek konvekcijskega člena zaradi osnega gibanja cevovoda. Ta člen postane pomemben pri večjih premikih cevovoda.
- Vsi prostorski odvodi so pomnoženi s korekcijskim faktorjem zaradi osnega raztezanja $\mu$. Osni premiki cevovoda so običajno nekaj velikostnih redov manjši od prečnih premikov, zato: $\mu \cong 1$.
- Člen $u_y / R_p$ predstavlja prispevek prečnega gibanja cevi k ravnovesju mase. Člen v ITK predstavlja mehanizem vozliščne sklopitve in postane različen od nič v krivinah. Člen vozliščne sklopitve je najpomembnejši novi člen, brez katerega ni mogoče opisati ITK.

## G.3. Dinamika poljubno ukrivljenega cevovoda

Obravnavani cevovodi so poljubno ukrivljene 1D konstrukcije v prostoru. Za opis takega cevovoda je najprimernejši splošni parameter krožnega loka *s*. Izpeljava temelji na osnovnih zvezah elastomehanike med napetostmi in deformacijami, ter na drugem in tretjem Newtonovem zakonu. Po izpeljavi dobimo naslednji dve enačbi za osno nihanje cevovoda:

$$\frac{1}{ES_t}\frac{\partial N_x}{\partial t}-\frac{\nu R}{Ee}\frac{\partial p}{\partial t}-\frac{\partial u_x}{\partial s}=-\frac{u_y}{R_p} \quad \text{in} \quad m_s\frac{\partial u_x}{\partial t}-\frac{\partial N_x}{\partial s}=-\frac{Q_y}{R_p}+SF_{k,t}+S_tF_{t,gx}+\frac{F_x}{\Delta s} \tag{G-9}$$

Enačbi sta močno sklopljeni s termodinamiko tekočine preko diferencialnega člena v katerem nastopa časovni odvod tlaka. Prečno in rotacijsko nihanje je sklopljeno, zato enačbe vedno pišemo skupaj, hkrati pa štiri enačbe prečnega in rotacijskega nihanja predstavljajo osnovne enačbe Timošenkovega nosilca (dodatek Appendix F, Taylor in Yau 2003 [110], Menez et al. 2005 [87]). Timošenkove enačbe nihanja lahko zapišemo za dve ravnini, prva je ravnina ukrivljenosti cevovoda (koleno), druga pa je pravokotna na prvo ravnino. Osnovni pojavi ITK se najlažje opišejo, če se uporabi ravninski cevovod, zato je velik poudarek v tej disertaciji namenjen takim cevovodom. Enačbe prečnega in rotacijskega gibanja cevovoda v ravnini ukrivljenosti so:

$$\frac{1}{\kappa S_tG}\frac{\partial Q_y}{\partial t}-\frac{\partial u_y}{\partial s}=\frac{u_x}{R_p}+\frac{u_z}{T_p}-\varphi_z \quad \text{in} \quad m_T\frac{\partial u_y}{\partial t}-\frac{\partial Q_y}{\partial s}=\frac{N_x-Sp}{R_p}+\frac{Q_z}{T_p}+m_Tg\cos(\gamma)-\frac{F_y}{\Delta s} \tag{G-10}$$

$$\frac{1}{EI_t}\frac{\partial M_z}{\partial t}-\frac{\partial \varphi_z}{\partial s}=-\frac{\varphi_y}{T_p} \quad \text{in} \quad I_t\rho_t\frac{\partial \varphi_z}{\partial t}-\frac{\partial M_z}{\partial s}=-\frac{M_y}{T_p}+Q_y \tag{G-11}$$

Čeprav so cevovodi simetričnega okroglega preseka, se enačbe za gibanje v ravnini ukrivljenosti in v pravokotni ravnini med seboj razlikujejo. Razlike so v členih izvirov:

$$\frac{1}{\kappa S_tG}\frac{\partial Q_z}{\partial t}-\frac{\partial u_z}{\partial s}=-\frac{u_y}{T_p}-\varphi_y \quad \text{in} \quad m_T\frac{\partial u_z}{\partial t}-\frac{\partial T_z}{\partial s}=-\frac{Q_y}{T_p}+m_Tg\cos(\gamma)-\frac{F_z}{\Delta s} \tag{G-12}$$

$$\frac{1}{EI_t}\frac{\partial M_y}{\partial t}-\frac{\partial \varphi_y}{\partial s}=\frac{\varphi_x}{R_p}-\frac{\varphi_z}{T_p} \quad \text{in} \quad I_t\rho_t\frac{\partial \varphi_y}{\partial t}-\frac{\partial M_y}{\partial s}=\frac{M_x}{R_p}+\frac{M_z}{T_p}+Q_z \tag{G-13}$$

Enačbi torzijske dinamike cevovoda sta:

$$\frac{1}{GJ_t}\frac{\partial M_x}{\partial t}-\frac{\partial \varphi_x}{\partial s}=-\frac{\varphi_y}{R_p} \quad \text{in} \quad \rho_tJ_t\frac{\partial \varphi_x}{\partial t}-\frac{\partial M_x}{\partial s}=-\frac{M_y}{R_p} \tag{G-14}$$

Ob predpostavki, da je cevovod raven, odpadejo vsi členi v izvirih, ki imajo v delitelju radij ukrivljenosti cevi $R_p$ ali radij torzijske ukrivljenosti cevi $T_p$, saj se v takih primerih oba parametra približujeta neskončnosti. Enačbe (G-9) do (G-14) se poenostavijo in postanejo identične standardnim enačbam, ki se uporabljajo v simulacijah ITK (Wiggert, Hatfield in Stuckenbruck [143]). Primerjava pokaže, da so členi z radijem ukrivljenosti in torzijskim radijem ukrivljenosti novi, predstavljajo pa mehanizem vozliščne sklopitve. Simulacije ITK v poljubno ukrivljenih cevovodih niso mogoče brez teh členov. To pomanjkljivost standardnih enačb rešujejo tako, da cevovod razrežejo na odsekoma ravne odseke, kolena in vozliščno sklopitev pa opišejo z dodatnimi enačbami (Tijsseling [115]). Enačbe dinamike cevovoda so uporabne tudi za opis nihanja cevovoda (Lavooij in Tijsseling [75]), izračun lastne frekvence in statičnih sil in premikov cevovoda (z in brez polnila - vode).

## G.4. Fizikalni modeli za opis ITK

Za opis ITK lahko uporabimo različne modele za različno kompleksne pojave. Osnovni in tukaj največkrat uporabljeni model za simulacije eksperimentov je osem-enačbni kvazi-dvofazni model ITK za

ravninski cevovod, ki je v nadaljevanju podrobneje predstavljen. Najbolj splošni model sestavlja 18 enačb z naslednjimi osnovnimi spremenljivkami (Tiselj [122] ali Hirsch [57]):

- 6 spremenljivk za tekočino: hitrost vsake faze $v_g$ in $v_f$, tlak $p$, volumski delež pare $\alpha$ in specifična notranja energija vsake faze $e_g$ and $e_f$.
- 12 spremenljivk za konstrukcijo: osna hitrost cevi $u_x$ in osna sila $N_x$, prečni hitrosti cevi $u_y$ in $u_z$ in prečni sili $Q_y$ in $Q_z$, rotacijski hitrosti $\varphi_z$ in $\varphi_y$ in upogibna momenta $M_z$,in $M_y$, ter torzijska rotacijska hitrost $\varphi_x$ in torzijski moment $M_x$.

Izbran set osnovnih spremenljivk je najprimernejši in najučinkovitejši za splošne simulacije ITK. Fizikalne modele, sestavljene iz parcialnih diferencialnih enačb prvega reda zapišemo v naslednji vektorski obliki:

$$\mathbf{A}\frac{\partial\vec{\psi}}{\partial t}+\mathbf{B}\frac{\partial\vec{\psi}}{\partial s}=\vec{S} \qquad \text{oz. po preureditvi} \qquad \frac{\partial\vec{\psi}}{\partial t}+\mathbf{C}\frac{\partial\vec{\psi}}{\partial s}+\vec{R}=0 \tag{G-15}$$

kjer sta **A** in **B** matriki sistema, $\vec{\psi}$ je vektor osnovnih spremenljivk, $\vec{S}$ in $\vec{R}$, sta vektorja izvirov, **C** pa je Jacobijeva matrika. Sistemi enačb so hiperbolični, kar pomeni da je Jacobijeva matrika diagonalizabilna, lastne vrednosti obstajajo, so realne, število neodvisnih lastnih vektorjev je enako dimenziji Jacobijeve matrike. Diagonalizacija Jacobijeve matrike je osnoven korak pri uporabi izbrane numerične metode.

**Zapis osnovnih enačb z osnovnimi spremenljivkami.** Preureditev enačb (G-3), (G-4) in (G-5) tako, da v diferencialnih členih nastopajo samo osnovne spremenljivke, ter vključitev zveze za specifično deformacijo prečnega preseka in enačbe stanja tekočine, da ohranitvene enačbe v naslednji obliki, ki je dejansko primerna za uporabo v fizikalnih modelih ITK:

$$\begin{aligned}
&\alpha_k\left(\left(\frac{\partial\rho_k}{\partial p}\right)_{e_k}+\rho_k\frac{2R}{Ee}\left(1-\nu^2\right)\right)\frac{\partial p}{\partial t}+\rho_k\frac{\partial\alpha_k}{\partial t}+\alpha_k\left(\frac{\partial\rho_k}{\partial u_k}\right)_p\frac{\partial e_k}{\partial t}-\alpha_k\rho_k\frac{2\nu}{ES_t}\frac{\partial N_x}{\partial t}+\\
&\alpha_k\left(\left(\frac{\partial\rho_k}{\partial p}\right)_{e_k}+\rho_k\frac{2R}{Ee}\left(1-\nu^2\right)\right)\left(u_x+\mu v_k\right)\frac{\partial p}{\partial s}+\rho_k\left(u_x+\mu v_k\right)\frac{\partial\alpha_k}{\partial s}+\\
&\alpha_k\left(\frac{\partial\rho_k}{\partial e_k}\right)_p\left(u_x+\mu v_k\right)\frac{\partial e_k}{\partial s}-\alpha_k\rho_k\frac{2\nu}{ES_t}\left(u_x+\mu v_k\right)\frac{\partial N_x}{\partial s}+\mu\alpha_k\rho_k\frac{\partial v_k}{\partial s}=\frac{u_y}{R_p}\alpha_k\rho_k-i\Gamma_g
\end{aligned} \tag{G-16}$$

$$\alpha_k\rho_k\frac{\partial v_k}{\partial t}+\alpha_k\rho_k\left(u_x+\mu v_k\right)\frac{\partial v_k}{\partial s}+\mu\alpha_k\frac{\partial p}{\partial s}=i\Gamma_g\left(v_k-v_i\right)+iF_i+F_{k,gx}-F_{k,t} \tag{G-17}$$

$$\begin{aligned}
&\alpha_k\rho_k\frac{\partial e_k}{\partial t}+\alpha_k\rho_k\left(u_x+\mu v_k\right)\frac{\partial e_k}{\partial s}+\mu\alpha_k p\frac{\partial v_k}{\partial s}+\mu p v_k\frac{\partial\alpha_k}{\partial s}+\mu\alpha_k v_k p\frac{2R}{Ee}\left(1-\nu^2\right)\frac{\partial p}{\partial s}-\\
&\mu\alpha_k v_k p\frac{2\nu}{ES_t}\frac{\partial N_x}{\partial s}=Q_{ik}-i\Gamma_g\left(h_k-e_k\right)
\end{aligned} \tag{G-18}$$

**Izotermični kvazi-dvofazni model ITK.** Ohranitvene enačbe v osnovnih spremenljivkah se ob določenih predpostavkah dodatno poenostavijo. V obravnavanih eksperimentih vedno nastopa voda pri skoraj konstantni sobni temperaturi in zaradi specifičnih lastnosti stanja take tekočine, se kontinuitetna in gibalna enačba za kapljevino poenostavita v:

$$\frac{1}{\rho_f c_f^2}\frac{\partial p}{\partial t}-\frac{2\nu}{ES_t}\frac{\partial N_x}{\partial t}+\left(u_x+\mu v_f\right)\frac{1}{\rho_f c_f^2}\frac{\partial p}{\partial s}-\frac{2\nu}{ES_t}\left(u_x+\mu v_f\right)\frac{\partial N_x}{\partial s}+\mu\frac{\partial v_f}{\partial s}=\frac{u_y}{R_p} \tag{G-19}$$

$$\rho_f\frac{\partial v_f}{\partial t}+\rho_f\left(u_x+\mu v_f\right)\frac{\partial v_f}{\partial s}+\mu\frac{\partial p}{\partial s}=F_{f,gx}-F_{f,t} \tag{G-20}$$

kjer je $c_f$ efektivna hitrost zvoka definirana s poenostavljeno zvezo:

$$c_{0,f}^2 \cong \left(\frac{\partial p}{\partial \rho_f}\right)_{e_f} \quad \text{in po Kortewegovi enačbi:} \quad \frac{1}{c_f^2} = \frac{1}{c_{0,f}^2} + \rho_f \frac{2R}{Ee}(1-\nu^2) \tag{G-21}$$

Dobljeni sistem dveh parcialnih diferencialnih enačb je izredno pomemben za simulacije ITK v ravninskih cevovodih z enofazno tekočino pri sobni temperaturi, saj enačbe za paro in energijsko enačbo v takšnih primerih lahko zanemarimo. Sami enačbi omogočata opis enofaznega toka, z dodatno ravnovesno enačbo za volumski delež pare, pa dobimo izredno zanimiv in zmogljiv kvazi-dvofazni sistem enačb za simulacije izotermnih oz. adiabatnih dvofaznih hitrih prehodnih pojavov.

Model dvofaznega toka, oziroma kavitacije se imenuje kvazi-dvofazen, zato ker temelji na predpostavki, da je med kavitacijo absolutni tlak v tekočini konstanten in enak tlaku nasičenja pare ($p = p_{sat}$). Taka predpostavka je izpolnjena le v izotermnem toku tekočine, saj je tlak nasičenja sicer funkcija temperature. Uporabili smo naslednjo ravnovesno enačbo za volumski delež pare $\alpha$ (Simpson [103]):

$$\frac{\partial \alpha}{\partial t} + \frac{\partial \alpha v_f}{\partial s} = 0 \quad \Rightarrow \quad \frac{\partial \alpha}{\partial t} + v_f \frac{\partial \alpha}{\partial s} + \alpha \frac{\partial v_f}{\partial s} = 0 \tag{G-22}$$

Enačba preprosto kaže, da je volumski delež pare neposredno odvisen od inercije vodnih stolpcev v dveh sosednjih odsekih cevi. Termični vplivi na dvofazni tok se ne upoštevajo.

**Nelinearni osem-enačbni model kvazi-dvofaznega toka v ravninskem cevovodu.** V disertaciji smo se omejili na kvazi-dvofazni model dvofaznega toka in na cevne konstrukcije v ravnini. Osnovni model je tako sestavljen iz dveh enačb za opis prehodnega pojava v tekočini, dveh enačb osnega nihanja in štirih enačb prečnega nihanja cevovoda. Osnovne matrike sistema v vektorski obliki se zapiše:

$$\mathbf{A} = \begin{bmatrix} 0 & \frac{1}{\rho_f c_f^2} & 0 & -\frac{2\nu}{ES_t} & 0 & 0 & 0 & 0 \\ \rho_f & 0 & 0 & 0 & 0 & 0 & 0 & 0 \\ 0 & 0 & m_s & 0 & 0 & 0 & 0 & 0 \\ 0 & -\frac{\nu R}{Ee} & 0 & \frac{1}{ES_t} & 0 & 0 & 0 & 0 \\ 0 & 0 & 0 & 0 & 0 & \frac{1}{\kappa G S_t} & 0 & 0 \\ 0 & 0 & 0 & 0 & m_T & 0 & 0 & 0 \\ 0 & 0 & 0 & 0 & 0 & 0 & 0 & \frac{1}{EI_t} \\ 0 & 0 & 0 & 0 & 0 & 0 & \rho_t I_t & 0 \end{bmatrix} \tag{G-23}$$

$$\mathbf{B} = \begin{bmatrix} \mu & (u_x + \mu v_f)\frac{1}{\rho_f c_f^2} & 0 & -(u_x + \mu v_f)\frac{2\nu}{ES_t} & 0 & 0 & 0 & 0 \\ \rho_f (u_x + \mu v_f) & \mu & 0 & 0 & 0 & 0 & 0 & 0 \\ 0 & 0 & 0 & -1 & 0 & 0 & 0 & 0 \\ 0 & 0 & -1 & 0 & 0 & 0 & 0 & 0 \\ 0 & 0 & 0 & 0 & -1 & 0 & 0 & 0 \\ 0 & 0 & 0 & 0 & 0 & -1 & 0 & 0 \\ 0 & 0 & 0 & 0 & 0 & 0 & -1 & 0 \\ 0 & 0 & 0 & 0 & 0 & 0 & 0 & -1 \end{bmatrix} \tag{G-24}$$

$$\vec{S}^T = \left\{ \frac{u_y}{R_p},\ F_{f,gx} - F_{f,t},\ f_x(s,t) - \frac{Q_y}{R_p},\ -\frac{u_y}{R_p},\ \frac{u_x}{R_p} + \frac{u_z}{T_p} - \varphi_z,\ \frac{N_x - Sp}{R_p} + \frac{T_z}{T_p} + f_y(s,t),\ -\frac{\varphi_y}{T_p},\ -\frac{M_y}{T_p} + Q_y \right\} \tag{G-25}$$

Vektor osnovnih spremenljivk: $\vec{\psi}^T = \{v, p, u_x, N_x, u_y, Q_y, \varphi_z, M_z\}$.

**Linearni osem-enačbni model kvazi-dvofaznega toka v ravninskem cevovodu.** Ob predpostavki, da je cev popolnoma ravna, če zanemarimo zunanje sile in trenje in upoštevamo akustično aproksimacijo, ki pravi, da so členi konvekcije zanemarljivi v primerjavi z zvočno hitrostjo potovanja tlačnih valov, se sistem enačb definiran z matrikami od (G-23) do (G-25) poenostavi:

$$\mathbf{A} = \begin{bmatrix} 0 & \frac{1}{\rho_f c_f^2} & 0 & -\frac{2\nu}{ES_t} & 0 & 0 & 0 & 0 \\ \rho_f & 0 & 0 & 0 & 0 & 0 & 0 & 0 \\ 0 & 0 & m_s & 0 & 0 & 0 & 0 & 0 \\ 0 & -\frac{\nu R}{Ee} & 0 & \frac{1}{ES_t} & 0 & 0 & 0 & 0 \\ 0 & 0 & 0 & 0 & 0 & \frac{1}{\kappa G S_t} & 0 & 0 \\ 0 & 0 & 0 & 0 & m_T & 0 & 0 & 0 \\ 0 & 0 & 0 & 0 & 0 & 0 & 0 & \frac{1}{EI_t} \\ 0 & 0 & 0 & 0 & 0 & 0 & \rho_t I_t & 0 \end{bmatrix} \quad \text{in} \quad \mathbf{B} = \begin{bmatrix} 1 & 0 & 0 & 0 & 0 & 0 & 0 & 0 \\ 0 & 1 & 0 & 0 & 0 & 0 & 0 & 0 \\ 0 & 0 & 0 & -1 & 0 & 0 & 0 & 0 \\ 0 & 0 & -1 & 0 & 0 & 0 & 0 & 0 \\ 0 & 0 & 0 & 0 & -1 & 0 & 0 & 0 \\ 0 & 0 & 0 & 0 & 0 & -1 & 0 & 0 \\ 0 & 0 & 0 & 0 & 0 & 0 & -1 & 0 \\ 0 & 0 & 0 & 0 & 0 & 0 & 0 & -1 \end{bmatrix} \tag{G-26}$$

Pri čemer je vektor izvirov: $\vec{S}^T = \{0,\ 0,\ 0,\ 0,\ -\varphi_z,\ 0,\ 0,\ Q_y\}$. Predstavljeni linearni model je dejansko enak modelu, ki so ga uporabili Tijsseling, Vardy in Fan [114] v njihovih simulacijah ITK v (odsekoma) ravnih cevovodih. Tijsseling, Vardy in Fan so v primeru cevovoda s koleni, cevovod razdelili na več ravnih odsekov s konstantnimi geometrijskimi in materialnimi karakteristikami, na kolenih pa so uporabili ustrezne sklopitvene relacije (robne pogoje). V simulacijah so uporabili konstantne lastnosti tekočine, zato je ta sistem enačb znan tudi kot linearni sistem s konstantnimi karakteristikami. Linearni model smo uporabili za primerjavo z rezultati Tijsselinga, Vardya in Fana [114].

**Začetni in robni pogoji.** Za uspešno simulacijo morajo biti začetni in robni pogoji definirani tako, da v sistem ne vnašajo dodatnih valov oz. motenj. Tijsseling [118] predpostavlja, da mora biti na začetku simulacije sistem cevovod-tekočina vedno v ravnovesju. Pri določanju začetnih vrednosti je potrebno upoštevati razlike med relativnimi in absolutnimi vrednostmi osnovnih spremenljivk. Uporabili smo točne lastnosti tekočine (vode), kar pomeni, da mora biti začetni tlak v sistemu absoluten in je tako običajno različen od zunanjega tlaka. V izogib začetnemu neravnovesju je potrebno ustrezno prilagoditi zunanji tlak. V takem primeru je potrebno prišteti napetosti zaradi notranjega tlaka v cevovodu. Najpreprostejši način izračuna ravnovesnih absolutnih vrednosti osnovnih spremenljivk, se izvede tako, da se pred simulacijo prehodnega pojava naredi izračun, v katerem se poišče ravnovesno stanje. Vrednosti spremenljivk v ravnovesju se nato uporabi kot začetne vrednosti pri prehodnem pojavu.

## G.5. Numerična shema

V preteklosti se je na področju ITK najpogosteje uporabljala metoda karakteristik, ki je zelo primerna za reševanje linearnih sistemov enačb s konstantnimi koeficienti. Sistem enačb, ki vsebuje enačbe (G-16), (G-17) in (G-18) je nelinearen, tudi parametri, ki nastopajo v matrikah (na primer od (G-23) do (G-25)) niso konstantni, zato metoda karakteristik ni primerna. Uporabili smo karakteristično privetrno numerično metodo visoke ločljivosti, ki temelji na metodah končnih razlik. Privetrna metoda končnih razlik je primerna za reševanje nelinearnih sistemov, edini pogoj je, da je sistem enačb hiperboličen. Izbrano numerično metodo smo uspešno uporabili tudi pri razvoju programa WAHA [126].

Po vpeljavi karakterističnih spremenljivk $\delta\vec{\xi} = \mathbf{L}^{-1}\delta\vec{\psi} + \mathbf{\Lambda}^{-1}\mathbf{L}^{-1}\vec{R}\delta s$, lahko vektorsko obliko enačb (G-15) zapišemo tudi v karakteristični obliki:

$$\frac{\partial\vec{\xi}}{\partial t} + \mathbf{\Lambda}\frac{\partial\vec{\xi}}{\partial s} = 0 \tag{G-27}$$

kjer je **Λ** matrika lastnih vrednosti (karakteristik) Jacobijeve matrike **C**. Enačbo rešujemo s privetrno shemo, ki omogoča ustrezno ločevanje pozitivnih in negativnih karakteristik (zgornji indeks – za negativne in + za pozitivne karakteristike):

$$\vec{\xi}_j^{n+1} = \vec{\xi}_j^n - (\mathbf{\Lambda}^+)_{j-1/2}^n \left(\vec{\xi}_j^n - \vec{\xi}_{j-1}^n\right)\frac{\Delta t}{\Delta x} - (\mathbf{\Lambda}^-)_{j+1/2}^n \left(\vec{\xi}_{j+1}^n - \vec{\xi}_j^n\right)\frac{\Delta t}{\Delta x} \qquad \text{(G-28)}$$

kjer velja

$$\mathbf{\Lambda}^+ = diag\left(\lambda_1^+,...,\lambda_M^+\right) \text{ in } \lambda_p^+ = \left|\lambda_p\right| \cdot f_p^+ \qquad \text{ter} \qquad \mathbf{\Lambda}^- = diag\left(\lambda_1^-,...,\lambda_M^-\right) \text{ in } \lambda_p^- = \left|\lambda_p\right| \cdot f_p^- \qquad \text{(G-29)}$$

Indeks *p* teče po vseh *M* lastnih vrednostih, korekcijski faktor $f_p$ pa je definiran z enačbo:

$$f_p^+ = max\left(0, \frac{\lambda_p}{|\lambda_p|}\right) \qquad \text{in} \qquad f_p^- = min\left(0, \frac{\lambda_p}{|\lambda_p|}\right) \qquad \text{(G-30)}$$

Matrika $\mathbf{\Lambda}^+$ vsebuje vse pozitivne karakteristike, ki potujejo proti desni, matrika $\mathbf{\Lambda}^-$ vsebuje vse negativne karakteristike, ki potujejo proti levi. Matriko karakteristik **Λ** lahko rekonstruiramo z delnima matrikama $\mathbf{\Lambda}^+$ in $\mathbf{\Lambda}^-$ v vmesni točki *j-1/2* in času *n* s pomočjo zveze: $\mathbf{\Lambda}_{j-1/2}^n = \left(\mathbf{\Lambda}^+\right)_{j-1/2}^n + \left(\mathbf{\Lambda}^-\right)_{j-1/2}^n$.

Shema v enačbi (G-28) je 1. reda natančnosti po kraju in času in je stabilna, če je izpolnjen CFL pogoj:

$$\Delta t \le \frac{\Delta x}{|\lambda_{max}|} \qquad \text{(G-31)}$$

**Karakteristična privetrna shema visoke resolucije.** Osnovna ideja privetrnih shem visoke resolucije je, da so rezultati na gladkih rešitvah najmanj drugega reda natančnosti, medtem ko je v območju nezveznih (strmih) rešitev, uporabljena metoda prvega reda z večjo numerično difuzijo (LeVeque [77,78], Hirsch [57], Toro [128]). Po izpeljavi, ki presega okvir tega povzetka, dobimo karakteristično privetrno shemo visoke resolucije, ki je v osnovi enaka enačbi (G-28). Spremenijo se le korekcijski faktorji definirani v enačbi (G-30):

$$f_p^+ = max\left(0, \frac{\lambda_p}{|\lambda_p|}\right) + \frac{\phi_p}{2}\left(|\lambda_p|\frac{\Delta t}{\Delta x} - 1\right) \qquad \text{in} \qquad f_p^- = min\left(0, \frac{\lambda_p}{|\lambda_p|}\right) - \frac{\phi_p}{2}\left(|\lambda_p|\frac{\Delta t}{\Delta x} - 1\right) \qquad \text{(G-32)}$$

Prvi člen v korekcijskih faktorjih je že znan smerni faktor, drugi člen pa je popravek drugega reda natančnosti določen z omejitvenim faktorjem $\phi_p$ (ang. limiter). Omejitveni faktorji so izpeljani s pomočjo teorije TVD (ang.: total variation diminishing). Numerična shema je TVD, če se celotna variacija (TV) s časom ne povečuje (LeVeque [77,78]). Poznamo več enačb za izračun omejitvenega faktorja, največ se uporabljajo *Minmod*, *Superbee* in *VanLeer*. Če omejitveni faktor postane enak *0*, potem numerična metoda postane metoda prvega reda natančnosti. TVD shema ne generira numeričnih oscilacij.

Po transformaciji karakterističnih spremenljivk nazaj v osnovne dobimo dejansko uporabljeno shemo:

$$\vec{\psi}_j^{n+1} = \vec{\psi}_j^n - \mathbf{C}_{j-1/2}^+ \left(\vec{\psi}_j^n - \vec{\psi}_{j-1}^n\right)\frac{\Delta t}{\Delta x} - \mathbf{C}_{j+1/2}^- \left(\vec{\psi}_{j+1}^n - \vec{\psi}_j^n\right)\frac{\Delta t}{\Delta x} - \mathbf{D}_{j-1/2}^+ \vec{R}_{j-1/2}^n \Delta t - \mathbf{D}_{j+1/2}^- \vec{R}_{j+1/2}^n \Delta t \qquad \text{(G-33)}$$

Karakteristična privetrna shema drugega reda natančnosti pa ima poleg številnih prednosti, tudi pomanjkljivost, saj v rešitev vnaša numerično disipacijo (pravzaprav je numerična disipacija nujno potrebna za stabilnost numerične sheme). Z optimalno izbiro časovnega koraka, uporabo *Superbee* omejitvenega faktorja: $\phi_p = \max\left(0, \min\left(2\theta, 1\right), \min\left(\theta, 2\right)\right)$ in povečevanjem števila računskih volumnov na enoto dolžine, se numerično disipacijo lahko bistveno zmanjša.

**Členi z izviri.** Členi z izviri predstavljajo poseben numeričen problem, saj v določenih primerih postanejo togi. To pomeni, da je potreben integracijski korak bistveno krajši od časovnega koraka definiranega s CFL pogojem (G-31). V uporabljenih členih izvirov nastopata dve vrsti togosti. Prva je posledica temperaturne in mehanske relaksacije v dvofaznem toku (temperatura kapljevine oz. pare ni v nasičenju, hitrosti faz na medfazni ploskvi različni), druga pa zaradi integrirane enačbe nihanja v enačbah Timošenkovega nosilca. Prvi problem se reši z dvokoračno shemo razcepa operatorjev, drugega pa z zmanjšanjem časovnega koraka in implicitnimi iteracijami. Velja, da je celotna numerična shema stabilna, če je časovni korak napredovanja določen po enačbi:

$$\Delta t \le \min\left\{\frac{2\pi}{10}\sqrt{\frac{I_t\rho_t}{\kappa S_t G}}, \frac{\Delta x}{|\lambda_{\max}|}\right\} \tag{G-34}$$

pri čemer prvi člen predstavlja togost izvirov v enačbah Timošenkovega nosilca, drugi pa je CFL pogoj.

## G.6. Računski primer

Vardy and Fan [132] sta raziskovala enofazno ITK v cevovodih obešenih na dolgih jeklenih vrveh. V ta namen sta izdelala eksperimentalno napravo v laboratoriju za hidravliko Univerze v Dundeju (Velika Britanija). Interakcija med tekočino in konstrukcijo v eksperimentalnih napravah je zelo intenzivna. Cevovodi so obešeni na jeklenih vrveh in tako izolirani od okolice. Različni vplivi začetnih pogojev, robnih pogojev, podpor, iniciacije hitrega prehodnega pojava ipd. so izločeni. Slika G-2 kaže obravnavani cevovod z enim kolenom. Hitri prehodni pojav se prične, ko na levi rob cevovoda z določeno hitrostjo udari kladivo (udarna cev). V osnovi enofazne eksperimente je Tijsseling [113] dopolnil z dvofaznimi eksperimenti (zmanjšal je začetni tlak v cevi). Tijsseling [39, 113] je poudaril, da so v času raziskav njegovi eksperimenti edini v katerih sta tako ITK kot kavitacija zelo močni in sta hkrati tudi ustrezno dokumentirani z eksperimentalnimi meritvami (www.win.tue.nl/fsi/). Vsi potrebni podatki o konstrukciji in tekočini so zbrani v tabeli G-3, več podrobnih podatkov pa se lahko dobi v Vardy in Fan [132] ter Tijsseling [39, 113]. V disertaciji smo obravnavali primere z enofaznim in dvofaznim tokom.

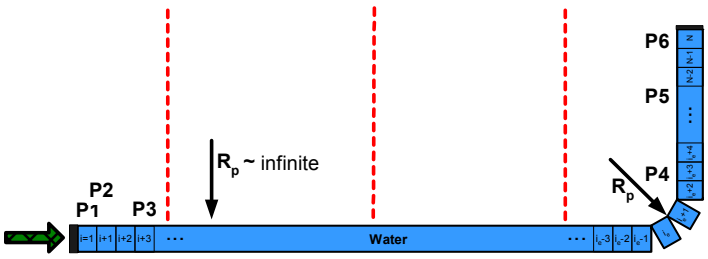


Slika G-2 Numerična shema eksperimenta v cevovodu z enim kolenom.

*Tabela G-3: Lastnosti stanja in materiala za cevovod, vodo in udarno cev.*

| Cevovod | Voda | Udarna cev |
|---|---|---|
| L = 4.51 + 1.34 m | v = 0 m/s | $L_{rod}$ = 5.006 m |
| R = 0.02601 m | K = 2.14 GPa | $R_{rod}$ = 0.02537 m |
| e = 0.003945 m | $p_{1F}$ = 2.0 MPa | $E_{rod}$ = 200 GPa |
| E = 168 GPa | $p_{2F}$ = 0.30, 0.67, 0.87, 1.08, 1.24 MPa | $Y_{rod}$ = 80109.7 kg/s |
| $\rho_t$ = 7985 kg/m$^3$ | T = 20 °C | $v_{0,rod}$ = 0.809 m/s |
| $\nu$ = 0.29 | $\rho_f$ = 999 kg/m$^3$ | $\rho_{rod}$ = 7848 kg/m$^3$ |
| $m_{1,2}$ = 1.312 / 0.3258 kg | | |

**Enofazni eksperiment.** Začetni tlak v cevovodu je bil *p = 20 bar*, kar je zadosten tlak, da med celotnim hitrim prehodnim pojavom v cevi ostane tok enofazen. Upoštevali smo dodatni masi ($m_1$ in $m_2$ v tabeli G-3) na koncih cevovoda zaradi pokrova cevi, prav tako smo upoštevali faktor fleksibilnosti zaradi ovalizacije prereza v kolenu.

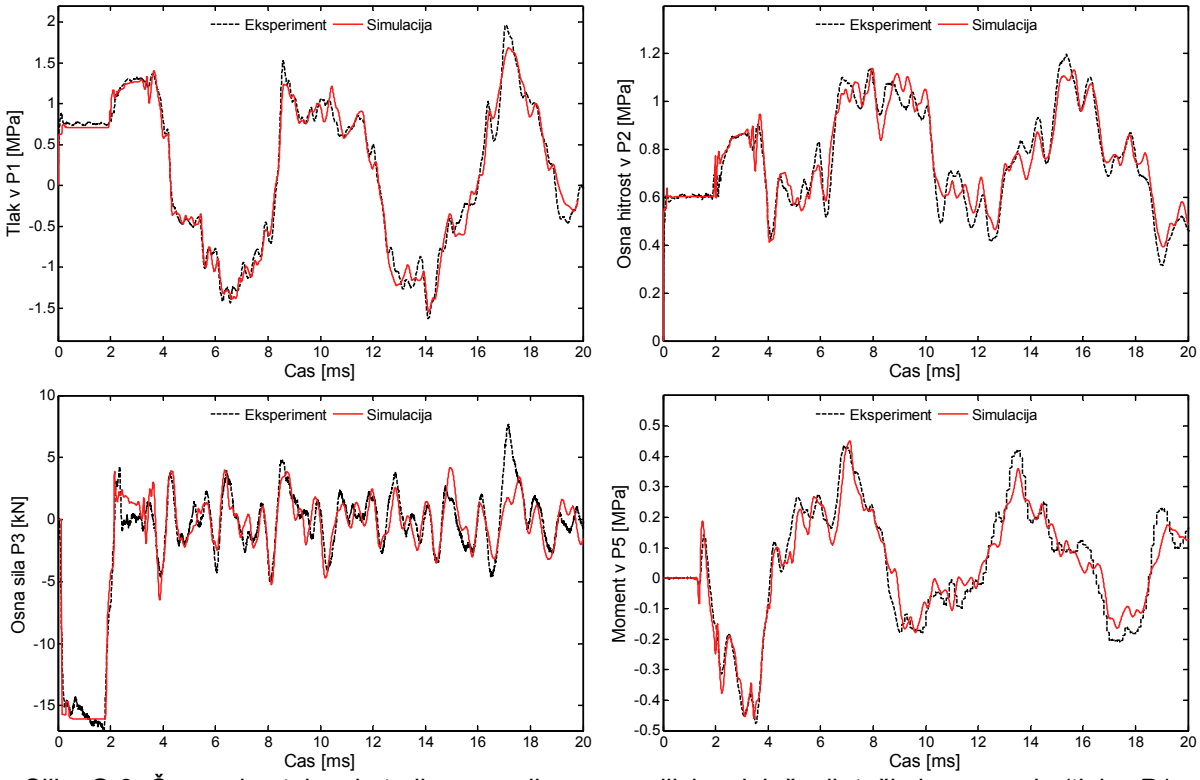


Slika G-3: Časovni potek nekaterih osnovnih spremenljivk v določenih točkah cevovoda (tlak v P1, osna hitrost cevi v P2, osna sila v P3 in moment v P5). Primerjava med simulacijo in eksperimentom.

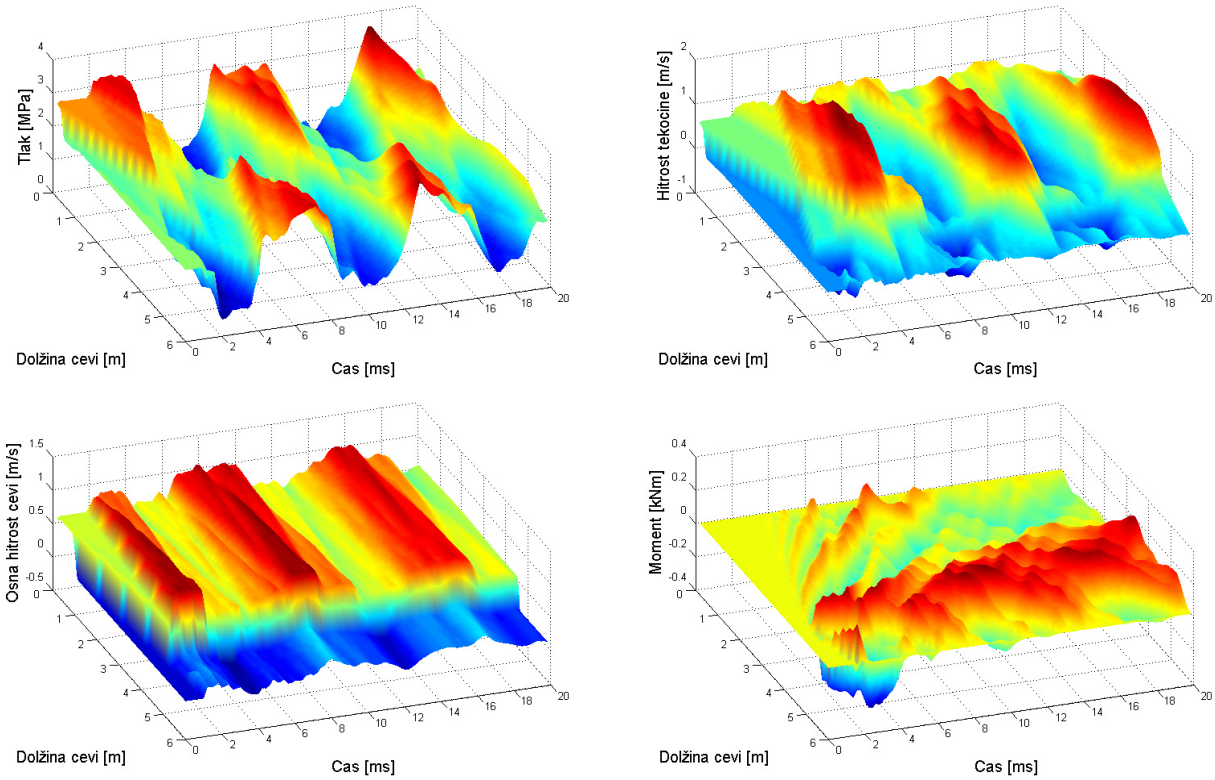


Slika G-4: Osnovne spremenljivke v ravnini čas-prostor.

Slika G-3 prikazuje primerjavo različnih osnovnih spremenljivk z merjenimi. Ujemanje med eksperimentom in simulacijo je izjemno, naš program lahko razglasimo kot preverjen in točen za računanje enofaznih hitrih prehodnih pojavov v poljubno ukrivljenih cevovodih. Potrebno je poudariti, da uspešna simulacija tega eksperimenta ni možna brez ustreznega upoštevanja mehanizmov vozliščne in

Poissonove sklopitve med tekočino in konstrukcijo. Slika G-4 prikazuje nekatere osnovne spremenljivke v ravnini čas-pozicija, kar omogoča zelo pregledno analizo razvoja hitrega prehodnega pojava tako v tekočini kot v stenah cevovoda.

**Faktor upogljivosti zaradi ovalizacije prereza.** Von Karman [133] je že leta 1911 pojasnil, da je togost kolena v primerjavi z ravnim odsekom iste cevi bistveno zmanjšana zaradi ovalizacije prereza, zato je vpeljal faktor upogljivosti in faktor povečanja napetosti. Njegova priporočila so še danes v uporabi praktično nespremenjena. Po ASME standardu (ASME, B&PVC, Class 1 components, NB-3686 [9]) se vztrajnostni moment prereza cevi $I_t$ v kolenu zmanjša za faktor upogljivosti $k$ definiran po enačbi:

$$k = \frac{1.65R^2}{eR_p}\left[\frac{1}{1+6\frac{p}{E}\left(\frac{R}{e}\right)^{7/3}\left(\frac{R_p}{R}\right)^{1/3}}\right] \tag{242}$$

Del enačbe izven oglatega oklepaja predstavlja najpogosteje uporabljeno enačbo, del v oglatem oklepaju pa predstavlja korekcijo zaradi stabilizacijskega učinka notranjega tlaka v cevovodu. Slika G-5 kaže, da je faktor upogljivosti različen od *1* na kolenu, desna slika pa kaže izboljšavo rezultata zaradi upoštevanja ovalizacije. Uporaba faktorja upogljivosti ne vpliva na lastne vrednosti, vpliva pa na lastne vektorje. Upoštevanje faktorja upogljivosti v simulacijah je možno samo s karakteristično privetrno numerično shemo, kar predstavlja prednost izbrane numerične metode.

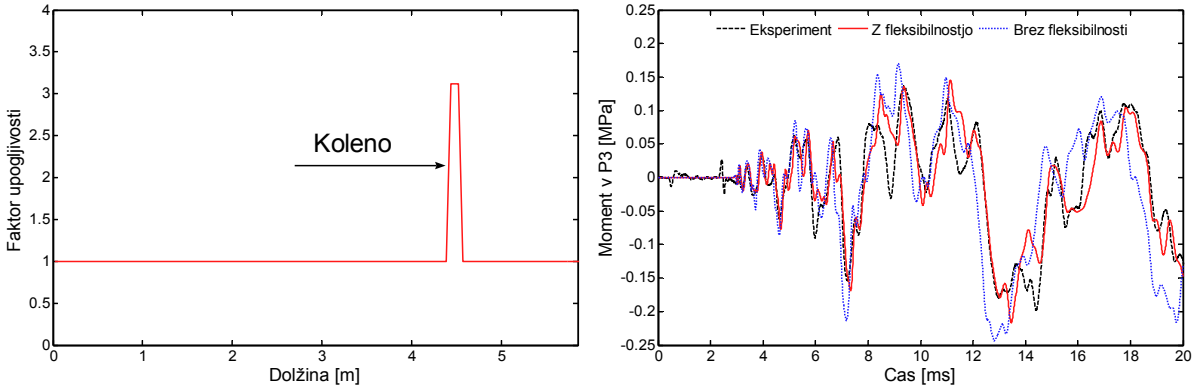


Slika G-5: Levo vzdolžni prerez cevi s faktorjem upogljivosti in desno časovni potek momenta v točki P3: primerjava z in brez upoštevanja faktorja upogljivosti.

**Odebelitev cevovoda.** ASME standard (Boiling and Pressure Vessel code NB-3641), predvideva odebelitev cevovoda na mestih, kjer se bo cev kasneje krivila (mehanska izdelava kolen). Za ostra kolena ($R_p$ < *3R*) se priporoča povečanje stene cevi za *25%*. Slika G-6 kaže, da bi morebitna odebelitev stene vplivala na lastne vrednosti sistema in posledično na rezultate (zmanjšani maksimalni momenti). V eksperimentu uporabljena cev ni bila odebeljena na kolenu. Karakteristična privetrna numerična shema je za upoštevanje te izboljšave fizikalnega modela bolj primerna kot metoda karakteristik.

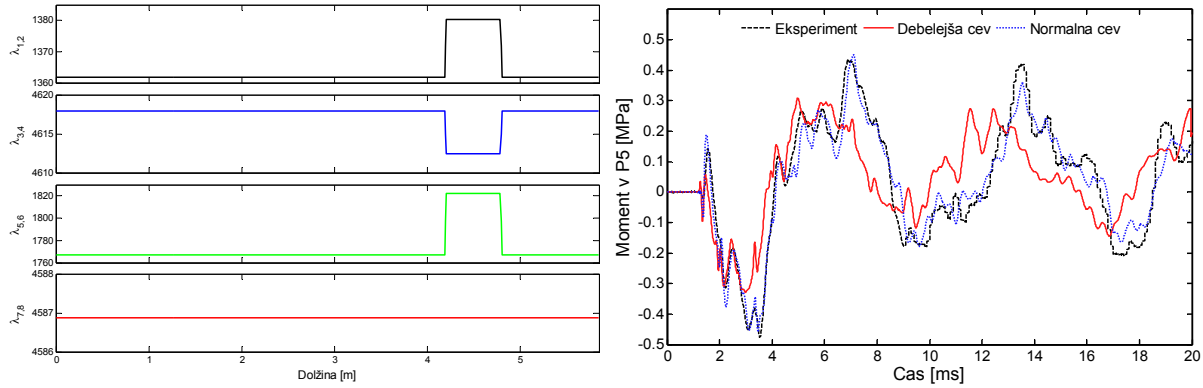


Slika G-6: Levo vzdolžni prerez lastnih vrednosti, desno časovni potek momenta v P5.

**Enačbe stanja tekočine.** Uporaba karakteristične privetrne sheme omogoča uporabo natančnejših enačb stanja tekočine, kar pomeni, da se lastnosti stanja računajo v vsakem časovnem koraku v vsakem računskem volumnu. Obravnavani eksperiment je bil opravljen pri sobni temperaturi, točne vrednosti pa avtorji niso navedli. Tabela G-4 in slika G-7 kažeta, da je točna začetna temperatura zelo pomembna za izračun. Stanje tekočine vpliva na karakteristično hitrost potovanja valov v tekočini in tabela G-4 kaže, da v samo *6* stopinj hladnejši vodi, valovi potujejo *20 m/s* počasneje. Ob splošno sprejetem dejstvu, da se lastnosti tekočine v hladni vodi praktično ne spreminjajo, pa tabela G-4 in slika G-7 kažeta, da razlike v gostoti ali modulu stisljivosti vodita k razlikam v zvočni hitrosti. Primerjali smo tudi uporabo konstantnih in točnejših lastnih vrednosti. Izkaže se, da je v enofaznih eksperimentih ta razlika zelo majhna in ne opravičuje uporabe natančnejših lastnosti stanja, medtem ko brez točnejših lastnosti stanja ni možno računati prehodnih pojavov v topli/vroči vodi oziroma v dvofaznem toku.

*Tabela G-4: Lastnosti stanja tekočine (voda).*

| Parameter | T = 293 | T = 287 |
|---|---|---|
| Gostota [kg/m$^3$] | 999.12 | 1000.16 |
| Modul stisljivosti [GPa] | 2.1887E9 | 2.1401E9 |
| Zvočna hitrost [m/s] | 1480.1 | 1462.8 |

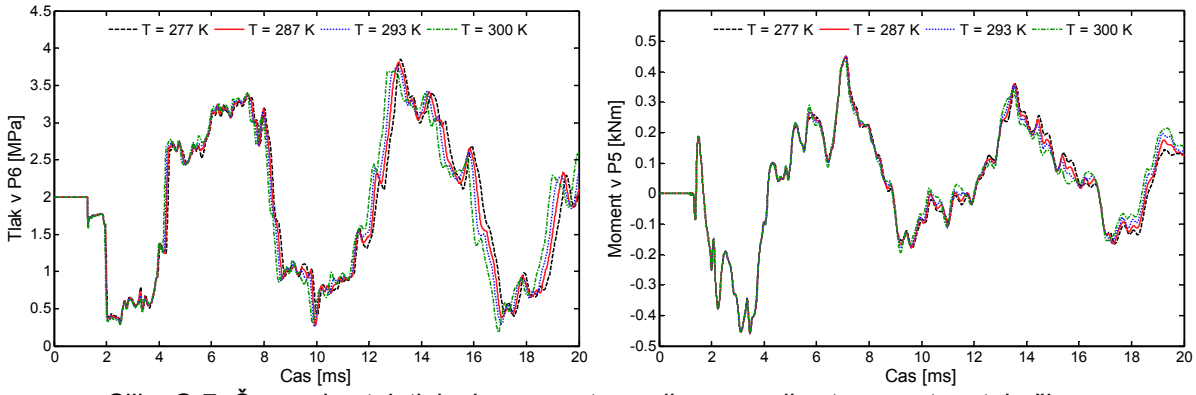


Slika G-7: Časovni potek tlaka in momenta s prikazom vpliva temperature tekočine.

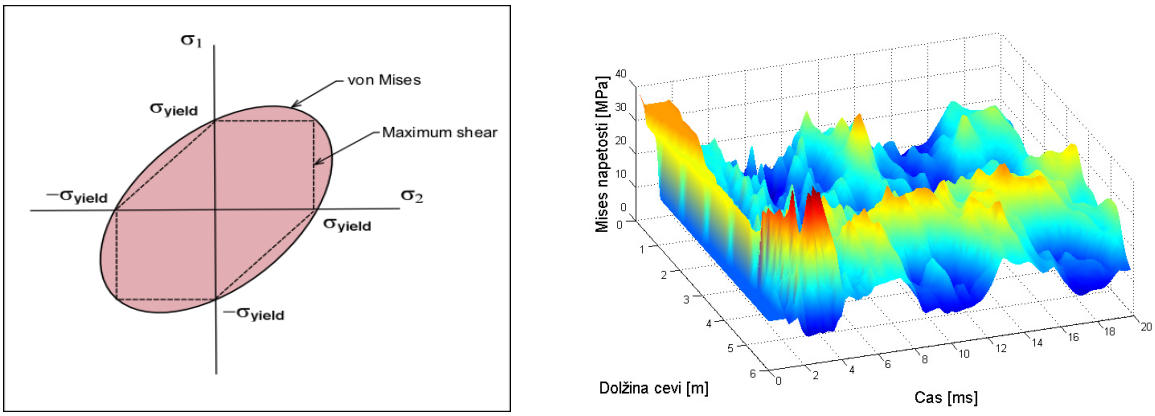


Slika G-8: Levo meja elastičnosti po von Misesu v 2D, desno ovojnica napetosti po von Misesu.

**Napetosti po von Misesu.** Napetost po von Misesu je skalarna vrednost kompleksnega napetostnega tenzorja, definirana kot:

$$\sigma_v = \frac{1}{\sqrt{2}}\sqrt{\left(\sigma_{xx}-\sigma_{yy}\right)^2+\left(\sigma_{yy}-\sigma_{zz}\right)^2+\left(\sigma_{zz}-\sigma_{xx}\right)^2+6\left(\tau_{xy}^2+\tau_{yz}^2+\tau_{zx}^2\right)} \tag{243}$$

Če je napetost po von Misesu manjša od meje elastičnosti ($\sigma_v < \sigma_y$), potem lahko predpostavimo elastične deformacije. Na primer, v 2D konstrukcijah, kamor prištevamo tudi cevovode, mora biti napetostno stanje določeno s $\sigma_1$ in $\sigma_2$ znotraj elipse (slika G-8 levo). Slika kaže tudi konzervativnejši

Tresca kriterij (črtkana črta). Slika G-8 desno kaže položaj in časovni potek napetosti po Misesu (ovojnica največjih napetosti). Kritični del konstrukcije pri obravnavanem prehodnem pojavu je koleno na začetku, ko skozi koleno potuje prvi napetostni val. Največje napetosti so $\sigma_{v,max}$ = *50 MPa*, medtem ko je tipična meja elastičnosti v jeklu $\sigma_y$ = *250 MPa*. Trajanje največjih napetosti je kratko – pulziranje.

**Dvofazni eksperimenti.** Če začetni tlak v cevovodu znižamo, med hitrim prehodnim pojavom pride do kavitacije. Kavitacija je lahko zmerna ali močna, odvisno od začetnega tlaka v sistemu (slike od G-9 do G-11). Glede na uporabljen preprost kvazi-dvofazen model dvofaznega toka in kompleksnost pojava lahko zaključimo, da je ujemanje med meritvijo in eksperimentom zelo dobro. Magnituda in časovni potek največjih napetosti, tlakov in kavitacije sta opisana zelo dobro. Opaziti je možno, da ujemanje nekoliko upada z naraščanjem intenzivnosti kavitacije. Razloge za neujemanje lahko pripišemo (i) uporabi poenostavljenega model dvofaznega toka, (ii) eksperimentalni nezanesljivosti (Tijsseling [113] je pokazal da je ponovljivost relativno dobra, pada pa s povečevanjem intenzivnosti kavitacije), (iii) drugim napakam, kot je na primer numerična disipacija, nepopolni fizikalni modeli, ipd.

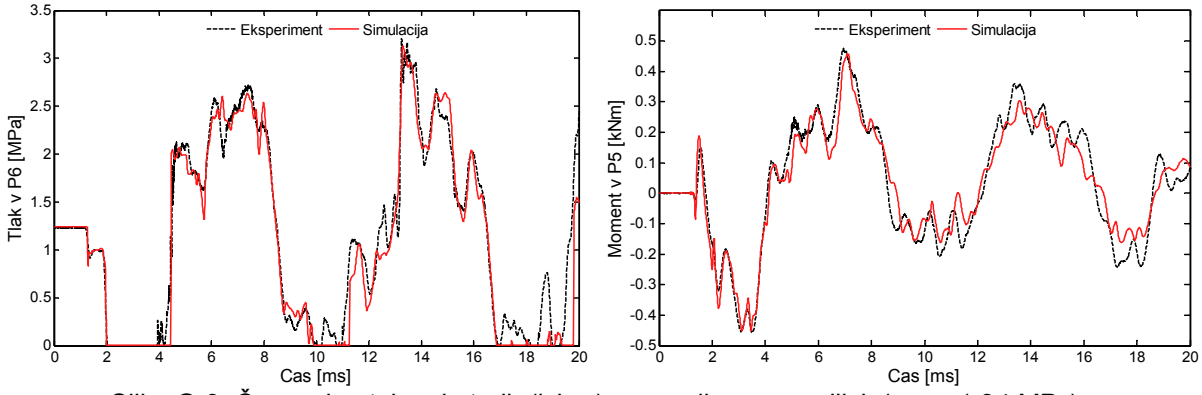

Slika G-9: Časovni potek nekaterih (izbor) osnovnih spremenljivk ($p_{2F}$ = *1.24 MPa*).

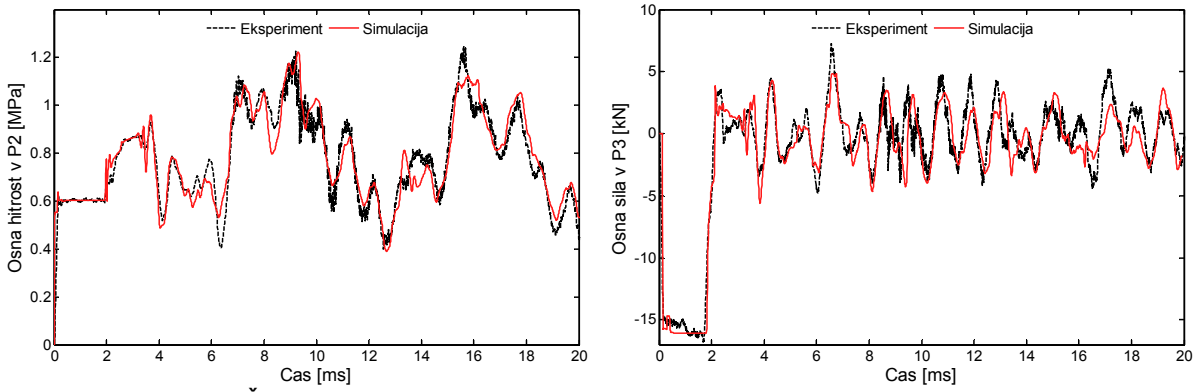

Slika G-10: Časovni potek nekaterih (izbor) osnovnih spremenljivk ($p_{2F}$ = *1.08 MPa*).

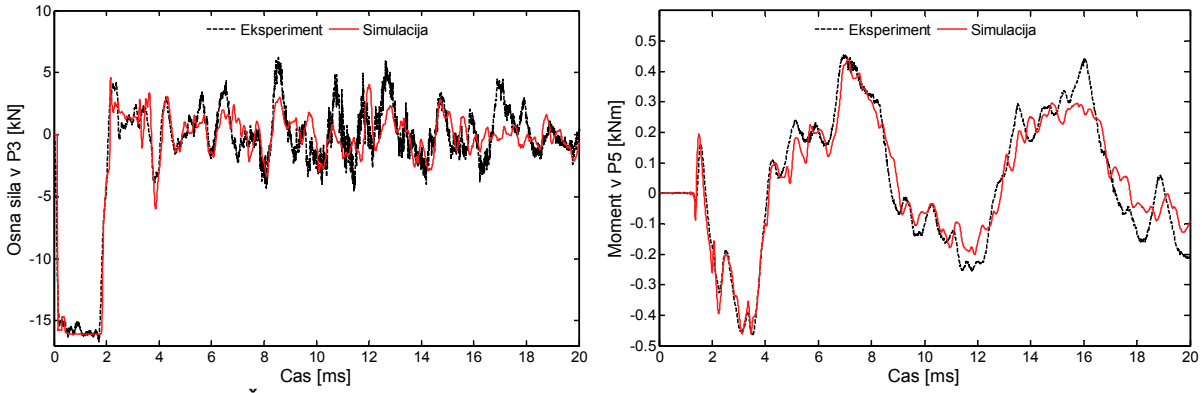

Slika G-11: Časovni potek nekaterih (izbor) osnovnih spremenljivk ($p_{2F}$ = *0.30 MPa*).

**Volumski delež pare.** Slika G-12 kaže volumski delež pare za primer močne kavitacije z in brez upoštevanja ITK mehanizmov. Vidimo, da ITK sicer vpliva na porazdelitev pare vendar minimalno.

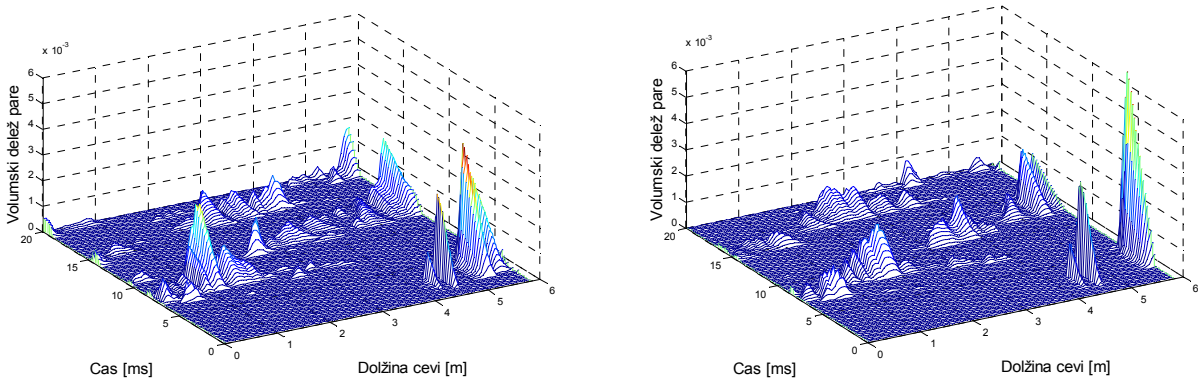


Slika G-12: Volumski delež pare za primer močne kavitacije ($p_{2F}$ = *0.3 MPa*). Levo z upoštevanjem učinkov ITK in desno brez upoštevanja.

**Von Mises napetosti v dvofaznem toku.** Slika G-13 kaže primerjavo napetosti za primer z zmerno in močno kavitacijo, rezultate pa primerjamo tudi s sliko G-8 desno kjer ni kavitacije. Najpomembnejša ugotovitev je, da kavitacija ne vpliva bistveno na napetosti oziroma na sam potek ITK in hitrega prehodnega pojava. Opaziti je le, da so največje napetosti dosežene v enofaznem primeru, najnižje maksimalne napetosti pa v dvofaznem primeru z močno kavitacijo. Razlog je v tem, da je v enofaznem primeru začetni tlak v cevi največji, kar seveda povzroči največje napetosti v stenah cevovoda. Sama kavitacija pa na ITK ne vpliva bistveno.

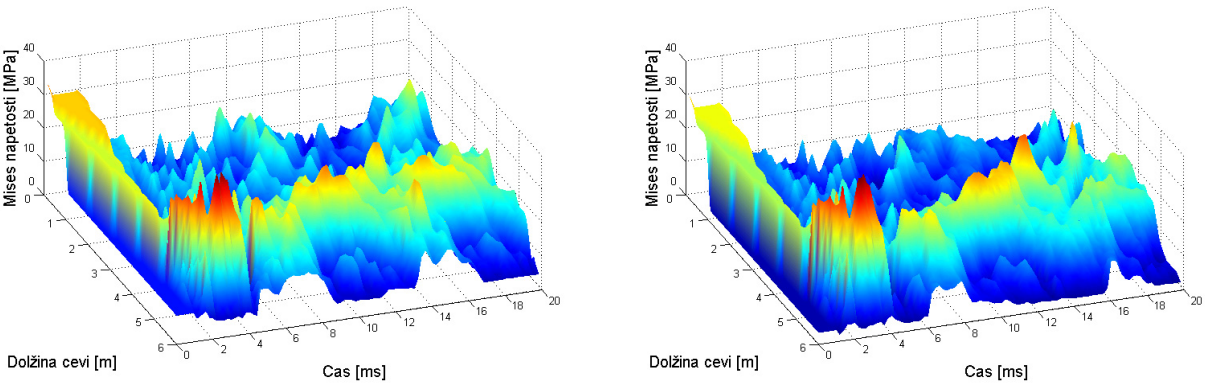


Slika G-13: Ovojnica napetosti po von Misesu za primer zmerne (levo, $p_{2F}$ = *1.08 MPa*) in močne (desno, $p_{2F}$ = *0.3 MPa*) kavitacije.

# G.7. Zaključek

Obravnavali smo interakcijo med tekočino in konstrukcijo (ITK) med hitrimi prehodnimi pojavi v tekočini. Ugotovili smo, da je ITK intenzivna v *mehkih* in slabo podprtih cevovodih v katerih se pretaka skoraj nestisljiva tekočina (eno ali dvofazna). Uporaba togega in preveč podprtega cevovoda je dokaj preprosta rešitev, toda v takih cevovodih, še posebno v jedrskih elektrarnah, bi nastopile velike notranje sile zaradi termičnih obremenitev. Izmenjava kinetične energije med tekočino in cevovodom je v osnovi ugoden pojav, ki pa ga je potrebno ustrezno kontrolirati. Kontrola ITK med hitrimi prehodnimi pojavi ni možna brez ustreznih orodij za numerične simulacije. Za opis ITK v cevnih sistemih so najprimernejši enodimenzionalni sistemi parcialnih diferencialnih enačb, ki vsebujejo tako enačbe za tekočino kot enačbe za konstrukcijo, in ki so nato numerično rešeni z enotno numerično proceduro. V tej disertaciji so na novo izpeljane diferencialne enačbe za tekočino in konstrukcijo, uporabljena je nova numerična metoda, vse skupaj pa smo prevedli v računalniški program.

Izpeljali smo enodimenzionalno splošno ohranitveno enačbo termo-hidrodinamike v poljubno ukrivljenem, premikajočem in deformabilnen cevovodu (Lagrangejev koordinatni sistem). Iz splošne ohranitvene enačbe smo izpeljali kontinuitetno, gibalno in energijsko ravnovesno enačbo. V enačbah se pojavijo novi členi in nove spremenljivke, s katerimi je upoštevana dinamika in ukrivljenost cevovoda. Iz splošnih ohranitvenih enačb je izpeljanih več sistemov enačb, ki so primerni za opis hitrih prehodnih pojavov v različnih tekočinah (izotermični eno in kvazi-dvofazni model, šest-enačbni dvofazni model, tri-enačbni dvofazni model toplotnega in mehanskega ravnovesja). Izpeljali smo tudi 1D fizikalne modele osne, rotacijske, prečne in torzijske dinamike poljubno ukrivljenega cevovoda. Pojavi se več novih členov, vsi pa predstavljajo mehanizem vozliščne sklopitve v kolenih. Različni modeli termo-hidrodinamike in različni fizikalni modeli dinamike cevovoda so nato združeni v več sistemov enačb za opis pojava ITK v cevovodih različne kompleksnosti. Vsi sistemi so sestavljeni iz parcialnih diferencialnih enačb prvega reda, so hiperbolični, lastne vrednosti je možno določiti analitično ali pa numerično. Osnovni fizikalni model ITK v disertaciji je osem-enačbni model sklopitve izotermičnega kvazi-dvofaznega toka in ravninskega cevovoda.

Enačbe smo reševali s karakteristično privetrno shemo končnih razlik visoke resolucije in drugega reda natančnosti. Numerična shema je eksplicitna, občasno pa uporabimo tudi implicitne iteracije, ker so členi izvirov togi in bi bil potreben časovni korak integracije nesprejemljivo majhen. Najpomembnejša prednost uporabljene numerične metode je možnost reševanja nelinearnih sistemov oziroma sistemov enačb s spremenljivimi parametri. Tako je možno uporabiti enačbe stanja tekočine, ki ustrezajo dejanskemu termodinamičnemu stanju tekočine, upoštevanje geometrijskih in materialnih sprememb v cevovodu (prečni prerez, debelina cevi, ukrivljenost cevi, drugačna togost cevi ipd.), možnost upoštevanja dvofaznega toka na poljubnih delih cevovoda, upoštevanje zunanjih obremenitev, togih ali elastičnih podpor, ipd. Numerična metoda vnaša numerično disipacijo, ki pa jo je možno relativno enostavno nadzirati in zmanjševati. Točnost numerične metode smo preverili z uveljavljeno metodo karakteristik, ujemanje rezultatov je zelo dobro, malenkostna odstopanja v nezveznostih lahko pripišemo numerični disipaciji in drugačnemu konceptu računanja.

Rezultate smo preverjali tudi z analitičnimi enačbami, pokazali smo, da je z našim pristopom možno določiti lastno frekvenco nihanja poljubno ukrivljenega cevovoda, prav tako je z veliko natančnostjo možno določiti klasične spremenljivke statike konstrukcij: notranje sile, premike, momente, ipd. Ugotovili smo, da na osno sklopitev cevovoda in tekočine v veliki meri vpliva stisljivost tekočine, medtem ko na prečno sklopitev vpliva predvsem masa tekočine. Pokazali smo obstoj valov imenovanih znanilci in nasledniki, prav tako smo pokazali, da valovi znanilci v določenih primerih lahko preko Poissonovega mehanizma sklopitve povzročijo izredno kavitacijo v sistemu. Izpeljali in preverili smo poenostavljen model dvofaznega toka. S tako imenovanim kvazi-dvofaznim modelom smo uspešno in natančno simulirali več dvofaznih eksperimentov. Vgradili in preverili smo model zmanjšanja togosti kolena zaradi pojava ovalizacije. Uporabili smo tudi debelostenski fizikalni model in pokazali, da upoštevanje debeline cevi za simulacijo praktičnih primerov, ni bistveno. Iz inženirskega stališča je najpomembnejši rezultat napetost izračunana po metodi von Misesa. Največje obremenitve cevovoda so kratkotrajne, pojavljajo pa se na različnih in večinoma v naprej nepredvidljivih delih cevovoda. Mesto in čas največje obremenitve cevovoda je možno napovedati samo z ustrezno računalniško simulacijo.

Izpeljani napredni fizikalni modeli in uporabljena karakteristična privetrna numerična shema so bili prevedeni v računalniški program, ki smo ga obširno in uspešno testirali z obstoječimi eksperimentalnimi in numeričnimi podatki. Vidimo dve možnosti za nadaljevanje raziskav in razvoj programa. Prva je uporaba šest-enačbnega dvotekočinskega modela dvofaznega toka tekočine, druga pa uporaba vseh enačb dinamike konstrukcije, s katerimi bo mogoče opisati dinamiko prostorskega cevovoda. Poudariti je potrebno, da se omenjeni izboljšavi v veliki meri nanašata na programersko delo in iskanje ustreznih računalniških rešitev, medtem ko so teoretične osnove že podane v disertaciji. Obstaja tudi možnost, da se s fizikalnimi modeli in izkušnjami pridobljenimi med izvajanjem raziskav, nadgradi obstoječi termo-hidrodinamični program WAHA, tako, da ga bo mogoče uporabiti tudi za simulacije prehodnih pojavov z upoštevanje interakcije med tekočino in konstrukcijo.

# IZJAVA O AVTORSTVU

Spodaj podpisani Janez Gale izjavljam, da predložena disertacija predstavlja rezultate lastnega znastveno raziskovalnega dela.

Janez Gale